

A Structural Design Methodology for Freeform Timber Plate Structures Using Wood-Wood Connections

Présentée le 14 août 2020

à la Faculté de l'environnement naturel, architectural et construit
Laboratoire de construction en bois
Programme doctoral en génie civil et environnement

pour l'obtention du grade de Docteur ès Sciences

par

Anh Chi NGUYEN

Acceptée sur proposition du jury

Prof. C. J. D. Fivet, président du jury
Prof. Y. Weinand, directeur de thèse
Dr P. Sejkot, rapporteur
Dr A. Liew, rapporteur
Prof. A. Frangi, rapporteur

Education is an admirable thing,
but it is well to remember from time to time
that nothing that is worth knowing can be taught.
— Oscar Wilde

À mes parents

Acknowledgements

I would like to thank my supervisor, Prof. Yves Weinand, for giving me the opportunity to work on this exciting research topic, as well as the National Centre of Competence in Research Digital Fabrication and EPFL for supporting this research. I would also like to express my gratitude to the members of the thesis jury, presided by Prof. Corentin Fivet, namely Dr. Petr Sejkot, Dr. Andrew Liew and Prof. A. Frangi. Their insightful comments and suggestions were highly appreciated and allowed me to reflect on my work and improve the present manuscript.

My sincere thanks goes to all the people who contributed in this thesis and helped me completing it. I would like to show my appreciation to my colleagues from IBOIS, Stéphane Roche, Andrea Štitić, Julien Gamero, Aryan Rezaei Rad, Petras Vestartas, Martin Nakad, Nicolas Rogeau and Bertrand Himmer, for their advice and valuable discussions, as well as their continuous encouragement. Special thanks to Francois Perrin for his help in the laboratory and for his positive words of support throughout this doctoral research. I am also grateful to Francine Sallin for making my life at IBOIS easier and to the team of technicians of the Structural Engineering Group GIS-GE of EPFL for their assistance in the laboratory.

I would like to pay my special regards to my friends, who supported me throughout this thesis. I am deeply thankful for the amazing people I met in Lausanne, Åsa, Robert, Oscar, Solenne, Marta, Conny, Emma, Andrew, Tomás and Lucia. In particular, I would like to express my heartfelt gratitude to Niels for his loving support and encouragement, especially during the stressful times of this thesis, and for proofreading my thesis manuscript.

Most importantly, I would like to thank my family for their unconditional love and support. My deepest gratitude goes to my parents who encouraged me every step of my life. They have always inspired me to do my best and this thesis is therefore dedicated to them.

Lausanne, April 3, 2020

A. C.

Abstract

Over the past decades, timber has gained popularity as a sustainable building material because of the rising environmental awareness. Furthermore, the resurgence of timber has also been encouraged by the advent of the digital age during the 21st century. The development of computer-aided design programming and digital fabrication tools has stimulated significant advances in both architecture and engineering. Within this context, researchers have shown a growing interest in wood-wood connections, inspired by traditional woodworking joints. Geometrically complex timber structures assembled with joints integrated in their plates have been developed using algorithmic geometry processing. However, although their design and fabrication have been automated, research focused on automated numerical tools for their structural analysis has been very limited.

This thesis is providing a design methodology for the structural analysis of timber plate structures composed of a large number of discrete planar elements and wood-wood connections. A finite element model, in which the semi-rigid behaviour of the connections is implemented using springs, is proposed. It is applied to a specific case study, namely the Annen Plus SA head office project in Manternach, Luxembourg, which consists of a series of double-layered double-curved timber plate shells. A design framework is introduced to automate the generation of the model and integrate structural analysis into the existing design and fabrication workflow.

The numerical model was built for both small- and large-scale structures through custom scripts and subsequently assessed through experimental investigations: first, laboratory tests were performed on small assemblies with simplified geometry; secondly, a displacement study was carried out onsite on a 24-metre span structure. Results obtained with the semi-rigid spring model were found to be in good agreement with experimental tests. The proposed model was therefore validated for the serviceability limit state. Furthermore, the semi-rigidity of the connections in translation as well as in rotation was shown to highly influence the model and is therefore crucial for the accuracy of the model.

Based on experimental tests observations, an alternative structural system was proposed and compared to the initial one through numerical investigations within the proposed design framework. A significant influence on the structure's performance was found, demonstrating the possibilities for structural optimisation.

Acknowledgements

Finally, a three-dimensional finite element model for wood-wood connections was investigated. It aimed to predict their semi-rigid behaviour, generally characterised through experimental tests, necessary for their implementation in global models. The material model was evaluated based on shear load tests performed on different engineered wood products. Stiffness and load-carrying capacity of the connections were approximated with numerical simulations. However, experimental tests remain necessary to precisely predict the behaviour of the joints.

This thesis highlights the importance of adopting an integrated design strategy encompassing engineering and fabrication aspects for geometrically complex timber structures, as well as establishing a link between local behaviour of the connections and global behaviour of the structure. The gained knowledge can facilitate the design and realisation of large-scale freeform timber structures using wood-wood connections.

Key words: *timber plate structures, wood-wood connections, digital fabrication, finite element method, semi-rigidity, spring model*

Résumé

Au cours des dernières décennies, le bois a gagné en popularité en tant que matériau de construction durable en raison de la prise de conscience environnementale croissante. De plus, la réapparition du bois dans le domaine de la construction a également été encouragée par l'avènement de l'ère numérique au cours du 21^{ème} siècle. Le développement de la conception assistée par ordinateur et des outils de fabrication numérique a stimulé des avancées significatives tant en architecture qu'en ingénierie. Dans ce contexte, les chercheurs ont montré un intérêt croissant pour les connexions bois-bois, inspirées des joints traditionnels. Des structures en bois géométriquement complexes et assemblées avec des joints intégrés dans leurs plaques ont donc été développées. Cependant, bien que leur conception et leur fabrication aient été automatisées, peu de recherches ont été réalisées en ce qui concerne le développement d'outils numériques automatisés pour leur analyse structurelle.

Cette thèse propose une méthode de modélisation numérique pour l'analyse structurelle de structures en bois composées d'un grand nombre de panneaux et de connexions bois-bois. Un modèle d'éléments finis, dans lequel le comportement semi-rigide des connexions est représenté par des ressorts, est proposé. Il est appliqué à un projet spécifique, à savoir le siège social de la société Annen Plus SA à Manternach, au Luxembourg, qui consiste en une série de coques en bois à double couche à double courbure. Un cadre de conception est introduit pour automatiser la génération du modèle et intégrer l'analyse structurelle au processus de conception et de fabrication existant.

Le modèle numérique a été construit pour des structures de petite et de grande taille à l'aide de scripts personnalisés et a ensuite été évalué par des études expérimentales : tout d'abord, des tests en laboratoire ont été effectués sur des petites structures avec une géométrie simplifiée ; ensuite, une étude de déplacement a été réalisée sur chantier sur une structure de 24 mètres de portée. Les résultats obtenus avec le modèle de ressorts semi-rigides concordent avec les tests expérimentaux et le modèle proposé a donc été validé pour l'état limite de service. En outre, il a été démontré que la semi-rigidité des connexions en translation ainsi qu'en rotation influence fortement le modèle et est donc cruciale pour la précision du modèle.

Sur base d'observations faites lors des tests expérimentaux, un système structurel alternatif a été proposé et comparé au système initial, au moyen du modèle numérique développé et dans le cadre de conception proposée. Une influence significative sur la performance structurelle a

Acknowledgements

été trouvée, démontrant les possibilités d'optimisation structurelle.

Enfin, un modèle tridimensionnel d'éléments finis pour les connexions bois-bois a été étudié. Il visait à prédire leur comportement semi-rigide, généralement caractérisé par des tests expérimentaux, nécessaire à leur mise en œuvre dans des modèles globaux. Le modèle de matériau a été évalué sur base d'essais de cisaillement effectués sur différents types de panneaux en bois. La rigidité et la capacité des assemblages bois-bois ont été approximées par des simulations numériques. Cependant, des tests expérimentaux restent nécessaires pour prédire avec précision le comportement des assemblages.

Cette thèse souligne l'importance d'adopter une stratégie de conception intégrée englobant les aspects d'ingénierie et de fabrication pour les structures en bois géométriquement complexes, ainsi que d'établir un lien entre le comportement local des connexions et le comportement global de la structure. Les connaissances acquises peuvent permettre de faciliter la conception et la réalisation de grandes structures en bois de forme complexe utilisant des connexions bois-bois.

Mots clés : *structures en bois, assemblages bois-bois, fabrication digitale, méthode d'éléments finis, semi-rigidité, modèle de ressorts*

Zusammenfassung

Holz, ein nachhaltiger Baustoff, hat aufgrund des gestiegenen Umweltbewusstseins während der vergangenen Jahrzehnte deutlich an Popularität gewonnen. Darüber hinaus hat das Aufkommen des digitalen Zeitalters im 21. Jahrhundert seinen Beitrag geleistet. Die Entwicklung von Programmen zum Computer unterstütztes Entwerfen und für digitale Fertigungswerkzeuge, hat sowohl in der Architektur als auch im Ingenieurwesen bedeutende Fortschritte hervorgerufen. In diesem Zusammenhang haben Forscher ein wachsendes Interesse an Holz-Holz-Verbindungen gezeigt, inspiriert von traditionellen Techniken zur Holzverbindung. Geometrisch komplexe Holzstrukturen, die mit in ihre Platten integrierten Verbindungen zusammengefügt werden, wurden mit Hilfe von algorithmischen Geometrie-Prozessen entwickelt. Obwohl Entwurf und Herstellung automatisiert wurden, war die Forschung nach automatisierten, numerischen Methoden für die Strukturanalyse sehr begrenzt.

In dieser Arbeit wird eine Entwurfsmethodik für die Strukturanalyse von Holzplattenstrukturen, die sich aus einer großen Anzahl von diskreten flächigen Elementen und Holz-Holz-Verbindungen zusammensetzen, präsentiert. Es wird ein Finite-Element-Model vorgeschlagen, in dem das halbstarre Verhalten der Verbindungen mit Hilfe von Federn implementiert wird. Dieses wird auf eine spezifische Fallstudie angewendet, nämlich für das Projekt des Hauptsitzes von Annen Plus SA in Manternach, Luxemburg. Die vorgeschlagene Struktur besteht aus einer Reihe von zweischichtigen, doppelt gekrümmten Holzplattenschalen. Dazu wird ein Design-Framework eingeführt, um die Erzeugung des Finite-Element-Model zu automatisieren und die Strukturanalyse in den bestehenden Design- und Fertigungsablauf zu integrieren.

Das numerische Modell wurde sowohl für kleine als auch für große Strukturen mit Hilfe von benutzerdefinierten Skripten erstellt und anschließend durch experimentelle Untersuchungen bewertet: Erstens wurden Labortests an kleinen Baugruppen mit vereinfachter Geometrie durchgeführt; zweitens wurde eine Verschiebungsstudie *in-situ* an einer Struktur mit einer Spannweite von 24 Metern durchgeführt. Die Ergebnisse, die mit dem halbstarren Federmodell erzielt wurden, stimmten mit den experimentellen Tests gut überein. Das vorgeschlagene Modell wurde daher für den Grenzzustand der Gebrauchstauglichkeit validiert. Darüber hinaus zeigte sich, dass die Halbstarreheit der Verbindungen sowohl in Translation als auch in Rotation einen hohen Einfluss auf das Modell hat und daher für die Genauigkeit des Modells entscheidend ist.

Acknowledgements

Basierend auf experimentellen Testbeobachtungen wurde ein alternatives Struktursystem vorgeschlagen und mit Hilfe von numerischen Untersuchungen innerhalb des vorgeschlagenen Konstruktionsrahmens mit dem ursprünglichen System verglichen. Es wurde ein signifikanter Einfluss auf die Leistungsfähigkeit der Struktur gefunden, was die Möglichkeiten der Struktur-optimierung aufzeigte.

Schließlich wurde ein dreidimensionales Finite-Element-Model für Holz-Holz-Verbindungen untersucht. Es zielte darauf ab, ihr halbsteifes Verhalten vorherzusagen, das im Allgemeinen durch experimentelle Tests charakterisiert wird, welche wiederum für die Umsetzung in globale Modelle notwendig sind. Das Materialmodell wurde auf der Grundlage von Scherbelastungsversuchen bewertet, die an verschiedenen Holzwerkstoffprodukten durchgeführt wurden. Steifigkeit und Tragfähigkeit der Verbindungen wurden mit numerischen Simulationen approximiert. Um das Verhalten der Verbindungen genau vorherzusagen ist es jedoch weiterhin notwendig experimentelle Tests durchzuführen.

Diese Thesis unterstreicht die Bedeutung einer integrierten Entwurfsstrategie, die sowohl Ingenieur- und Fertigungsaspekte für geometrisch komplexe Holzstrukturen umfasst als auch eine Verbindung zwischen dem lokalen Verhalten der Holz-Holz-Verbindungen und dem globalen Verhalten des Bauwerks herstellt. Die gewonnenen Erkenntnisse können den Entwurf und die Realisierung von großflächigen Freiform-Holzstrukturen mit Holz-Holz-Verbindungen erleichtern.

Schlüsselwörter: *Holzplattenstrukturen, Holz-Holz-Verbindungen, digitale Fertigung, finite element method, Halbstarrheit, Federmodell*

Contents

Acknowledgements	v
Abstract (English/Français/Deutsch)	vii
List of figures	xvi
List of tables	xxi
1 Introduction	1
1.1 Background	1
1.1.1 Resurgence of Timber	1
1.1.2 Wood-Wood Connections	2
1.1.3 Timber Plate Structures Using Wood-Wood Connections	7
1.2 Research Motivation	13
1.2.1 Problem Statement	13
1.2.2 Research Objectives	14
1.2.3 Methodology	14
1.2.4 Scope	15
1.3 Case Study: Annen Plus SA Head Office	16
1.3.1 Project Description	16
1.3.2 Construction System	16
1.3.3 Construction Material	17
1.3.4 Fabrication and Assembly Process	18
2 Numerical Modelling	19
2.1 Introduction	19
2.2 Design Framework	20
2.3 Finite Element Model Generation	21
2.3.1 Geometry of the Specimens	22
2.3.2 Definition of the Finite Element Model	23
2.3.3 Automatic Generation of the CAD-FEM Exchange Geometry	28
2.3.4 Automatic Generation of the Finite Element Model	31
2.4 Results and Discussion	34
2.4.1 Spring Model for the Connections	34

Contents

2.4.2	Automatic Generation of the Numerical Model	35
2.4.3	Stiffness Components Influence	37
2.5	Conclusions	39
3	Experimental Investigations on Small-Scale Structures	41
3.1	Introduction	41
3.2	Experimental Tests	42
3.2.1	Specimens	42
3.2.2	Test Setup	44
3.2.3	Boundary Conditions	44
3.2.4	Instrumentation	45
3.3	Numerical Model	47
3.3.1	Semi-Rigid Spring Model	47
3.3.2	Material Model	48
3.3.3	Semi-Rigidity of the Connections	48
3.3.4	Mesh Properties	50
3.3.5	Loads and Boundary Conditions	50
3.4	Results and Discussion	51
3.4.1	Experimental Tests	51
3.4.2	Comparison between Experimental and Numerical Results	53
3.5	Conclusions	57
4	Experimental Investigations on a Large-Scale Structure	59
4.1	Introduction	59
4.2	Experimental Tests	61
4.2.1	Specimens	61
4.2.2	Fabrication and Assembly	62
4.2.3	Supports	63
4.2.4	Loading Procedure	63
4.3	Instrumentation	65
4.3.1	Total Station	65
4.3.2	Terrestrial Laser Scanner	66
4.4	Numerical Model	70
4.4.1	Semi-Rigid Spring Model	70
4.4.2	Boundary Conditions and Loads	71
4.5	Results and Discussion	71
4.5.1	Discrete Target Positions	72
4.5.2	Displacement Fields	74
4.6	Conclusions	79

5	Alternative Structural System	81
5.1	Introduction	81
5.2	Structural Systems	82
5.2.1	Initial Herringbone Pattern	82
5.2.2	Shifted Herringbone Pattern	83
5.3	Application to a Large-Scale Structure	86
5.3.1	Design Framework	87
5.3.2	Mesh Segmentation	87
5.3.3	Curvature Analysis	88
5.3.4	Generation of Wood-Wood Connections	88
5.3.5	Full Arch	89
5.4	Numerical Modelling	90
5.4.1	Semi-Rigid Spring Model	90
5.4.2	Contact Modelling	91
5.4.3	Specimens	92
5.4.4	Loads and Boundary Conditions	93
5.5	Results and Discussion	93
5.5.1	Vertical Displacements	93
5.5.2	Forces in the Connections	95
5.6	Conclusions	97
6	3D Finite Element Model for Wood-Wood Connections	99
6.1	Introduction	99
6.2	Experimental Tests	101
6.2.1	Materials	101
6.2.2	Experimental Setup	102
6.2.3	Specimens	103
6.2.4	Loading Procedure	104
6.3	Numerical Model	105
6.3.1	Material Model	106
6.3.2	Continuum Damage Model	106
6.3.3	Failure Modes	108
6.3.4	Damage Evolution	109
6.3.5	Subroutine Algorithm	111
6.3.6	Contact Modelling	112
6.3.7	Mesh	113
6.3.8	Material Properties	115
6.4	Results and Discussion	118
6.4.1	Analysis Procedure	118
6.4.2	Spruce OSB 18/25 mm double-layered	119
6.4.3	Spruce LVL 21 mm double-layered	122
6.4.4	Spruce LVL 39 mm single-layered	125

Contents

6.4.5	Beech LVL 40 mm single-layered	127
6.4.6	CLT 27 mm double-layered	129
6.5	Conclusions	132
7	Conclusions and Outlook	135
7.1	Conclusions	135
7.1.1	Achieved Results	135
7.1.2	Applications to Other Structures	136
7.1.3	Summary	137
7.2	Outlook	137
	Funding	139
A	Experimental Tests on Through-Tenon Wood-Wood Connections	141
A.1	Tension Tests	141
A.2	Shear Tests	142
A.3	Out-of-Plane Shear Tests	143
A.4	Bending Tests	144
A.5	Summary	145
	Bibliography	158
	Curriculum Vitae	

List of Figures

1.1	Global share of buildings and construction final energy and emissions in 2017. Adapted from [114].	1
1.2	The development of wood-wood connections has followed the three successive waves of wood processing technology. Adapted from [94].	3
1.3	Examples of dovetail woodworking joints.	3
1.4	Single-degree-of-freedom (1-DOF) multiple tab-and-slot joints (MTSJ).	5
1.5	Consecutive rotations of the Bryant angles θ_1 , θ_2 and θ_3 defining the geometry of 1-DOF MTSJ.	5
1.6	Serpentine Gallery Pavilion, London, United Kingdom, 2005.	7
1.7	ICD/ITKE Research Pavilion, Stuttgart, Germany, 2011.	8
1.8	Landesgartenschau Exhibition Hall, Schwäbisch Gmünd, Germany, 2014.	9
1.9	Timber Pavilion of the Vidy Theatre, Lausanne, Switzerland, 2017.	10
1.10	Timber folded plate structure with MTSJ-TT.	11
1.11	Prototypes of the Annen Plus SA head office, Manternach, Luxembourg, ongoing.	12
1.12	Design of the Annen Plus SA head office.	16
1.13	Construction system of double-layered double-curved timber plate shells developed by Robeller et al. [80].	17
1.14	Assembly of the Annen Plus SA head office arches.	18
2.1	Design framework proposed for the structural analysis of freeform timber plate structures.	21
2.2	Geometry of the 5×3 boxes prototype.	22
2.3	Schematic representation of the numerical modelling of timber plates.	24
2.4	Schematic representation of the numerical model for TT wood-wood connections.	25
2.5	Mesh convergence with regard to the maximum vertical displacements and total CPU time.	27
2.6	Mesh for displacement studies using S4R elements, resulting from the mesh convergence study.	27
2.7	Mesh convergence with regard to the normal stresses, axial forces and total CPU time.	28
2.8	Comparison between the 3D model geometry and the FEM geometry.	29
2.9	Plane-line intersection methods used to generate the CAD-FEM geometry.	29

List of Figures

2.10	Contour modelling steps of the FEM geometry using plane-plane and line-plane intersection methods.	30
2.11	Joinery modelling steps of the FEM geometry.	31
2.12	Steps for the generation of the FE model in the FEA software.	33
2.13	Vertical displacements of the bottom layer of the 5×3 boxes prototype with simply supported boundary conditions and under self-weight, using one rigid spring per connection ($n = 1$).	34
2.14	Vertical displacement of a 5×3 boxes prototype with simply supported boundary conditions and under self-weight according to the number of springs in parallel distributed along the connections.	35
2.15	Application of the same code generating the CAD-FEM exchange geometry to a set of arches.	35
2.16	Influence of each DOF on the vertical displacement of a 5×3 boxes prototype with simply supported boundary conditions and under self-weight.	37
3.1	Geometry of the 5×3 tested specimens.	43
3.2	One of the three replicates of the 5×3 boxes prototype assembled at the Laboratory for Timber Constructions (IBOIS), EPFL.	43
3.3	Three-point bending test setup for the 5×3 boxes prototypes and measurement instrumentation.	44
3.4	Boundary conditions applied for the tests on 5×3 boxes prototypes.	45
3.5	Digital image correlation system setup with a measurement area of about 3×2 m.	46
3.6	Speckle pattern used for the DIC data acquisition.	47
3.7	Semi-rigid spring model.	48
3.8	Modelling of the boundary conditions.	50
3.9	Load-displacement curves obtained at midspan with LVDTs U_N and U_S	51
3.10	Failure of the 5×3 boxes prototype.	52
3.11	Total load and rotation of the supports, measured by two inclinometers, over time.	53
3.12	Load vs. midspan deflection. Comparison between the linear regression of experimental tests and the numerical results for a load of 50 kN.	54
3.13	Comparison of the vertical displacements between DIC for the test on specimen #1 and the semi-rigid model with hinged rotational stiffness k_4 and k_6 for a load of 50 kN.	55
3.14	Forces per unit width in the X -direction for a surcharge load of 50 kN.	55
3.15	Force in the connections.	56
4.1	Illustration of the Annen Plus SA head office project in Manternach, Luxembourg.	61
4.2	Geometry of the tested prototypes of arch n°22 and half of n°21.	62
4.3	Supports of arch n°22.	63
4.4	Loading procedure for large-scale tests.	64
4.5	Total station setup.	66
4.6	Terrestrial laser scanner survey procedure.	67

4.7	Photograph illustrating the 3D laser scanner FARO [®] Focus ^S 150 and spheres n°4 and 5.	68
4.8	Pre-processing of the point clouds for Load case n°1.	69
4.9	Area of 1 × 1 cm extracted from the pre-processed point cloud of Load case n°1.	69
4.10	Cloud-to-cloud distances computation.	70
4.11	Numerical modelling of the boundary conditions applied on the coarse mesh area of vertical plates.	71
4.12	Comparison between the displacements measured with the total station and results predicted by a rigid model and semi-rigid models with k_4 and k_6 either rigid or hinged.	73
4.13	Distances computation for test n°1 using the least square best fitting plane.	75
4.14	Distances computed from laser scans.	76
4.15	Displacements predicted by the semi-rigid numerical model, with rotational stiffness k_4 and k_6 hinged.	77
4.16	Evaluation of the built geometry.	78
5.1	Initial assembly system developed by Robeller et al. [80] for double-layered double-curved timber plate shells using wood-wood connections.	82
5.2	Continuous failure paths appearing in the initial assembly system due to the herringbone pattern, illustrated for arch n° 22 of the Annen Plus SA head office.	83
5.3	The shifted herringbone pattern introduces gaps in the structure, such that the shape of the horizontal plates was modified.	83
5.4	Assembly sequence of the alternative structural system.	84
5.5	Zones of abutment resulting from the shifted herringbone pattern.	85
5.6	Contact for abutment angles β less than tenon angles α , defined by the insertion vector \mathbf{v}_i	85
5.7	Contact for abutment angles β larger than tenon angles α , defined by the insertion vector \mathbf{v}_i	85
5.8	Possible additional improvement of the structural system by the addition of wood-wood connections between vertical plates.	86
5.9	A feedback loop for structural optimisations is integrated in the design framework introduced in Chapter 2.	87
5.10	Generation of the shifted herringbone pattern.	87
5.11	Curvature analysis.	88
5.12	Generation of through-tenon wood-wood connections for the bottom layer of the shell structure.	89
5.13	General appearance of arch n°22 of the Annen head office project using two difference patterns, axonometry.	89
5.14	General appearance of arch n°22 of the Annen head office project using two difference patterns, top view.	90
5.15	Contact modelling of the abutment zones for abutment angles β less than tenon angles α	91

List of Figures

5.16	Contact modelling of the abutment zones for abutment angles β greater than tenon angles α	92
5.17	Geometry of the 5×5 specimen considered for numerical investigations applying the initial herringbone pattern.	92
5.18	Geometry of the 28-boxes specimen considered for numerical investigations applying the shifted herringbone pattern.	93
5.19	Vertical displacement fields obtained at the bottom layer of the studied specimens for a distributed load of 2 kN/m^2 applied on the top layer.	94
5.20	Load vs. maximum vertical displacement curves for the two structural systems with and without modelling of the contact of abutment zones.	95
5.21	Forces per unit width in the X -direction at the bottom layer of the studied specimens for a distributed load of 2 kN/m^2 applied on the top layer.	96
6.1	Materials used for investigations on TT connections.	101
6.2	Side view of the experimental shear setup.	102
6.3	Shear test specimens.	103
6.4	Experimental protocol prescribed in EN 26891 [24].	105
6.5	Definition of the material directions.	106
6.6	Damage evolution laws.	111
6.7	Flowchart illustrating the algorithm of the USDFLD subroutine for the continuum damage model.	111
6.8	Contact modelling using surface-to-surface interactions illustrated for specimen T2-50.	113
6.9	Mesh convergence study performed for specimen T3-50 under a load of $25 \% F_{\max}$	113
6.10	Stresses along a path passing through the notches (dotted line), which represent singularity points with theoretically infinite stresses, for mesh sizes varying from 10 to 2 mm with steps of 1 mm.	114
6.11	Mesh for the sample T3-50 - Refined mesh element size of 2 mm at the vicinity of the tenon and coarse mesh element size of 16 mm away from this region of interest.	115
6.12	Normal distribution with mean μ and a standard deviation σ for material property parameters X	115
6.13	(a) General shape of the load-displacement curves (b) Tiny asperities at the surface of the faces in contact that are crushed during the first loading.	119
6.14	Load-displacement curves of T1 specimens.	120
6.15	Failure pictures of T1-50 specimens.	120
6.16	Compression failure photographs of T1-80 specimens	121
6.17	Slip modulus of T1 specimens.	121
6.18	Shear stress distribution and shear stress profile along the tenon for specimen T1-80.	122
6.19	Load-displacement curves of T2 specimens.	123
6.20	Failure photographs of T2 specimens.	123

6.21 Slip modulus of T2 specimens.	124
6.22 Shear stress distribution and shear stress profile along the tenon for specimen T2-150.	124
6.23 Load-displacement curves of T3 specimens.	125
6.24 Failure photographs of T3 specimens.	125
6.25 Slip modulus of T3 specimens.	126
6.26 Shear stress distribution and shear stress profile along the tenon for specimen T3-150.	127
6.27 Load-displacement curves of T4 specimens.	127
6.28 Failure photographs of T4 specimens.	128
6.29 Slip modulus: (a) T4-50 (b) T4-100 (c) T4-150.	129
6.30 Shear stress distribution and shear stress profile along the tenon for specimen T4-150.	129
6.31 Load-displacement curves of T5 specimens.	130
6.32 Failure photographs of T5 specimens.	130
6.33 Slip modulus of T5 specimens.	131
6.34 Shear stress distribution and shear stress profile along the tenon for specimen T5-150.	131
A.1 Results of tension load tests on one single through-tenon connection.	142
A.2 Results of shear load tests on two through-tenon connections.	142
A.3 Experimental setup for out-of-plane shear.	143
A.4 Results of out-of plane shear load tests on two through-tenon connections. . .	143
A.5 Bending test setup developed by Roche [83].	144
A.6 Results of bending tests on one single through-tenon connection.	144

List of Tables

1.1	Comparison of shell structures using finger joints developed by the ICD/ITKE.	9
2.1	Size-related parameters of small- and large-scale prototypes composed of 15 and 200 boxes respectively.	36
2.2	Time of each step of the generation of the finite element model for small- and large-scale structures.	36
2.3	Influence of each degree-of-freedom (DOF) on the vertical displacements compared with a rigid model.	38
3.1	Elastic properties of 40 mm thick BauBuche Q panels used for the orthotropic material model [9, 33].	49
3.2	Spring stiffness values used in the FE model for each of the six degrees of freedom.	49
4.1	Displacements of the 16 targets measured with the total station for test n°1 and 2.	72
5.1	Maximum load applied to reach the maximum load-carrying capacity in tension.	97
6.1	Characteristics of the materials used for investigations on TT connections.	101
6.2	Characteristics of the 15 specimens studied, with corresponding geometrical parameters illustrated in Figure 6.3	103
6.3	Elastic properties (mean values) [117, 9, 33, 19].	116
6.4	Poisson's ratio values from literature for spruce and spruce LVL.	117
6.5	Mechanical properties (characteristic values) in MPa [117].	117
6.6	Fracture energy values in N/mm for spruce and beech [88].	118
6.7	Results of T1 specimens.	121
6.8	Results of T2 specimens.	123
6.9	Results of T3 specimens.	126
6.10	Results of T4 specimens.	128
6.11	Results of T5 specimens.	131
A.1	Summary of experimental test results of wood-wood connections for translational degrees of freedom.	145
A.2	Summary of experimental test results of wood-wood connections for the rotational degree of freedom about y.	145

1 Introduction

1.1 Background

1.1.1 Resurgence of Timber

The recent increase in timber construction for both small and large structures has been driven by environmental concerns on the one hand. According to the 2018 Global Status Report of the United Nations Environment and International Energy Agency [114], buildings and construction sector are responsible for 36 % of global final energy use and 39 % of global energy- and process-related carbon dioxide (CO₂) emissions. Among the latter, 28 % come from the manufacture of building construction materials (see Figure 1.1). Furthermore, global buildings energy demand is growing, mainly due to population and floor area growths, both outpacing advances towards sustainable buildings and construction. By 2060, the buildings sector is expected to double, which would correspond to an addition of 230 billion square metres of new buildings. To meet emissions reduction commitments set by the Paris Agreement and limit global temperatures increase to less than 2°C above pre-industrial levels, the global average building energy intensity per square metre needs to be decreased by at least 30 % compared to 2015 [113].

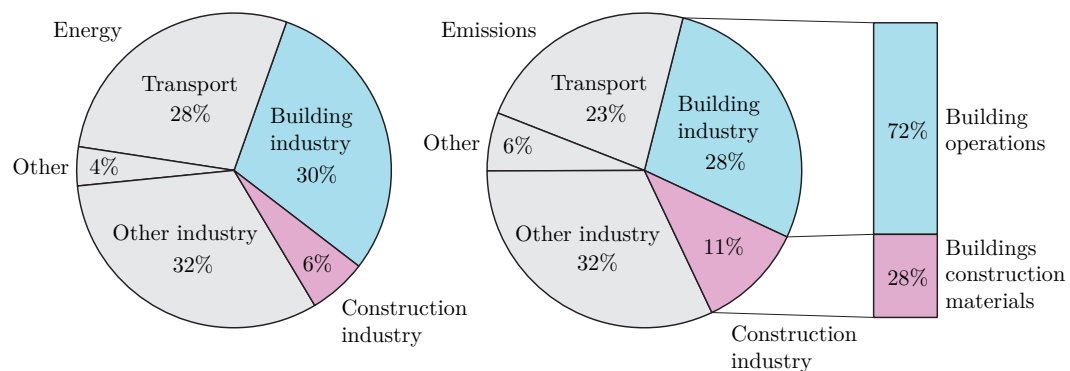


Figure 1.1 – Global share of buildings and construction final energy and emissions in 2017. Adapted from [114].

In light of this, the use of wood-based materials in the construction industry plays an important role to address climate change, wood being a renewable natural resource that can act as carbon sink and offset CO₂ emissions. In particular, a shift from traditional concrete and steel structures to construction using wood-based materials has the potential to significantly reduce energy and emissions during production [38, 68].

On the other hand, timber's resurgence during the 21st century is also linked to the advent of the digital age. The rise of computational design and digital fabrication tools have changed the building industry and stimulated innovation in timber construction. Design exploration of complex structures was made possible through parametric geometry definition scripts, supported by planarisation algorithms to obtain freeform shapes with planar elements [102]. Moreover, as it is a workable material, timber has been pioneering digital fabrication, allowing customised shapes to be produced without being considerably more costly and time-consuming than regular shapes [103]. These advances have been encouraged by the development of engineered wood panel products, available in large dimensions and with improved mechanical properties in comparison with sawn timber, such that high strength-to-weight ratio and flat-packed prefabricated elements facilitating their transport could therefore be obtained. Altogether, significant developments and advances in timber construction, from both architecture and engineering fields, have allowed thin plate shell structures and large spans to be built, widening the range of applications of timber as a construction material.

1.1.2 Wood-Wood Connections

With the rise of digital fabrication and increasing popularity of timber, researchers have shown a growing interest in wood-wood connections, also referred to as integral mechanical attachment [63]. Computer-numerical-control (CNC)-fabricated wood-wood connections, inspired by traditional woodworking joints used in furniture and cabinetmaking, have been developed and applied to both timber frame and timber plate structures. They were shown to be a competitive solution to connect thin timber plates for structural applications, in comparison with standard joining techniques.

Development of Wood-Wood Connections

The development of wood-wood connections can be divided in three periods of time overlapping each other and associated to advances in wood processing technology defined by Schindler [94]: hand-tool, machine-tool and information-tool technologies. The first wave of processing technology is related to the use of traditional woodworking joints, which goes back to ancient times, with examples found in Egyptian furniture and coffins [21]. Over time, timber joinery has been developed in Europe and Asia for furniture and building constructions. Multiple dovetail joints were used to connect two panels to form corner joints in cabinetmaking (see Figure 1.3a), whereas in building constructions, handcrafted load-bearing joints were only used to connect linear elements (see Figure 1.3b). In addition to their mechanical resistance

to shear forces and their ability to transfer bending moments, dovetail joints were providing a solution to the poor dimensional stability of timber subject to swelling, shrinking as well as out-of-plane warping [78]. Throughout the centuries, the geometry of dovetail joints has been improved to increase their mechanical strength [21].

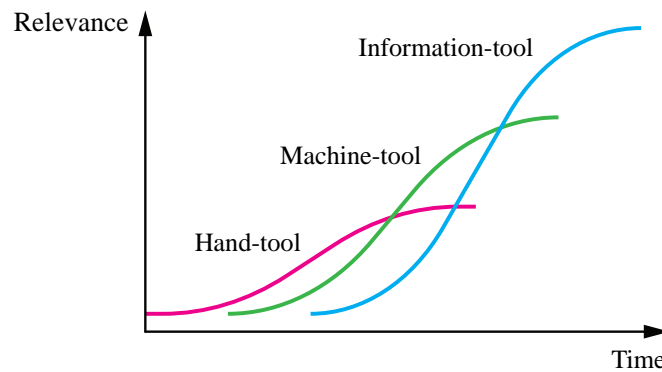


Figure 1.2 – The development of wood-wood connections has followed the three successive waves of wood processing technology. Adapted from [94].

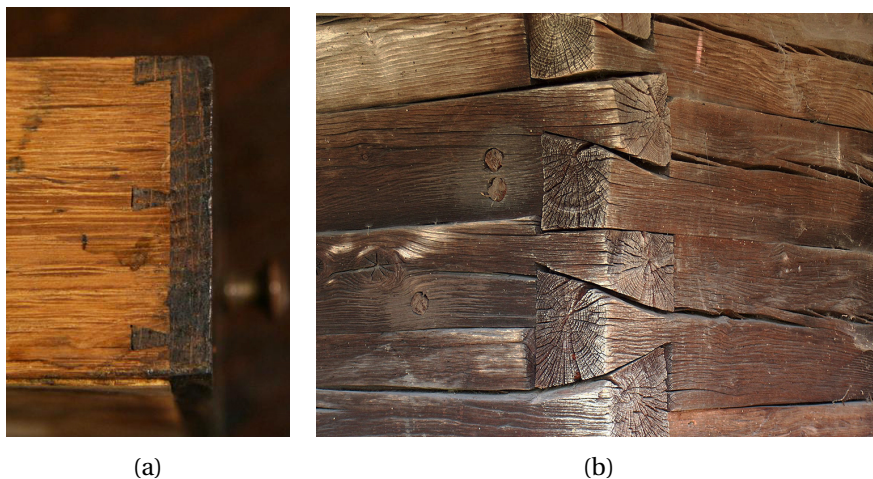


Figure 1.3 – Examples of dovetail woodworking joints: (a) Cabinetmaking joints dating from about 1780. Reproduced with permission from [58]. © 1998-2019 Harp Gallery Antique Furniture. (b) Joints used for linear beam elements. Photograph by Dumitru Rotari, distributed under a CC-BY 2.5 license.

Machine-tool technology was brought by the industrial revolution in the 19th century. Although some joinery machines were developed during this period [77, 41], dovetail and finger joints were largely replaced by metallic fasteners and adhesive bonding because their automated crafting could hardly be acquired with the existing technologies. This change was boosted by the development of dimensionally stable engineered wood products, such as particle boards, in the 20th century, as the consideration of swelling, shrinking and warping was not required anymore in the furniture industry [78].

The last wave of technological development was brought by computer-aided manufacturing (CAM). If numerical control was already developed in the 1940s and 1950s, 5-axis CNC machines started to be used for woodworking by the end of the 1970s only and were applied to carpentry joints in the middle of the 1980s [83]. With the integration of computer-aided design (CAD) programming, CNC-fabricated wood-wood connections were further developed in modern prefabricated timber frame structures between linear beams. Digital fabrication and algorithmic geometry processing brought a higher precision compared to crafted wood joinery, with rapid and simple assembly of the elements. However, their application in timber plate elements is much more recent. In fact, although engineered timber panels such as plywood were already fabricated in the 1920s, their use was principally limited to cladding and cross bracing of timber frame structures. Load-bearing edgewise connections became required when primary load-bearing structures made with cross-laminated timber panels (CLT) or laminated veneer lumber (LVL) were designed [78].

Wood-Wood Connections for Timber Plate Structures

Over the past decades, digitally fabricated wood-wood connections have been developed in the context of timber plate structures.¹ Single mortise-and-tenon joints were first used, for instance in the *Serpentine Gallery Pavilion 2005* [59, 60], before the number of tab and slots along the edges of the plates was increased, similarly to multiple dovetail joints used in cabinetmaking. In particular, finger joints have been used in several examples, such as the *ICD/ITKE Research Pavilion 2011* [97, 43, 50] and the *Landesgartenschau Exhibition Hall* [53, 46].

To overcome the need for additional connectors such as mechanical fasteners and adhesives to transfer loads between plates, Robeller [78] developed single-degree-of-freedom (1-DOF) integral mechanical attachment for the edgewise connection of thin timber plates. These joints have the advantage of providing high rotational stiffness in addition to high in-plane shear resistance with resistance to axial forces and out-of-plane shear forces in comparison with finger joints, which are 3-degrees-of-freedom (3-DOFs) joints. Moreover, these multiple tab-and-slot joints (MTSJ) have a locator feature in addition to their load bearing function. In fact, as five DOFs are restrained, the remaining DOF determines the vector of insertion of the plates and hence their position. This allows their fast and precise assembly, such that a pertinent assembly sequence of elements can reduce or eliminate the need for expensive or complex formworks or temporary supports. Closed-slot joints, also referred to as through-tenon joints (MTSJ-TT), were subsequently developed by Roche [84]. The presence of an embedment in closed-slot joints was shown to add ductility, strength and stiffness to the joint in rotation, therefore also improving the structure's behaviour [106]. Figures 1.4a and 1.4b illustrate 1-DOF MTSJ with open and closed slots respectively. First applications of these joints consisted in folded plate structures with open-slot joints [78, 106] and following investigations have led to the construction of building-scale structures using closed-slot joints [79, 30].

¹Timber plate structures using wood-wood connections are reviewed in more detail in Subsection 1.1.3.



Figure 1.4 – Single-degree-of-freedom (1-DOF) multiple tab-and-slot joints (MTSJ): (a) Open-slot and (b) Closed-slot (MTSJ-TT). Reproduced from [104].

The geometry of 1-DOF MTSJ is defined by three Bryant angles θ_1 , θ_2 and θ_3 , which are the xyz convention of the Euler angles [27]. As illustrated in Figure 1.5, the locking faces of the joints, which are the faces of the tabs and slots in contact, are defined by three consecutive rotations θ_1 , θ_2 and θ_3 . These rotations are applied on the planes P , P' and P'' , with the initial plane P being defined according to the normal vectors \mathbf{n}_0 and \mathbf{n}_1 of the mid-planes of the plates, with $\mathbf{u}_1 = \mathbf{n}_0 \times \mathbf{n}_1$, $\mathbf{u}_2 = \mathbf{n}_0$ and $\mathbf{u}_3 = \mathbf{u}_1 \times \mathbf{u}_2$. However, because of fabrication constraints, possible joint geometries restricted, as the CNC fabrication process allows only limited tool inclination and dihedral angle.

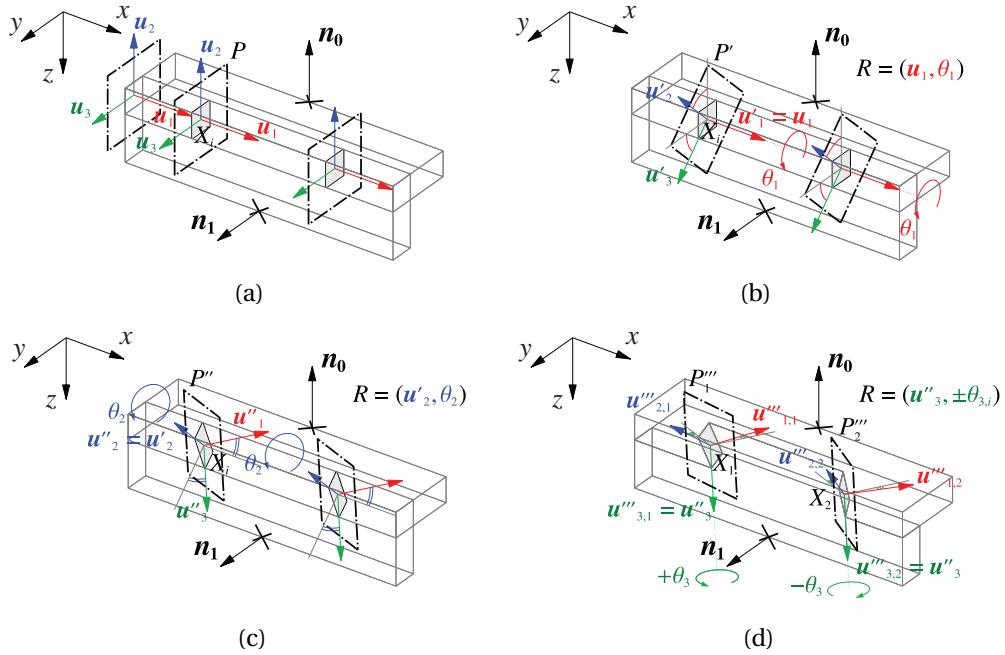


Figure 1.5 – Consecutive rotations of the Bryant angles θ_1 , θ_2 and θ_3 defining the geometry of 1-DOF MTSJ: (a) Initial plane P defined by the normal vectors of the plates \mathbf{n}_0 and \mathbf{n}_1 (b) Rotation θ_1 around \mathbf{u}_1 resulting in plane P' (c) Rotation θ_2 around \mathbf{u}'_2 resulting in plane P'' (d) Rotation θ_3 around \mathbf{u}''_3 resulting in planes P'''_1 and P'''_2 . Adapted from [85].

Mechanical Behaviour of Multiple Tab-and-Slots Joints

Connections substantially influence the global behaviour of timber structures and are therefore one of their key components. In particular, the semi-rigidity of the connections has to be taken into account in the model since simplifications considering the connections as rigid or hinged lead to under- and overestimated displacements respectively [81, 105]. However, the mechanical behaviour of wood-wood connections has mostly been investigated in the context of timber frame structures and models predicting their behaviour have mainly been developed in the case of old historic buildings rather than for angular connections of plates.

For finger joints, limited characterisation of the connections in terms of stiffness and load-carrying capacity has been done through experimental tests performed for specific case studies [43, 53]. More recently, Roche [86, 85, 84, 83] and Dedijer [17] studied the semi-rigid behaviour of 1-DOF MTSJ under bending and shear loading respectively for folded plate structures, considering different joint configurations. Through experimental investigations, they found that combinations of Bryant angles θ_1 , θ_2 and θ_3 highly influence the mechanical behaviour of the joints. Furthermore, MTSJ were proven to be an efficient solution for the assembly of thin plates. The moment-resisting behaviour of 1-DOF MTSJ has been further investigated through a simplified analytical model as well as a three-dimensional (3D) solid finite element (FE) model. However, both models showed limitations to predict the behaviour of 1-DOF MTSJ and generally underestimated their rotational stiffness [85, 83].

Alternative to Standard Joining Techniques

MTSJ have been shown to be a good alternative to standard joining techniques, with competitive moment-resisting properties in comparison with screwed connections and with a faster assembly than glued connections [85, 106]. Additionally, wood-wood connections have the advantage to overcome some of their drawbacks. In fact, although glued connections are considered rigid, they remain difficult to be achieved onsite because curing requires controlled climate conditions regarding moisture and temperature. Moreover, building-scale structures involve additional mechanical fasteners, such as for the *Thannhausen Musikprobensaal*, consisting of a folded plate structure in which glue-laminated timber panels were connected with glued mitre joints and complementary screws [95]. For these reasons, glued wood-wood connections were suggested as an unfeasible solution for building-scale timber folded structures [106]. Steel connections are therefore generally used for timber plate structures. However, the European Standard EN 1995 [23] imposes minimum spacing to the edge of the plates that is proportional to the diameter of the fasteners, such that, for thin timber plates (below eight times the diameter of the fastener), the minimum plate thickness is defined according to this diameter and not with regard to structural requirements.

Wood-wood connections, which are directly integrated in the plates, have the advantage to be free of these constraints and can therefore lead to an optimisation of the material use. Furthermore, these joints do not require a minimum panel thickness.

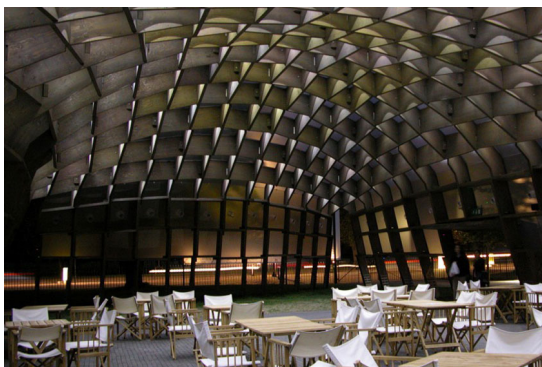
1.1.3 Timber Plate Structures Using Wood-Wood Connections

Computational design and digital fabrication tools have led to the realisation of integrally-attached timber plate structures with various shape topologies. Through custom-developed programs, the design and fabrication of structures with a large number of geometrically different plates was made possible. For their structural analysis, numerical models based on the finite element method (FEM) were generally used.

Single Tab-and-Slot Joints

The first shell structures applying similar joining techniques to traditional wood-wood connections were using single tab-and-slot joints to connect a large number of unique elements. An example built in 2005 is the 17 m span *Serpentine Gallery Pavilion 2005* [59, 60], illustrated in Figure 1.6a. It consisted of 427 unique prefabricated elements made of 69 mm thick spruce LVL panels and assembled with mortise-and-tenon joints (see Figure 1.6b). Locking bolts were added onsite to facilitate the assembly of the structure. Plates were positioned vertically to form a grid rather than a continuous shell. In this reciprocal system, elements were mutually interlocked, such that the structure could only be erected following a specific and unique assembly path.

For its design, a digital workflow was applied, from the geometry definition, to the direct transfer of data for fabrication, to the robotic fabrication of all components. A structural analysis was performed with the finite element analysis (FEA) software Oasys GSA (Arup, London, United Kingdom), considering all plate components as two one-dimensional (1D) beam elements. Rotations were hinged with no implementation of the semi-rigid properties of the connections [100].



(a)



(b)

Figure 1.6 – Serpentine Gallery Pavilion, London, United Kingdom, 2005: (a) Interior view (b) Mortise-and-tenon joints with bolts. Reproduced with permission from [5], © 2016 Balmond Studio.

Multiple Tab-and-Slot Joints

Multiple tab-and-slot joints, similar to traditional multiple joints used in cabinetmaking, have been subsequently developed at the end of the 2000s. After the development of 1-plane joints, such as the half-lap jigsaw (or puzzle) joints used for the *ICD/ITKE Research Pavilion 2010* [40], 2-plane finger joints have been developed. They have been employed in regular structures like the *WikiHouses* [69], and in folded timber sandwich structures [1]. Concurrently, they have been applied to several segmented plate shells, such as the *ICD/ITKE Research Pavilion 2011* [97, 43, 50] and the *Landesgartenschau Exhibition Hall* [53, 46], illustrated in Figures 1.7 and 1.8 respectively. These structures were both developed at the University of Stuttgart by the Institute for Computational Design and Construction (ICD) and the Institute of Building Structures and Structural Design (ITKE). More recently, finger joints have also been implemented in the *BUGA Wood Pavilion 2019* [61] by these institutes.

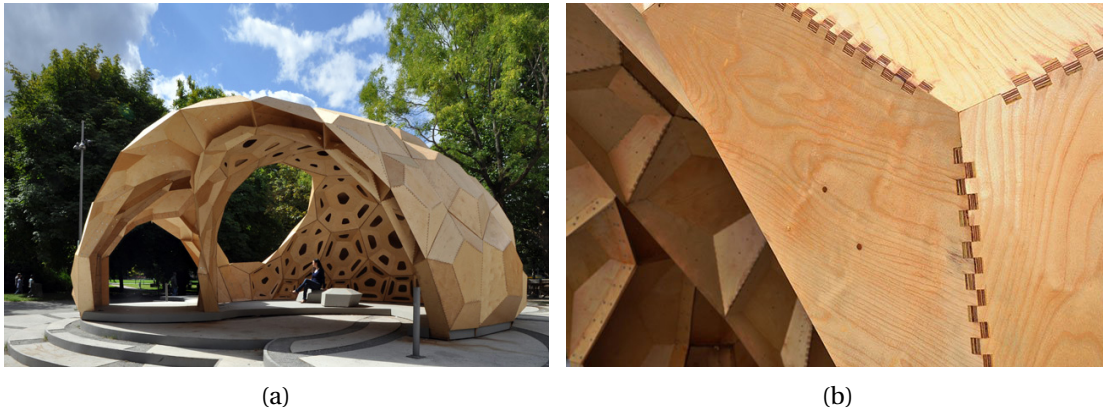


Figure 1.7 – ICD/ITKE Research Pavilion, Stuttgart, Germany, 2011: (a) Exterior view. Reproduced from [50]. (b) Glued finger joints. Reproduced from [43].

The three latter structures are all double-curved plate shells composed of a large number of unique plate elements and finger joints, as presented in Table 1.1. For the *ICD/ITKE Research Pavilion 2011*, 6.5 mm thick plywood plates were assembled through glued finger joints to form 59 prefabricated "cell" modules, themselves connected with bolts onsite. For the *Landesgartenschau Exhibition Hall*, 50 mm thick plywood plates were assembled in a single step, with crossing screws added to the finger joints with high in-plane shear resistance to resist axial forces and out-of-plane shear forces [46]. For the *BUGA Wood Pavilion 2019*, hollow building segments were robotically assembled and connected with removable bolts onsite.

These structures were built following a "co-design" strategy [62, 61] in order to integrate design, engineering and fabrication to allow computational feedback and, in particular, to transfer the complex geometry to a FEA software and modify the design according to the results. This was achieved through the development of custom-scripts generating the machine code for the digital fabrication of the plates as well as the FE model. For the *ICD/ITKE Research Pavilion 2011* and the *Landesgartenschau Exhibition Hall*, plates were modelled considering plane shell elements and springs connecting two nodes at the opposite sides of neighbouring panels

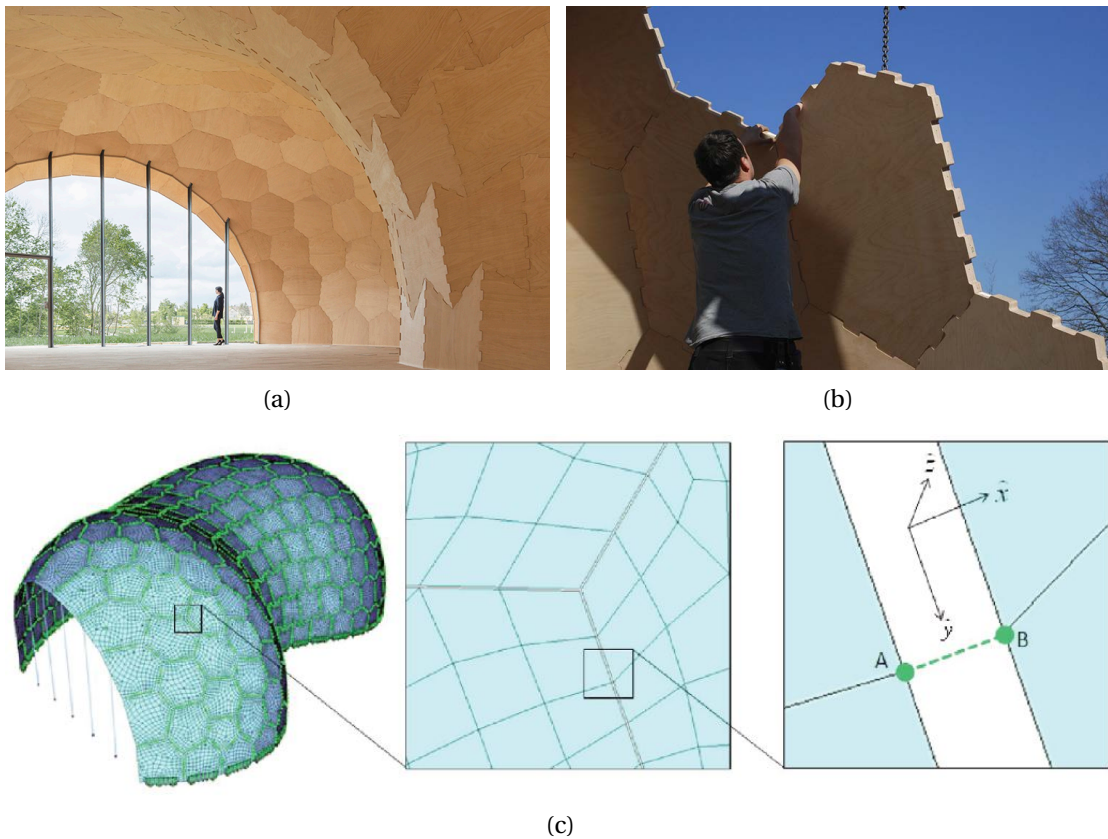


Figure 1.8 – Landesgartenschau Exhibition Hall, Schwäbisch Gmünd, Germany, 2014: (a) Exterior view (b) Screwed finger joints (c) Finite element model in which the semi-rigid connections were modelled with springs connecting two nodes at the opposite sides of neighbouring panels. Reproduced from [53].

were implemented for the semi-rigid behaviour of the connections, as illustrated in Figure 1.8c for the *Landesgartenschau Exhibition Hall*. Failure criteria were also implemented in the numerical model. For the research pavilion, spring stiffness values implemented in the FE model of the global structure were retrieved from experimental shear load tests performed on the finger joints. For the exhibition hall, the stiffness and failure criteria of the finger joints and the crossing screws were evaluated through simplified analytical models. The bending stiffness of screwed finger joints was determined through four-point bending tests [53].

Table 1.1 – Comparison of shell structures using finger joints developed by the ICD/ITKE.

Structure	Material	Number of unique elements	Number of finger joints
ICD/ITKE Research Pavilion 2011	birch plywood	855	> 100 000
Landesgartenschau Exhibition Hall	beech plywood	243	7 356
BUGA Wood Pavilion 2019	spruce LVL	376	17 000

Single-Degree-of-Freedom Joints

In his thesis, Robeller [78] developed 1-DOF MTSJ joints for folded plate structures to avoid the use of mechanical fasteners and adhesive bonding (see Subsection 1.1.2). Their first application was for the *Mendrisio Pavilion* in 2013, consisting in a 13 m span curved-folded thin-shell structure made of 77 mm thick CLT panels. They have subsequently been applied to single-layered folded plate structures [81, 106] made with 21 mm thick spruce LVL panels and to a double-layered double-curved timber plate shell made with 15 mm birch plywood plates [80]. Snap-fit joints have also been developed for the design of a double-layered structure [78]. These prototypes have finally led to the construction of the timber pavilion of the Vidy theatre in 2017, first realisation of a building-scale double-layered timber folded plate structure (see Figure 1.9). The 16 to 20 m span structure is composed of 304 unique shaped CLT plates (45 mm thick) assembled with MTSJ-TT.



Figure 1.9 – Timber Pavilion of the Vidy Theatre, Lausanne, Switzerland, 2017: (a) Exterior view. Reproduced from [30] (b) Interior view. Photograph by Ilka Kramer.

These structures assembled with 1-DOF MTSJ were designed and fabricated using automated digital tools. Custom CAD plugins were developed for an automated digital modelling and fabrication of each structure. They were programmed with the Visual C# language and the RhinoCommon software development kit (SDK) on the CAD software Rhino[®], version 5.0 (Robert McNeel & Associates, Seattle, USA). The visual programming software Grasshopper[®] (Robert McNeel & Associates, Seattle, USA) was used as a user interface, allowing a real-time preview of the 3D geometry in function of the chosen input design parameters. In the same manner, a digital fabrication tool was developed to generate a 5-axis CNC machine G-code [79, 80, 106].

Regarding the structural analysis of these integrally-attached timber plate structures, the generation of numerical models was not integrated into the existing digital design-to-fabrication workflow. For the Vidy theatre, bending tests were executed on single- and double-layered connections to investigate their rotational stiffness and failure modes [30] and design calculations were performed concurrently using a simplified FE model.

For single-layered timber folded plate structures, however, a more accurate numerical model was developed. In her thesis, Stitic [104] first investigated the mechanical behaviour of assemblies using either open-slot, glued closed-slot or closed-slot joints (MTSJ-TT). A pulley-based test setup similar to the one suggested by Wong [120] was developed to simulate surfacic loading, as illustrated in Figure 1.10a. Numerical investigations were subsequently carried out considering MTSJ-TT since they were found to have the highest load-bearing capacity compared to the two other studied connection details. A FE model was built considering conventional plane shell elements to model the plates. For the connections, two simplified representations were considered to model their semi-rigid behaviour, as illustrated in Figure 1.10c: (i) using strip elements along the edges of the plates, such as developed for glass structures by Bagger [3]; (ii) considering a set of springs per connection. The two numerical models showed satisfying results compared to experimental testing results. Additionally, a macro-modelling approach considering 1D beam and column elements was investigated and was shown to decrease computational costs [105].

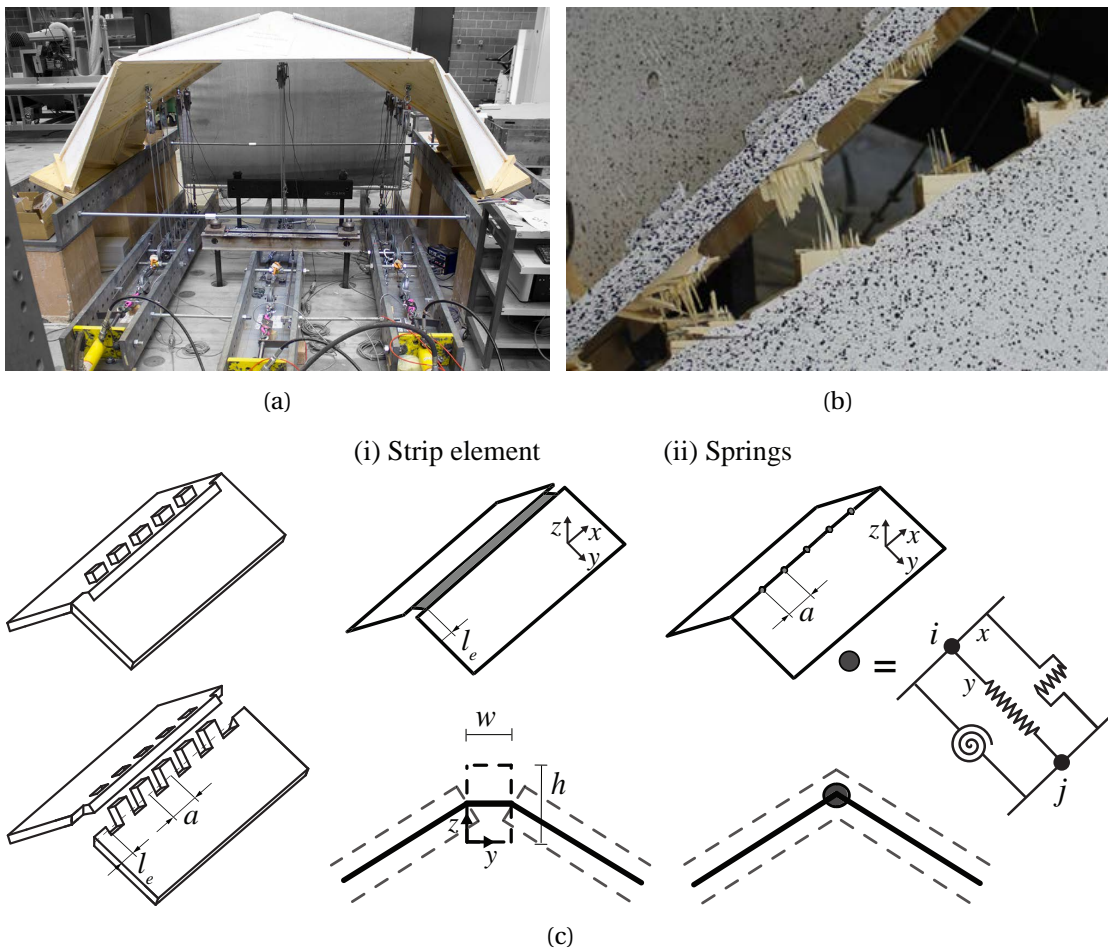


Figure 1.10 – Timber folded plate structure with MTSJ-TT: (a) Pulley-based loading test setup. Reproduced from [106] (b) Failure of MTSJ-TT. Photograph by Andrea Stitic. (c) Connection detail representation using (i) strip elements (ii) springs. Adapted from [105].

Recently, the construction system developed for double-layered double-curved shell structures using MTSJ and MTSJ-TT [80] has been applied to large-scale timber arches for the Annen Plus SA Head Office project using 40 mm thick beech LVL panels. Large-scale prototypes of 25 m span have been built (see Figure 1.11), using the same CAD programming tools of the design-to-fabrication workflow developed for smaller double-layered double-curved timber shells [80].



Figure 1.11 – Prototypes of the Annen Plus SA head office, Manternach, Luxembourg, ongoing: (a) Exterior view (b) Interior view.

Additional Wood Connectors

Concurrently to the development of structures with joints integrated in the panels only, structures using wood-wood connections with additional wood connectors have also been developed. For example, the *Swissbau Pavilion 2005* [91], consisted in 1200 individually shaped oriented strand board (OSB) elements with mitre joints and dovetail grooves, connected with dovetail connectors. Another example is the double-curved Kobra structure, built at the TU Graz Faculty of Architecture in 2012, made of 51 planar polygons of 95 mm thick spruce CLT panels and sewing joints [93, 92, 119]. More recently, this assembly method has been applied to the *Timberdome*, composed of 59 CLT plates (100 mm thick) with dovetail grooves and dovetail-shaped wood connectors [82].

1.2 Research Motivation

1.2.1 Problem Statement

As reviewed in the state of the art, presented in Section 1.1, geometrically complex timber plate structures using wood-wood connections have been increasingly developed over the past decades. However, further investigations regarding their mechanical characterisation and numerical modelling are required for their structural design. In particular, the following aspects still present challenges or knowledge gaps.

Valid Numerical Model for Complex Geometries

Although advanced numerical modelling has become more reliable, especially with the use of engineered timber products characterised by more homogeneous properties on the one hand, and the development of computer-aided engineering (CAE) software on the other hand, modelling uncertainties remain. This is particularly the case for wood-wood connections, which are a key component of timber plate structures. Different numerical models, taking into account their semi-rigid behaviour, have been developed. However, they have only been evaluated through experimental tests for single-layered timber folded plate structures [105]. A numerical model is needed that can both accurately predict the mechanical behaviour of the structure and be computationally efficient for complex geometries with a large number of connections.

Automatically Generated Numerical Model

Successful examples of timber plate structures using wood-wood connections have shown that their design and fabrication can be automated using CAD programming and digital fabrication tools [79, 105]. For structures composed of a large number of singular shaped panels with different joint parameters, an automatic generation of their numerical model is also required since a manual implementation is too cumbersome and expensive [43, 53]. However, research focusing on the development of automated numerical tools and methods for their structural analysis has been very limited. Furthermore, design and fabrication workflows are usually limited to research and are less frequently applied to large building structures [103].

Large-Scale Experiments

Experimental tests remain necessary to fully understand the mechanical behaviour of timber plate structures and assess the numerical models developed [120]. However, loading tests performed on structures with wood-wood connections have only been executed in the laboratory [107, 106].

Mechanical Behaviour of Wood-Wood Connections

The semi-rigid behaviour of wood-wood connections highly influences the mechanical behaviour of the structure and therefore needs to be taken into account in global numerical models [105]. However, wood-wood connections have not been completely characterised and their properties are usually retrieved from experimental tests performed on the single connections. Previous experimental investigations have been limited to the study of shear- and moment-resisting behaviour of MTSJ made of spruce LVL and a material model using 3D solid elements has only been investigated for their semi-rigid moment-resisting behaviour [17, 84, 85].

1.2.2 Research Objectives

This thesis aims to provide a design methodology for the structural analysis of freeform timber plate structures with wood-wood connections. Considering the problem statement presented in Subsection 1.2.1, several objectives can be determined to reach this goal:

- Provide a numerical modelling method that is applicable to complex geometries and both computationally efficient and accurate;
- Automate the generation of the numerical model;
- Assess the numerical model for both small- and large-scale assemblies;
- Enable feedback loops between design and structural analysis;
- Develop a numerical model to predict the behaviour of wood-wood connections, necessary for global numerical models of the structure.

1.2.3 Methodology

In order to reach the research's objectives stated in Subsection 1.2.2, a numerical model based on the FEM is proposed, as FE models are generally used when analytical solutions cannot be found, such as for complex structures [105]. Custom tools are developed to automate the generation of the numerical model and a design framework is proposed to integrate it into the existing design and fabrication workflow. The design framework, the description of the FE model with the representation of its structural elements and methods for their automatic generation are presented in Chapter 2.

The numerical model is then assessed through experimental tests on both small- and large-scale structures performed in the laboratory and onsite respectively. Experimental tests and comparisons with the FE model are presented in Chapters 3 and 4 for small- and large-scale structures respectively.

To establish a link between design and structural analysis, the potential optimisation of the studied structural system is investigated within the proposed design framework. An alternative structural system is suggested and compared to the initial system based on numerical investigations using the FE model developed. Results of this work are presented in Chapter 5.

Finally, a 3D FE model for wood-wood connections is developed based on the continuum damage model of Sandhaas [88] applied by Roche et al. [85] for MTSJ. An experimental shear loading test campaign is used to assess the model. The material model and results of numerical simulations are presented in Chapter 6.

1.2.4 Scope

The research is conducted based on a specific case study, namely the Annen Plus SA head office project, presented in Section 1.3. Therefore, numerical and experimental investigations are mainly carried out according to the geometry and the construction system of double-layered double-curved timber plate shell structures of the project. However, the methods are developed with the prospect of being easily applicable to other types of timber plate structures.

Structural Analysis

Structural analysis is conducted through FE models built within the FEA software AbaqusTM, version 6.12 (Dassault Systèmes, Vélizy-Villacoublay, France). Scripts are developed to generate the model using the Abaqus Scripting Interface, which is an extension of the Python programming language [16]. Gravity and experimental loading only are considered, discarding other parameters influencing the structural behaviour such as moisture content and temperature. Furthermore, the long-term behaviour of the structure is not investigated.

Connections

Wood-wood connections studied in this thesis are the 1-DOF MTSJ recently developed by Robeller [78] and Roche et al. [84], presented in Subsection 1.1.2. Their design is generated using CAD programming and their fabrication is executed with a 5-axis CNC machine. In this thesis, 1-DOF MTSJ are referred to as wood-wood connections and 1-DOF MTSJ-TT as through-tenon (TT) wood-wood connections.

Materials

The materials investigated in this thesis are engineered wood products. For the global study, beech LVL panels, used in the Annen Plus SA head office project, are considered. For numerical investigations on wood-wood connections, four engineering wood products are studied, namely OSB, spruce LVL, beech LVL and spruce CLT.

1.3 Case Study: Annen Plus SA Head Office

1.3.1 Project Description

The Annen Plus SA head office in Manternach, Luxembourg is the first full-scale realisation of double-layered double-curved timber plate shells. Its roof structure consists of a series of 23 discontinuous and individually shaped shells with spans ranging from 22.5 m to 53.7 m and constant height and width of 9 and 6 m respectively [80]. Figure 1.12a illustrates a model of the project showing the 23 double-curved shells. Their design was inspired by Eladio Dieste's Gaussian masonry vaults, such as built at the end of the 1970s for the Port Warehouse in Montevideo presented in Figure 1.12b [72]. The Annen Plus SA project will accommodate a 5800 m² facility including a timber prefabrication factory space and offices [80].



Figure 1.12 – Design of the Annen Plus SA head office: (a) Model of the project. © 2015 Valentiny hvp architects / Yves Weinand. (b) Masonry vaults of the Port Warehouse (1977-1979), designed by Eladio Dieste. Reproduced from [2]. © 2004 Princeton Architectural Press.

1.3.2 Construction System

The construction system of double-layered double-curved timber plate shells, developed by Robeller et al. [80] and applied to the Annen Plus SA head office, is illustrated in Figure 1.13. All plates of the structure are assembled using wood-wood connections, referred to as MTSJ and MTSJ-TT [78, 84]. The two layers of each shell are composed of thin timber plates, namely $H_{i,1}$ and $H_{i,2}$ for top and bottom layers respectively, characterised by a dihedral angle between neighbouring plates close to 180°. Vertical plates $V_{i,1}$ and $V_{i,2}$ are introduced to connect these horizontal plates with TT connections, with tenons integrated in horizontal plates and mortises in vertical plates. The latter are themselves assembled with dovetail joints. Each arch can also be seen as an assembly of four-sided hexahedra-shaped boxes B_i composed of two horizontal plates, corresponding to the two layers of the structure, and two vertical plates allowing their assembly through TT connections. The two remaining open sides of each box are closed by neighbouring boxes, such that vertical plates are shared between every neighbouring box.

All wood-wood connections used in the structure are 1-DOF joints associated with unique insertion vectors, such that each arch is formed following a unique assembly path. Vertical plates $V_{i,1}$ and $V_{i,2}$ are first assembled following the insertion vector w_i and horizontal plates $H_{i,1}$ and $H_{i,2}$ are subsequently inserted in the vertical plates following v_i . Four-sided boxes thus formed individually are then assembled together along u_i . The interlocking of the plates allows the remaining DOF of the connections to be blocked.

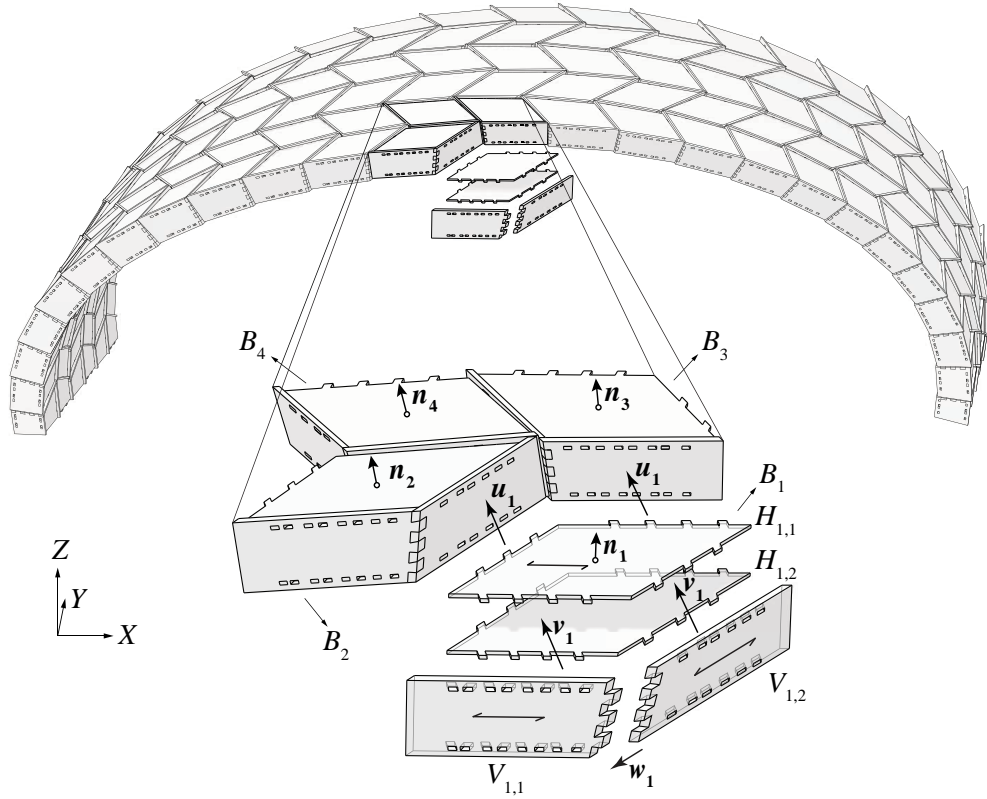


Figure 1.13 – Construction system of double-layered double-curved timber plate shells developed by Robeller et al. [80]. Each arch is formed by the assembly of four-sided hexahedra-shaped boxes B_i composed of two horizontal plates $H_{i,1}$ and $H_{i,2}$, corresponding to the two layers of the structure, and two vertical plates $V_{i,1}$ and $V_{i,2}$.

1.3.3 Construction Material

BauBuche Q panels (Pollmeier Massivholz, Kreuzburg, Deutschland) used for the project are 40 mm thick beech LVL panels made of 3 mm thick layers of beech peeled veneers, glued together longitudinally and cross-wised into a panel, unlike BauBuche S panels presenting longitudinal layers only [9]. Since the structure presents connections at each plate's edge, with membrane efforts induced in different directions, crosswise layers panels were preferably chosen. They provide better stiffness properties and higher lateral bending and shear strength. The composition of the 14 veneer layers in BauBuche Q panels is ||| – ||||| – ||| (| for longitudinal, – for crosswise veneer layer).

1.3.4 Fabrication and Assembly Process

In previous research, CAD plugins have been developed to automate the design and fabrication of double-layered double-curved timber plate shell structures, starting from a double-curved surface defining the shape of the shell, referred to as the design target surface [80]. For the Annen Plus SA head office project, all panels are cut with a 5-axis CNC milling machine with a 20 mm diameter tool for maximum angles of less than 45° and with a 25 mm diameter tool for larger tilt angles. All plates forming the boxes are prefabricated and manually assembled onsite following a unique assembly path, as described in Subsection 1.3.2. Structures are assembled lying on their longitudinal side and lifted up with a crane in one single assembly to their final vertical position (see Figure 1.14). Two screws per edge of the horizontal plates are added between horizontal and vertical plates in order to maintain their position during the assembly of the boxes.



Figure 1.14 – Assembly of the Annen Plus SA head office arches. Structures assembled lying on their longitudinal side are positioned by lifting them up with a crane in one single assembly. © 2019 Annen Plus SA.

2 Numerical Modelling

This chapter is based on: A. C. Nguyen, P. Vestartas and Y. Weinand, Design Framework for the Structural Analysis of Free-Form Timber Plate Structures using Wood-Wood Connections, *Automation in Construction*, 107:102948, 2019. doi:10.1016/j.autcon.2019.102948.

2.1 Introduction

Recent advances in timber construction have led to the realisation of various geometrically complex timber plate structures assembled with innovative wood-wood connections inspired by traditional woodworking joints (see Chapter 1, Subsection 1.1.3). Although the assembly of these structures is still mainly carried out manually, both design and fabrication have been successfully automated using computer-aided design (CAD) programming and computer-aided manufacturing (CAM) processes. However, limited research has focused on the development of automated tools for their structural analysis. A numerical model is needed that can both be automatically generated and accurately predict the mechanical behaviour of large assemblies.

Simplified models based on the finite element method (FEM) are usually adopted as they are computationally efficient in comparison with exact three-dimensional (3D) finite element (FE) models involving a large number of 3D solid elements [57]. Furthermore, connections between plates substantially influence the behaviour of the assembly and often constitute weak points of timber plate structures. Their semi-rigid behaviour therefore needs to be implemented in the global model of the assembly since simplifications considering the connections as rigid or hinged lead to under- and overestimated displacements respectively [81, 105]. In light of this, while plane shell elements are generally applied to timber plates, two numerical approaches exist for wood-wood connections. On the one hand, spring elements can be used to model the semi-rigidity of the connections, as previously utilised for finger joints and through-tenon (TT) wood-wood connections, referred to as multiple tab-and-slot joints (MTSJ) [50,

53, 105]. On the other hand, strips of fictitious material along edges of connected plates can be introduced, such as developed for glass structures by Bagger [3] and applied to timber folded plate structures by Stitic et al. [105]. Both numerical models have shown satisfying results compared to experimental tests performed on timber folded plate structures. However, springs were found to be more efficient than strip elements, which are less convenient to use for complex geometries [105].

Discrepancies exist among researchers regarding the implementation of springs. For both the *ICD/ITKE Research Pavilion 2011* and the *Landesgartenschau Exhibition Hall* (presented in Chapter 1, Section 1.1.3), single springs were used to connect two nodes at the opposite sides of neighbouring plates. For the research pavilion, axial springs acting in the direction of the edges of the finger joints were used exclusively to take into account their semi-rigid behaviour [50]. Moreover, custom tools were developed to generate the FE model of this pavilion made of more than 100 000 finger joints. For the *Landesgartenschau Exhibition Hall*, four springs modelling axial, in-plane shear, out-of-plane shear and bending stiffness, acting in the corresponding directions of the local coordinate system of the joints, were introduced [53, 46]. For the folded plate structures studied by Stitic et al. [105], up to seven springs were distributed along the length of the TT connections with axial, in-plane shear and rotational stiffness implemented and remaining degrees of freedom (DOFs) considered rigid. It was shown that increasing the number of joints distributed along the length of the connections was converging to results in better agreement with experimental tests.

In this chapter, a design framework is proposed for the structural analysis of freeform timber plate structures using wood-wood connections. Within this framework, described in Section 2.2, a semi-rigid spring model is developed for the thesis case study, namely the Annen Plus SA head office composed of double-layered double-curved timber plate shells (see Chapter 1, Section 1.3). The FE model as well as the representation of the structural elements in an exchange geometry between CAD software and finite element analysis (FEA) software are defined in Section 2.3. Methods to generate this CAD-FEM geometry using CAD programming are presented, followed by the steps to generate the FE model using a custom code in Python programming language. Finally, computational aspects are discussed in Section 2.4, to evaluate the automatic generation of the model for both small- and large-scale structures, and semi-rigid modelling methods are analysed.

2.2 Design Framework

The design framework proposed for the structural analysis of freeform timber plate structures is presented in Figure 2.1. It was developed from the existing design-to-fabrication workflow used for double-layered double-curved timber plate structures, starting from a double-curved surface, referred to as the design target surface. Although the design framework was applied to the specific case study of this thesis (described in Chapter 1, Section 1.3), the methods presented can be applied to other types of structures.

The design framework can be divided into two distinct steps, with the final objective of obtaining a numerical model that can lead to accurate structural design calculations. The first step of the design framework consists of the automatic generation of the numerical model. To achieve this step, an exchange geometry is defined in order to import the complex geometry of the 3D model from a CAD software to an FEA software, which constitutes a heterogeneous data exchange [36]. Therefore, the computational tool developed for automated digital modelling and fabrication has to include the generation of a third output file, in addition to the 3D model and the fabrication files. This CAD-FEA exchange geometry is defined according to the numerical model and its assumptions. The model is then built in an FEA software using a custom scripting code. In the second step of the design framework, the mechanical behaviour of the structure is investigated through experimental tests. Results are compared to numerical simulations to assess the model, which is validated if a good agreement with experimental tests is found.

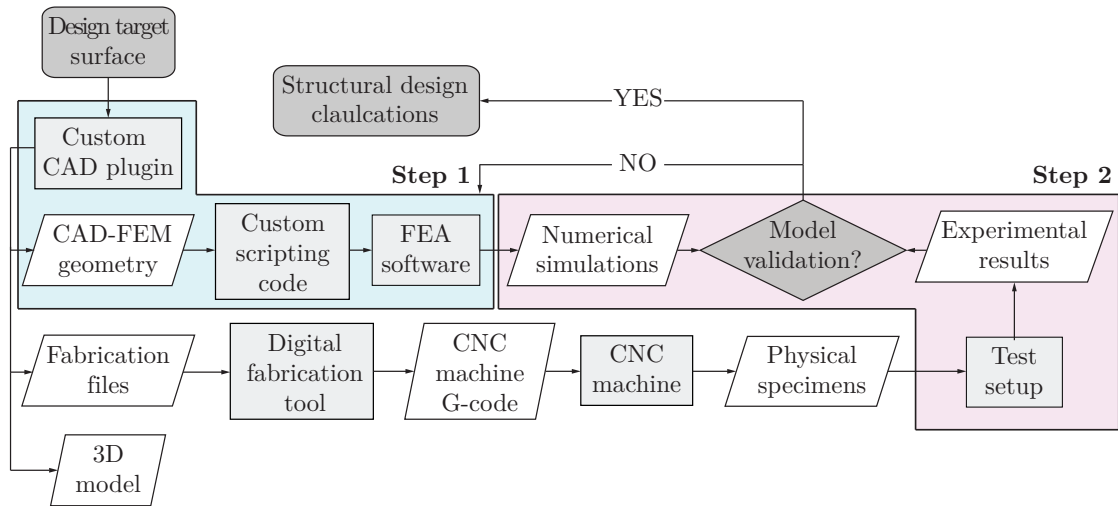


Figure 2.1 – Design framework proposed for the structural analysis of freeform timber plate structures. Step 1 consists of the generation of the finite element model from a design target surface, defining the general shape of the assembly. The CAD-FEM geometry is defined in order to import the complex assembly geometry from a CAD software to an FEA software. Step 2 encompasses investigations on the mechanical behaviour of the structure and the assessment of the numerical through experimental tests, with the final objective of obtaining a numerical model that can lead to accurate structural design calculations.

2.3 Finite Element Model Generation

The first step of the design framework, consisting in the FE model generation, was achieved on geometries associated to the thesis case study. Several assumptions were first taken to define the model. The CAD-FEM geometry was then generated and a custom Python scripting code was developed to import this exchange geometry information in the FEA software, in this case AbaqusTM, version 6.12 (Dassault Systèmes, Vélizy-Villacoublay, France).

2.3.1 Geometry of the Specimens

Two geometries were investigated: a 5×3 boxes prototype and an entire double-curved arch made of 200 boxes with a total span of 24 m. The geometry of the 5×3 boxes prototype, 6.9 m long, 2.6 m wide and 0.76 m high (with a static height of 0.6 m), was defined according to the 24 m span arch scale 1:1 (see Figure 2.2). Fifteen boxes were extracted at midspan, as it is the most critical part of the arch. Their geometry was then simplified by removing the double curvature and setting identical dimensions of the boxes per row of the prototype. This was done to facilitate the experimental tests but also to have a better control of the parameters influencing the behaviour of the assembly and establish a more pertinent comparison with the numerical model. All TT connections were set to a tab length of 72.5 mm and Bryant angles (as defined in Chapter 1, Figure 1.5) $\theta_1 = 0^\circ$, $\theta_2 = 25^\circ$ and $\theta_3 = 0^\circ$.

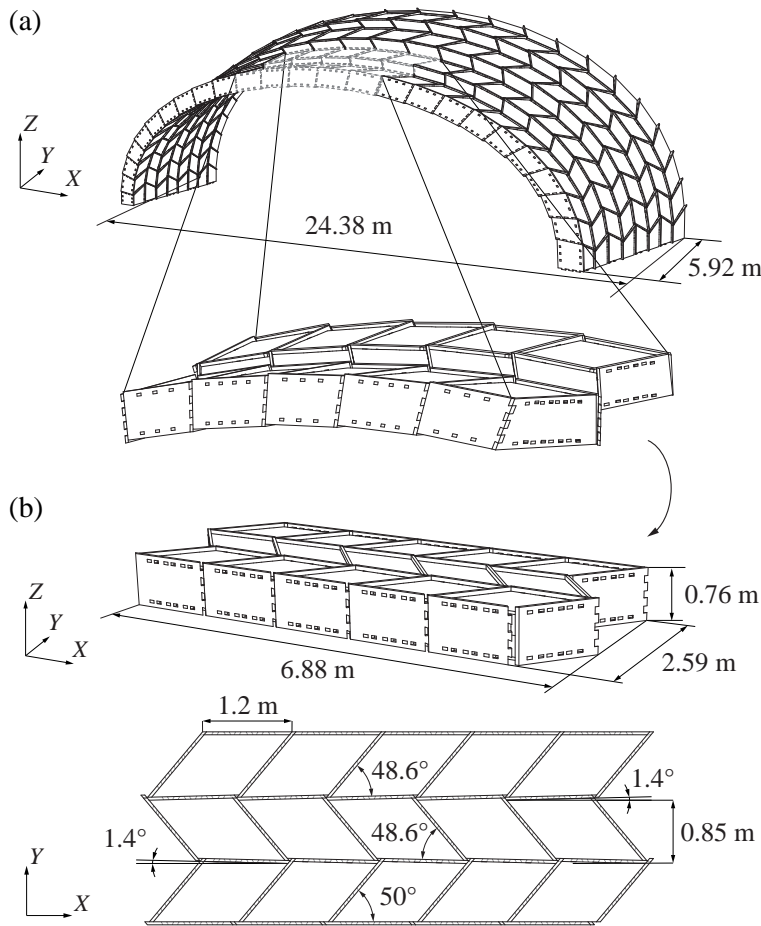


Figure 2.2 – Geometry of the 5×3 boxes prototype: (a) The boxes were extracted from a 24 m span arch scale 1:1 at midspan, as it is the most critical part of the arch (b) The geometry was simplified by removing the curvature and setting similar dimensions of the boxes per row of the prototype. This was done to facilitate the experimental tests but also to have a better control of the parameters influencing the behaviour of the assembly and establish a more pertinent comparison with the numerical model.

2.3.2 Definition of the Finite Element Model

Plates Modelling

The material was modelled as orthotropic, since the implementation of the exact mechanical properties would otherwise have been exceedingly tedious. The mathematical model was defined considering plate theory as the structure can be decomposed in discrete planar continuous elements. From a structural point of view, the behaviour of a planar structure is dependent on the loading direction: axial forces occur for an acting force parallel to the surface (plate mechanism) and flexural forces appear when the surface is perpendicularly loaded (slab mechanism). However, the global shell obtained with segmental plates introduces a noncoplanarity of the plates giving rise to axial and flexural forces in the structure. External loading is thus supported by the coupling of these two mechanisms, increasing the strength of the structure [70].

A numerical model was developed since the proposed mathematical model cannot be calculated analytically due to form complexity, material properties and boundary conditions [105]. Structural analysis of plate shell structures is usually performed with the FEM due to its ease of implementation. Since an exact 3D modelling is computationally expensive for large structures, model simplifications were applied. As the structure can be decomposed in discrete planar continuous elements, plate theory was considered for the mathematical model and plates were modelled as shell elements, as opposed to solid elements, since their thickness t is significantly smaller than the two other dimensions L_i ($t/L_i < 0.05$) [16].

In AbaqusTM, panels can be modelled using conventional or continuum shell elements. In the first case, the body is discretised considering a reference surface (top, bottom or mid-surface), meaning that the 3D body is reduced to a two-dimensional surface with a thickness defined by the section property. Conventional shell elements have displacement and rotational DOFs and use linear or quadratic interpolation. In the case of continuum shell elements, the discretisation is performed on the entire 3D body and the element's thickness is defined by the nodal geometry. Continuum shell elements have solely displacement DOFs and use linear interpolation. They have similar behaviour (kinematic and constitutive) to conventional shell elements but appear as 3D continuum solids. Additionally, a more accurate through-thickness response is provided by using continuum shell elements in comparison with conventional shells, as they give a better prediction of transverse shear deformation and take thickness change into account [16]. However, due to the small thickness-length ratio of the plates, through-thickness strains were neglected and conventional shell elements were used over continuum shell elements for all plates.

As illustrated in Figure 2.3, midsurfaces of the horizontal plates were extended to form closed boxes with the vertical plates. They were then reduced by about 0.1 % to introduce a small gap of 0.5 mm to implement the spring elements, used to model the connections, with their local coordinate system xyz . The optimal gap size has to be infinitely close to zero to avoid further eccentricity contributions, which are already accounted for in the spring stiffness

values implemented. However, the size of the gap was found to have a limited influence on the results as a gap of 4 mm led to an increase of displacements of 2 %.

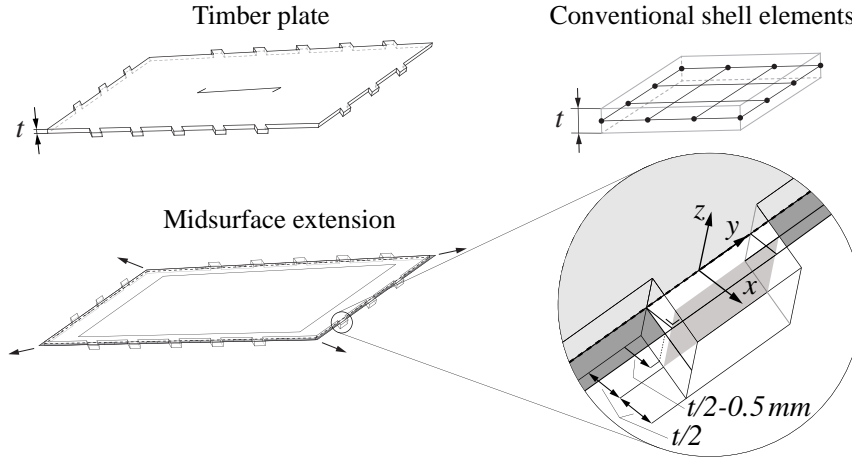


Figure 2.3 – Schematic representation of the numerical modelling of timber plates. Midsurfaces of timber plates, modelled as conventional shell elements, were extended by $t/2-0.5 \text{ mm}$ to leave a small gap for the implementation of springs with their local coordinate system xyz .

Connections Modelling

For double-layered double-curved timber plate shells, one issue of the geometry lies in the large dihedral angle φ between horizontal plates (close to 180° , as shown in Figure 2.4), which is required to obtain the curvature of the shell. As a consequence, each shell is composed of tilted horizontal plates with a vertical plate in between and shared TT connections. Since strip elements, which have been applied to model semi-rigid connections in previous research [105], are difficult to obtain for tilted edges, a spring model was developed in this study. Springs have the advantages to be easily implemented, computationally efficient and easily applicable to other numerical software packages [7].

The semi-rigidity of TT joints was introduced in the model by means of springs with stiffness values corresponding to the mechanical properties of the joints in the three translational and three rotational DOFs. All six components k_i were first considered uncoupled, such that their stiffness matrix K can be expressed as Equation 2.1 [48]:

$$K = \begin{bmatrix} k_{t,x} & 0 & 0 & 0 & 0 & 0 \\ 0 & k_{t,y} & 0 & 0 & 0 & 0 \\ 0 & 0 & k_{t,z} & 0 & 0 & 0 \\ 0 & 0 & 0 & k_{R,x} & 0 & 0 \\ 0 & 0 & 0 & 0 & k_{R,y} & 0 \\ 0 & 0 & 0 & 0 & 0 & k_{R,z} \end{bmatrix} = \begin{bmatrix} k_1 & 0 & 0 & 0 & 0 & 0 \\ 0 & k_2 & 0 & 0 & 0 & 0 \\ 0 & 0 & k_3 & 0 & 0 & 0 \\ 0 & 0 & 0 & k_4 & 0 & 0 \\ 0 & 0 & 0 & 0 & k_5 & 0 \\ 0 & 0 & 0 & 0 & 0 & k_6 \end{bmatrix} \quad (2.1)$$

In previous research, discrete nodes were connected either by a single spring at the edges of the tenons [53] or by springs distributed along the length of the connections [105] (see Figure 2.4i). In the latter case, the stiffness of each spring $k_{\text{spring},i}$ was determined as follows:

$$k_{\text{spring},i} = \frac{k_i}{n} \quad (2.2)$$

with n the number of springs in parallel and k_i the stiffness value of the connection for the component i .

In the model proposed, a kinematic coupling with all DOFs constrained was applied between the edge corresponding to the location of the joint and its midpoint (see Figure 2.4ii), as used by Sejkot et al. [99].

Due to the presence of vertical plates between neighbouring horizontal plates, springs were placed in a series on both sides of the vertical plates. Therefore, spring stiffness values k_i for each DOF i had to be doubled:

$$k_i = \frac{1}{k_{i,1}} + \frac{1}{k_{i,2}} \quad (2.3)$$

$$k_{i,1} = k_{i,2} = 2 \cdot k_i \quad (2.4)$$

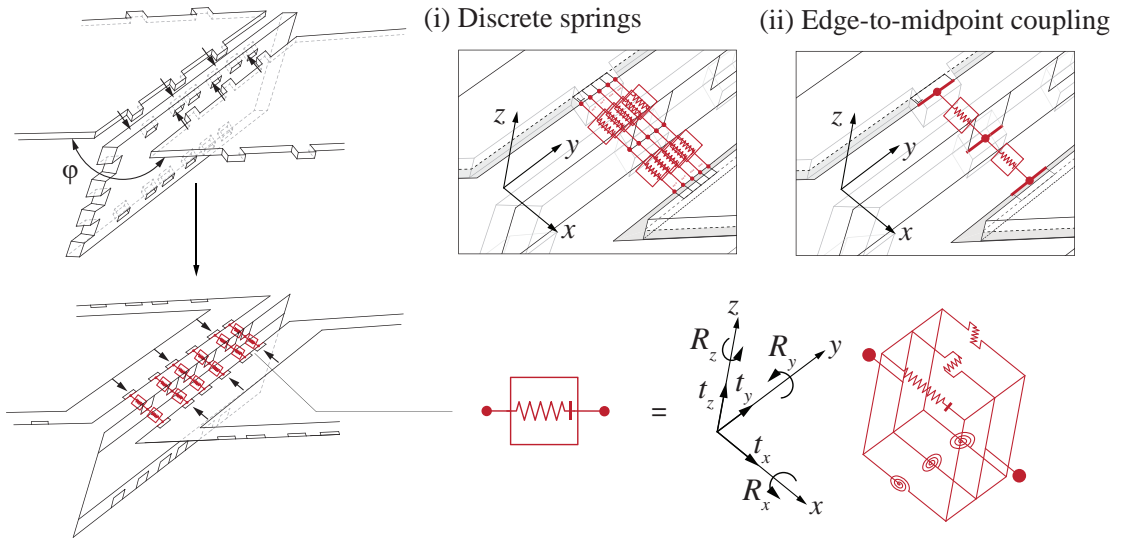


Figure 2.4 – Schematic representation of the numerical model for TT wood-wood connections. A spring model was adopted because of the large dihedral angle φ between horizontal plates. Due to the presence of vertical plates between neighbouring horizontal plates, springs were placed in a series on both sides of the vertical plates. Springs with 6 DOFs (3 translational and 3 rotational) were implemented. (i) Model with springs distributed over the length of the connection. (ii) Model with kinematic edge-to-midpoint coupling model.

In order to identify the edges to be coupled and connected by spring elements, the midsurfaces of the plates were partitioned in order to identify the position of the joints in the CAD-FEM exchange geometry.

Dovetail joints connecting vertical plates along their shared edge were considered as rigid connections since the interlocking of the plates blocks the rotation at this connection. Vertical plates connected to each other were imported in the FEA software as one individual part.

Mesh Properties

Sources of modelling uncertainties can be linked to the mesh element type and the mesh density. Finite strain (also defined as large strain) S4R elements, 4-noded with 6 DOFs, were chosen for the mesh because of their robustness and as they are multi-purpose shell elements with hourglass control. The uniformly reduced integration helps to prevent shear and membrane locking. These elements take transverse shear effects through the plate thickness into account for thick shells using the Reissner-Mindlin theory but converges to the classical theory for thin shells as the thickness decreases, neglecting transverse shear strains [16].

A mesh convergence study was carried out to assess the reliability of the results. It was performed on the 5×3 boxes prototype, simply supported (more details on the modelling of the boundary conditions can be found in Section 3.3.5), under self-weight and considering rigid beam connectors. Mesh seed sizes varying from 20 to 50 mm with steps of 10 mm and from 5 to 20 mm with steps of 2.5 mm were computed. Figure 2.5 presents the error on the maximum vertical displacements, with respect to the displacement for the lower seed size of 5 mm, according to the density of elements, which corresponds to the number of elements per square meter. The total CPU time of the numerical simulation, obtained using a Lenovo Intel® Core™ i7-4800MQ CPU @ 2.7 GHz with 16 GB of RAM 1600 MHz (Lenovo Group Limited, Beijing, China) is also indicated. To minimise the computation time for large models while providing sufficiently accurate results with regard to the displacements, a seed size of 20 mm, leading to a relative error below 1 %, was chosen.

A refined meshing strategy was adopted to decrease the computation time of the numerical model for the chosen mesh size of 20 mm. Since strains are concentrated at the location of the joints, plates were partitioned to have a local mesh refinement at the vicinity of the joints and a coarser mesh away from these regions. Fine elements of 20 mm were applied around the plate edges and coarser elements of 50 mm were used for the remaining area (see Figure 2.6). The computation time was reduced by 50 % without significantly changing the results compared to a uniform mesh of 20 mm (< 0.4 % difference).

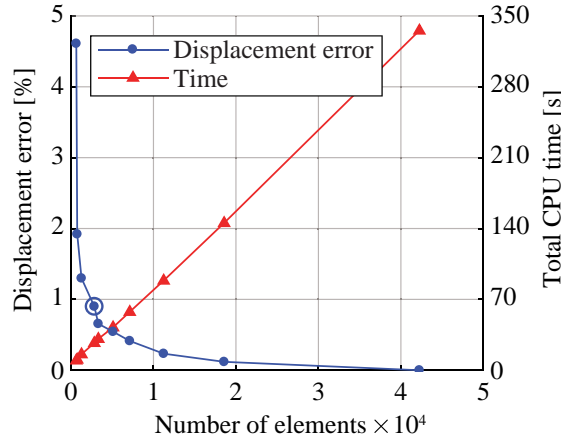


Figure 2.5 – Mesh convergence with regard to the maximum vertical displacements and total CPU time. A seed size of 20 mm (marked with a circle), leading to a relative error with respect to the displacement for the lowest seed size of 5 mm below 1 %, was chosen in order to minimise the computation time for large models while providing sufficiently accurate displacement results.

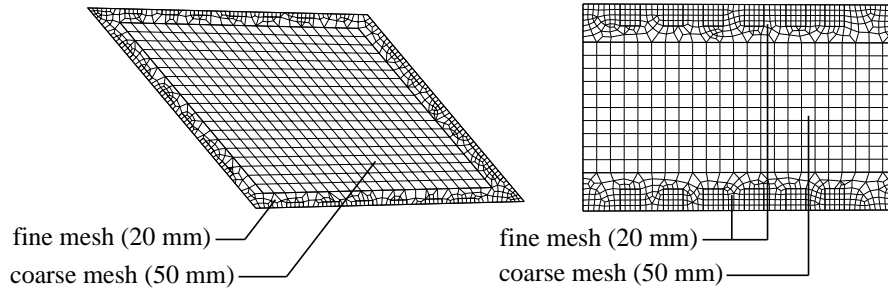


Figure 2.6 – Mesh for displacement studies using S4R elements, resulting from the mesh convergence study. A refined mesh strategy was adopted to decrease the computation time of the numerical model for the chosen mesh size of 20 mm. Since strains are concentrated at the location of the joints, plates were partitioned to have a local mesh refinement with 20 mm elements at the vicinity of the joints and coarser elements of 50 mm away from these regions.

However, stresses were found to not converge for the study performed on 5×3 boxes prototype for mesh sizes ranging from 5 to 50 mm (see Figure 2.7a). A supplementary mesh sensitivity analysis was thus carried out with regard to the forces obtained in the connections, in prospect of experimental and numerical results comparison of these forces. To achieve it, a determined force F was applied to one connection of a timber plate and the error between the applied force F and the total force in the tenon F_{tot} , retrieved from numerical simulations, was calculated for different mesh element sizes. The total force per tenon F_{tot} resulting from the model was calculated as follows:

$$F_{\text{tot}} = \sum_{i=1}^n SF1_i \cdot \delta_i = \sum_{i=1}^n \int_{-h/2}^{h/2} \sigma_{11,i}(z) dz \cdot \delta_i \quad (2.5)$$

with $SF1_i$ the direct membrane force per unit width in local 1-direction (in this case, axial direction of the connection), δ_i the length of the mesh element and h the thickness of the plate and $\sigma_{11,i}$, the normal stress.

Results of the mesh convergence study for the analysis of forces in the connections are presented in Figure 2.7b for mesh element sizes varying from 2.5 to 30 mm. The 2.5 mm mesh size step was chosen because of the tab length of 72.5 mm in the 5×3 boxes prototype. To confirm the convergence shape of the curve, mesh sizes of 3 and 4 mm were also investigated (grey markers in Figure 2.7). The smallest element size of 2.5 mm, leading to a relative error of 0.5 % between the force applied F and the total force in the tenon obtained, was chosen. A refined mesh strategy was then also adopted considering coarse elements of 50 mm.

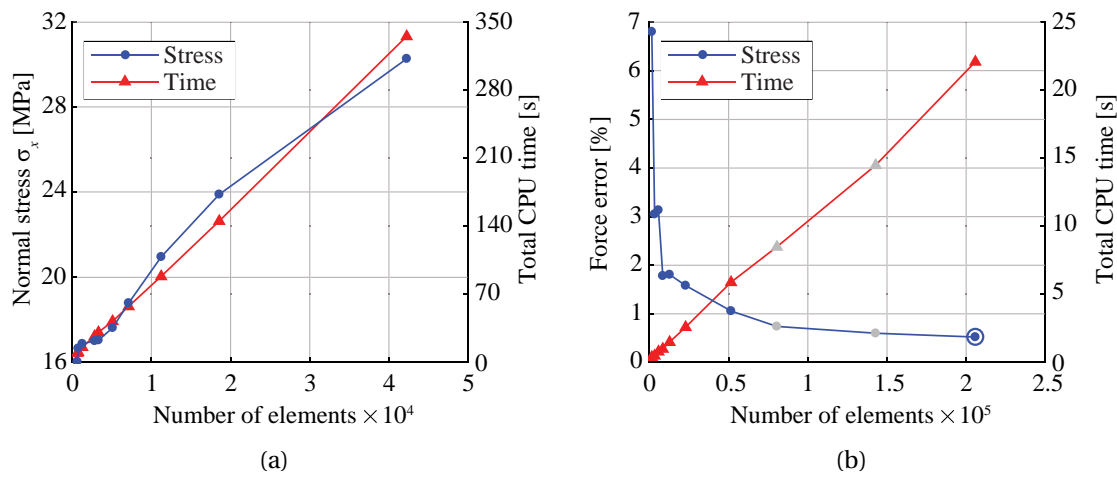


Figure 2.7 – Mesh convergence with regard to the normal stresses, axial forces and total CPU time. (a) For the 5×3 boxes prototype, normal stress σ_x did not converge. (b) A supplementary mesh convergence study, carried out on one single plate, showed that the forces in the connections converge. A mesh size of 2.5 mm (marked with a circle), leading to a relative error with respect to the force applied below 1 %, was chosen. Additional mesh sizes of 3 and 4 mm (grey markers) were investigated to confirm the convergence shape of the curve.

2.3.3 Automatic Generation of the CAD-FEM Exchange Geometry¹

The generation of the CAD-FEM exchange geometry, which is defined by the FE model presented in Subsection 2.3.2, was implemented in the existing CAD plugin developed for double-layered double-curved timber plate shells [80]. In this existing tool, two main classes called *box* and *plate* are defined and all boxes are composed of four plates: one top, one bottom and two side plates (see Figure 2.8a). These data structures include indexing, adjacency properties, base plane and additional information helping the iteration over a collection of box components, while computing joinery between neighbouring box plates [80]. The same discretisation method applied for the segmented timber shell system was used for the FEM

¹The generation of the CAD-FEM exchange geometry was developed by the publication co-author, P. Vestartas.

geometry. However, the detailing phase differed depending on fabrication requirements and structural analysis application. As a consequence, while the first model consisted of two polylines per plate, the CAD plugin was modified to represent the FEM geometry by four point outlines connected with line segments (see Figure 2.8b). In order to apply a refined meshing strategy, each outline was divided in subparts: outer outline and inner curve form an area for fine mesh, whereas the inner curve is only used for a coarser mesh. Joinery areas were represented as a series of rectangular elements perpendicular to each edge.

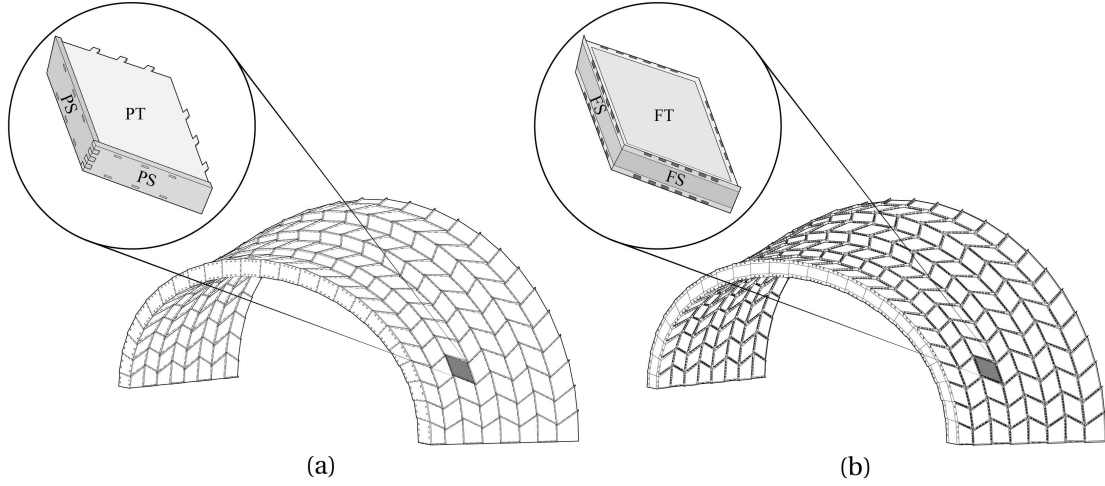


Figure 2.8 – Comparison between the 3D model geometry and the FEM geometry: (a) The design geometry (3D model) is represented as a set of 4 plates: two top plates (PT) and two side plates (PS). Each plate consists of 2 polylines used for CNC cutting. (b) The FEM geometry is represented as 4 surfaces: two top surfaces (FT) and two side surfaces (FS). The surfaces contain joinery elements, as well as fine and coarse subdivision areas.

Plane-plane and line-plane intersection methods (see Figure 2.9) were applied in the proposed geometrical method.

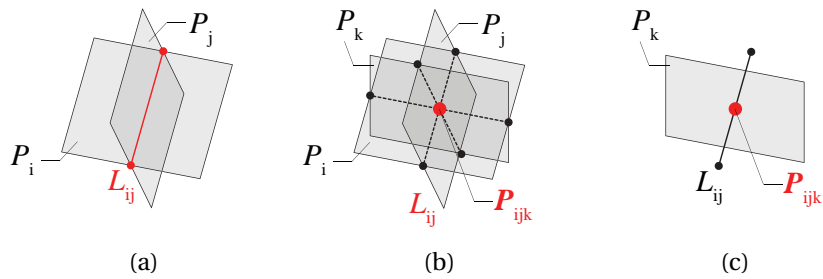


Figure 2.9 – Plane-line intersection methods used to generate the CAD-FEM geometry: (a) Plane-plane (b) Plane-plane-plane (c) Line-plane.

The procedure used to compute the FEM contour geometry for each plate is illustrated in Figure 2.10. All planes P_j from box B_i were derived from base mesh edge direction and normal. Top and bottom contours were obtained by retrieving the lines L_{jj+1} at the intersection between the planes P_j and P_{j+1} and subsequently intersecting them with top and bottom

planes P_T and P_B (see Figure 2.10a). In the same manner, side plate contours were computed by retrieving the lines L_{0T} , L_{2T} , L_{0B} and L_{2B} at the intersection between the planes P_0 , P_2 , P_T and P_B and subsequently intersecting them with the side plane P_3 . The same operation was repeated for P_0 (see Figure 2.10b). Finally, outlines for coarse mesh were obtained by offsetting neighbour planes in the direction of their normal and intersecting them with a base plane (see Figure 2.10c). This geometrical operation is valid when angles between planes are not close to 180° ; otherwise, a bisector plane must be added for computing the outline. While the side plates of each box are connected by dovetail joints in the design model, side surfaces were connected by the same edge in the FE model (FS-FS common edge in Figure 2.8) according to the defined FE model.

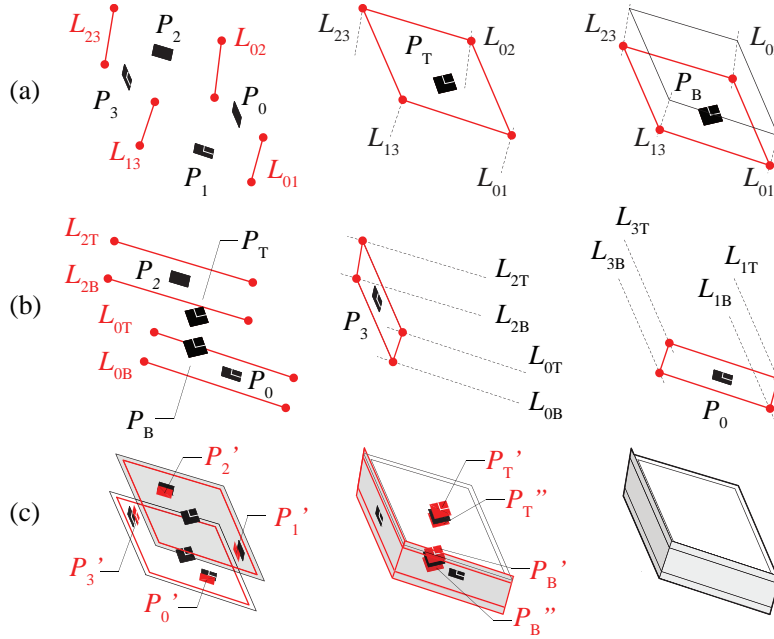


Figure 2.10 – Contour modelling steps of the FEM geometry using plane-plane and line-plane intersection methods: (a) Top and bottom contours (b) Side contours (c) Offset of outlines for coarse and fine mesh areas.

In the design model, the geometry of each tenon is characterised by three Bryant angles defining the insertion vector; however, in the FEM geometry, connections can be simplified to orthogonal shapes. Joinery areas were therefore represented by a set of interpolated rectangles perpendicular to an edge and computed using line-plane intersections, as illustrated in Figure 2.11. The coarse and fine meshing areas of each box, M_{coarse} and M_{fine} respectively, were first identified since the joinery areas are located in M_{fine} (see Figure 2.11a). The planes P_E and $P_{E,\text{opp}}$ were used to compute the joinery areas of edge E and opposite edge E_{opp} respectively. They were defined as the planes xz , with the local x -axis determined by the cross product between the edge vector $\mathbf{e}/\mathbf{e}_{\text{opp}}$, of the edge E/E_{opp} , and the normal of the adjacent plate plane $\mathbf{n}_i/\mathbf{n}_{i+1}$, corresponding to the y and z -axis respectively (see Figure 2.11b–c). The planes P_E and $P_{E,\text{opp}}$ were then copied along the edges E and E_{opp} (see Figure 2.11d).

Rectilinear elements were then created to identify the joints using plane-line intersection (see Figure 2.11e-f). The height of the rectangles of the current plate was set slightly higher (1 mm) than the ones of the adjacent plate in order to identify the direction of the tenons in the FE model.

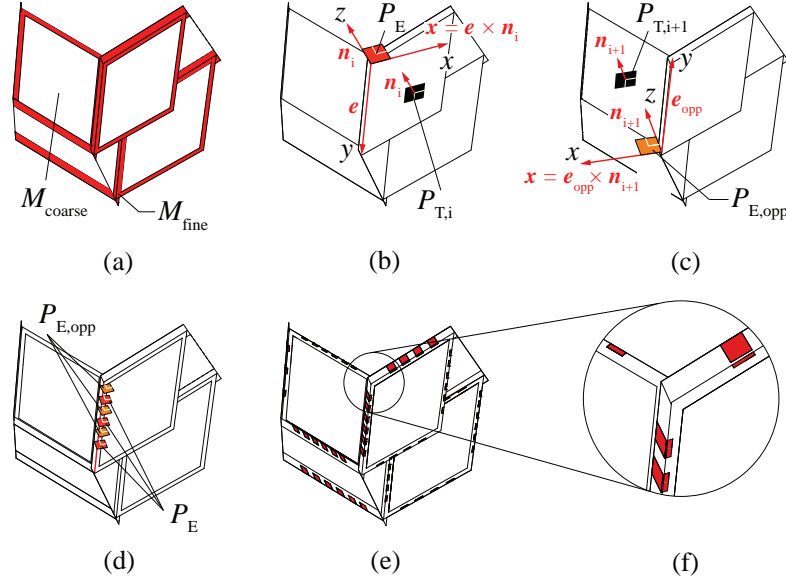


Figure 2.11 – Joinery modelling steps of the FEM geometry: (a) Joinery zones are located in the fine mesh area M_{fine} (b)-(c) Planes P_E and $P_{E,\text{opp}}$, used to compute the joinery areas of edge E and opposite edge E_{opp} respectively, are the planes xz of the connection (d) Planes P_E and $P_{E,\text{opp}}$ are copied along the edges E and E_{opp} (e)-(f) Rectilinear elements are obtained from the intersection of planes P_E and $P_{E,\text{opp}}$ with the plate outlines.

Finally, the resulting geometry was returned to the CAD interface and prepared for export to the FEA software.

2.3.4 Automatic Generation of the Finite Element Model

For structures with a large number of joints and uniquely shaped plates, a manual implementation of all parts of the structures and their connections in the FEA software would be too tedious. Consequently, a custom code in Python programming language was developed to generate the model from the CAD geometry exported to SAT files. The FE model was generated in the FEA software AbaqusTM, using the Abaqus Scripting Interface. It was chosen as the geometry can be imported directly from a CAD software. However, the same principles can be applied to other platforms. In the CAD software used, in this case Rhinoceros[®], version 6.0 (Robert McNeel & Associates, Seattle, WA, USA), all boxes are numbered and organised; however, their import process into AbaqusTM is not. An algorithm was thus implemented to connect all plates together. The model was generated using the following steps, illustrated in Figure 2.12:

1. The CAD-FEM exchange geometry was imported from SAT files for horizontal plates from both layers and for vertical plates. All horizontal plates were imported as individual parts, while pairs of vertical plates connected by dovetail joints were imported as joined parts. All lengths were multiplied by a scale factor between the CAD software geometry (in this case in mm) and the FEA software using the SI units (i.e. Newton, Pascal, kilogram, second and metre).
2. Material properties and section properties were assigned to all parts located within a defined bounding box. The material orientation of the plates was defined using the discrete method of orientation of AbaqusTM with the normal axis direction in the z -direction of each plate face (through-thickness direction) and the primary axis direction x defined by the vector (1,0,0), in the fibre direction.
3. A coarse mesh was generated on each part located within the bounding box with defined seed size and element properties.
4. Potential edges corresponding to the location of the tenons were identified. These edges have a minimum and maximum possible length and are located on the outline of the parallelogram for horizontal plates and inside of the polygon for vertical plates. The identification of these edges, the coordinates of their centre point and the direction of the tenon were stored in two lists for horizontal and vertical plates respectively.
5. The edges were partitioned at their midpoint, suppressing the coarse mesh around the plates.
6. The mesh was re-generated with a refined seed size or with the same coarse seed size, depending on whether a refined meshing strategy was adopted or not.
7. Dependent part instances were created and assembled to form the whole geometry. As opposed to their independent counterparts, dependent instances refer to the original geometry of the parts imported; operations such as meshing and partitioning are performed on individual parts and not on instances.
8. Corresponding centre vertices from the two lists created were found and pairs were stored in a new list. Reference points were created for each centre point that was found to have a corresponding centre point and kinematic couplings were applied to the reference points and their edges.
9. Finally, 6-DOFs springs characterised by a stiffness k_i were implemented between the pairs of vertices to connect horizontal and vertical plates.

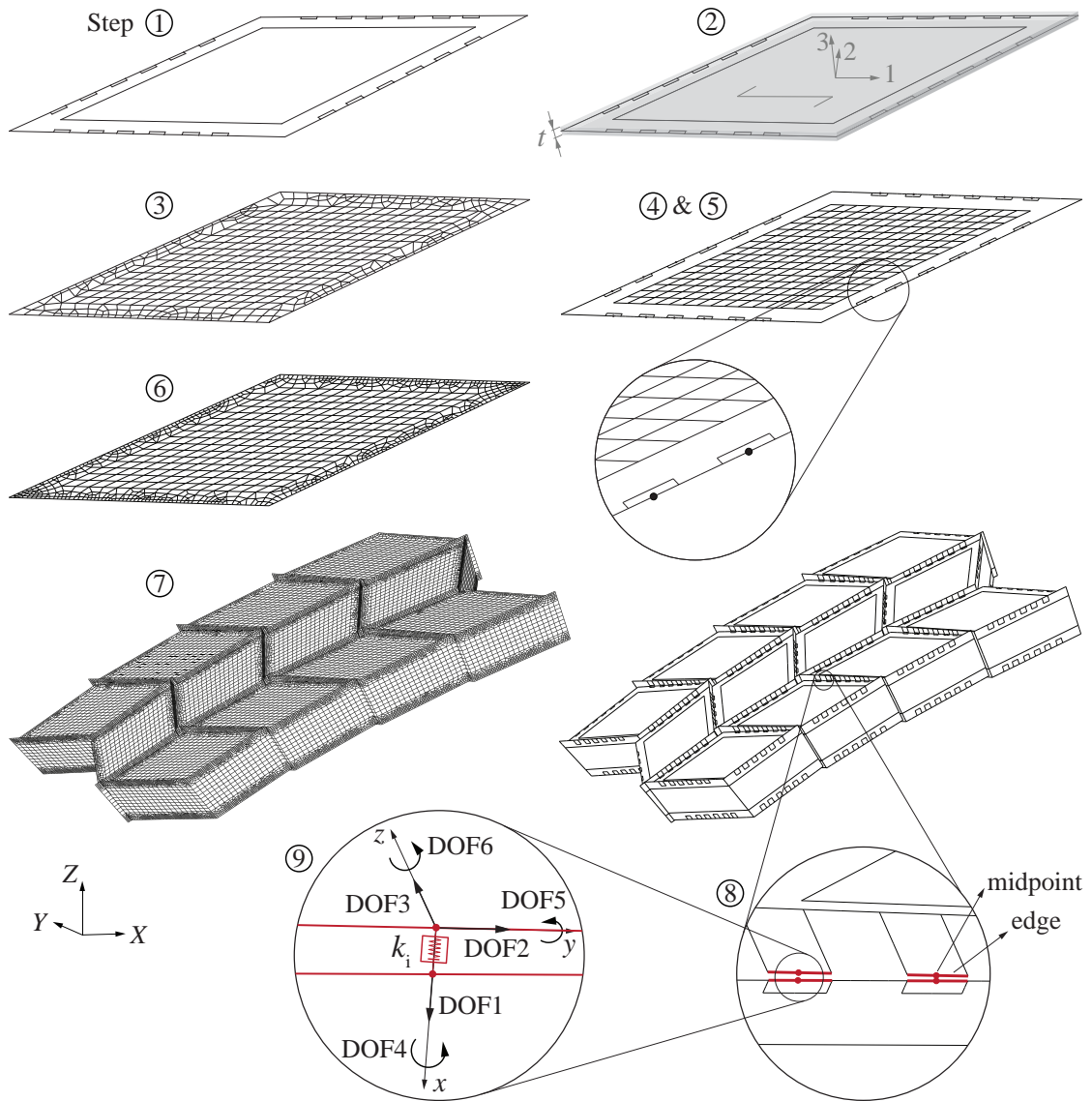


Figure 2.12 – Steps for the generation of the FE model in the FEA software: ① Importation of all horizontal plates as individual parts (pairs of vertical plates connected by dovetail joints are imported as joined parts) ② Assignment of material and section properties with their local coordinate system ③ Coarse mesh generation ④ Identification of the connection positions ⑤ Partitioning of the edges of the tenons at their midpoint ⑥ Fine mesh re-generation ⑦ Assembly of the instances ⑧ Edge-to-midpoint coupling ⑨ Generation of the springs with 6 degrees of freedom (3 translational and 3 rotational), each characterised by a stiffness k_i .

2.4 Results and Discussion

In this section, CAD-FEM geometry and semi-rigid spring model, obtained using custom scripts following the methods presented in Section 2.3, are both evaluated. Computational aspects are discussed, as well as questions related to the semi-rigid modelling of the connections, which is expected to have a significant influence on the results.

2.4.1 Spring Model for the Connections

To evaluate the spring model, a comparison was made between two spring modelling methods for the connections:

- (i) with discrete springs distributed along the length of the connections (see Figure 2.4i);
- (ii) with unique springs kinematically coupled to the edges of the tenons as used in the model proposed (see Figure 2.4ii).

In the first model (i), it was observed that springs only act locally on the nodes that are connected, as illustrated in Figure 2.13 presenting the vertical displacements of the bottom layer of the 5×3 boxes prototype with simply supported boundary conditions and under self-weight, using one rigid spring per connection ($n = 1$ in Equation 2.2).

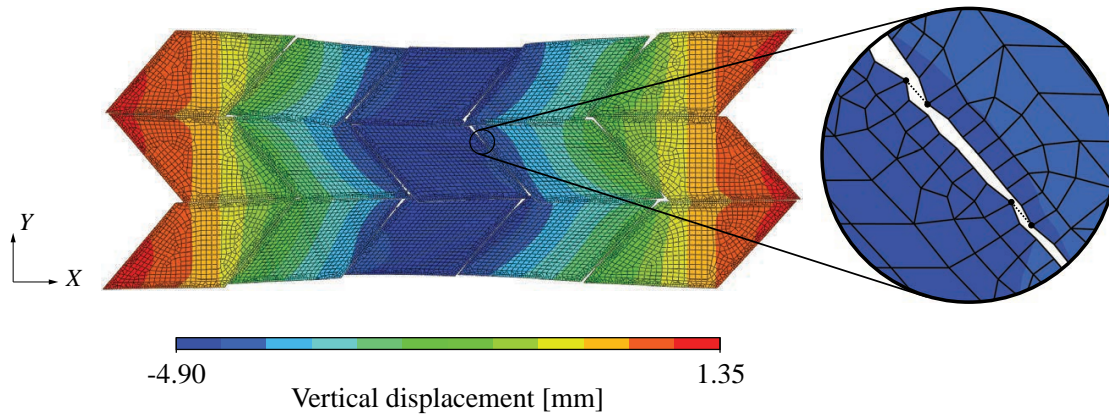


Figure 2.13 – Vertical displacements of the bottom layer of the 5×3 boxes prototype with simply supported boundary conditions and under self-weight, using one rigid spring per connection ($n = 1$). The springs were shown to act only locally on the nodes that are connected.

By increasing the number of springs in parallel n , the global response of the prototype was shown converge to stiffer results (see Figure 2.14). The model (ii) with a coupling between the edge of the tenon and its midpoint would therefore correspond to an infinite number of springs distributed along the connection and its use is therefore pertinent.

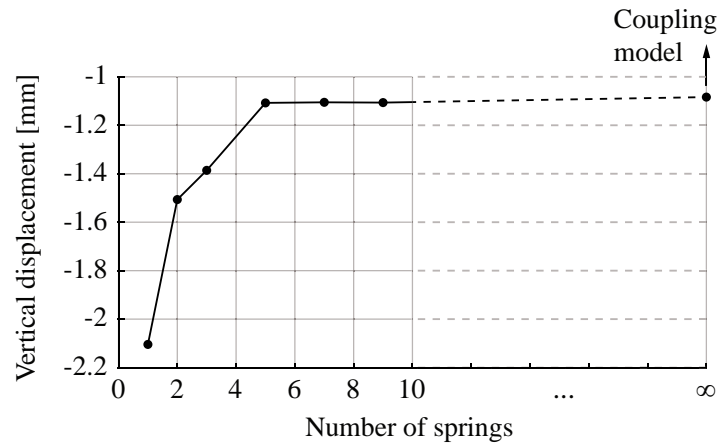


Figure 2.14 – Vertical displacement of a 5×3 boxes prototype with simply supported boundary conditions and under self-weight according to the number of springs in parallel distributed along the connections. The model with a coupling between the edge of the tenon and its midpoint corresponds to an infinite number of springs distributed along the connection.

2.4.2 Automatic Generation of the Numerical Model

The CAD-FEM geometry was successfully generated for both small- and large-scale structures. The aim of an automated generation was to avoid a manual process of transforming a large amount of plate elements to the defined exchange geometry. As a result, automation helped in decreasing the processing time of an initial manual generation of the FEM geometry, both time-consuming and containing user errors such as floating-point errors. Moreover, it allowed the application of the same code to a set of arches (see Figure 2.15).

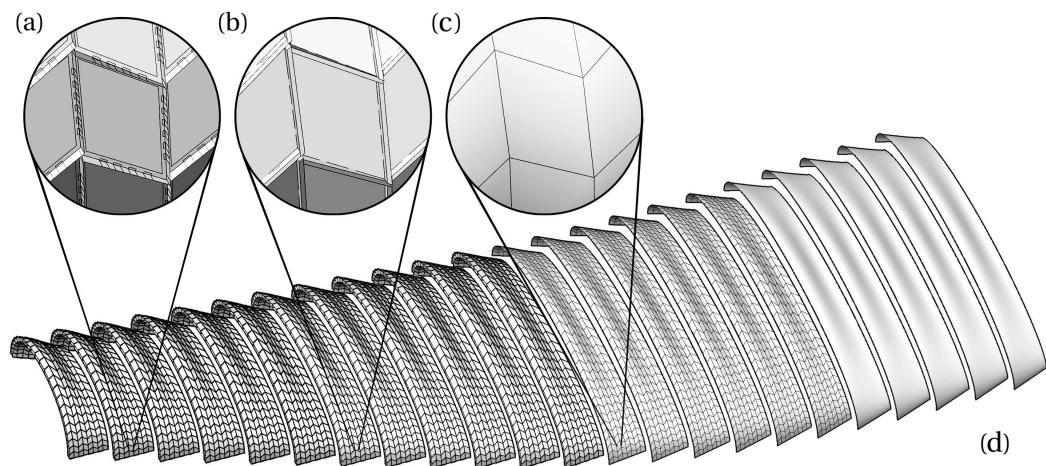


Figure 2.15 – Application of the same code generating the CAD-FEM exchange geometry to a set of arches: (a) FEM geometry (b) Design geometry (3D model) (c) Mesh subdivision (d) Design target surface.

The numerical model was then obtained from the CAD-FEM exchange geometry. Table 2.1 presents the total number of variables and the minimum memory required (corresponding to the maximum amount of memory allocated by the analysis required to keep critical scratch data in memory [16]) for a small-scale prototype made of 5×3 boxes (15 boxes) and a full-scale arch of 24 m span (200 boxes).

Table 2.1 – Size-related parameters of small- and large-scale prototypes composed of 15 and 200 boxes respectively.

Parameter	15 boxes	200 boxes
Total number of variables	377 562	4 314 636
Min. memory required [Mb]	150	1 715

Table 2.2 presents the time taken for each step of the generation of the FE model in the FEA software described in Subsection 2.3.4. For 15 boxes, AbaqusTM bushing connectors were used for the spring connections whereas for 200 boxes, AbaqusTM springs were used, as the implementation of bushing connectors took several hours. Vertical panels were imported as joined parts since it was shown that the implementation of tie constraints between singular vertical panels drastically increases the model generation time.

Table 2.2 – Time of each step of the generation of the finite element model for small- and large-scale structures.

Step	Description	Time ^a for 15 boxes	Time ^a for 200 boxes
1	Importation of the parts	3.3 s	42.3 s
2	Material and properties assignment	0.4 s	2.5 s
3	Coarse mesh generation	5.7 s	55.1 s
4	Identification of the connections	34.8 s	4.5 min
5	Partitioning of edges	17.4 s	3.8 min
6	Fine mesh re-generation	3.7 min	42.8 min
7	Assembly of the instances	0.1 s	7.0 s
8	Edge-to-midpoint coupling	4.1 s	2.3 min
9	Generation of the springs	45.8 s	5.3 min
Total generation of the FE model		5.6 min	64.2 min

^a Time obtained using a Lenovo Intel[®] CoreTM i7-4800MQ CPU @ 2.7 GHz with 16 GB of RAM 1600 MHz.

Although the model can be built relatively fast compared to a manual implementation of all elements and properties, the numerical model for a full arch obtained is particularly heavy because of the large number of variables involved in the model (see Table 2.1). Consequently, additional manual implementations and modifications of the model can take several minutes, which makes the verification of the model also unpractical. It is therefore important to include all modelling aspects, including boundary conditions and loads, in the custom scripting code for large-scale models.

Furthermore, it is apparent that the most time-consuming step is step 6, corresponding to the re-generation of the mesh. However, the times presented in Table 2.2 are linked to the FEA software used, in this case AbaqusTM. The total model generation time could therefore be reduced by using external meshing libraries in C++ or a faster FE library such as OpenSees (UC Regents, Berkeley, CA, USA), which does not require a graphical user interface (GUI) and could thus allow to generate the models faster [56].

2.4.3 Stiffness Components Influence

The influence of each DOF was investigated by comparing a model with fully rigid connections and models in which each of the 6 DOFs was individually released while keeping the 5 remaining components blocked. Results obtained for simulations performed on a 5×3 boxes prototype with simply supported boundary conditions, under self-weight and using the spring coupling model are presented in Figure 2.16.

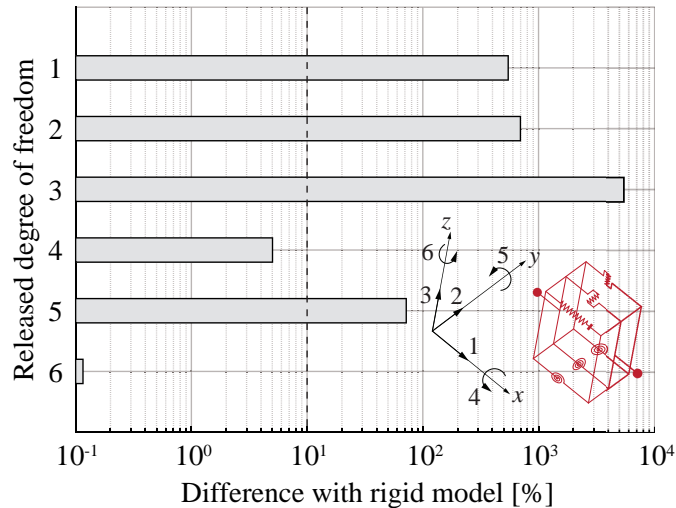


Figure 2.16 – Influence of each DOF on the vertical displacement of a 5×3 boxes prototype with simply supported boundary conditions and under self-weight. The bars represent the difference between the displacements obtained when each of the 6 DOFs were individually released, while keeping the 5 remaining components blocked, and a rigid model in which all 6 DOFs were blocked.

Components 1 and 2 were shown to have a high influence on the vertical displacement of the structure compared to a rigid model ($> 700\%$). The maximum displacement obtained when the DOF 3 was released gave an infinite vertical displacement ($> 10^7$ mm). This is explained by the fact that it represents the motion in the z -direction; if this component is free, the vertical displacement is not blocked and very high values are thus obtained. A maximum value of 600 mm, corresponding to the height of the boxes was therefore considered and the maximum vertical displacement was found to be 55 000 % higher than for a rigid model. Regarding rotations, the DOF 5 highly influenced the vertical displacements of the structure ($> 80\%$)

compared to components 4 and 6, which had a limited influence (7.6 % and 0.2 % respectively). The semi-rigidity of the connections for the components 1, 2, 3 and 5 had an influence higher than 10 % on the vertical displacements. Stiffness values in axial and shear loading, as well as bending were thus considered as important to be implemented in the final model.

The interaction between translational and rotational stiffness components was investigated to determine the potential coupling terms that might have to be considered in further studies. The stiffness k_3 was not investigated as considering this component free led to infinite displacements. For pairs of DOFs, results obtained with both components released were compared to the superposition of the results with the same components individually released. Results are presented in Table 2.3.

Table 2.3 – Influence of each degree-of-freedom (DOF) on the vertical displacements compared with a rigid model.

DOF	Both released [mm]	Superposition [mm]	Difference [%]
1, 4	10.9	11.0	1.0
1, 5	11.7	311.1	2560.8
1, 6	10.8	11.0	2.4
2, 4	13.1	12.8	-2.6
2, 5	14.0	34.0	143.8
2, 6	10.8	12.5	16.4
1, 2	21.6	29.4	35.7

When k_1 and k_4 are both free, vertical displacements are approximately equal to the superposition of the vertical displacements when the two components are separately released (1.0 % difference). Same observations were made for components k_1 and k_6 and k_2 and k_4 (absolute difference below 3 %). This was expected because of the limited influence of the rotational components k_4 and k_6 below 10 %. Coupling terms might be necessary between components k_2 and k_6 , as well as k_1 and k_2 . However, major differences occurred between components k_1 and k_5 as well as between k_2 and k_5 . To take into account coupling terms for these DOFs, the stiffness matrix K has to be modified to Equation 2.6:

$$K = \begin{bmatrix} k_1 & 0 & 0 & 0 & k_{15} & 0 \\ 0 & k_2 & 0 & 0 & k_{25} & 0 \\ 0 & 0 & k_3 & 0 & 0 & 0 \\ 0 & 0 & 0 & k_4 & 0 & 0 \\ k_{51} & k_{52} & 0 & 0 & k_5 & 0 \\ 0 & 0 & 0 & 0 & 0 & k_6 \end{bmatrix} \quad (2.6)$$

2.5 Conclusions

This chapter presents methods to automate the generation of an FE model for the structural analysis of complex timber plate structures with a large number of wood-wood connections. In particular, a design framework is proposed to integrate the generation of the model into the existing design and fabrication workflow.

An FE model using springs with an edge-to-midpoint coupling approach to model the semi-rigid behaviour of wood-wood connections was developed. Based on the case study of this thesis (see Chapter 1, Subsection 1.3), the existing CAD plugin, generating the 3D model and fabrication files of double-layered double-curved timber plate shells, was modified to obtain a CAD-FEM geometry. The latter was then implemented in an FEA software. Although the numerical model and the methods to generate it were presented and applied to a specific type of structure, they are easily applicable to various plate structures using wood-wood connections.

The first step of the proposed design framework, consisting of the generation of the numerical model, was achieved in this chapter. The numerical model was successfully generated for both small- and large-scale structures composed of 15 and 200 boxes respectively, using custom developed scripts, avoiding a tedious and time-consuming manual implementation. Another advantage over a manual generation is that it prevents random human errors. The time to generate the numerical model in the FEA software AbaqusTM, from the import of the CAD-FEM geometry to the generation of the thousands of springs was found to be of about 6 min and 1 hour for 15 and 200 boxes assemblies respectively. However, for large-scale assemblies, the model was found to be heavy and unpractical for verification and modifications performed outside of the scripting interface because of the millions of variables defined in the model.

The edge-to-midpoint coupling applied in the proposed spring model was proven pertinent in comparison with a model using individual springs distributed over the length of the connections. It prevents peak values at discrete nodes and is equivalent to an infinite number of discrete springs distributed along the edge. Semi-rigidity of the connections in translation as well as in rotation was shown to be of importance, with translational components (k_1 , k_2 , k_3) and rotational component around y (k_5) having the highest influence on vertical displacements. Moreover, main potential coupling terms between stiffness components k_1 and k_5 as well as k_2 and k_5 were identified.

3 Experimental Investigations on Small-Scale Structures

This chapter is based on: A. C. Nguyen, P. Vestartas and Y. Weinand, Design Framework for the Structural Analysis of Free-Form Timber Plate Structures using Wood-Wood Connections, *Automation in Construction*, 107:102948, 2019. doi:10.1016/j.autcon.2019.102948.

3.1 Introduction

In Chapter 2, a design framework for the structural analysis of freeform timber plate structures using wood-wood connections was introduced. Its first step, consisting in the generation of a numerical model, was achieved: a finite element (FE) model was defined and successfully automated for a series of double-layered double-curved timber plate shells using custom-developed scripts. The second step of the proposed design framework encompasses structural investigations on the global mechanical behaviour of the structure through experimental tests. While different numerical models have been applied to timber plate structures using wood-wood connections, few experimental tests have been executed on full assemblies. Pertinent examples can only be found for single-layered timber folded plate structures [81, 106].

Past research has highlighted the importance of including the semi-rigid behaviour of wood-wood connections in numerical models [81, 105]. In the FE model developed, it was considered using springs with six degrees of freedom (DOFs). Preliminary investigations carried out in Chapter 2 showed that specific DOFs highly influence the global behaviour of the structure. However, spring stiffness values have not yet been determined. In previous research, spring stiffness values were obtained either from experimental tests or using simplified analytical models. For instance, all finger joints of the *ICD/ITKE Research Pavilion 2011* were modelled by springs with stiffness values retrieved from experimental shear load tests [50]. For the *Landesgartenschau Exhibition Hall*, in-plane shear stiffness of the finger joints and axial and out-of plane shear stiffness of the crossing screws were approximated with simplified analytical

models, while the bending stiffness was obtained from four-point bending tests [53]. In the spring model developed for timber folded plate structures studied by Stitic et al. [105], axial stiffness was calculated analytically, whereas shear and rotational stiffness were retrieved from experimental tests. Additionally, the remaining DOFs were considered rigid by assigning them high spring stiffness values of 10^9 N/mm and 10^{15} N-mm/° for translational and rotational components respectively.

In this chapter, the second step of the proposed design framework is accomplished by performing experimental tests on a series of specimens and comparing the results with numerical simulations, with the objective of evaluating the FE model developed. The geometry of the tested specimens and the three-point bending test setup are described in Section 3.2. The numerical model is subsequently presented in Section 3.3. Finally, results of experimental tests are discussed and compared to numerical simulations in Section 3.4.

3.2 Experimental Tests

3.2.1 Specimens

Tests were performed on three replicates of a 5×3 boxes prototype with a geometry as illustrated in Figure 3.1a. The number of boxes was chosen such that at least one box was surrounded by other boxes and to reduce the side effects implied by the boundary conditions. As described in Chapter 2, Subsection 2.3.1 and illustrated in Chapter 2, Figure 2.2, the geometry was based on the dimensions of 15 boxes extracted from a full 24 m span double-layered double-curved shell scale 1:1 at midspan. The size of each box was set to a length of 1.2 m, a width of 0.85 m, a static height of 0.6 m and an offset length equal to 80 mm between the boxes. Each replicate was made of 68 plates, forming a 6.88 m long and 2.59 m wide specimen in total. All through-tenon (TT) wood-wood connections were set to a unique geometry, with a tab length of 72.5 mm and Bryant angles (as defined in Chapter 1, Figure 1.5) $\theta_1 = 0^\circ$, $\theta_2 = 25^\circ$ and $\theta_3 = 0^\circ$. Additional panels were added such that the prototype was closed at all its edges.

The prototypes were built from BauBuche Q panels (Pollmeier Massivholz, Creuzburg, Deutschland), which are 40 mm thick beech LVL panels made of 3 mm thick layers of beech peeled veneers, glued together longitudinally and cross-wised into a panel in a composition ||| – ||||| – ||| (| for longitudinal, – for crosswise veneer layer) [9]. Panels were cut with a 5-axis CNC milling machine with a 20 mm diameter tool. They were fabricated by Annen Plus SA and assembled at the Laboratory for Timber Constructions (IBOIS), EPFL (see Figure 3.2).

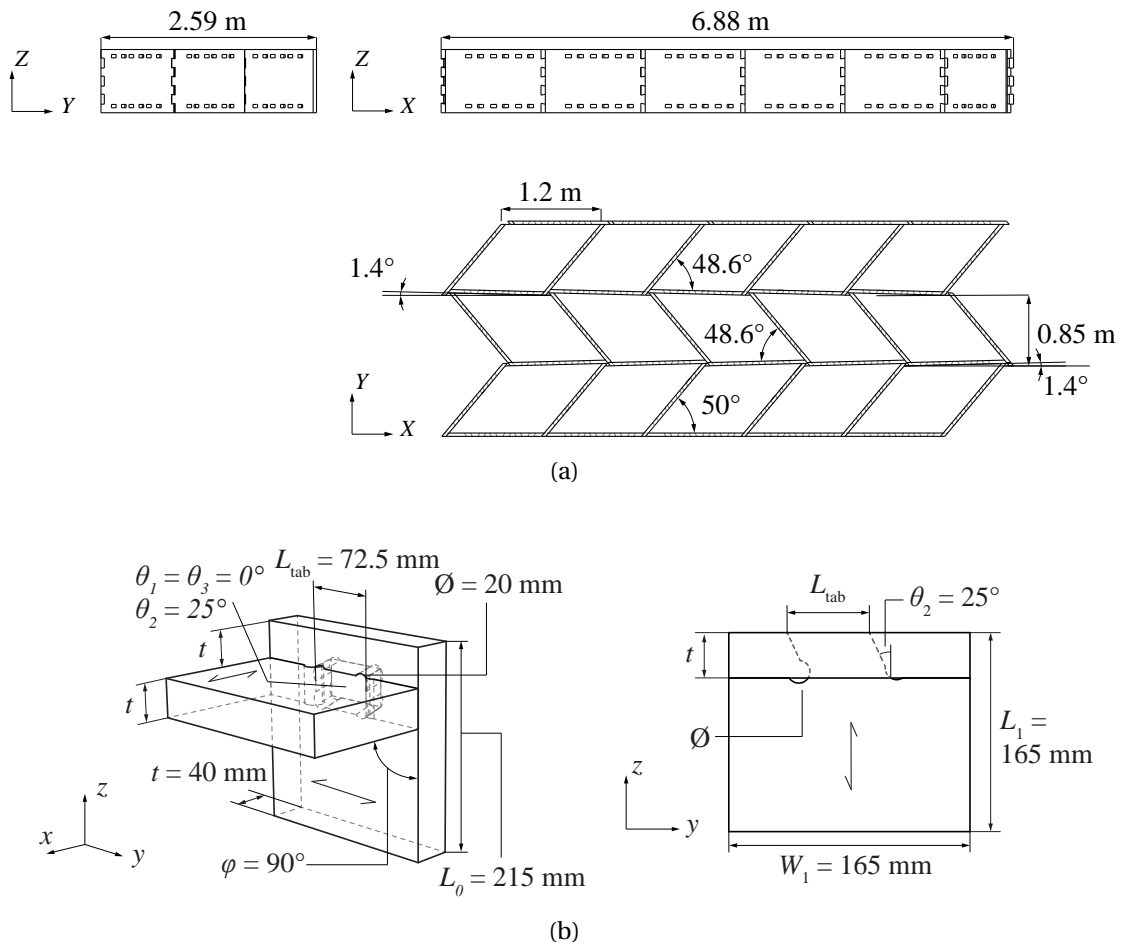


Figure 3.1 – Geometry of the 5 × 3 tested specimens: (a) Structure's global geometry parameters (b) Through-tenon wood-wood connections geometry parameters.



Figure 3.2 – One of the three replicates of the 5 × 3 boxes prototype assembled at the Laboratory for Timber Constructions (IBOIS), EPFL.

3.2.2 Test Setup

Three-point bending tests were performed using the test setup illustrated in Figure 3.3. Load was applied through a 200 kN capacity w+b hydraulic jack (walter+bai ag, Löhningen, Switzerland) on the three top panels at midspan of the prototypes, using a HEB 240 steel profile to distribute the loads. As performed by Stitic et al. [106] for tests on folded plate structures, the loading procedure described in the European Standard EN 26891 [24] was followed.

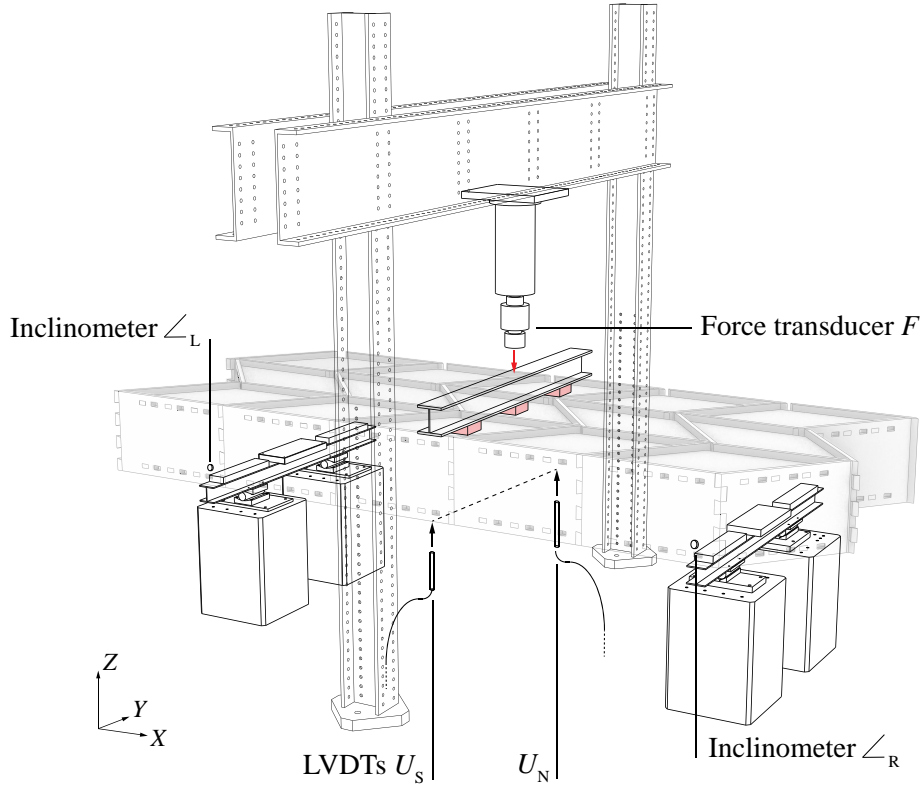


Figure 3.3 – Three-point bending test setup for the 5×3 boxes prototypes and measurement instrumentation.

3.2.3 Boundary Conditions

Prototypes were simply supported: rotation was allowed along the two supported edges and horizontal translation was allowed along one edge, such that the structure was pinned on one side and rolled on the other side (see Figure 3.4). The supports consisted in four concrete blocks of $0.75 \times 0.75 \times 1.04$ m, on which the steel rotulas were fixed. Two HEA 160 steel profiles were attached to the rotulas at the bottom flange and were screwed to the structure through 60 mm thick cross-laminated timber (CLT) plates at the top flange.

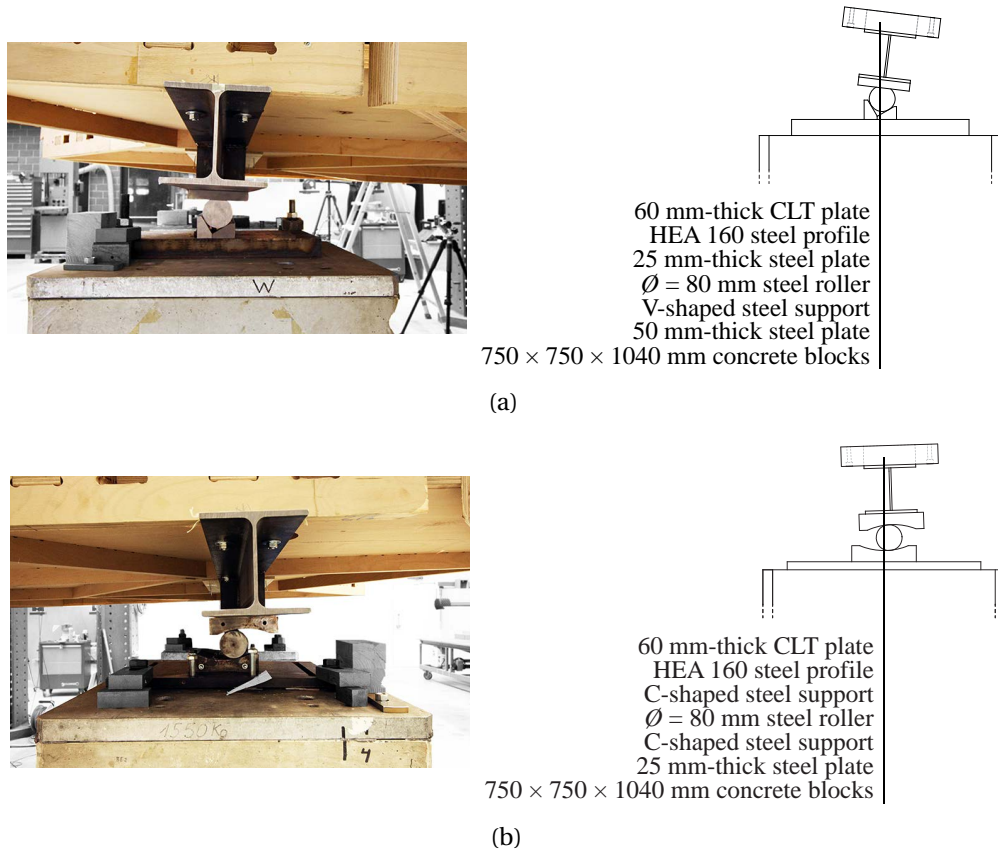


Figure 3.4 – Boundary conditions applied for the tests on 5×3 boxes prototypes: (a) Pinned support (b) Roller support.

3.2.4 Instrumentation

The prototypes were monitored with a pair of linear variable differential transformers (LVDTs) WA100 (HBM, Darmstadt, Germany) with a measuring range of 100 mm. They were placed at midspan on each side of the specimens to measure the vertical displacements of the vertical plates. The hydraulic jack was equipped with a force transducer of 200 kN nominal force. Two AccuStar® (Measurement Specialties, Inc., Hampton, VA, USA) electronic inclinometers with a sensing range between -60° and 60° were placed above the supports to control their rotation.

The upper layer of the structure was partially tracked with a three-dimensional (3D) digital image correlation (DIC) system to obtain displacement fields. As illustrated in Figure 3.5, a set of two cameras was placed 3.5 m above the area of interest on a very stiff steel profile to avoid vibrations during the test. Due to the limited height of the columns, the whole top surface could not be acquired. A DIC measurement area of about 3×2 m was captured by the two cameras. The full width of the prototype and approximately a third of the length was comprised within the field of view, such that three boxes could be measured.

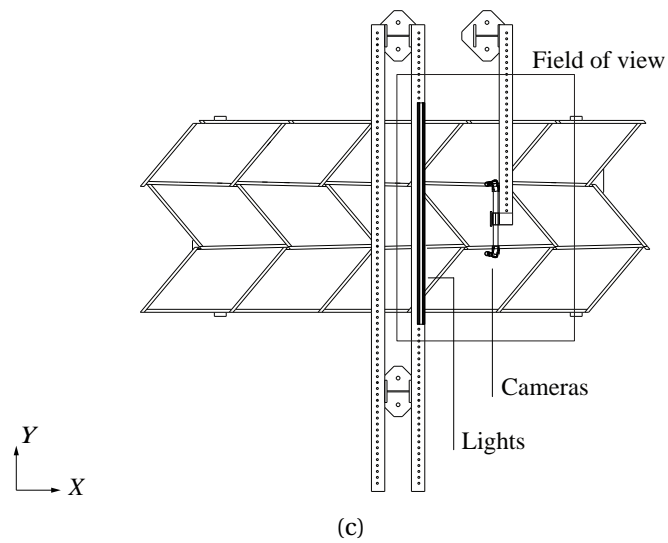
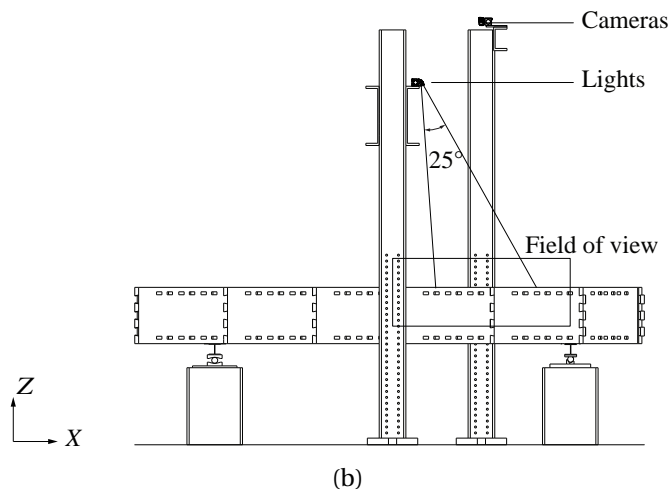
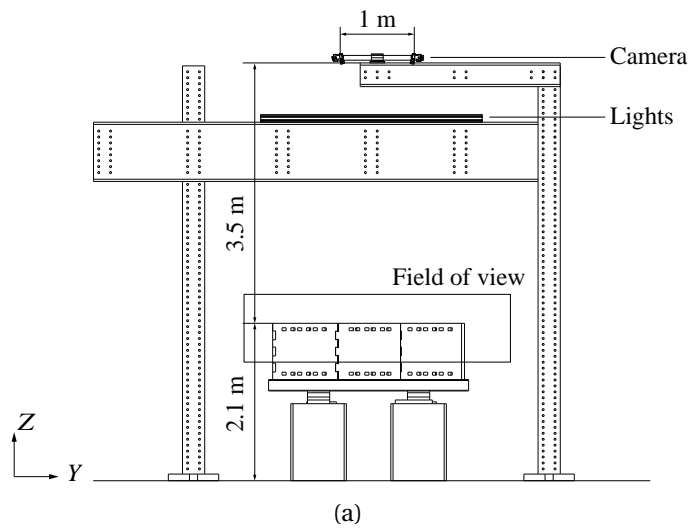


Figure 3.5 – Digital image correlation system setup with a measurement area of about 3×2 m:
(a) Front view (b) Side View (c) Top view.

High-resolution cameras were required because of the large dimensions of the prototype. Two SVCam Cameras model HR 29050 (SVS-Vistek GmbH, Seefeld, Germany) with 29 MegaPixels and dual GigE vision interface were utilised. They were used with 35 mm Zeiss Distagon ZF-I lenses (Carl Zeiss, AG, Oberkochen, Germany) with aperture f/8 and BP 525 green bandpass filters (Midwest Optical Systems, Inc., Palatine, IL, USA). They were mounted with an angle in between of 17.5° . The top surface of the prototype was illuminated with one pair of green LED EFFI-FLEX (EFFILUX, Les Ulis, France) light bars with 90 and 60 LEDs each. They were fixed with a small inclination to illuminate the area of interest on a 3 m long aluminium profile, itself mounted on the steel beam above the prototype, at midspan, onto which the hydraulic jack was fixed.

The DIC area of interest of the prototype was covered with two coats of matte white paint and a speckle pattern with speckle sizes between 1 and 5 mm was obtained using a pneumatic paint sprayer with black paint. Images were acquired with a speed of 2 Hz and exposure time of about $35\,000\ \mu\text{s}$. Calibration of the DIC system was carried out for each individual test using a target of $12 \times 9 - 50\text{ mm}$ with equally spaced markers and performed with three positions combined with multiple inclinations per box. The control of the DIC system as well as data treatment were performed using the VIC 3D™ software (Correlated Solutions, Inc., Irmo, SC, USA).



Figure 3.6 – Speckle pattern used for the DIC data acquisition. Speckle sizes between 1 and 5 mm were obtained by applying black paint on two coats of matte white paint with a pneumatic paint sprayer.

3.3 Numerical Model

3.3.1 Semi-Rigid Spring Model

The finite element spring model developed in Chapter 2 was used to simulate the experimental tests. In this model, plates were modelled as conventional shell elements and wood-wood connections were represented by springs with six DOFs (three translational and three rotational) to take into account their semi-rigid behaviour (see Figure 3.7).

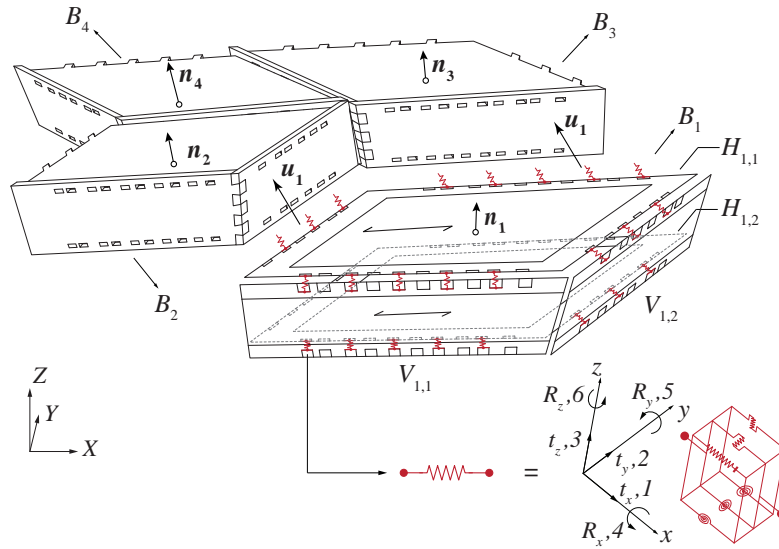


Figure 3.7 – Semi-rigid spring model: plates were modelled as conventional shell elements and wood-wood connections as springs with six degrees of freedom (three translational and three rotational).

The model was automatically generated in the finite element analysis (FEA) software AbaqusTM, version 6.12 (Dassault Systèmes, Vélizy-Villacoublay, France) according to the methods presented in Chapter 2, Section 2.3.4.

3.3.2 Material Model

Orthotropic material properties of each plate were implemented considering a single orthotropic layer with a defined local orientation for each plate: parallel to the grain (direction 1), perpendicular to the grain along the veneer layer and across the plate thickness (directions 2 and 3 respectively). Material properties were considered linear elastic, such that the analysis was limited to linear kinematics, with mean values of elastic properties presented in Table 3.1. Poisson ratio values, not provided by the manufacturer, were retrieved from literature for beech [9, 33]. Material and contact nonlinearities were not considered.

3.3.3 Semi-Rigidity of the Connections

In previous studies, spring stiffness values implemented in global FE models were retrieved from either experimental or analytical investigations. Simplified analytical models for axial and shear stiffness used by Stitic et al. [105] and Li et al. [53] respectively were based on Hooke's law, which provides analytical expressions of the stiffness according to the elastic or shear modulus. However, stiffness and capacity of TT connections cannot be accurately predicted using this method. Likewise, the more advanced analytical model for the rotational stiffness of TT connections developed by Roche [83] still showed limitations and has only been

Table 3.1 – Elastic properties of 40 mm thick BauBuche Q panels used for the orthotropic material model [9, 33].

Property	Symbol	Value	Units
Density	ρ_{mean}	800	kg/m ³
Elastic modulus 11	E_{11}	13200	N/mm ²
Elastic modulus 22	E_{22}	2200	N/mm ²
Elastic modulus 33	E_{33}	2200	N/mm ²
Shear modulus 12	G_{12}	820	N/mm ²
Shear modulus 13	G_{13}	430	N/mm ²
Shear modulus 23	G_{23}	430	N/mm ²
Poisson's ratio 12	ν_{12}	0.365	–
Poisson's ratio 13	ν_{13}	0.464	–
Poisson's ratio 23	ν_{23}	0.726	–

evaluated for spruce LVL. In the present study, simplified analytical models were therefore discarded. Stiffness and capacity of the TT connections investigated were obtained from experimental tests performed on recently developed test setups for the DOFs that were found to have a high influence on the model (above 10 %), namely k_1 , k_2 , k_3 and k_5 , as determined in Chapter 2, Subsection 2.4.3. These tests were performed on small-samples with TT connections characterised by a tab length of 72.5 mm and Bryant angles $\theta_1 = 0^\circ$, $\theta_2 = 25^\circ$ and $\theta_3 = 0^\circ$, corresponding to the connections of the 5×3 boxes prototype studied. Experimental tests are reported in Appendix A and spring stiffness k_i used for each DOF are presented in Table 3.2. The contribution of the screws added for the assembly of the plates (see Chapter 1, Subsection 1.3.4) was neglected because of their limited number in the structure.

For k_1 , a spring with the axial stiffness in tension and a high value of 10^9 N/mm in compression, to be considered rigid, was implemented. For rotational components around x and z , not determined experimentally, two sets of spring stiffness values were considered: with both k_4 and k_6 either rigid, by assigning them a high stiffness value of 10^{15} N·mm/°, or hinged, by assigning them a low stiffness value of 0.1 N·mm/°. In this manner, lower and upper bounds of the semi-rigid model were obtained for displacements.

Table 3.2 – Spring stiffness values used in the FE model for each of the six degrees of freedom.

Symbol	Component	Value	Units
k_1	translation x	417	N/mm
k_2	translation y	15 009	N/mm
k_3	translation z	9 489	N/mm
k_4	rotation around x	$0.1 - 10^{15}$	N·mm/°
k_5	rotation around y	170 190	N·mm/°
k_6	rotation around z	$0.1 - 10^{15}$	N·mm/°

3.3.4 Mesh Properties

Conventional plate shell elements with finite strain S4R elements were applied with coarse and refined mesh sizes of 50 and 20 mm respectively for the displacement study, as determined in Chapter 2, Subsection 2.3.2. For the analysis of the forces in the connections, fine elements were reduced to 2.5 mm, while keeping coarse elements of 50 mm, according to the mesh convergence study performed in Chapter 2, Subsection 2.3.2.

3.3.5 Loads and Boundary Conditions

Three steps of loading were defined in the model. In the first one, gravity load was implemented on the whole model. In the second one, the initial weight of the 230×230 mm wooden blocks and the load distributing beam was simulated by pressure load on 230×230 mm areas on the top plates located at midspan. Finally, the load was applied on the same areas to simulate the loading of the hydraulic jack.

Regarding the boundary conditions, the same modelling approach as presented in Stitic et al. [105] was used (see Figure 3.8). In fact, when the structure is loaded, supports rotate around the Y -axis and the centre of mass is therefore not aligned to the centre of rotation of the steel rollers, resulting in nonlinear secondary moment effects [105]. Supports were therefore represented by 2.7 m long and 0.16 m wide steel plates with equivalent weight as the actual setup. They were defined as rigid bodies associated with reference points RP at a distance corresponding to the distance between the centre of mass C_m and the centre of rotation C_r of the actual supports.

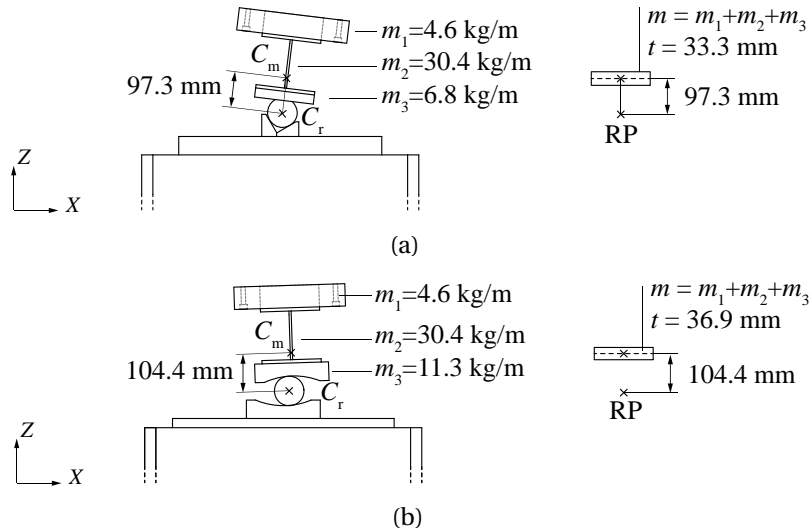


Figure 3.8 – Modelling of the boundary conditions: (a) Pinned support and (b) Roller support. Supports were represented by steel plates with equivalent length, width, weight and distance between the centre of rotation C_r and the centre of mass C_m as the actual setup. They were defined as rigid bodies associated with reference points RP.

Boundary conditions were applied to the reference points with free rotation along the global Y-axis for both supports and additional free translation along the global X-axis for the rolled support. Coupling constraints were assigned to the regions of the structure resting on the supports with corresponding reference points as control points.

3.4 Results and Discussion

3.4.1 Experimental Tests

Figure 3.9 presents the load-displacement curves obtained at midspan with LVDTs U_N and U_S , on the north and south sides of the prototype respectively (see Figure 3.3), for each of the three 5×3 boxes replicates. The average maximum additional load at failure $F_{\max, \text{avg}}$ was found to be of 107.23 kN with a coefficient of variation $c_{v, F_{\max}}$ of 6.95 %, which was considered to be sufficiently low for timber material, with the coefficient of variation c_v defined as:

$$c_v = \frac{\sigma}{\mu} \quad (3.1)$$

where σ is the standard deviation and μ the average.

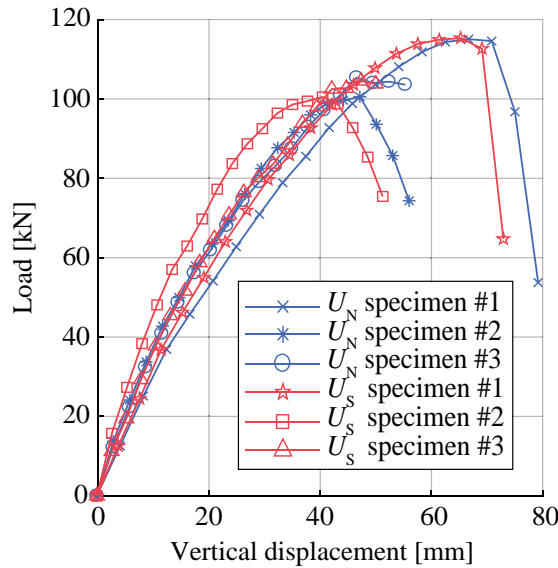


Figure 3.9 – Load-displacement curves obtained at midspan with LVDTs U_N and U_S , on the north and south sides of the prototype respectively (see Figure 3.3), for each of the three 5×3 boxes replicates.

The structure failed because of the failure of TT connections at the bottom layer of the structure in the areas highlighted in Figure 3.10a, at the junction between boxes and not within boxes themselves. The herringbone pattern used in the design of the structure was found to enable the apparition of continuous failure paths at the stretched bottom layer. The joints presumably

failed due to a combination of shear and traction, as observed in Figure 3.10b. Dovetail joints connecting the vertical panels appeared to be undamaged. As the rotation of these connections is blocked by the interlocking of the panels, the hypothesis of modelling rigid dovetail joints was assumed to be sufficient to predict the behaviour of the structure.

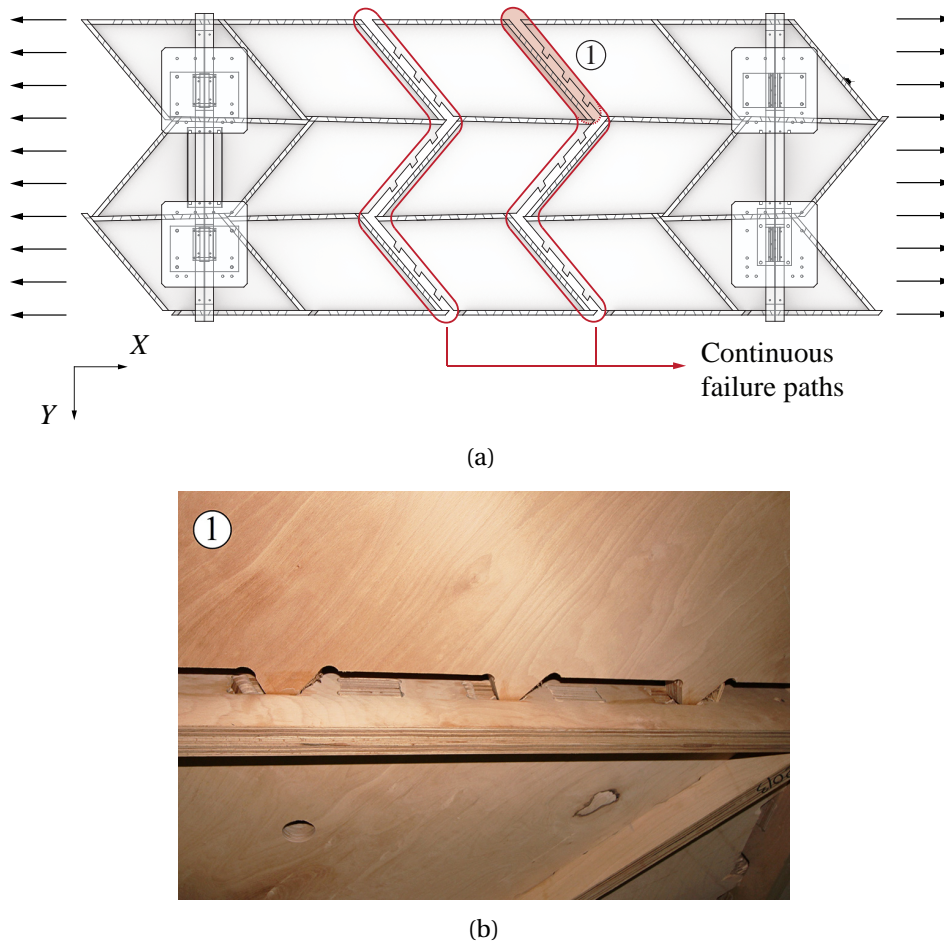


Figure 3.10 – Failure of the 5×3 boxes prototype: (a) Continuous failure paths appearing at the stretched bottom layer of the structure and attributed to the herringbone pattern used for the structure's design. (b) Failure of the through-tenon wood-wood connections at the junction between boxes at the bottom layer, presumably due to a combination of shear and traction.

The rotation of the supports, measured by the two inclinometers, is presented in Figure 3.11 with respect to the evolution of the applied load with time. It can be observed that when the prototype reaches failure, the rotation of the supports, which was approximately symmetric until then, starts diverging on each side.

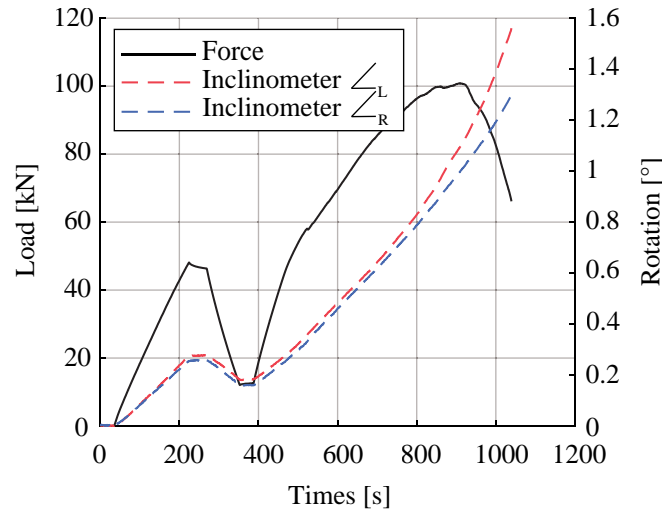


Figure 3.11 – Total load and rotation of the supports, measured by two inclinometers, over time. When the prototype reaches failure, the rotation of the supports, which was approximately symmetric until then, starts diverging on each side.

3.4.2 Comparison between Experimental and Numerical Results

Displacement Study

To compare experimental to numerical results in terms of displacements, the maximum load considered was about 50 kN, which corresponds approximately to the maximum allowable displacement for serviceability limit state (SLS), to limit the study to linear kinematics. Moreover, initial displacements due to gravity and due to the weight of the distributing steel beam and the wooden blocks were subtracted from the displacements obtained in the subsequent loading steps. In fact, experimental measurements were taken after the disposition of the specimen on the supports and of loading elements on the specimen. Propagated effects of gravity and initial loading could thus be considered in the model. Figures 3.12a and 3.12b present the results of the proposed spring model compared to the linear regression of experimental tests for a load of 50 kN for the north and the south side of the prototype respectively.

A large dispersion in the results can be observed in the linear range. In fact, the coefficient of variation of the stiffness $c_{v,k}$ was found to be of 16.63 %. Moreover, at the beginning of the test for a load under 5 kN, a very stiff behaviour can be observed. This can be attributed to the initial stiffness of the connections that has a very high values, due to the high friction forces between the tenon and the mortise of the joints (see also Chapter 6, Subsection 6.4.1).

The vertical displacements obtained with the semi-rigid model with rigid rotational stiffness k_4 and k_6 were shown to be underestimated by 3.9 and 11.7 % for the north and south sides respectively compared to the experimental tests. The semi-rigid model with hinged rotational stiffness k_4 and k_6 was shown to be on the safe side with displacements overestimated by 16.9

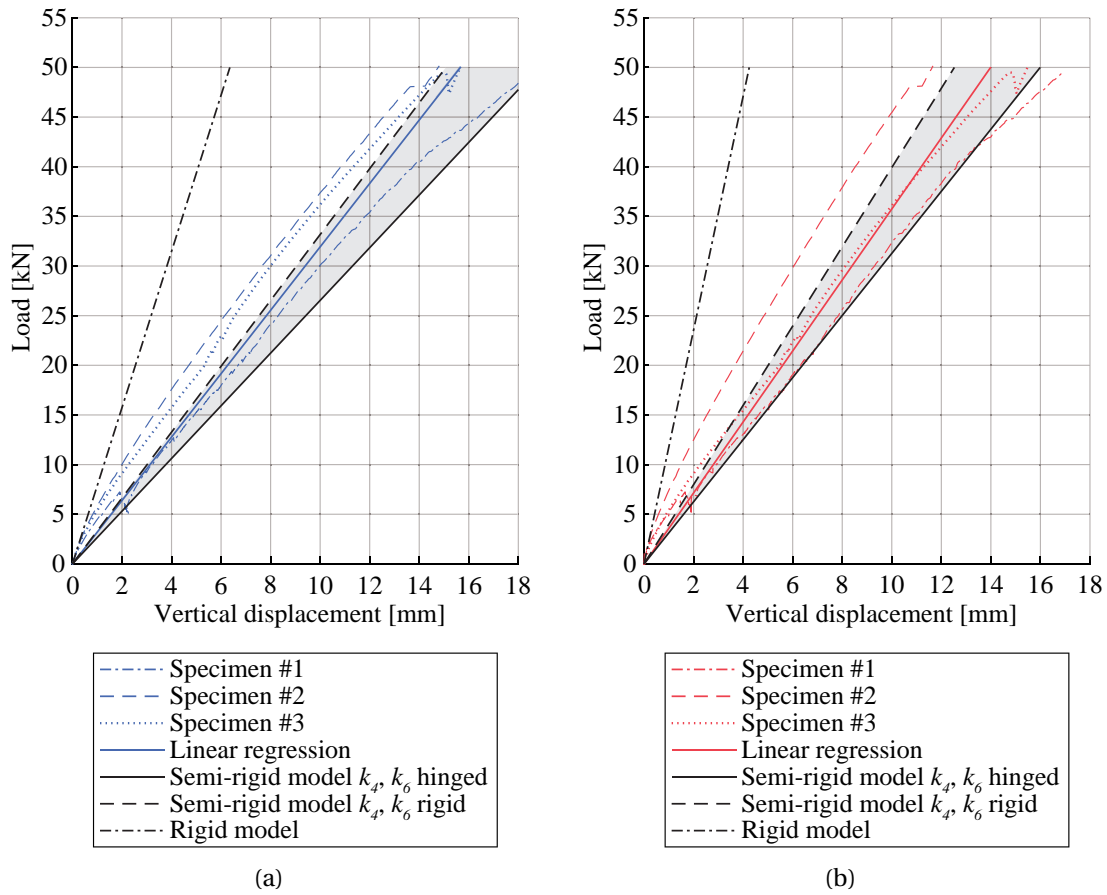


Figure 3.12 – Load vs. midspan deflection. Comparison between the linear regression of experimental tests and the numerical results for a load of 50 kN, which approximately corresponds to the maximum allowable displacement for SLS: (a) North side (b) South side.

and 12.5 % for the north and south sides respectively compared to the experimental tests. Therefore, the rotational stiffness around x and z , k_4 and k_6 respectively, were shown to have a limited influence on the numerical results and it can be observed that the linear regression of the three experimental tests falls between the lower and upper bounds of the semi-rigid models. In comparison, a rigid model was found to be 146.5 and 188.0 % more rigid for the north and south sides respectively. Nonlinear geometric analysis was performed using the NLgeom step option in AbaqusTM, such that the stiffness matrix is updated after each loading increment. However, very low deviation (< 1 %) from the linear analysis was observed.

Figure 3.13 presents the comparison between the vertical displacements measured on the first specimen with DIC and displacement fields simulated by the semi-rigid model with hinged rotational stiffness k_4 and k_6 . Although differences can be observed between the measurements and the numerical simulations, the range of displacements values is similar.

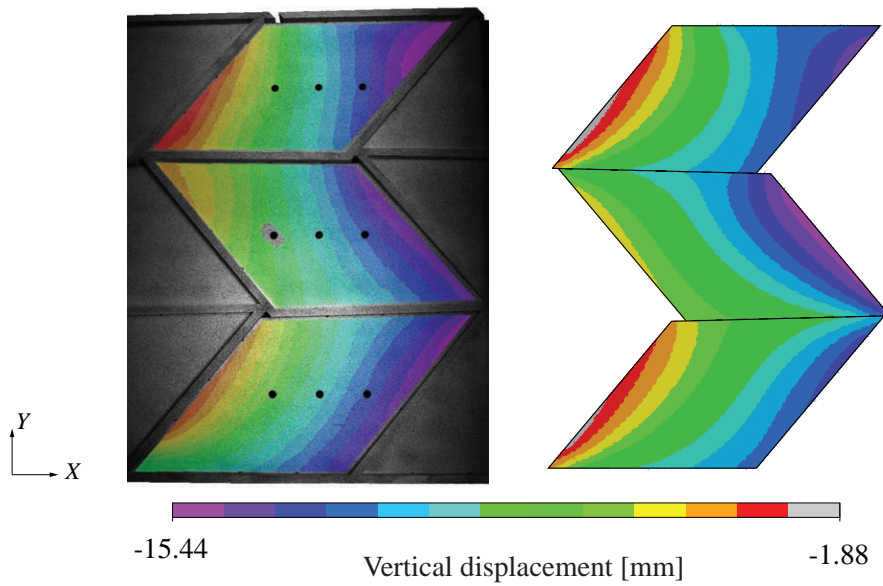


Figure 3.13 – Comparison of the vertical displacements between DIC for the test on specimen #1 and the semi-rigid model with hinged rotational stiffness k_4 and k_6 for a load of 50 kN.

Forces in the Connections

As observed in Subsection 3.4.1, the failure of the connections presumably occurred mainly due to tension and shear loads in the tenons. As shown in Figure 3.14, presenting the forces per unit width in the X -direction at the bottom layer of the prototype, obtained with the semi-rigid model with rotational stiffness k_4 and k_6 both hinged for a surcharge load of 50 kN, concentrations of forces appeared around the connections. Results of experimental tests and numerical simulations were therefore also compared in terms of forces in the connections.

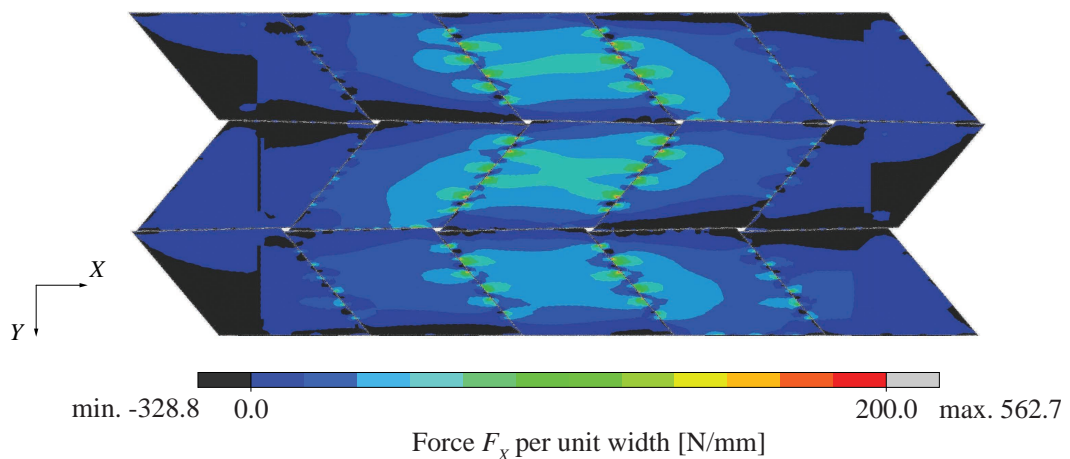


Figure 3.14 – Forces per unit width in the X -direction for a surcharge load of 50 kN.

According to the numerical model, the most loaded tenon at the bottom layer of the structure for both tension and shear appeared to be the one marked with a circle in Figure 3.15a. For the average maximum additional load on the structure at failure $F_{\max, \text{avg}} = 107.23 \text{ kN}$, axial and lateral forces of 18.29 kN and 10.48 kN respectively were found in the connections, using the semi-rigid model with both rotational stiffness k_4 and k_6 hinged respectively. For a surcharge load of 50 kN, approximately corresponding to the maximum allowable displacement for SLS, these forces were of 7.95 kN and 4.56 kN respectively. The force distributions along the length of the connection for axial and lateral forces are presented in Figures 3.15b and 3.15c respectively, for the semi-rigid model with k_4 and k_6 rigid under 50 kN. For a surcharge load of 50 kN, the axial force of 7.95 kN calculated with the numerical model appeared to be above the average maximum load-carrying capacity of the connection under tension loads, $F_{\max, \text{avg}}$ of 6.47 kN (see Appendix A). However, this result is consistent with the three-point bending tests due to the presence of lateral forces in the connections and because the average maximum load-carrying capacity of the joints in shear of about 46.83 kN is much higher (see Appendix A). However, for design purposes, combined actions should not be considered as they cannot be accurately quantified.

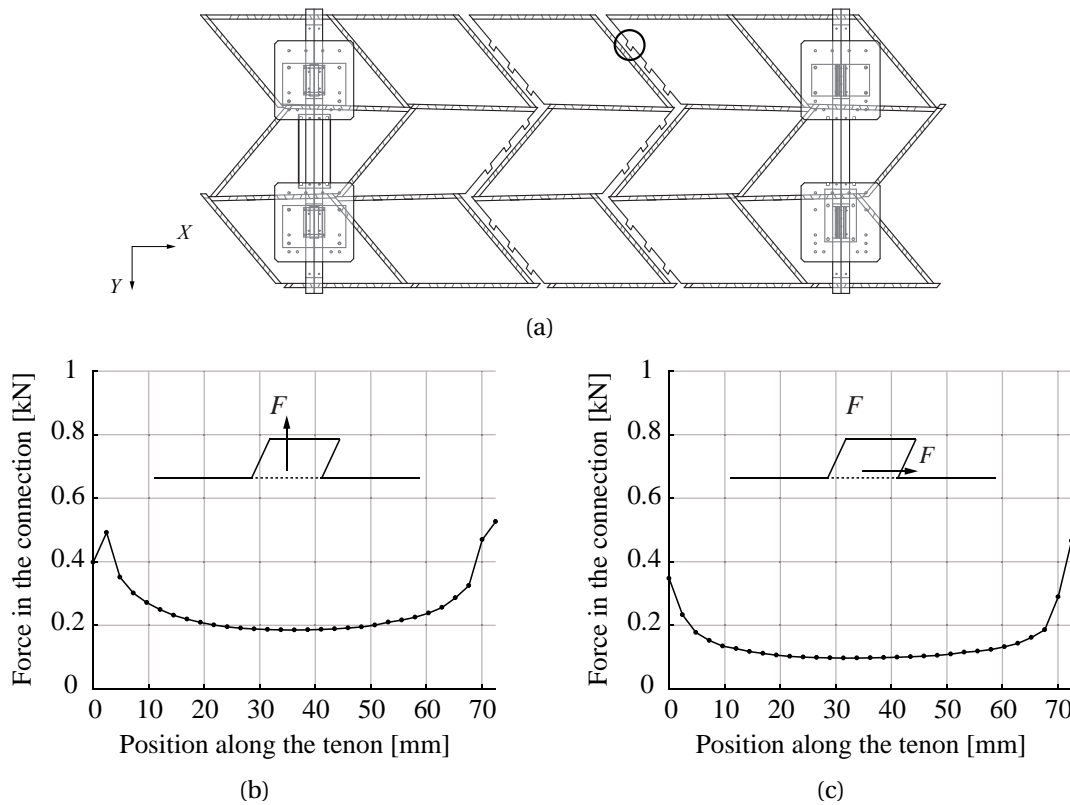


Figure 3.15 – Force in the connections: (a) Position of the most loaded tenon, marked with a circle, for both tension and shear, at the bottom layer of the structure (b) Distribution of axial forces along the length of the most loaded connection for a load of 50 kN using a semi-rigid model with k_4 and k_6 hinged (c) Distribution of lateral forces along the length of the most loaded connection for a load of 50 kN using a semi-rigid model with k_4 and k_6 hinged.

3.5 Conclusions

In this chapter, three point bending tests performed in the laboratory on small-scale assemblies composed of 5×3 boxes are presented. They were performed to assess the semi-rigid spring model developed in Chapter 2 and give more insight on the mechanical behaviour of double-layered timber plate structures assembled with TT wood-wood connections. In the numerical simulations, stiffness values for components k_1 , k_2 , k_3 and k_5 were retrieved from experimental tests, while rotational stiffness k_4 and k_6 were considered either rigid or hinged.

The destructive loading tests showed that the structure failed because of the failure of the connections at the stretched bottom layer of the structure, presumably due to a combination of shear and tension loads. Furthermore, the presence of continuous failure paths, which can be attributed to the construction system, and more particularly to the herringbone pattern applied in the design of the structure, was highlighted. Vertical displacements predicted by the semi-rigid model were shown to be in good agreement with experimental investigations for the linear elastic part. A semi-rigid model with rigid rotational components about x and z was found to be closer to experimental tests, while a model with hinged rotational components about x and z provided more conservative results. Furthermore, taking the semi-rigidity of the joints in the model was shown to be essential since the average of the semi-rigid models was shown to be 3 % less stiff than experimental tests, whereas a rigid model was 190 % stiffer in average for both sides of the specimen. Forces in the connections obtained with the numerical model were found to be consistent with the experimental tests. To obtain a conservative design of the structure, forces in each connection should be verified against the load-carrying capacity of the connections for each component.

Nonlinear geometric analysis was found to have very little influence on the numerical results. Furthermore, considering the results obtained, the coupling terms discussed in Chapter 2, Subsection 2.4.3 were discarded. Additional limitations of the model can be linked to friction and contacts, both neglected in the model. Moreover, a stiffer behaviour was observed at the beginning of the test. This can be attributed to the nonlinear behaviour of the connections, which would have to be implemented in the model to increase its accuracy in the first loading steps.

4 Experimental Investigations on a Large-Scale Structure

This chapter is based on: A. C. Nguyen and Y. Weinand, Displacement Study of a Large-Scale Freeform Timber Plate Structure Using a Total Station and a Terrestrial Laser Scanner, *Sensors*, 20(2), 413, 2020. doi:10.3390/s20020413.

4.1 Introduction

Over the past decades, geometrically complex and large-span timber structures have been achieved thanks to advances in both engineering and architecture. As reviewed in Chapter 1, significant research studies have especially focused on the development of timber plate structures using wood-wood connections inspired by traditional carpentry joints. These structures consist of a large number of singular planar elements connected at their edges by joints fully integrated in the plates. Research prototypes as well as building-scale assemblies have been built using computer-aided design (CAD) programming and digital fabrication tools [30, 49, 53, 78, 105, 61]. Various numerical models, mostly based on the finite element method, have been developed for their structural analysis but only limited experimental tests have been carried out on large-scale structures. However, experimental investigations remain necessary to better understand their mechanical behaviour and assess the numerical models developed. Furthermore, full-scale tests are required when physical models cannot be reduced to a small portion of the structure to analyse its global behaviour or when small-scale models cannot duplicate the behaviour of the real-size structure [66, 112]. Such limitations can result from material variability and execution tolerances, which might have a high influence on the mechanical behaviour of the global structure [66]. This is particularly the case for assemblies with a large number of complex joints, contributing to significant uncertainties [120, 66].

Full-scale experimental tests can be carried out either in the laboratory or in the field. Since timber plate structures using wood-wood connections have been developed relatively recently, only few building-scale structures have been built and laboratory tests have thus mostly been carried out for smaller spans. For shell structures in particular, loading tests remain difficult to execute as they are designed to transmit surfacic loads such as self-weight, snow and wind loads to the supports. Several methods can be used to simulate distributed loads on them. Traditional methods consist in pressure loading, vacuum loading or discrete loading systems, usually closely-spaced [34]. Pressure loading can be achieved through gravity using water or sand with a possible additional surcharge load. It can also be obtained with a gas pressure system or with a sealed air bag. Similarly to air pressure loading, vacuum loading is restricted to structures with continuously supported and sealed edges. Discrete loading can be carried out using suspended dead weights or with of a whiffle-tree system. More recently, innovative pulley-based loading systems have also been developed [120, 106]. Their advantages are their high flexibility, safety of the method and absence of variation of the applied load with deformation of the structure. Onsite, however, not all laboratory test methods can be applied and experimental tests on large-scale shells have not been reported in the literature. Examples of static loading tests achieved through pressure and discrete loading systems can nonetheless be found for timber frame and gridshell structures respectively. In Doudak et al. [20], tests were executed on a 8.5×17 m single-storey timber frame structure by applying a load of 3.3 kN/m^2 on patches of the roof using dead weights consisting of shingle bundles and by measuring the reaction forces. For the 60×60 m span *Multihalle* timber gridshell in Mannheim, Germany designed by Frei Otto, a discrete loading system, consisting of garbage bins hanging on the gridshell and filled with water, has been used. In this study, tests were performed with the objective of assessing the accuracy of the calculations by comparing the deflections measured at 13 points on the structure with the corresponding computed deflections [54].

Instrumentation for experimental testing depends on the variables of interest. In particular, displacements provide key information to better understand the behaviour of loaded structures as they give an indication on the stiffness of the structural system. Displacements measurements can be acquired using numerous techniques, such as global positioning system (GPS), linear variable differential transformers (LVDT), laser Doppler vibrometer (LDV) and total stations, which are examples of conventional equipment [13]. Each of them is characterised by different data acquisition methods and accuracy, such that they are not suitable for all applications. GPS sensors can measure both static and dynamic displacements but do not provide sufficient accuracy for displacements under 1 cm [123]. LVDTs are both accurate and low cost; however, as they measure contacting displacements between a limited number of target points on the structure and fixed reference points, they are unpractical for large-scale structures and usually require the presence of additional temporary structures [65]. LDVs have the advantage to measure non-contact displacements with comparable accuracy but are costly devices requiring high incident angles between the laser beams and the vibrating surface [65, 12]. Total stations have been used to measure displacements in numerous case studies because of their ease of use and accuracy in the millimetre range [35, 47, 15]. However, they allow measure-

ments on a limited number of target points. More recently, three-dimensional (3D) terrestrial laser scanning has also been used for several applications [6, 51, 124, 31]. With this technique, coordinates of millions of points forming a point cloud are collected. Massive sampling data in the few millimetres range can be obtained from laser scans but their processing is more complicated.

Based on the case study presented in Chapter 1, Subsection 1.3, a numerical model has been developed for the structural analysis of double-layered double-curved timber plate shells. Although the numerical model has been proposed and automated for both small- and large-scale structures (see Chapter 2), it has been validated against experimental investigations on small-scale prototypes only (see Chapter 3). Therefore, the aim of the present study is to assess the numerical model developed through experimental investigations on a large-scale structure and evaluate possible methods to acquire displacements of the loaded structure, using a total station and a terrestrial laser scanner. The design of the structure and loading procedure are first described in Section 4.2, followed by the displacement measurement methods and numerical modelling in Sections 4.3 and 4.4 respectively. Both methods are then compared to each other and to the numerical model in Section 4.5.

4.2 Experimental Tests

4.2.1 Specimens

The structure tested consisted in prototypes built for the Annen Plus SA head office project in Manternach, Luxembourg (see description of the case study in Chapter 1, Subsection 1.3). The second to last arch and half of its larger neighbouring arch (arch n°22 and half of arch n°21 respectively, as shown in Figure 4.1) were constructed by Annen Plus SA.

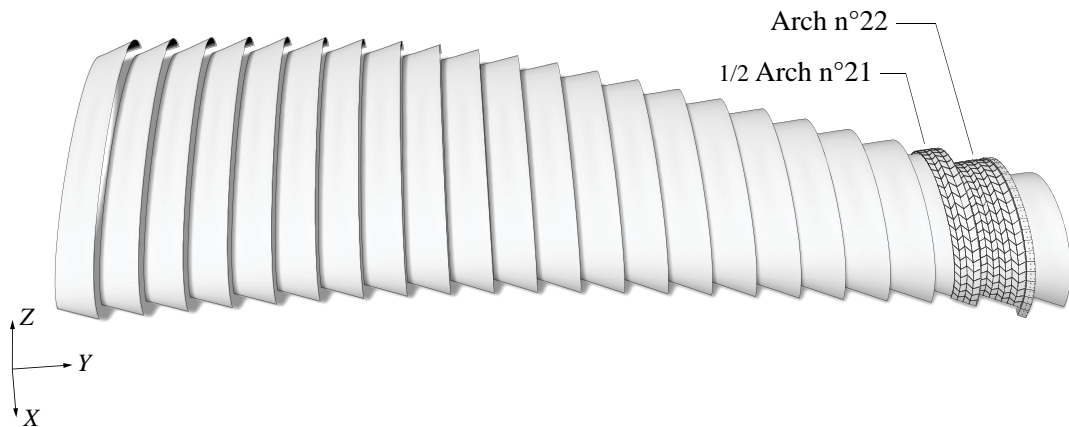


Figure 4.1 – Illustration of the Annen Plus SA head office project in Manternach, Luxembourg consisting in 23 double-layered double-curved timber plate shells, represented by their design target surfaces. Experimental tests were carried out on prototypes of arch n°22 and half of n°21.

Their goal was to verify the realisation of the supports of the structure for the project, as well as the connection between the arches. Therefore, only half of arch n°21 was constructed. For project purposes, a row of timber caps was added on arch n°22 along its entire open side and the two arches were connected by ten $100 \times 100 \times 5$ mm steel struts. The geometry of the tested prototypes, with a span of 25 m in average, is presented in Figure 4.2.

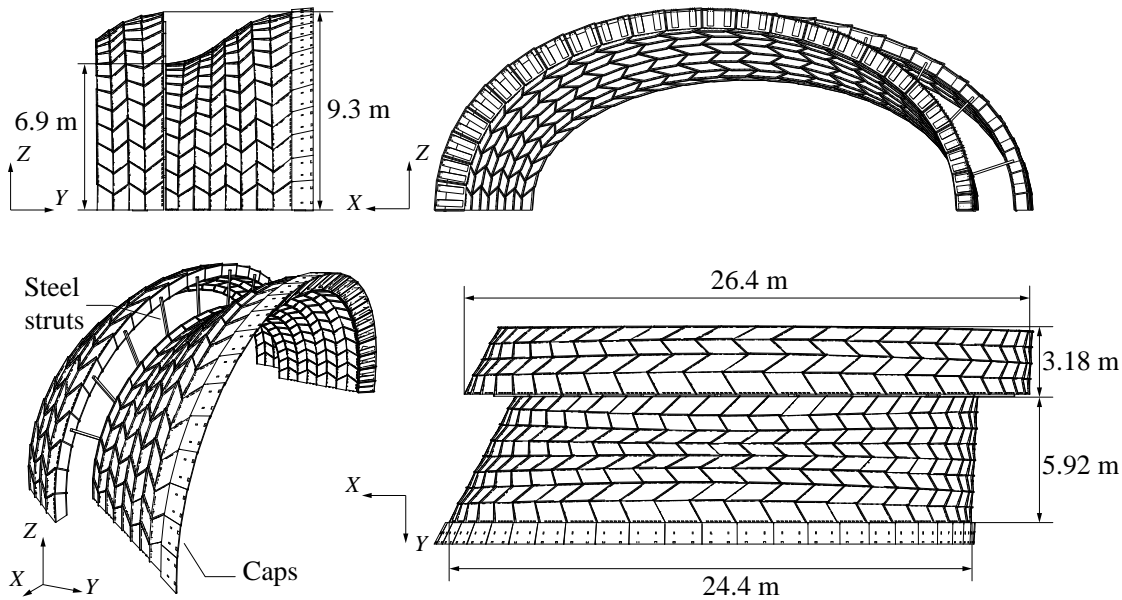


Figure 4.2 – Geometry of the tested prototypes of arch n°22 and half of n°21. For project purposes, a row of timber caps was added on arch n°22 along its entire open side and the two arches were connected by ten $100 \times 100 \times 5$ mm steel struts.

4.2.2 Fabrication and Assembly

The prototypes were built from 40 mm thick BauBuche Q panels (Pollmeier Massivholz, Creuzburg, Deutschland), which are beech laminated veneer lumber (LVL) panels, obtained by gluing fourteen layers of 3 mm thick beech peeled veneers longitudinally and cross-wised [9]. The composition of the panel is ||| – ||||| – ||| (| for longitudinal, – for crosswise veneer layer). The tested prototypes were made of 792 singular shaped plates forming 200 boxes for the full arch and 396 plates forming 100 boxes for the half arch. The arches with all their individual plates and different joint geometries were designed using custom developed CAD plugins. All plates of the structure were digitally fabricated by Annen Plus SA with a 5-axis computer numerical controlled (CNC) machine, using a 20 mm diameter tool for tilt angles inferior to 45° and of 25 mm for larger angles. Annen Plus SA manually assembled the arches lying on their side (XZ -plane in Figure 4.2), lifted them up individually in one single assembly and fixed them to the supports using a crane.

4.2.3 Supports

The supports of the structure are illustrated in Figure 4.3 for arch n°22. On both ends of the arches, 15 mm thick steel plates were fixed to vertical plates of two first rows of boxes by M16 bolts through BauBuche-Q spacers. These plates were welded to 25 mm thick steel plates, themselves fixed on concrete blocks with M27 tie rods anchored using grouting mortar.

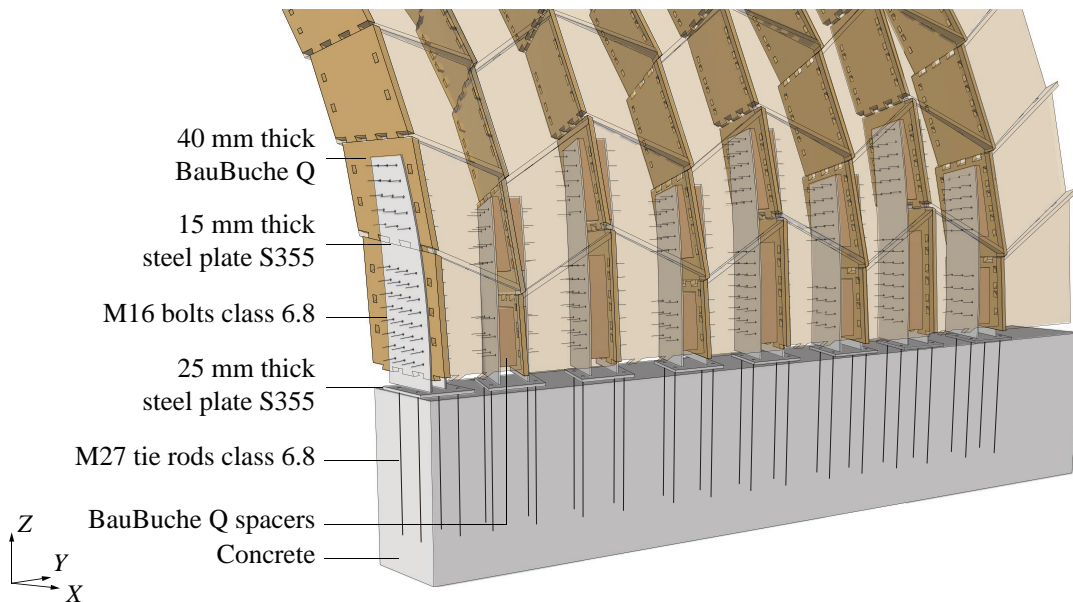


Figure 4.3 – Supports of arch n°22.

4.2.4 Loading Procedure

Static loading tests were conducted using pressure loading. Vacuum loading methods would not have been feasible because of the presence of gaps in the structure and the difficulty to seal all of its edges. Moreover, limited atmospheric pressure restricts the load magnitude that can be applied on it. Discrete point loading was discarded to avoid wind effects on the hanging masses. As illustrated in Figure 4.4a, pressure loading was achieved through gravity only by applying a surcharge load on top of the structure using 25 kg cement bags distributed over the top surface. The disadvantage of this method was that a large number of bags was necessary to obtain a sufficient load magnitude and the loading procedure was thus labour intensive. The top layer of the structure was only partially loaded as it corresponds to the worst load case with respect to the vertical displacements at midspan. The loaded area is highlighted in Figure 4.4b.

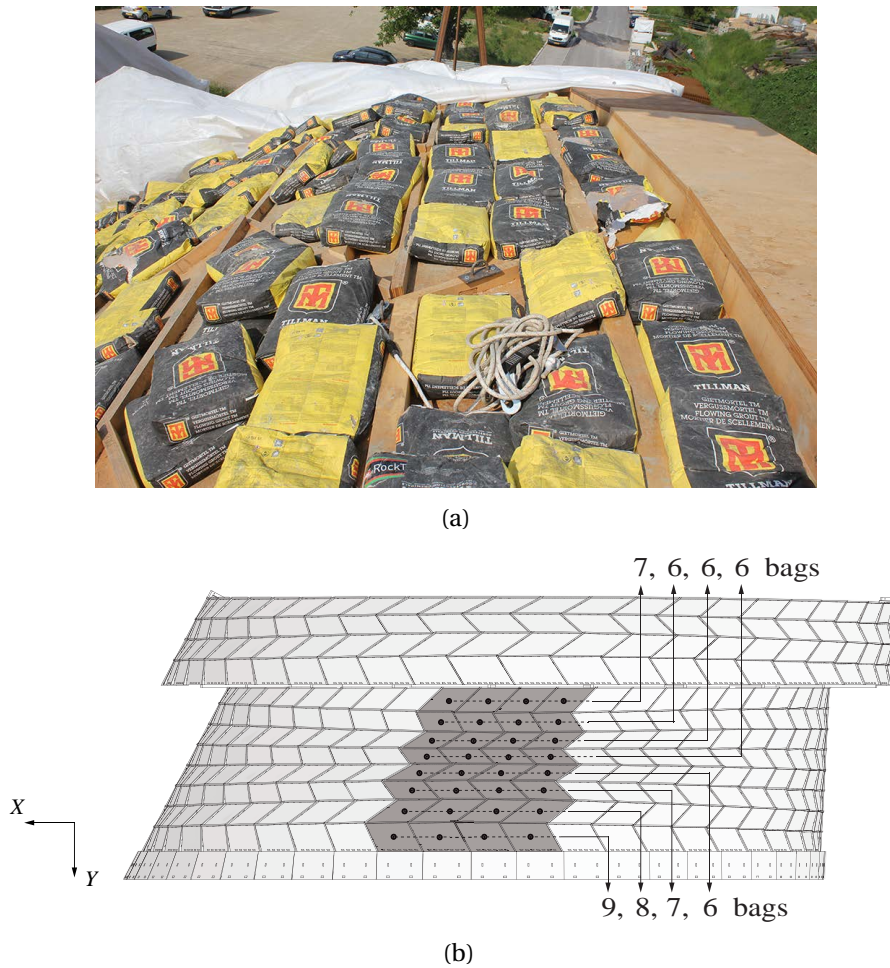


Figure 4.4 – Loading procedure for large-scale tests: (a) Loading of the structure using 25 kg cement bags (b) A distributing loading of 1.5 kN/m^2 in average was applied on the zone of the structure with a lower curvature (grey area). The varying number of cement bags leading to the average load is indicated.

Additional components were not necessary to retain the bags on the structure thanks to the low curvature of the structure in the XZ -plane in this area. Since the objective of the test was to compare onsite measurements with the numerical model, the loading method was considered acceptable as long as the specific surcharge load was accurately implemented in the numerical model. Furthermore, loading from the top allowed having a clear sight under the structure for displacement measurements. A non-destructive elastic test was performed by applying an average load of 1.5 kN/m^2 on the area of the structure. The number of bags placed on each box is indicated in Figure 4.4b. This number was adapted depending on the loaded surface of each box to correspond to an equivalent load of approximately 1.5 kN/m^2 .

Steel struts illustrated in Figure 4.2 and connecting the two arches were not directly mounted. The two tests were thus performed following the same loading procedure and with the identical surcharge load applied on arch n°22 only (as shown in Figure 4.4b):

- Test n°1: arch n°22 not connected to half of arch n°21, which was therefore not considered in the test measurements, on May 22, 2018 and;
- Test n°2: arch n°22 fixed to half of arch n°21 by steel struts, as illustrated in Figure 4.2), on May 23, 2018.

4.3 Instrumentation

Displacements were measured using a total station and a terrestrial laser scanner. Two sets of measurements were taken for each test, before and after loading respectively, such that four different load cases can be defined:

- Load case n°1: test n°1 before loading
- Load case n°2: test n°1 under final loading
- Load case n°3: test n°2 before loading
- Load case n°4: test n°2 under final loading

Considering the low load levels applied, the behaviour of the structure was assumed linear elastic, such that the effects of the load release after Load case n°2 were discarded and no influence on the displacements measured during test n°2 was taken into account.

4.3.1 Total Station

Total stations are easy to use and have the advantage to measure distances and angles with high accuracy. However, they have a low data sampling rate and need an unobstructed line of sight between the targets and the total station [15]. In this study, measurements were taken at 16 different positions on the structure using an electronic total station Leica Geosystems TCR 305 (Leica Camera AG, Wetzlar, Germany). It has an accuracy (standard deviation) of 5 mm + 2 ppm for reflective targets to a range of 1.5 to 80 m (according to ISO 17123-4) and of 5" (1.5 mgon) for angle measurements (according to ISO 17123-3) [52]. The total station was placed at a distance of about 10 m to the furthest measurement points in the *Y*-direction, in a clear line of sight to the 16 targets, as illustrated in Figure 4.5a. Microprismatic self-adhesive reflective targets of 3×3 cm and 0.5 mm thickness, both UV and weatherproof, were glued to aluminium plates (see Figure 4.5b), themselves screwed onto vertical panels of the structure at the 16 different positions indicated in Figure 4.5c.

To ensure that no movement of the device accidentally occurred before and after the measurements of the 16 targets, five reference targets were placed at stable locations. For both tests, successive measurements of the control points and the 16 targets were taken. It took about 10 min to acquire data for each sets of 16 points. All data was acquired onsite, taking

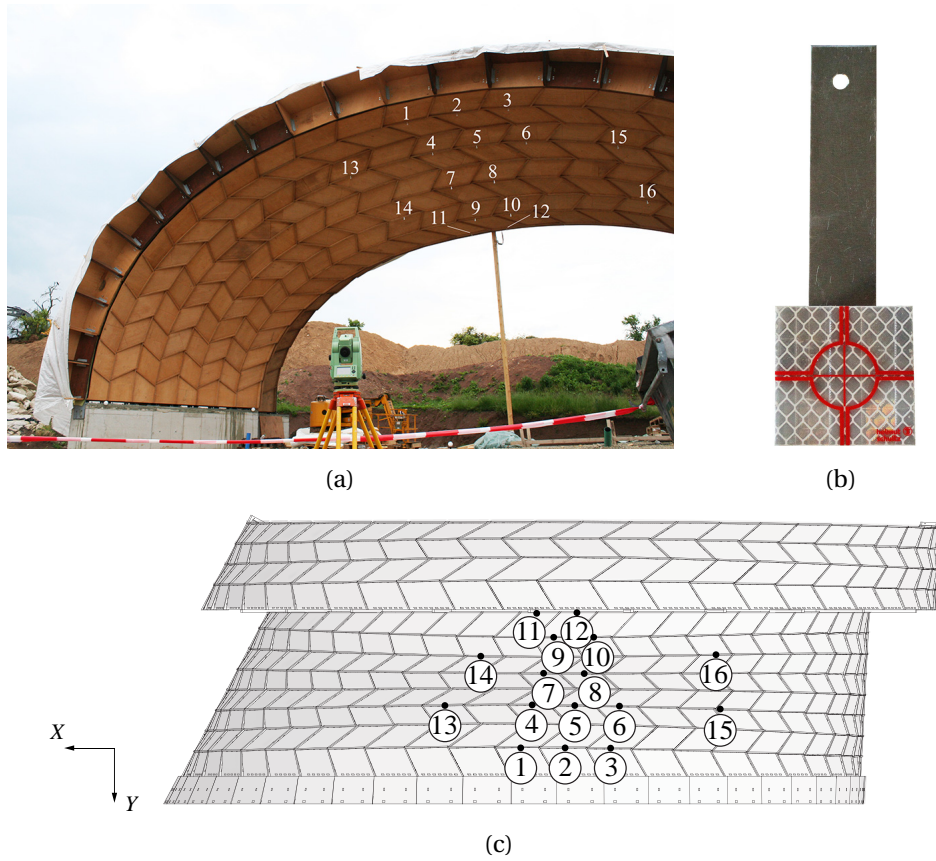


Figure 4.5 – Total station setup: (a) A clear line of sight between the targets and the total station is required (b) Reflective targets 3×3 cm (c) Position of the 16 targets on arch n°22.

about ten minutes per set of 16 points, and subsequently treated by computing the difference before targets position before and after loading for both tests. Sets of measurements for which successive control points measurements showed differences higher than 2 mm were discarded.

4.3.2 Terrestrial Laser Scanner

Terrestrial 3D laser scanners have been increasingly used for various applications. They allow fast acquisition of point clouds composed of millions of points through laser beam scanning. High-resolution 3D images can therefore be obtained and complex environments can be reconstructed. In this study, a laser scanner FARO® Focus^S 150 (FARO Technologies Inc., Lake Mary, FL, USA) was used to obtain point cloud measurements of the bottom surface of the arches. It scans at a measurement rate of 122 000 to 976 000 points per second with a visual field of 300° vertically and 360° horizontally, with an average 3D position accuracy of 3.5 mm at 25 m [25].

Survey Procedure

Before any measurement was taken, five artificial spherical targets were placed at the bottom corners and at the centre of arch n°22 (see Figure 4.6a). These survey markers were used for the registration of the scans. Their spherical shape prevents axis mapping mistakes [51]. Scans were acquired for both tests before and after loading. In order to collect data points over the entire bottom surface of the arches, they were performed from different stations, as indicated in Figure 4.6b. For test n°1, for which arch n°22 only was of interest, three scans were performed; for test n°2, five scans were performed in order to obtain data points for both arch n°22 and half arch n°21. Spheres n°4 and 5, as well as the laser scanner in one of the station position are illustrated in Figure 4.7.

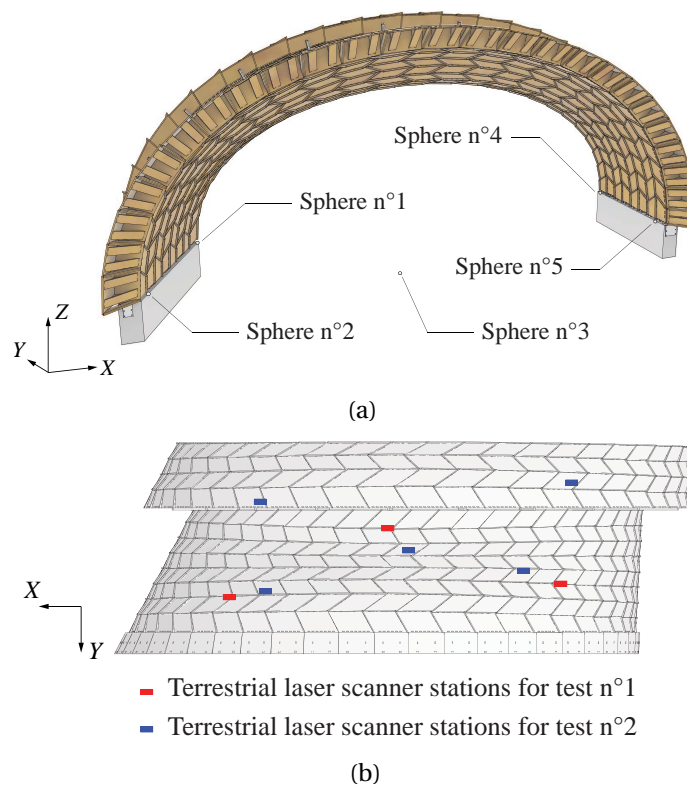


Figure 4.6 – Terrestrial laser scanner survey procedure: (a) Position of the five references spheres used for the registrations of the 3D laser scans (b) Position of the stations of laser scanning for test n°1 (red) and test n°2 (blue).

Before each scan, the alignment level of the scanner was verified. Each scan with a 1/5 resolution took approximately 8 min. This resolution corresponds to an acquisition of 8 192 points per 360° rotation, such that a full scan contains 28 million points (8192×3413) [25]. Photos were captured after each scan by the built-in digital camera of the laser scanner to obtain the exposure values of each point and hence the colours of the scan. Each point cloud contains millions of points with each point characterised by x , y and z coordinates and RGB values for their colour.

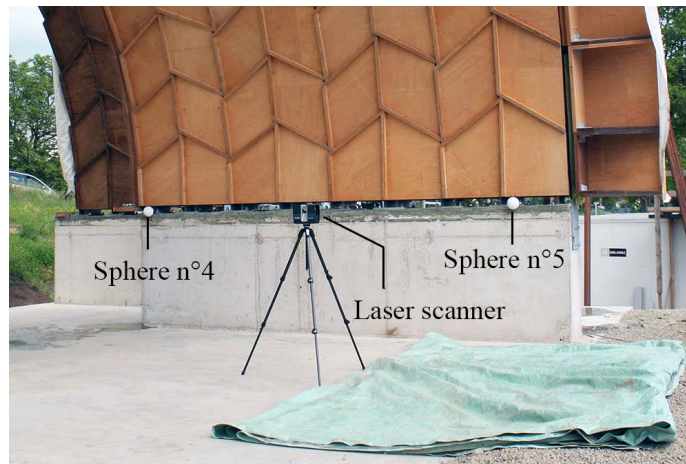


Figure 4.7 – Photograph illustrating the 3D laser scanner FARO® Focus^S 150 and spheres n°4 and 5.

Registration and Pre-Processing

Compared to total station measurements, processing point clouds is not straightforward and can be cumbersome, as point clouds first need to be registered before computing distances [110]. In fact, since each point cloud station for the measurements has its own local coordinate system xyz , all points clouds have first to be represented in the same global coordinate system XYZ . Overall, the registration and point cloud pre-processing were completed in four steps. For scans belonging to the same load case, an automatic registration was first performed in the FARO® SCENE software (FARO Technologies Inc., Lake Mary, FL, USA) using the spherical survey markers as references.

For both tests, sets of scans before and after loading were then registered by superposing spheres, in this case spheres n°2 and 5, for each load case by applying translations and rotations within FARO® SCENE. Point clouds were manually pre-processed in a CAD software, in this case Rhinoceros®, version 6.0 (Robert McNeel & Associates, Seattle, WA, USA), to remove unnecessary regions around the scanned object of interest, as illustrated in Figure 4.8 for scan data of Load case n°1. The resulting point cloud presented in Figure 4.8b contains about 34 million points and is illustrated for an area of 1×1 cm in Figure 4.9. According to Lee et al. [51], mapping errors of the sphere reference points need to be below 1 cm to ensure sufficient total accuracy of the measurements, in the few millimetres range for the present study. Registration were thus refined manually using the open source software CloudCompare [32] by aligning four pairs of points manually picked from the reference cloud and the cloud to be compared.

In order to compare the point clouds measured without loading with the 3D model geometry of the structure used for fabrication, bottom surfaces of the model were retrieved. A triangular mesh, which can be processed with CloudCompare, was applied on these surfaces and a point-pair alignment was then performed for four positions in CloudCompare.

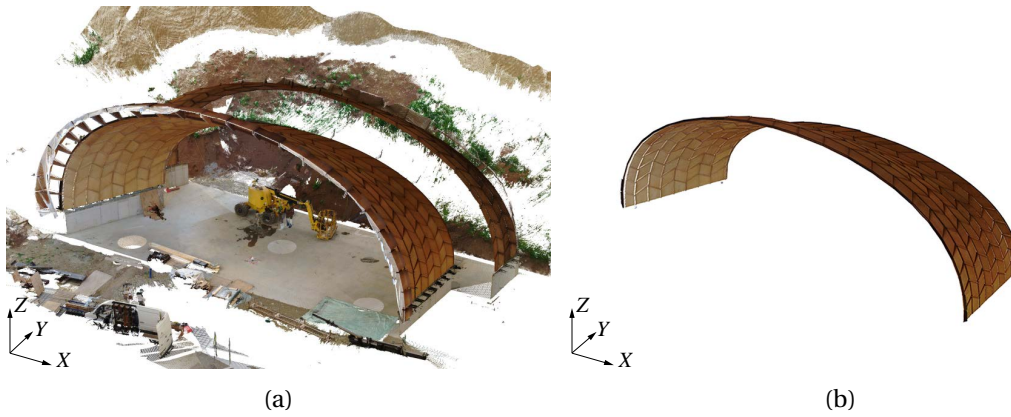


Figure 4.8 – Pre-processing of the point clouds for Load case n°1: (a) Raw point cloud (b) Pre-processed point cloud reduce to 34 million points.

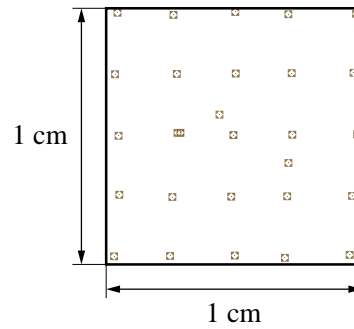


Figure 4.9 – Area of 1×1 cm extracted from the pre-processed point cloud of Load case n°1.

Distances Computation

Cloud-to-cloud distances were first computed using the nearest neighbour distance method, which consists in computing the Euclidean distance between a point of the compared cloud and the closest point of the reference cloud (see Figure 4.10a) [14]. Other methods consist in applying a mathematical model on the nearest point calculated with the Euclidian distance and a defined number of its neighbouring points in order to locally model a surface of the reference cloud. The distance between the point of the compared cloud and this mathematical model is then computed (see Figure 4.10b). Three mathematical models exist in CloudCompare: 2D1/2 Delaunay triangulation, least square best fitting plane and quadratic height function. Since the nearest neighbour method can be inaccurate if the reference point cloud is insufficiently dense, comparisons with the three distances computation methods available in CloudCompare were performed. For the comparison with the 3D model geometry, cloud-to-mesh distances computation was performed in CloudCompare by computing the distance between a point of the cloud and the nearest triangle of the mesh.

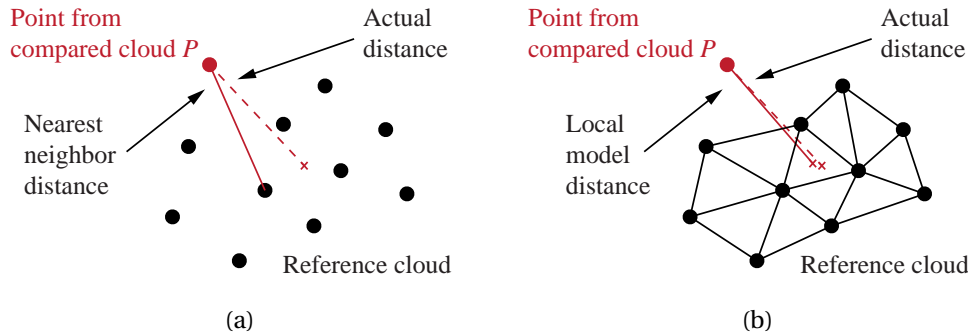


Figure 4.10 – Cloud-to-cloud distances computation: (a) Nearest neighbour distance method (b) Methods in which a local model is applied between the nearest point and a definite number of neighbouring points.

4.4 Numerical Model

4.4.1 Semi-Rigid Spring Model

A finite element (FE) model was built according to the model defined in Chapter 2, in which plates are modelled as conventional shell elements and wood-wood connections are represented by springs with six degrees of freedom (three translations and three rotations) to take into account their semi-rigid behaviour. The model was built using the same mean orthotropic material properties for BauBuche-Q panels as for the investigations conducted on small-scale prototypes (see Chapter 3, Table 3.1). Same two sets of stiffness values were used to model the semi-rigidity of the connections in each degree-of-freedom (see Chapter 3, Table 3.2): axial, in-plane shear and out-of-plane shear stiffness, k_1 , k_2 and k_3 respectively, as well as rotational stiffness about y , k_5 , were retrieved from experimental tests, reported in Appendix A, while simulations were performed with both k_4 and k_6 either rigid, by assigning them a high stiffness value of 10^{15} N·mm/°, or hinged, by assigning them a low stiffness value of 0.1 N·mm/°, such that lower and upper bounds were obtained for displacements using a semi-rigid modelling of the connections. A mesh composed of finite strain S4R elements was applied, using a fine mesh element size of 20 mm at the vicinity of the joints and a coarse mesh of 50 mm away from them, according to the mesh convergence study performed for small-scale prototypes (see subsection 2.3.2).

As a manual generation of the model would have been too cumbersome, time-consuming and probably containing human errors, the model was generated automatically in the finite element analysis software Abaqus™, version 6.12 (Dassault Systèmes, Vélizy-Villacoublay, France) using the Abaqus Scripting Interface [16] according to the methods described in Chapter 2. Linear kinematics were considered exclusively because of the low load levels applied on the structure. Geometrical nonlinearity was not considered as it was found to be essential only to precisely predict strains as well as displacements at higher loads, which was not the case in the present study [105].

4.4.2 Boundary Conditions and Loads

At each end of the structure, boundary conditions were applied on the coarse mesh area of vertical plates, as illustrated in Figure 4.11. Translations in X , Y and Z were blocked on the first row of boxes and translations in Y and Z were blocked on the second row of boxes. Steel struts between the arches were modelled as beam elements connected to the arches using tie constraints between the struts beams and points on the structure, coupled to the edge of the plates. Gravity was applied in a first step and the cement bags were modelled in a second step by applying pressure loads corresponding to the exact number of bags on each box. Although tests occur after the action of gravity, its implementation allowed taking into account propagated effects of gravity. Weather conditions were characterised by wind speeds under 11 km/h during test n°1 and under 17 km/h during test n°2. Since these speeds correspond to light and gentle breeze on the Beaufort scale respectively, effects of wind were discarded in the model [111].

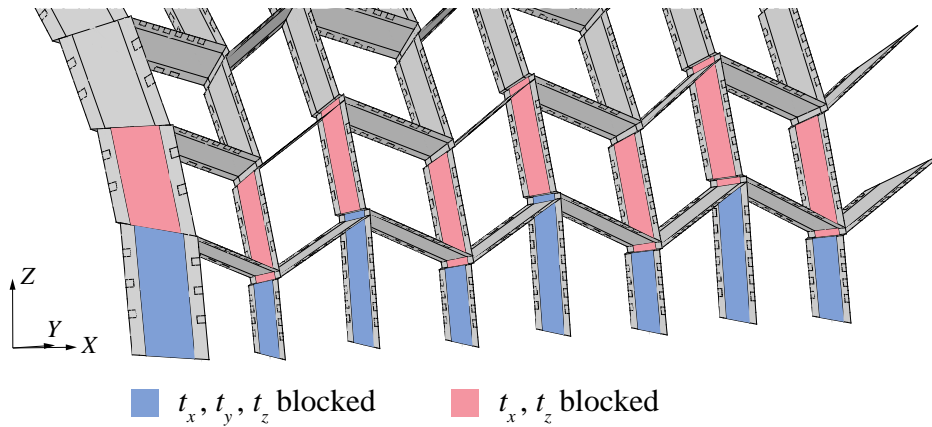


Figure 4.11 – Numerical modelling of the boundary conditions applied on the coarse mesh area of vertical plates. Translations in X , Y and Z were blocked on the first row of boxes (in blue) and translations in Y and Z were blocked on the second row of boxes (in red).

4.5 Results and Discussion

Displacements predicted with the numerical model were compared to the measurements taken at discrete target positions using the total station and to the displacement fields obtained at the bottom surface of the structure with the terrestrial laser scanner. To be able to establish a valid comparison, initial displacements due to gravity were subtracted from the final displacements obtained since experimental tests and measurements were executed after the disposition of the specimen on the supports. Furthermore, the theoretical geometry of the structure corresponding to the 3D design model was compared to the built prototype.

4.5.1 Discrete Target Positions**Total Station Measurements**

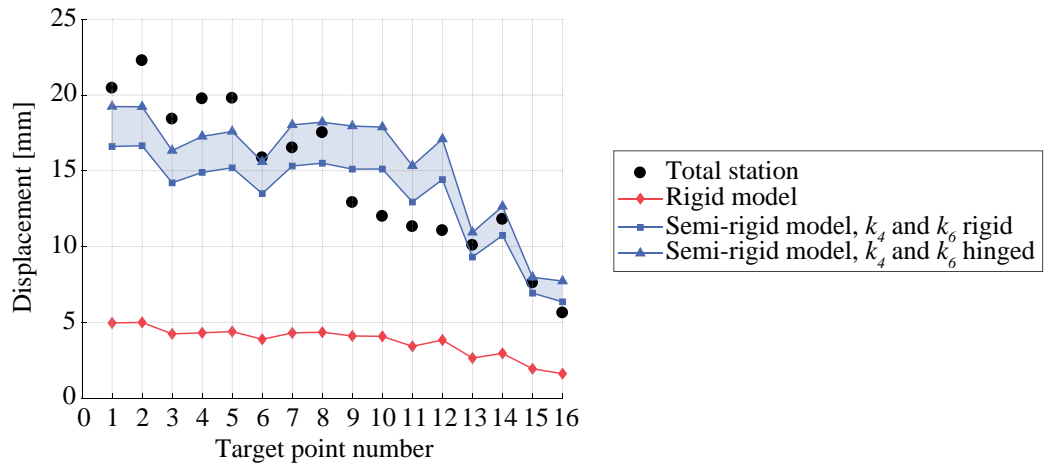
Three measurements of the 16 target positions were taken for each of the four load cases. Average differences of $0.05 \text{ mm} \pm 0.48 \%$ were observed between repetitive measurements and average values were therefore considered for each load case. Final displacements measured for the two tests are presented in Table 4.1. It can be observed that with the presence of half-arch n°21 connected through steel struts, displacements were increased by $15.1 \% \pm 6.2 \%$ for targets 9 to 12 but were reduced for all other targets by $22.4 \% \pm 7.3 \%$ in average. This could be explained by the fact that targets 9 to 12 were located close to the struts and therefore, the weight of half-arch n°21 increased the displacements locally. However, on the overall arch n°22, displacements were reduced as the presence of half-arch n°21 stiffens the structure.

Table 4.1 – Displacements of the 16 targets measured with the total station for test n°1 and 2. Averaged values on three repetitive measurements for each load case.

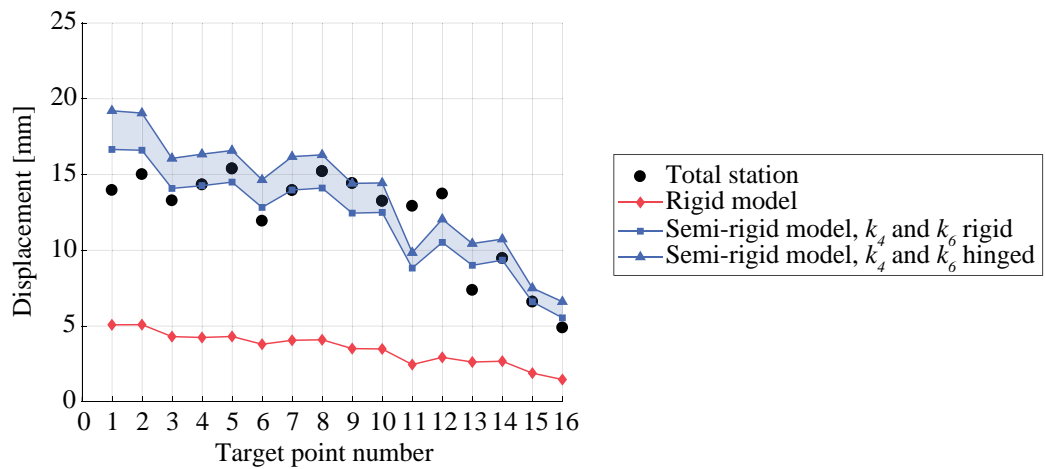
Target n°	Displacements [mm]		Difference [%]
	Test n°1	Test n°2	
1	20.5	14.0	-31.8
2	22.3	15.0	-32.6
3	18.4	13.3	-27.9
4	19.8	14.3	-27.5
5	19.8	15.4	-22.3
6	15.9	11.9	-24.8
7	16.5	13.9	-15.6
8	17.5	15.2	-13.2
9	12.9	14.4	+11.7
10	12.0	13.2	+10.4
11	11.3	12.9	+14.1
12	11.1	13.7	+24.1
13	10.1	7.4	-27.0
14	11.8	9.5	-19.8
15	7.6	6.6	-13.4
16	5.6	4.9	-13.2

Validation of the Numerical Model

Figure 4.12 presents the comparison between the displacements measured with the total station and results predicted by the numerical model with rigid connections and semi-rigid models with k_4 and k_6 either rigid or hinged.



(a)



(b)

Figure 4.12 – Comparison between the displacements measured with the total station and results predicted by a rigid model and semi-rigid models with k_4 and k_6 either rigid or hinged for: (a) test n°1 (b) test n°2. Target point numbers correspond to the 16 target points indicated in Figure 4.5c.

First, it can be observed that a rigid model led to highly underestimated displacements with values 72.3 % lower in average over all target points for both tests. Displacements obtained with the semi-rigid models were found to be of the same order of magnitude as the ones measured for both tests, with differences of 14.8 % in average. However, for test n°1, displacements of targets 9 to 12 were overestimated by 33.2 % in average and underestimated by 15.5 % for targets 1 to 6. These variations correspond to differences of 3.9 mm and 3.1 mm respectively and could be explained by the presence of caps, which was not considered in the numerical simulations, leading to an additional load that increases displacements in the area close to them and reduces displacements away from them. For test n°2, highest variations between the model and the measurements also appeared for targets located in the vicinity of the caps and close to steel struts and could be explained by inaccuracies in the modelling of the connections between the steel struts and the structure.

4.5.2 Displacement Fields

Cloud-Cloud Distances Computation

Registration and distances computation are important steps in the processing of the points clouds. Point clouds registration using the five spherical targets led to mapping errors of about 1 cm for different load cases. These errors were considered too high to provide a sufficient accuracy and, as suggested by Lee et al. [51], a manual registration was thus performed in the software CloudCompare considering four points at the bottom corners of arch n°22.

For test n°1, distances computed by applying local mathematical models on the nearest point and a defined number of its neighbouring points, as illustrated in Figure 4.10b, were compared with the ones obtained using the nearest neighbour distance (NND) method presented in Figure 4.10a. The three mathematical models available in CloudCompare were investigated, namely (i) 2D1/2 Delaunay triangulation, (ii) least square best fitting plane and (iii) quadratic height function. The displacement field obtained using (i) by fitting the model on the nearest point and its 6 neighbouring points was found to give similar results to the one obtained using the NND method. However, results using (ii) and (iii) on the nearest point and its 6 neighbouring points both led to noisy displacement fields with a large inaccurate area, as shown in Figure 4.13a for (ii). Analyses performed using (ii) and (iii) on the nearest point and its 99 neighbouring points increased the computing time and still led to small areas with errors, as illustrated in Figure 4.13b for (ii). Point clouds were thus found to be sufficiently dense to compute distances using the NND method and all other methods were therefore discarded for both tests.

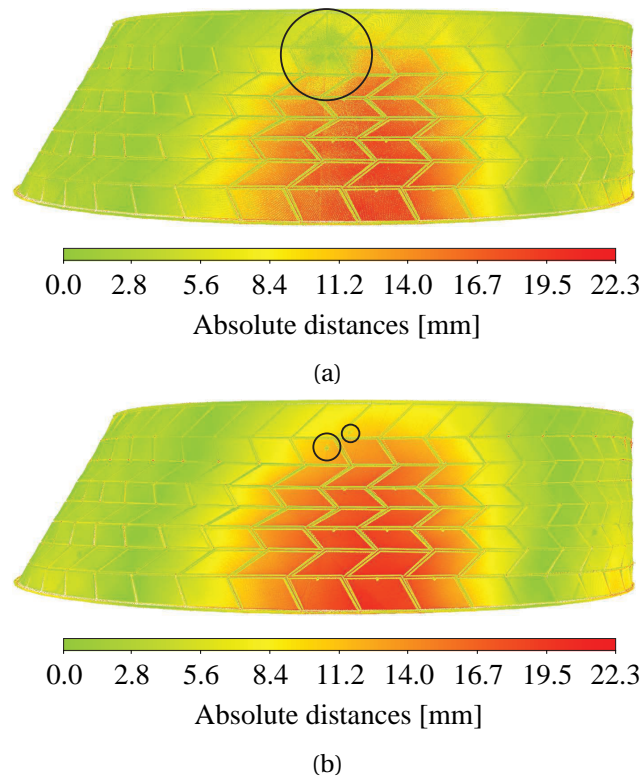


Figure 4.13 – Distances computation for test n°1 using the least square best fitting plane on: (a) the nearest point and its 6 neighbouring points (b) the nearest point and its 99 neighbouring points.

Total Station Measurements vs. Point Clouds

Absolute distances computed with CloudCompare for test n°1 and 2 are presented in Figure 4.14. Displacement fields obtained by laser scanning were first compared to total station measurements. It can be observed that point cloud distances computed were comparable for both tests, whereas higher differences could be observed with and without the presence of half arch n°1 using a total station. Although precise values at discrete points are difficult to obtain with point clouds, it was found that overall values using the two measuring methods differed: at the 16 target positions, results from laser scans were found to be 2.9 mm and 0.7 mm lower than total station measurements on average for test n°1 and 2 respectively. Furthermore, distances computed for specific target points gave differences of more than 60 % between the two methods. For example, for test n°1, points n°15 and 16, corresponding to values of approximately 3 and 1 mm respectively for the point cloud, had measured displacements of 7.6 and 5.6 mm with the total station. Similarly, values computed at the target points 11 and 12 using the point clouds were found to be 37 % and 4 % in average lower than the total station measurements at these locations for test n°1 and 2 respectively. Variations can be attributed to the registration of the point clouds to which results were shown to be very sensitive.

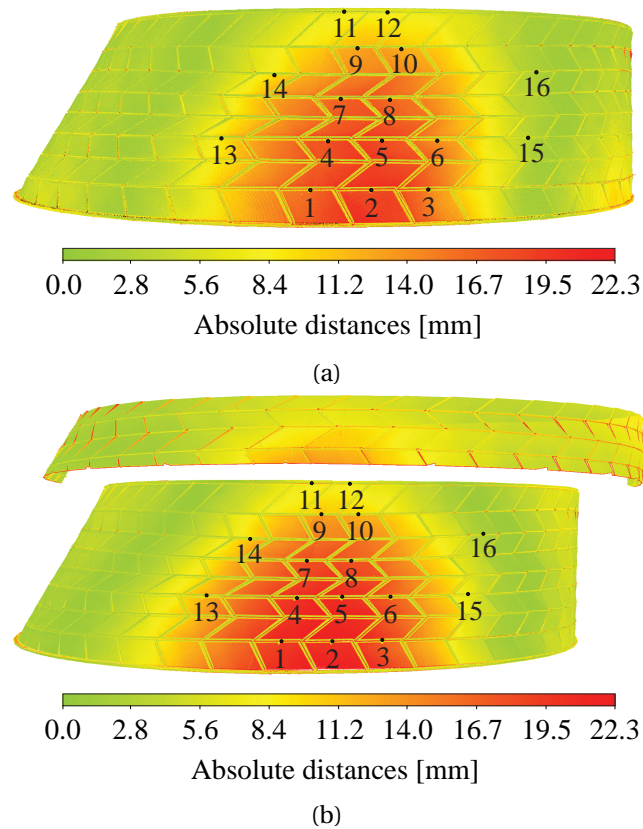


Figure 4.14 – Distances computed from laser scans for: (a) test n°1 (b) test n°2. Numbered points indicate the 16 target points where displacements were measured using a total station.

Validation of the Numerical Model

Displacement fields at the bottom layer of the structure predicted by the semi-rigid model with rotational stiffness of the connections k_4 and k_6 hinged are presented in Figures 4.15a and 4.15b for test n°1 and 2 respectively. Although uncertainties arose from the laser scans registration process, it can be observed that the same range of values was predicted by the semi-rigid model. However, the displacement field predicted was found to be closer to the one measured for test n°2 (see Figures 4.14b and 4.15b) than for test n°1 (see Figures 4.14a and 4.15a). For the latter, differences can be related to the presence of caps during the experimental tests (as explained in Subsection 4.5.1) and to point cloud registration errors.

Evaluation of the Built Geometry

Additionally, the reconstructed structure of arch n°22, obtained with laser scanning, was compared to the 3D design geometry of the CAD model to evaluate the gap between theoretical and as-built geometries. Absolute displacements between the point cloud of load case n°1 and the bottom surfaces extracted from the 3D design geometry were first computed. Results

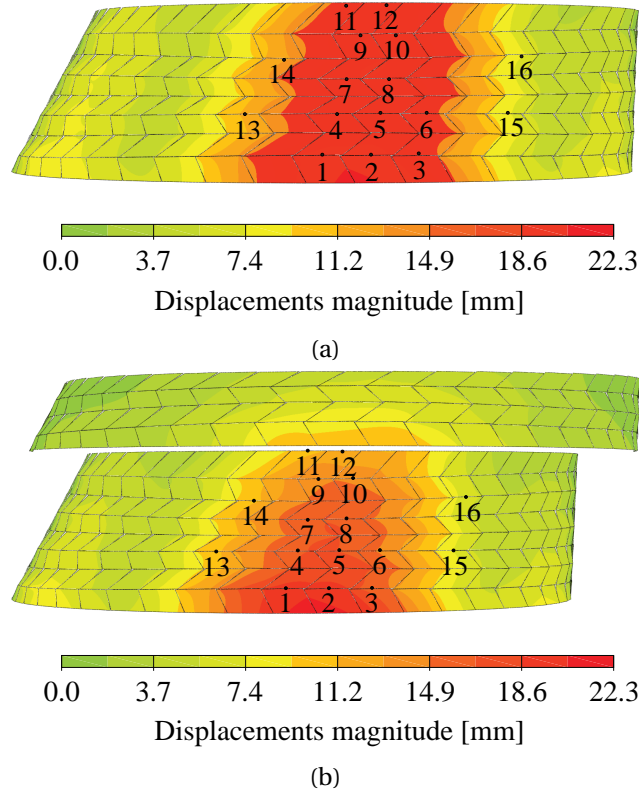


Figure 4.15 – Displacements predicted by the semi-rigid numerical model, with rotational stiffness k_4 and k_6 hinged for: (a) test n°1 (b) test n°2. Numbered points indicate the 16 target points where displacements were measured using a total station.

of the cloud-to-mesh distance computation are presented in Figure 4.16a. Since the laser scans of the structure were executed for arch n°22 under its own weight, displacements were computed for the self-weight load case to establish a valid comparison using the semi-rigid model with k_4 and k_6 hinged, leading to the largest displacements (see Figure 4.16b).

Large differences can be observed between the displacements predicted by the numerical model under self-weight only (see Figure 4.16b) and the cloud-to-mesh distance computation obtained for arch n°22 unloaded (see Figure 4.16b), with maximum differences between the two of about 65 mm. Considering the results obtained in Subsection 4.5.1 and sub-subsection 4.5.2, these variations cannot be attributed only to the presence of caps in the tested prototypes, inaccuracies of the model and uncertainties linked to the point cloud registration, especially for the large displacements observed on the right side of the structure in Figure 4.16a. It was inferred that part of these large differences can be attributed to initial imperfections of the structure, such as geometrical imperfections, linked to the variance in structural dimensions of all the elements, and assembly tolerances. Geometric variability can be due to unavoidable machining errors, alterations from handling and transportation of the elements as well as moisture content variations. Although machining tolerances are expected

to be low because of the precision of the 5-axis CNC cutting machine in the sub-millimetre range, tolerances can add up and lead to large geometric differences [10]. As suggested by Liew et al. [55], adjusting the boundary conditions according to the as-built geometry could reduce these variations, in particular regarding the large displacements appearing on the right side of the structure.

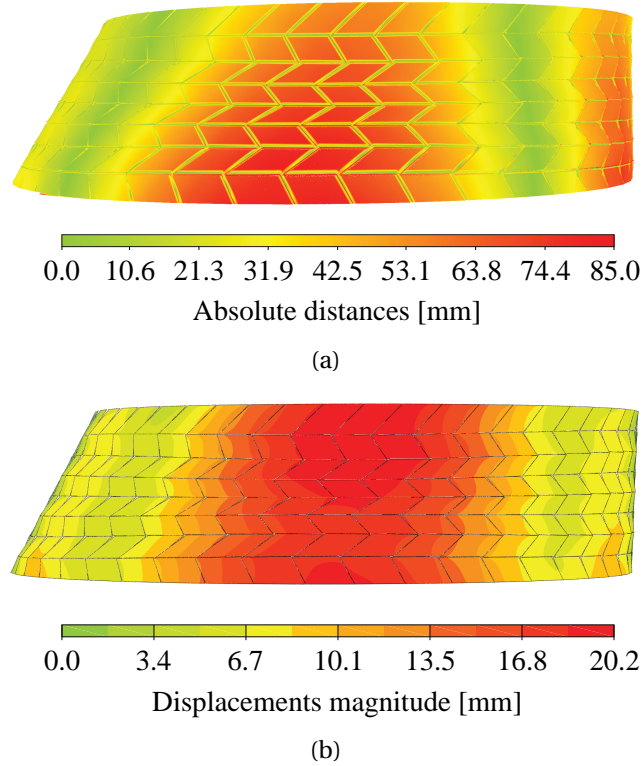


Figure 4.16 – Evaluation of the built geometry: (a) Displacements between initial point cloud before loading (load case 1) and bottom surfaces extracted from the 3D design geometry (b) Displacements obtained with the semi-rigid model with k_4 and k_6 hinged under self-weight only.

Influence of Initial Imperfections

In this chapter, a good correlation was found between the experimental tests performed on the as-built geometry and the numerical simulations performed on the design geometry. Nonetheless, initial imperfections might need to be taken into account in design calculations, as they can have a high influence on the structural stability of large-span structures [118]. To evaluate their impact on the global behaviour of the structure, the as-built geometry measured with laser scanning could be used as the initial geometry for numerical simulations. However, employing measured data as the starting point of calculations can be unpractical and is generally not possible since the erection process usually follows the design calculations. A sensitivity study should therefore be performed to assess the contribution of fabrication and

assembly tolerances, which could lead to a misalignment of the plates, on the mechanical behaviour of the structure. This analysis could be carried out by varying the initial geometry used for numerical simulations to determine the worst possible geometry or its equivalent simplified geometry, as suggested by Stranghöner and Azizi [108]. If their impact is found to be substantial, the modified geometry should be considered for structural design calculations.

4.6 Conclusions

In this chapter, static loading tests were performed on large-scale freeform timber plate shells, which were full-scale prototypes of the thesis case study described in Chapter 1, Subsection 1.3. A surcharge load of 1.5 kN/m^2 was applied on a defined area at the top of the structure using 25 kg cement bags. A comparison was made between the displacements predicted by the semi-rigid spring model developed in Chapter 2 and the displacements measured using two devices: a total station and a terrestrial laser scanner. The total station provided displacements of the structure at 16 target positions, while displacement fields were obtained by computing distances between point clouds from laser scanning.

The two measuring methods were first compared to evaluate their relevance. Total station measurements were found to give results with a higher precision of about 1-3 mm than laser scans for individual target points. However, point clouds from laser scans allowed the visualisation of displacement fields at the bottom surface of the structure, such that the two methods are complementary. Regarding laser scans processing, a precise registration was found to have a significance importance as it can highly influence the results. Georeferencing laser scan data could help reducing errors linked to this registration step, as well as increasing the number of survey markers. Regarding the distances computation of the point clouds, using the nearest neighbouring distance was found to be sufficiently efficient compared to other methods using local mathematical models.

The FE model was found to be in good agreement with the experimental tests. As for the investigations on small-scale structures, it was proven crucial to take into account the semi-rigidity of the connections to accurately predict the behaviour of the structure. In fact, a rigid modelling of the connections underestimated the displacements by about $72 \% \pm 4 \%$ in average, whereas semi-rigid models with k_4 and k_6 either rigid or hinged gave results with a difference of about $15 \% \pm 12 \%$ in average with respect to the total station displacements measured at the 16 target positions.

Furthermore, the unloaded structure, obtained with laser scanning, was compared to the 3D design geometry of the CAD model to evaluate the gap between theoretical and as-built geometries. Cloud-to-mesh distances computed showed large displacements occurring without the application of surcharge loads. If part of these displacements can be attributed to inaccuracies of the numerical model and point cloud registration errors, the accumulation of fabrication and construction tolerances appears to be the main reason of these large differences observed. To tackle this issue, an assessment of the parameters influencing the variations between

Chapter 4. Experimental Investigations on a Large-Scale Structure

3D design model and as-built geometry as well as an analysis of the impact of different initial geometries on the global behaviour of the structure are necessary to determine if initial imperfections need to be taken into account in design calculations.

In conclusion, the semi-rigid model developed was validated against full-scale experimental tests for the prediction of the displacements of the global structure in the linear elastic part, therefore allowing its serviceability limit state design. Furthermore, as concluded in Chapter 3, a semi-rigid model with hinged rotational components about x and z should be considered as it provides more conservative results.

5 Alternative Structural System

This chapter is based on: A. C. Nguyen, B. Himmer, P. Vestartas and Y. Weinand, Performance Assessment of Double-Layered Timber Plate Shells using Alternative Structural Systems. In C. Lázaro, K.-U. Bletzinger, E. Oñate, editors, *Proceedings of the IASS Annual Symposium 2019 – Structural Membranes 2019 Form and Force*, pages 2919–2926. International Centre for Numerical Methods in Engineering (CIMNE), Barcelona, 2019.

5.1 Introduction

Automated numerical tools necessary for the structural analysis of freeform timber plate structures using wood-wood connections have been successfully developed in Chapter 2, based on the double-layered double-curved timber plate shells of the thesis case study presented in Chapter 1, Section 1.3. The proposed finite element (FE) model has been assessed and validated through experimental tests performed on both small- and large-scale structures in Chapters 3 and 4 respectively. However, three-point bending tests carried out on small assemblies of fifteen boxes have pointed out challenges in the initial assembly system (see Chapter 3, Section 3.4.1). Namely, failure paths that can be attributed to the herringbone pattern applied in the box arrangement were appearing at the stretched bottom layer of the structure. In light of this, investigations on the use of an alternative pattern for the structural performance improvement of double-layered timber plate shells are carried out in this chapter.

Previous studies have mostly focused on ways to provide connections with sufficient load-bearing capacities, in order to be used not only in timber frame structures but also with timber plates [78]. In this chapter, the influence of the geometry patterns used in the assembly system on the global structural performance is investigated for the same case study. The goal is to modify the structure's geometry to enhance its mechanical behaviour without drastically changing its general appearance.

The alternative pattern, in which the continuous failure paths are interrupted, is proposed and described with its assembly sequence in Section 5.2. The methods to apply it to large-scale double-layered double-curved timber plate shells are discussed in Section 5.3. The numerical model, built within the design framework introduced in Chapter 2 and adapted for the resulting assembly, is described in Section 5.4. The two assemblies are then compared based on numerical investigations in terms of displacements and stiffness of the structural system, as well as forces in the connections in Section 5.5.

5.2 Structural Systems

Double-layered double-curved timber plate shells have been achieved through computer-aided design (CAD) programming. In particular, the first step of their design was to apply a tiling pattern to a double-curved surface, referred to as the target design surface [80]. In this study, two structural systems were studied based on the application of two different tiling patterns to segment the same target surface.

5.2.1 Initial Herringbone Pattern

The reference structural system, which uses the initial herringbone pattern, is illustrated in Figure 5.1. It was developed by Robeller et al. [80] and applied to the Annen Plus SA head office project, case study of this thesis described in Chapter 1, Section 1.3. In this system, each shell is composed of an assembly of hexahedra-shaped boxes B_i , each made of two vertical plates $V_{i,1}$ and $V_{i,2}$ and two horizontal plates $H_{i,1}$ and $H_{i,2}$. The latter form the two layers of the structure. Neighbouring horizontal plates are connected with single-degree-of-freedom (1-DOF) through-tenon (TT) wood-wood connections through vertical plates, which are themselves assembled with dovetail joints. Each box B_i share its vertical panels with neighbouring boxes. Boxes are individually formed and are then inserted along the vector of insertion, defined by the direction of the remaining DOF of the connections.

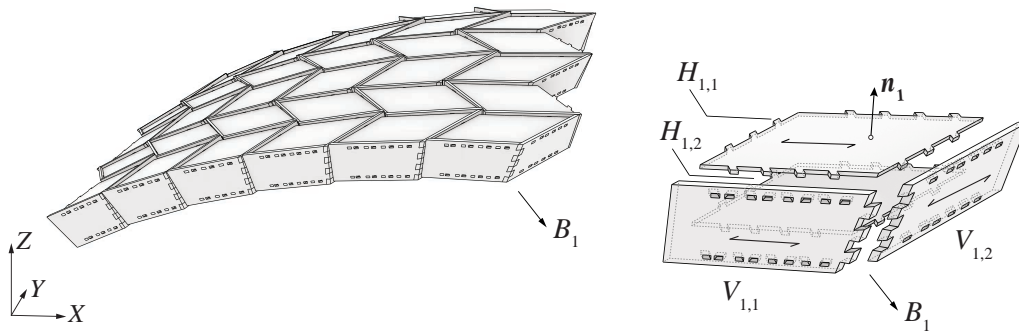


Figure 5.1 – Initial assembly system developed by Robeller et al. [80] for double-layered double-curved timber plate shells using wood-wood connections. Each shell is composed of an assembly of hexahedra-shaped boxes B_i , each made of two vertical plates $V_{i,1}$ and $V_{i,2}$ and two horizontal plates $H_{i,1}$ and $H_{i,2}$.

Three-point bending tests performed on a 5×3 boxes double-layered prototype have shown that TT wood-wood connections at the bottom stretched layer of the structure failed due to a combination of shear and tension loads. In particular, the construction system was weakened by continuous failure paths appearing due to the herringbone pattern used to segment the target surface (see Chapter 3, Section 3.4.1). The failure paths are illustrated in Figure 5.2 for a full arch, namely arch n°22 of the case study.

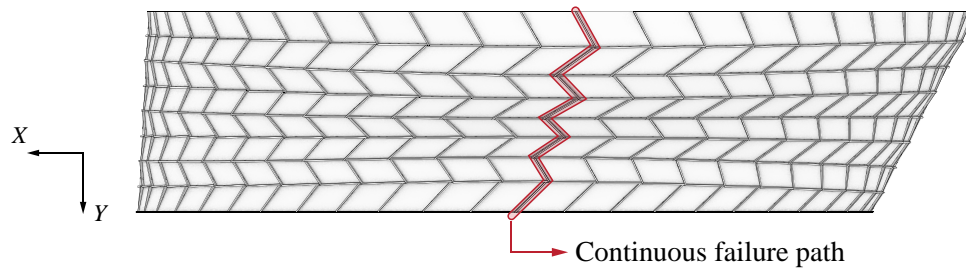


Figure 5.2 – Continuous failure paths appearing in the initial assembly system due to the herringbone pattern, illustrated for arch n° 22 of the Annen Plus SA head office.

5.2.2 Shifted Herringbone Pattern ¹

An alternative pattern was investigated in order to tackle the problems encountered with the initial system, without changing the target surface, constraint of the project, and the height of the boxes of 600 mm. In order to interrupt the continuous failure paths, boxes were shifted in every second row to obtain staggered rows. However, as seen in Figure 5.3, this shift introduces large gaps in the structure. The shape of horizontal plates was therefore modified: the quadrilaterals (without considering the tenons) used in the herringbone pattern (see Figure 5.3a), were replaced by non-convex octagons (see Figure 5.3b).

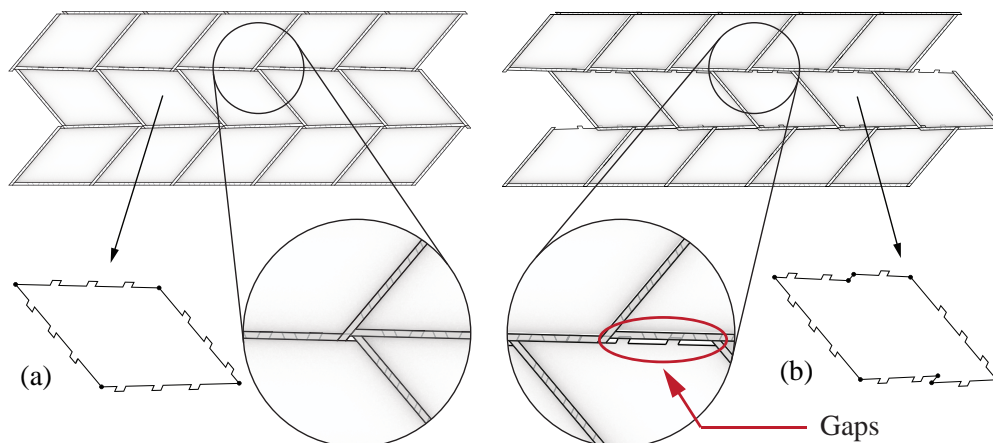


Figure 5.3 – The shifted herringbone pattern introduces gaps in the structure, such that the shape of the horizontal plates was modified: (a) Initial quadrilaterals (b) Non-convex octagons.

¹ The development of the structural system using a shifted herringbone pattern was performed in collaboration with the publication co-author, B. Himmer.

The application of a shifted herringbone pattern modifies the assembly sequence of the system. Figure 5.4 illustrates a possible solution to assemble quadrilateral- and non-convex octagonal-shaped plates. In the proposed assembly system, the first row of box elements B_i , with i being an odd number, are composed of two horizontal plates $H_{i,1}$ and $H_{i,2}$ and two vertical plates $V_{i,1}$ and $V_{i,2}$. These four-sided boxes are assembled in the same manner as in the initial construction system, described in Figure 5.1. After one row of these boxes is placed, a second row of boxes B_j , with j being an even number, consisting of three-sided boxes, is positioned. Vertical plates $V_{i,3}$ are then inserted along the vector \mathbf{u}'_i , before connecting four-sided boxes B_i to them. Subsequent rows are then obtained similarly. The proposed assembly sequence requires more steps and is therefore more complicated compared to the initial assembly system illustrated in Figure 5.1.

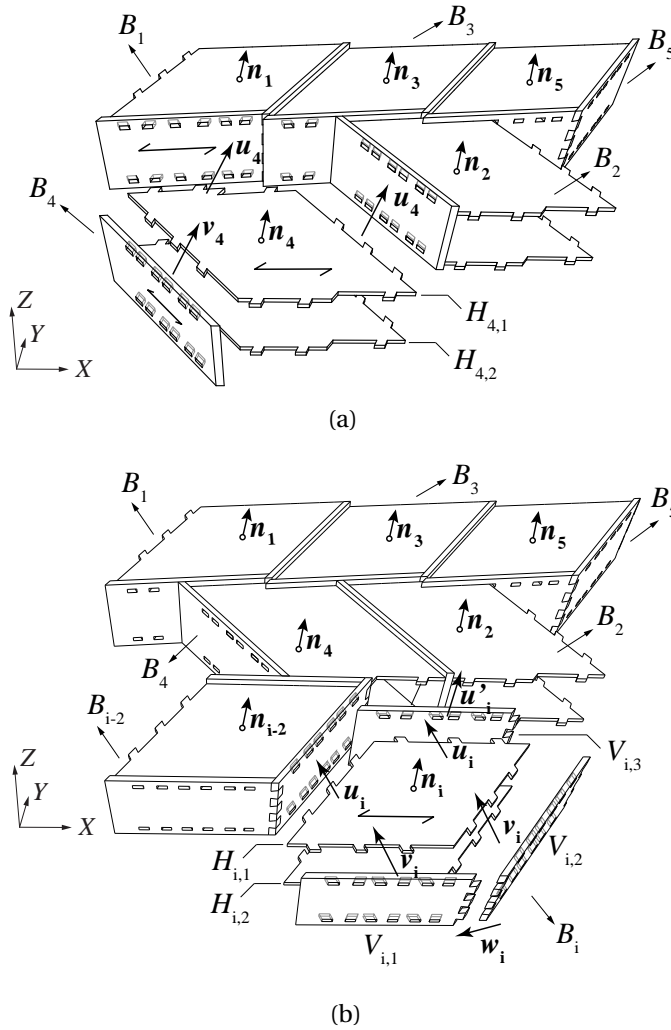


Figure 5.4 – Assembly sequence of the alternative structural system: (a) Three-sided box elements B_j are inserted along a vector of insertion \mathbf{u}_j (b) A row of vertical plates $V_{i,3}$ is first inserted, before connecting four-sided boxes B_i to them, along a vector of insertion \mathbf{u}_i .

The introduction of non-convex octagonal-shaped plates with the shifted herringbone pattern has the advantage to provide zones of abutment of the horizontal plates in the structural system, at the positions illustrated in Figure 5.5. However, Figure 5.6a shows that the shape of the plates had to be modified (dashed to solid lines) for abutment angles β less than tenon angles α , defined by the insertion vector \mathbf{v}_i and unique for each edge of the plates, to ensure their insertion. In this case, a small gap was introduced and the abutment zone was reduced to a contact line (see Figure 5.6b). For abutment angles β larger than tenon angles α , no modification of the plate shape was required, as seen in Figure 5.7a. The contact zone therefore remained the full area of the abutment (see Figure 5.7b).

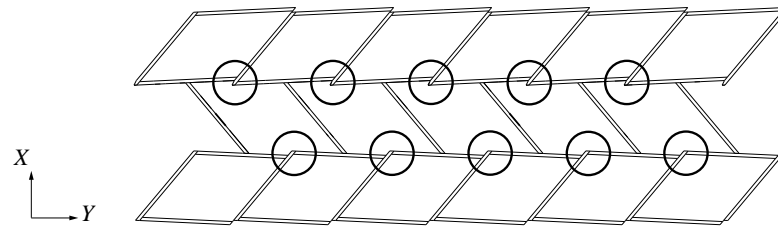


Figure 5.5 – Zones of abutment resulting from the shifted herringbone pattern.

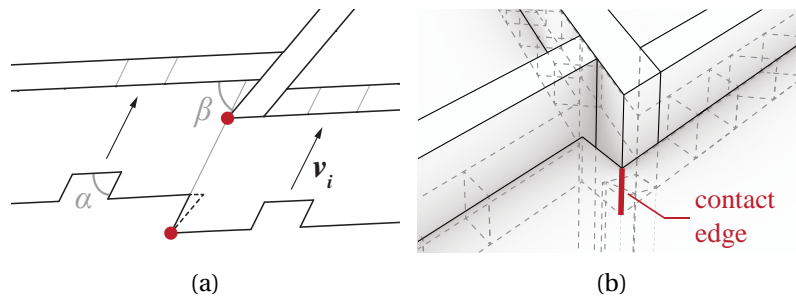


Figure 5.6 – Contact for abutment angles β less than tenon angles α , defined by the insertion vector \mathbf{v}_i : (a) The octagonal shape of the plates had to be modified (dashed to solid lines) to ensure their insertion (b) The shape modification introduced a small gap, such that the abutment zone was reduced to a contact line.

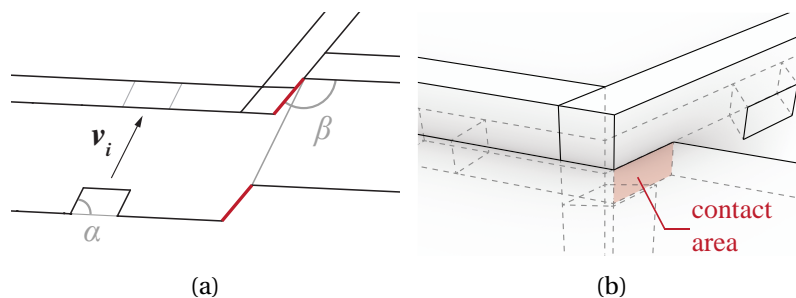


Figure 5.7 – Contact for abutment angles β larger than tenon angles α , defined by the insertion vector \mathbf{v}_i : (a) The octagonal shape of the plates did not have to be modified. (b) The contact zone remained the full area of the abutment.

Furthermore improvements could be made by adding wood-wood connections between vertical panels, at the positions indicated in Figure 5.8a. According to the assembly sequence illustrated in Figure 5.4, the insertion vector \mathbf{v}_i of the vertical plates would be identical to the insertion vectors of the horizontal plates with which three-sided boxes are formed. Vertical and horizontal plates would therefore be mutually interlocked. Since these connections would be more complicated to generate and to implement in the numerical model, this modification was discarded in the rest of the study.

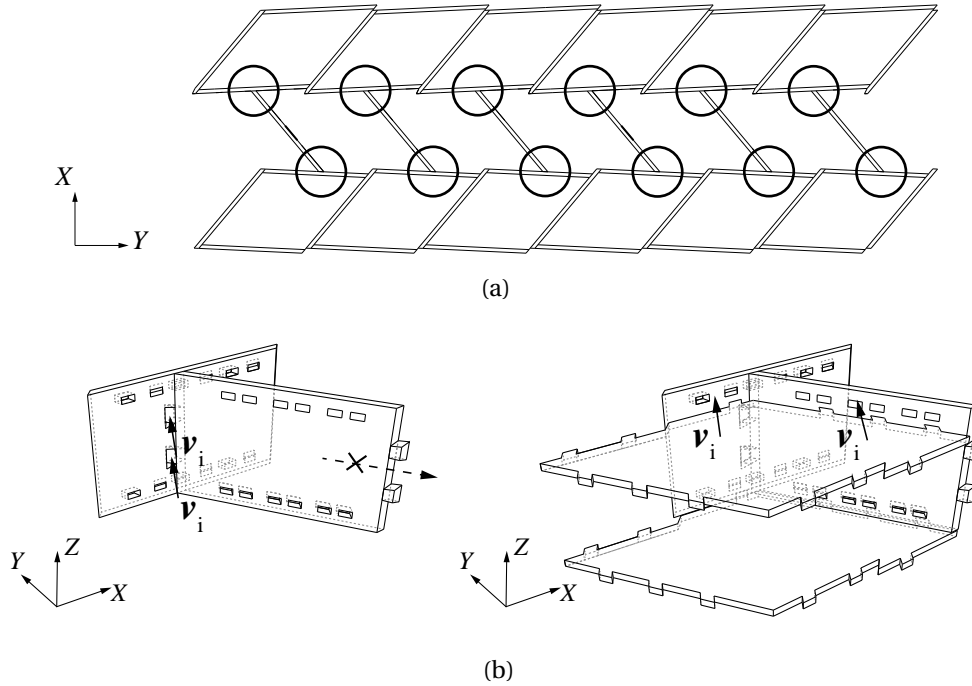


Figure 5.8 – Possible additional improvement of the structural system by the addition of wood-wood connections between vertical plates: (a) Location of the connections (b) Identical insertion vector \mathbf{v}_i between the insertion vectors of the horizontal plates into the vertical plates and of between vertical plates.

5.3 Application to a Large-Scale Structure²

In this section, the methods that have to be followed to apply the proposed alternative structural system to large-scale double-layered double-curved timber plate shells are presented. Investigations need to be integrated in the design framework introduced in Chapter 2 and the custom CAD plugin initially developed by Robeller et al. [80] requires modifications to apply the alternative structural system to entire arches.

²Preliminary investigations on the application of the shifted herringbone pattern to a large-scale structure were performed by the publication co-author, P. Vestartas.

5.3.1 Design Framework

In order to establish a link between design and structural analysis, the investigations of this chapter need to follow the design framework presented in Chapter 2 for the structural analysis of timber plate shells. In this manner, a feedback loop for structural optimisation can be implemented, as illustrated in Figure 5.9. To apply the alternative structural system starting from the target surface, both the custom CAD plugin and the custom scripting code generating the FE model need to be modified.

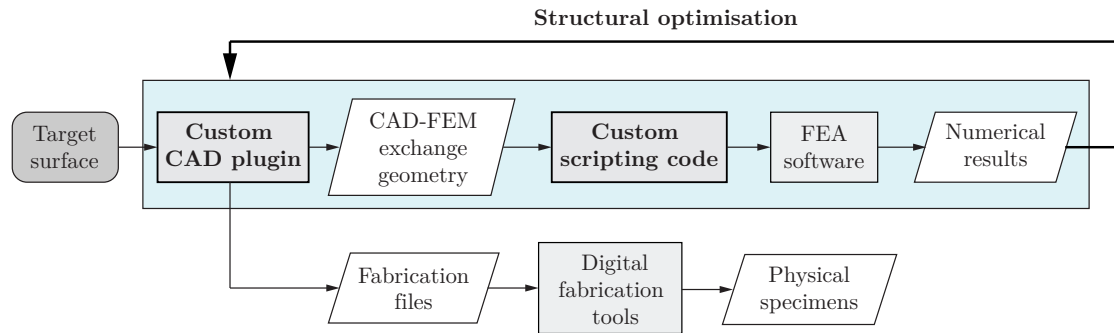


Figure 5.9 – A feedback loop for structural optimisations is integrated in the design framework introduced in Chapter 2.

5.3.2 Mesh Segmentation

Similarly to the initial CAD plugin, generating timber plate shells with the initial construction system, a tiling pattern first needs to be applied to a given target surface. Starting from a double-curved surface illustrated in Figure 5.10a, the mesh segmentation is obtained by applying the shifted herringbone pattern to it, as shown in Figure 5.10b.

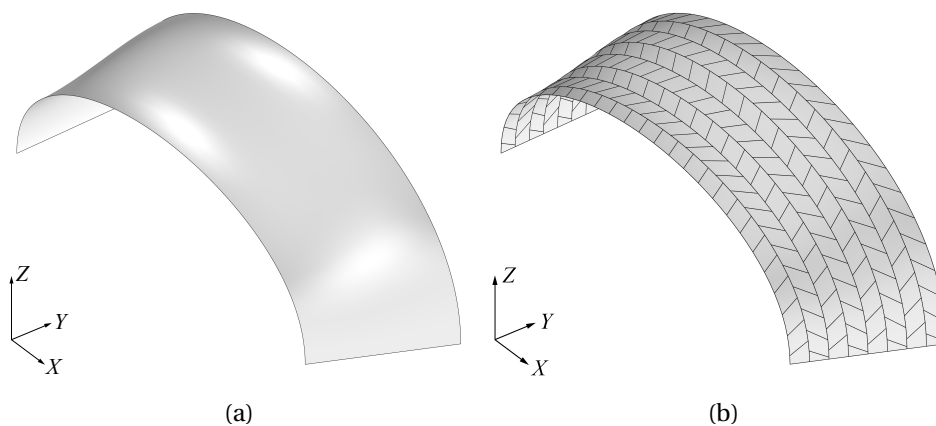


Figure 5.10 – Generation of the shifted herringbone pattern: (a) Initial double-curved surface, referred to as the target surface (b) Mesh segmentation obtained by applying the shifted herringbone pattern on the target surface.

5.3.3 Curvature Analysis

The curvature between neighbouring boxes needs to be analysed to determine if the remaining areas for joinery are sufficient to connect the boxes together. In fact, as illustrated in Figure 5.11a, the shift of the boxes can drastically decrease the area available for wood-wood connections for large angles between neighbouring boxes. To evaluate the angles between the alignment of mesh edges, closed boxes made of planar surfaces can be generated from mesh segments, as presented in Figure 5.11b. In this study, angles were found to be sufficiently low such that enough joinery areas were left for TT connections. In further work, optimisation of the planar faces could be performed to reduce these angles, such as done in previous research for the initial mesh segmentation using the herringbone pattern [80].

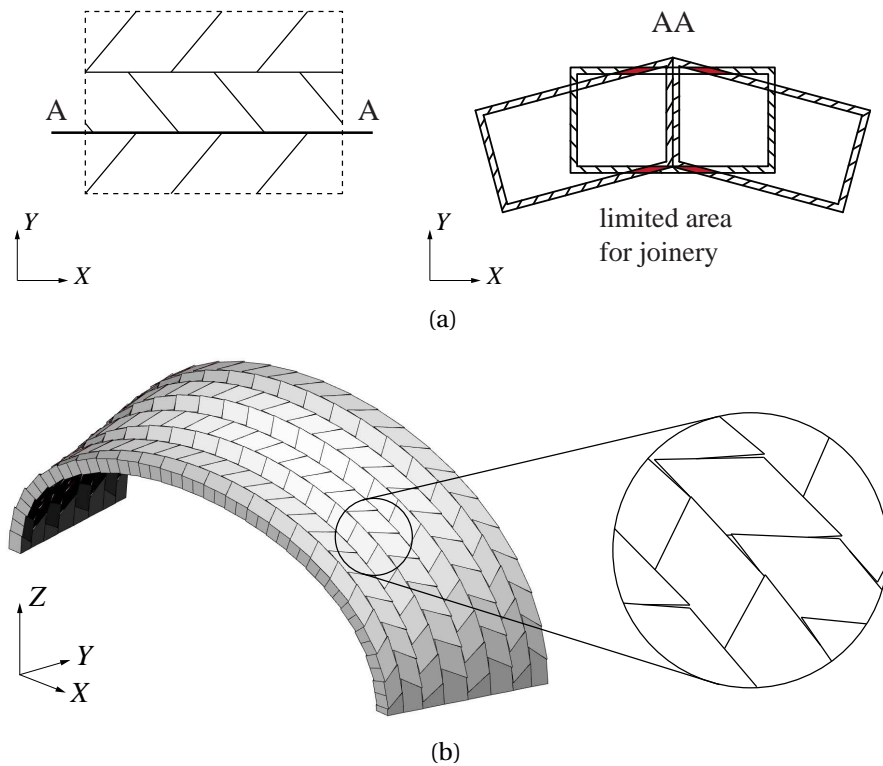


Figure 5.11 – Curvature analysis: (a) Reduction of the areas for joinery with the shifted herringbone pattern due to the shell's curvature (b) Shell composed of closed boxes made of planar surfaces used for curvature analysis.

5.3.4 Generation of Wood-Wood Connections

Insertion vectors have to be defined for each box, such that plate edges forming an obtuse angle share a unique insertion vector. This is illustrated in Figure 5.12a for the bottom layer of the shell structure. Tenons of TT connections can then be generated for horizontal plates in the same manner as for the initial assembly pattern, as shown in Figure 5.12b for the bottom layer.

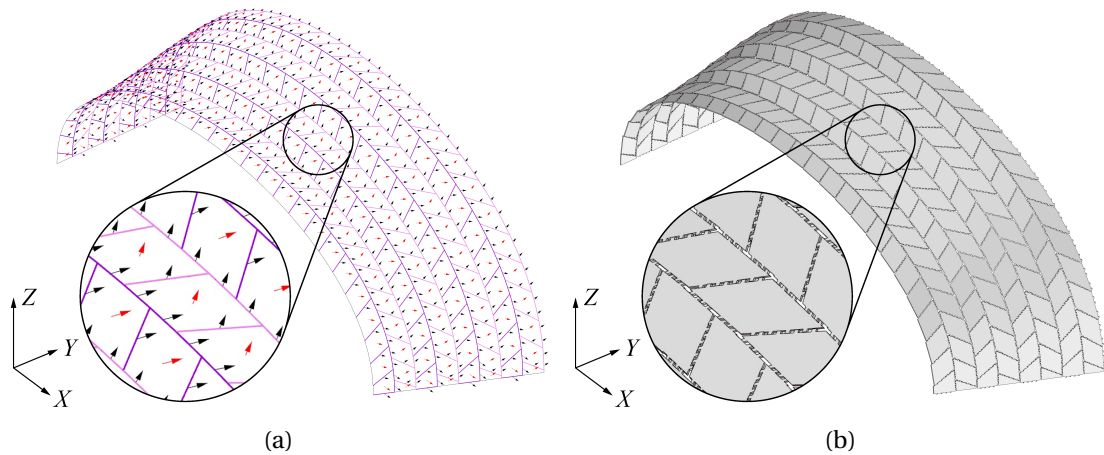


Figure 5.12 – Generation of through-tenon wood-wood connections for the bottom layer of the shell structure: (a) Insertion vectors have to be defined for each edge of the plates (b) Tenons of through-tenon connections are generated on the horizontal plates.

5.3.5 Full Arch

Vertical and top plates can be subsequently generated, in the same way as in the initial CAD plugin. Figures 5.13 and 5.14 illustrate the comparison between a structure in which the initial herringbone pattern was applied (see Figure 5.13a and 5.14a), namely arch n°22 of the Annen head office project, and the corresponding structure in which the shifted herringbone pattern was applied (see Figures 5.13b and 5.14b). As observed, the general appearance of the two structures is comparable.

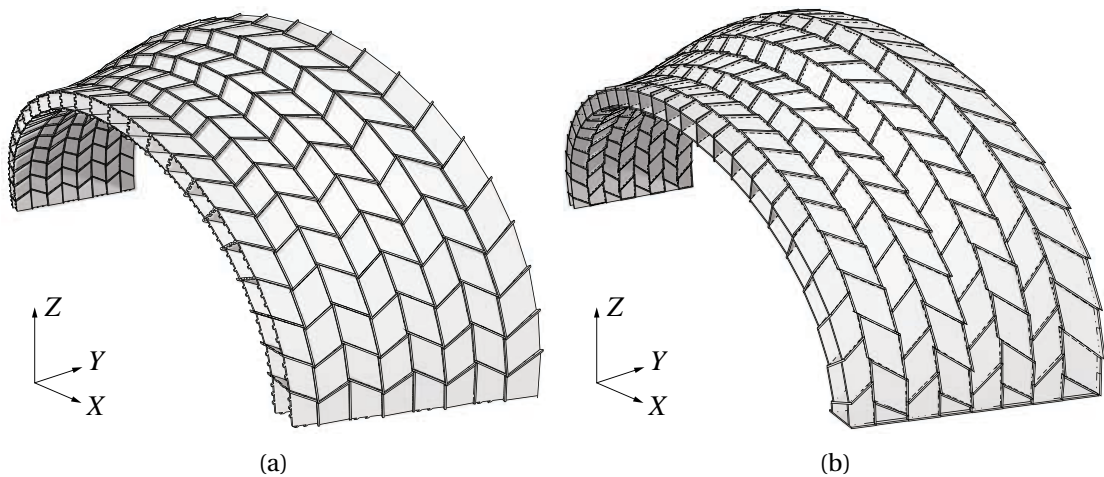


Figure 5.13 – General appearance of arch n°22 of the Annen head office project using two different patterns, axonometry: (a) Application of the herringbone pattern (b) Application of the shifted herringbone pattern.

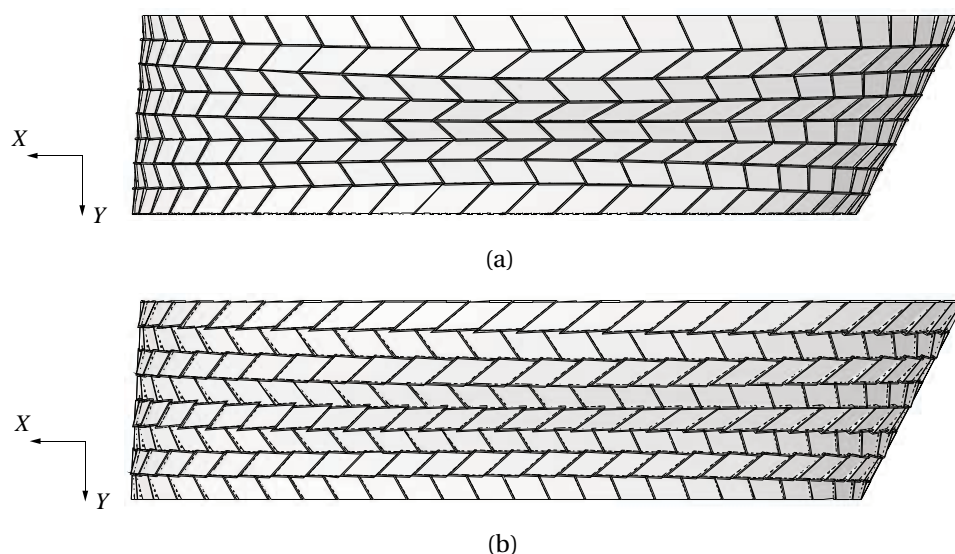


Figure 5.14 – General appearance of arch n°22 of the Annen head office project using two difference patterns, top view: (a) Application of the herringbone pattern (b) Application of the shifted herringbone pattern.

5.4 Numerical Modelling

5.4.1 Semi-Rigid Spring Model

The FE model, developed in Chapter 2 and validated against experimental tests performed on small- and large scale structures in Chapters 3 and 4 respectively, was used to compare the two structural systems. In this model, plates are modelled by their midsurface considering conventional shell elements and wood-wood connections are modelled using springs with 6 degrees of freedom (3 translational and 3 rotational), with stiffness values corresponding to the semi-rigidity of the connections in each component.

Plates were modelled considering a single orthotropic layer of material with properties defined parallel to the grain (direction 1), perpendicular to the grain along the veneer layer and across the plate thickness (directions 2 and 3 respectively). BauBuche Q panels (Pollmeier Massivholz, Creuzburg, Deutschland), used for the Annen head office and the prototypes tested in Chapters 3 and 4, were considered. They are 40 mm-thick beech laminated veneer lumber (LVL) panels with a characteristic density ρ_k of 730 kg/m³ obtained by gluing 3 mm thick beech peeled veneer layers. In the BauBuche-Q panels used, two layers are placed crosswise such that the composition of the 14 beech veneer layers is ||| – ||||| – ||| (| for longitudinal, – for crosswise veneer layer) [9]. Same material properties of BauBuche-Q panels used for the investigations conducted on small- and large-scale structures were considered in the model (see Chapter 3, Table 3.1).

Regarding the semi-rigid behaviour of the connections, axial, in-plane shear and out-of-plane shear stiffness (k_1 , k_2 and k_3 respectively), as well as rotational stiffness about y (k_5) were retrieved from experimental tests reported in Appendix A, Subsection 3.3.3. The values can be found in Chapter 3, Table 3.2. Stiffness k_4 and k_6 , shown to have a lower influence on the global behaviour, were considered hinged by assigning them a low stiffness value of 0.1 N·mm/°.

A mesh composed of finite strain S4R elements was applied, using a fine mesh element size of 2.5 mm at the vicinity of the joints and a coarse mesh of 50 mm away from them, according to the mesh convergence study performed in Chapter 2, Subsection 2.3.2.

The model was built in the finite element analysis (FEA) software Abaqus™, version 6.12 (Dassault Systèmes, Vélizy-Villacoublay, France) using the Abaqus Scripting Interface [16]. The custom scripting code automating the generation of the FE model was modified to take into account the non-octagonal shape of the plates.

5.4.2 Contact Modelling

Numerical simulations were performed with and without modelling of the contact zones of the abutments in order to evaluate their influence. They were modelled considering springs in series with an asymmetric behaviour, infinitely rigid in compression and free in traction. Since plates were modelled by their midsurface in the FEM geometry, the contact line through the thickness of the plate for abutment angles β less than tenon angles α (see Figure 5.6b) was modelled by a contact point, as illustrated in Figure 5.15a. This point, coupled to its neighbouring edges, was connected with springs to the plates in contact in the 3D geometry, as shown in Figure 5.15b.

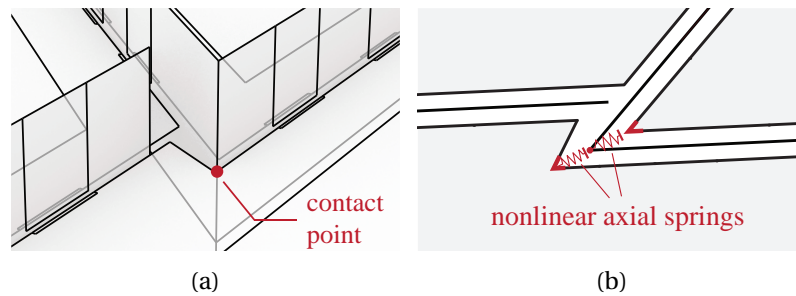


Figure 5.15 – Contact modelling of the abutment zones for abutment angles β less than tenon angles α : (a) The contact line through the thickness of the plate (see Figure 5.6b) was modelled by a contact point (b) The point, coupled to its neighbouring edges, and the corresponding plates in contact were connected with springs.

For the contact areas appearing for abutment angles β greater than tenon angles α (see Figure 5.7b), corresponding contact edges, illustrated in Figure 5.16a, were coupled to their midpoint and connected by springs connecting the corresponding edges in contact, as shown in Figure 5.16b.

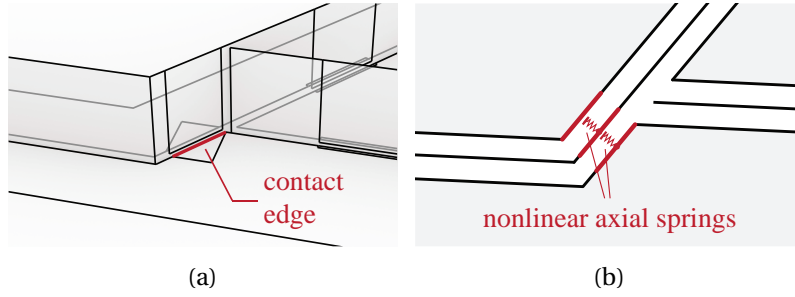


Figure 5.16 – Contact modelling of the abutment zones for abutment angles β greater than tenon angles α : (a) The contact areas through the thickness of the plate (see Figure 5.7b) were modelled by contact edges (b) The corresponding contact edges, coupled to their midpoint, were connected with springs.

5.4.3 Specimens

The geometries of the structures considered for numerical investigations are presented in Figures 5.17 and 5.18 for specimens applying the initial pattern and the shifted herringbone pattern respectively. For the first structural system illustrated in Figure 5.17, same geometric parameters as in the tested prototype of 5×3 boxes (see Chapter 3, Figure 3.1a) were considered. For the alternative structural system illustrated in Figure 5.18, three additional boxes were added to obtain symmetry. Furthermore, the tilt angle between the rows of boxes was increased from 1.4° to 2.7° in order to have a larger abutment contact area (see Figure 5.7b).

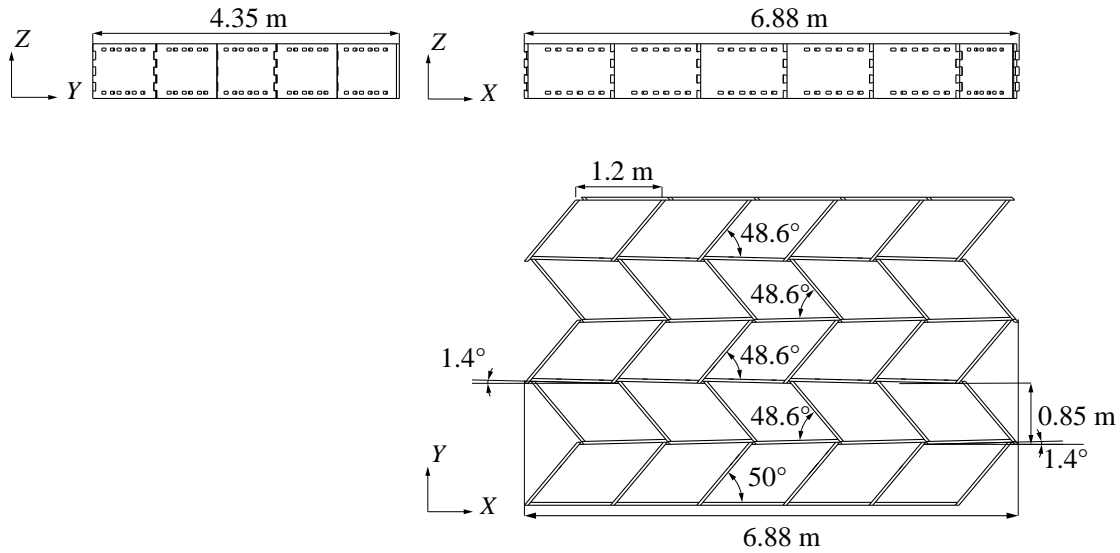


Figure 5.17 – Geometry of the 5×5 specimen considered for numerical investigations applying the initial herringbone pattern. Same geometric parameters as in the tested prototype of 5×3 boxes (see Chapter 3, Figure 3.1a) were considered.

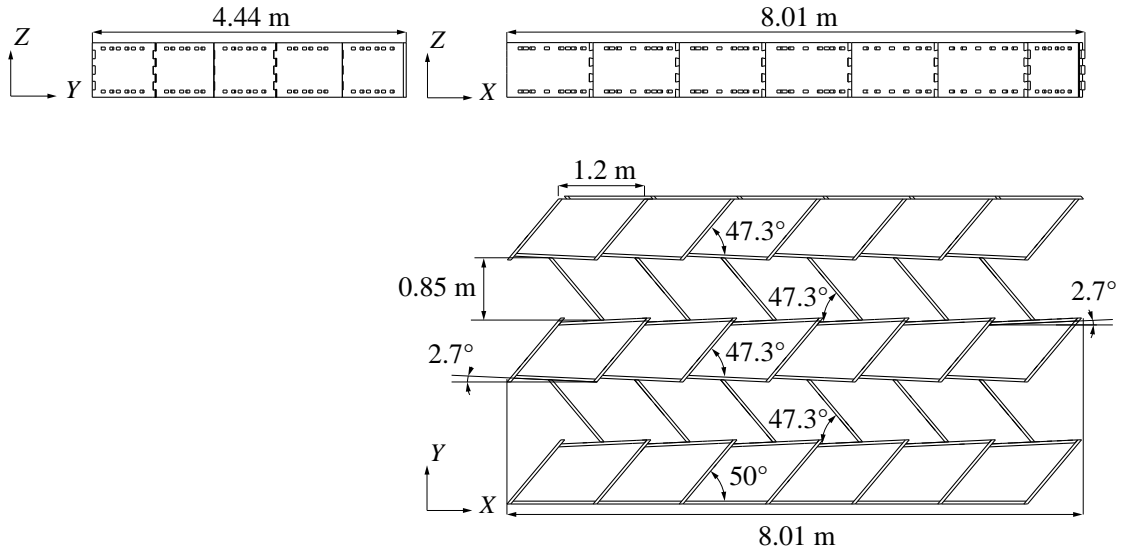


Figure 5.18 – Geometry of the 28-boxes specimen considered for numerical investigations applying the shifted herringbone pattern.

5.4.4 Loads and Boundary Conditions

Boundary conditions equivalent to the ones of the three-point bending tests performed a 5×3 boxes prototype were considered; namely pinned support on one side and roller support on the other one (see Chapter 3, Subsection 3.3.5 for more details on the modelling). A distributed load was simulated on the top layer of the structure.

5.5 Results and Discussion

The structural systems were compared in terms of vertical displacements and forces in the connections, similarly to the analysis performed in Chapter 3, Subsection 3.4.2 to compare experimental and numerical results for 5×3 boxes prototypes.

5.5.1 Vertical Displacements

Figure 5.19 presents the vertical displacement fields obtained at the bottom layer of the studied specimens for a distributed load of 2 kN/m^2 applied on their top layer. It can be observed that the use of the alternative structural system highly reduced the overall vertical displacements. Furthermore, displacements were found to be more distributed along the width of the specimen compared to the assembly in which the initial structural system was applied. For the latter, displacements were shown to be higher at the side of the specimen where vertical plates were not connected with dovetail joints (open side closed by additional vertical plates). Vertical displacements were further decreased by modelling abutment contacts.

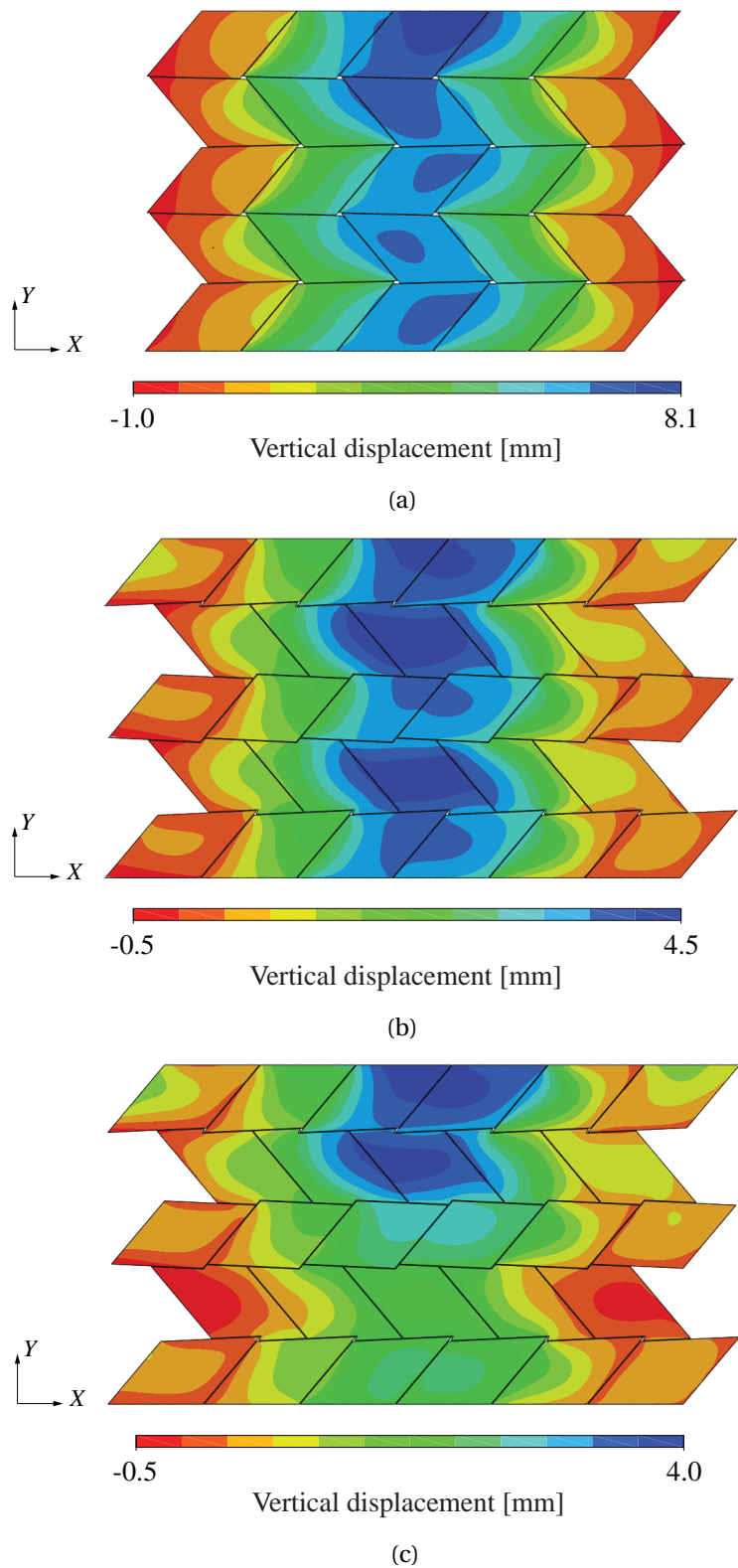


Figure 5.19 – Vertical displacement fields obtained at the bottom layer of the studied specimens for a distributed load of 2 kN/m² applied on the top layer: (a) Initial structural system (b) Alternative structural system (c) Alternative structural system with contact modelling.

Figure 5.20 presents the load-displacement curves obtained for the two specimens, modelling contact of abutment zones or not for the alternative structural system. System n°1 refers to the 5×5 boxes assembly using the initial herringbone pattern (see Figure 5.17), while system n°2 refers to the 28-boxes specimen applying the shifted herringbone pattern (see Figure 5.18). It can be observed that the major part of the stiffness increase was due to the structural system applied and not the contact modelling. With the alternative system, stiffness was increased by 83 % and 105 % without and with contact modelling respectively.

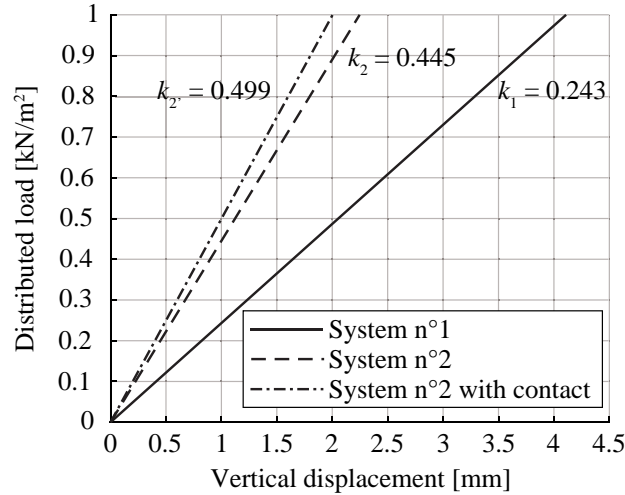
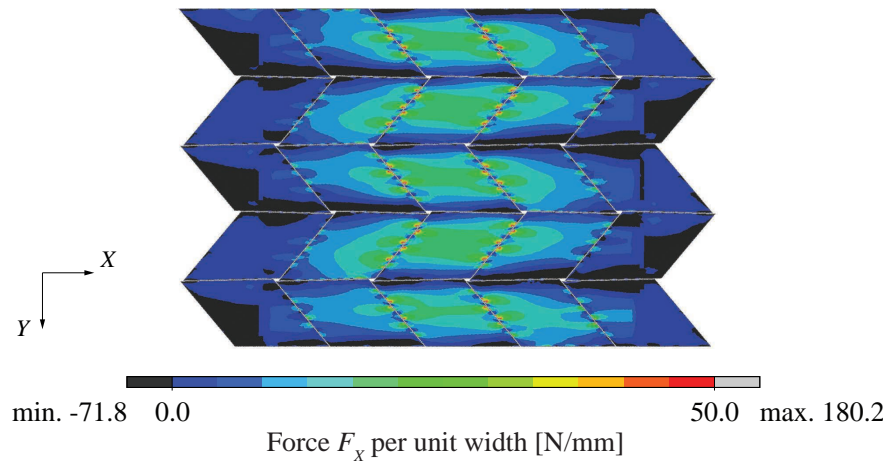


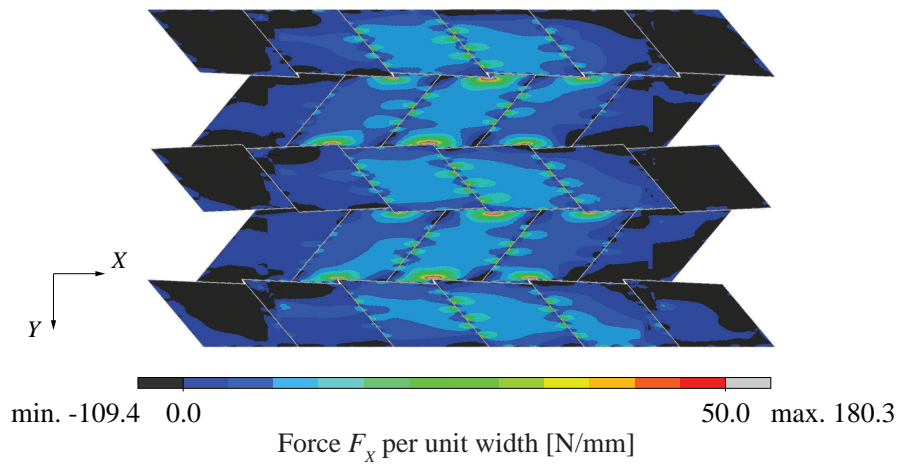
Figure 5.20 – Load vs. maximum vertical displacement curves for the two structural systems with and without modelling of the contact of abutment zones. System n°1 refers to the initial structural system. System n°2 refers to the proposed alternative system.

5.5.2 Forces in the Connections

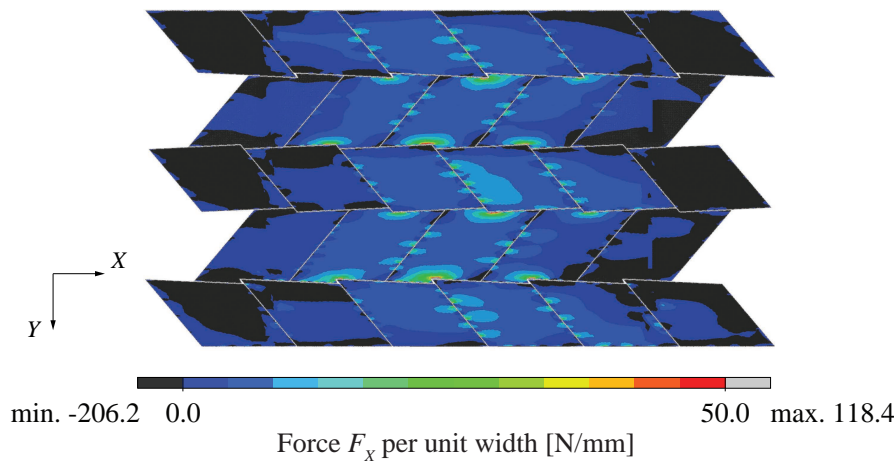
Figure 5.21 presents the forces per unit width in the X-direction obtained at the bottom layer of the studied specimens for a distributed load of 2 kN/m^2 applied on their top layer. It can be observed that forces contributing to the tensile stresses, that led to the failure of the joints and of the system in the three-point bending tests performed in Chapter 3, were drastically reduced when using an alternative structural system. Moreover, they were further decreased when modelling the abutment contacts. Instead, shear forces were shown to appear at the plate edges around the abutments when using the alternative structural system. This constitutes an improvement of the structural system as the maximum load-carrying capacity of TT connections is much higher in shear ($F_{\text{max,avg}} = 46.83 \text{ kN}$) than in tension ($F_{\text{max,avg}} = 6.47 \text{ kN}$), as seen in Appendix A.



(a)



(b)



(c)

Figure 5.21 – Forces per unit width in the X-direction at the bottom layer of the studied specimens for a distributed load of 2 kN/m² applied on the top layer: (a) Initial structural system (b) Alternative structural system (c) Alternative structural system with contact modelling.

To quantify the structural performance improvement, the distributed loads at which the first tenon reached the maximum load-carrying capacity of TT connections either in tension or in shear for the two structural systems were compared. In both cases, the maximum tensile force was reached before the maximum shear force in the connections. The distributed loads at which it occurred are presented in Table 5.1. It can be observed that the forces in the connections were reduced, such that the maximum applied load at failure was increased by 85 % and 229 %, without and with contact modelling respectively, using the shifted herringbone pattern instead of the initial herringbone pattern.

Table 5.1 – Maximum load applied to reach the maximum load-carrying capacity in tension.

Structural system	Load [kN/m] ²
System n°1	5.82
System n°2	10.76
System n°2 with contact modelling	19.15

5.6 Conclusions

In this chapter, an alternative structural system was investigated, in order to address the weaknesses of the initial structural system developed for double-layered double-curved timber plate structures (see Chapter 3). In the proposed design, the continuous failure paths, which were appearing at the bottom stretched layer of the initial system, were avoided by organising boxes in staggered rows, according to a shifted herringbone pattern. Methods were provided to integrate the generation of the suggested pattern in the design framework, introduced in Chapter 2, and apply it to full arches. The two systems were compared for small assemblies of 25 to 28 boxes, using the semi-rigid spring model developed in Chapter 2.

Based on numerical investigations, the assembly pattern was shown to have a significant influence on the studied structure's performance. The proposed design, involving additional abutment areas of the boxes, was shown to enhance the interlocking assembly of the plates and, therefore, the stiffness of the structural system by 76 %. Tensile forces in the connections were also significantly reduced, increasing the distributed load to reach the maximum load-carrying capacity of the connections in tension to 85 %. Moreover, abutment areas were shown to have the potential to further enhance the structural performance of the alternative system. The shifted herringbone pattern would have to be applied on full arches to accurately assess their structural improvement.

The study highlights the potential for the structural optimisation of double-layered double-curved timber plate shells and shows the importance of integrating structural analysis in the design and fabrication workflow to design efficient structural systems, taking into account fabrication constraints, as well as the ease of cut and assembly.

6 3D Finite Element Model for Wood-Wood Connections

This Chapter is based on: A. C. Nguyen, J. Gamarro, J. F. Bocquet and Y. Weinand, Numerical Investigations on the Shear Behaviour of Digitally Produced Wood-Wood Connections, manuscript in preparation for publication.

6.1 Introduction

As highlighted in Chapters 3 and 4, the mechanical behaviour of wood-wood connections highly influences the global behaviour of timber plate structures and therefore needs to be implemented in global numerical models. In particular, their stiffness and load-carrying capacity are important mechanical properties necessary to reliably predict the behaviour of the structure [90]. They are usually retrieved from experimental tests performed on the connections, since simplified analytical models are still very limited. However, several numerical models have also been developed to predict the mechanical behaviour of timber connections but mostly for standard joining techniques using mechanical fasteners. In fact, numerical modelling is largely used for complex structural analysis problems when analytical solutions are either cumbersome or non-existent. In addition, numerical models have the potential to replace expensive and time-consuming experimental tests, for which a limited number of parameter combinations can be tested. Nonetheless, timber modelling remains particularly arduous because of its asymmetric mechanical behaviour in tension and compression, characterised by brittle and ductile failure modes respectively, as well as largely different mechanical properties parallel- and perpendicular-to-grain.

Several research studies have focused on the numerical modelling of wood-wood connections, usually in the context of traditional timber frame structures. Two-dimensional (2D) finite element (FE) models have been applied to different types of carpentry joints, with and without mortise-and-tenon joints, considering Hill and Tsai-Wu criteria for ductile and brittle problems

respectively [26, 71, 116]. Three-dimensional (3D) models have also been developed for straight or dovetail traditional mortise-tenon joints. In Koch et al. [44], a fracture criterion was defined for multimodal failure modes, namely in tension perpendicular-to-grain, shear and rolling shear, while timber's ductile behaviour was modelled based on the Hill yield criterion in Sha et al. [101]. Rounded dovetail joints, more recently applied to timber frame structures, were also modelled based on the finite element method (FEM) using 3D solid elements. Reformulated Norris and Hashin failure criteria were applied by Tannert et al. [109], whereas modified Hill failure criteria were implemented by Xu et al. [121] to take wood damage evolution into account, in both cases for brittle failure modes. Regarding multiple dovetail joints, Sebera and Šimek [98] investigated the mechanical behaviour of furniture dovetail joints as used in traditional cabinetmaking through 3D models, with and without contact modelling. However, their study was limited as they were focusing on the influence of the Coulomb friction coefficient on the rotational stiffness and stress distribution.

Although investigations have been conducted on wood-wood connections, most numerical models have been developed for bolted and dowel-type steel-timber joints as they are more commonly used. For these connections, a large number of 2D and 3D numerical models have been built over the past decades, considering different modelling approaches for timber, whose modelling constitutes the main challenge, depending on the problem class of the post-elastic behaviour. For example, the classical theory of plasticity associated with Hill and Hoffman criteria have been used in continuum models for ductile problems, such as parallel-to-grain loading [18, 42, 122]. For brittle problems, such as perpendicular-to-grain loading, various models generally based on fracture mechanics have been built [4, 11, 96]. A probabilistic strength criterion based on a Weibull distribution has also been used by Moses et al. [64] within a continuum framework. Additionally, discrete lattice elements models have been developed [76]. However, since different failure mechanisms can occur in timber, combined approaches have also been used in multi-surface plasticity models. In particular, Sandhaas [88] has developed a model based on continuum damage mechanics to combine ductile and brittle failure modes for timber joints with slotted-in steel plates. Roche et al. [85] have applied this model to multiple tab-and-slot joints (MTSJ) with open slots made of spruce laminated veneer lumber (LVL). Their study was limited to the analysis of the semi-rigid moment-resisting behaviour of MTSJ. Compared to experimental test results, the rotational stiffness was found to be underestimated by the model and the behaviour in closing could not be predicted.

In this chapter, the model based on continuum damage mechanics initially developed by Sandhaas [88] and subsequently adapted by Roche et al. [85] for MTSJ is investigated with the objective of predicting the semi-rigid behaviour of digitally fabricated wood-wood connections. The material model is evaluated based on shear load tests performed through-tenon wood-wood connections (TT), considering different engineered wood products. Experimental materials and methods are presented in Section 6.2 and the numerical model is detailed in Section 6.3. Results of experimental and numerical investigations are then compared in Section 6.4.

6.2 Experimental Tests¹

6.2.1 Materials

Investigations on TT wood-wood connections were carried out on a series of commonly used engineering wood products illustrated in Figure 6.1, namely (1) and (1') Kronolux oriented strand board (OSB) type 3 panels (Kronospan, Jihlava, Czech Republic), (2) and (3) Kerto[®] laminated veneer lumber (LVL) Q-panels (Metsä Wood, Espoo, Finland), (4) BauBuche Q LVL panels (Pollmeier Massivholz, Creuzburg, Deutschland) and (5) dold[®] cross-laminated timber (CLT) panels (Dold Holzwerke, Buchenbach, Germany). Their characteristics, retrieved from the products certificates and technical sheets [87, 117, 9, 73, 19], are listed in Table 6.1.

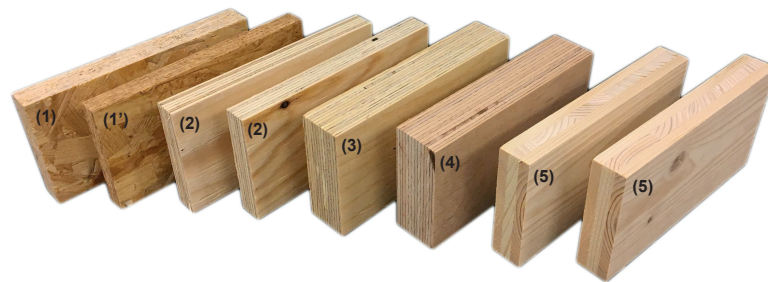


Figure 6.1 – Materials used for investigations on TT connections: (1) OSB type 3 25 mm (1') OSB type 3 18 mm (2) Spruce LVL 21 mm (3) Spruce LVL 39 mm (4) Beech LVL 40 mm (5) Spruce CLT 27 mm.

Table 6.1 – Characteristics of the materials used for investigations on TT connections.

ID	Type	Species	Thickness [mm]	Plies number	Lay-up	Lay-up thickness [mm]	Thickness tolerance [mm]
(1)	OSB 3	Spruce	25	3	–	-	+ - 0.8
(1')	OSB 3	Spruce	18	3	–	-	+ - 0.8
(2)	LVL	Spruce	21	7	– –	3 each	-1.03 +1.43
(3)	LVL	Spruce	39	13	– – –	3 each	-1.57 +1.97
(4)	LVL	Beech	40	14	– –	3 each ^a	+ - 1
(5)	CLT	Spruce	27	3	–	6.9/13.2/6.9	+ - 1

^a 2 mm were subtracted on the outer layers as a result from the finishing process

Certain choices of materials and panel thicknesses were made according to specific case studies using TT connections, such as the prefabricated standard timber elements recently developed for OSB panels [29] and the Annen Plus SA head office (case study of this thesis, described in Chapter 1, Section 1.3) for beech LVL. Additionally, spruce LVL and CLT

¹Experimental investigations were performed by the manuscript co-author, J. Gamarro.

were studied as they are widely distributed. Thicknesses were also chosen to obtain feasible joint configurations for the study of both single- and double-layered specimens, detailed in Subsection 6.2.3.

6.2.2 Experimental Setup

The experimental setup developed for shear loading tests on single TT connections is presented in Figure 6.2. It consisted in a custom rigid steel frame anchored inside a LFV-200 w+b universal static testing machine (walter+bai ag, Löhningen, Switzerland) with a maximum loading capacity of 200 kN. Specimens were positioned into the steel frame and a vertical load F was applied by the hydraulic jack on the specimen part with the mortise (5), through a 40 mm thick steel plate (1). The top of the tenon part (4) was rigidly fixed using a 15 mm thick steel plate (3), tightened with two bolts of 24 mm diameter on each side of the specimen (2). A 5 mm thick steel plate (6) was welded between the bolts, at their lower part, to prevent their lateral displacement. Additionally, a 40 mm thick beech LVL plate (7) was bolted to the setup to prevent the rotation of the tenon part. The position of the mortise part was maintained vertically with a 20 mm thick steel plate (8) and a steel bracket with 8 bolts of 12 mm diameter (11). The steel plate (8) was linked to the steel plate at the top of the tenon part (3) by two 12 mm diameter bolts (9) to stiffen the system laterally. Preliminary tests showed that a negligible lateral displacement of the experimental setup was measured by four linear variable differential transformers (LVDTs) mounted on the steel plates (3) and (8). Two oiled Teflon sheets (10) were placed between the steel plate (8) and the mortise part (5) to avoid friction between these parts. Two LVDTs were mounted on each side of specimens at the axis of the TT connection (12).

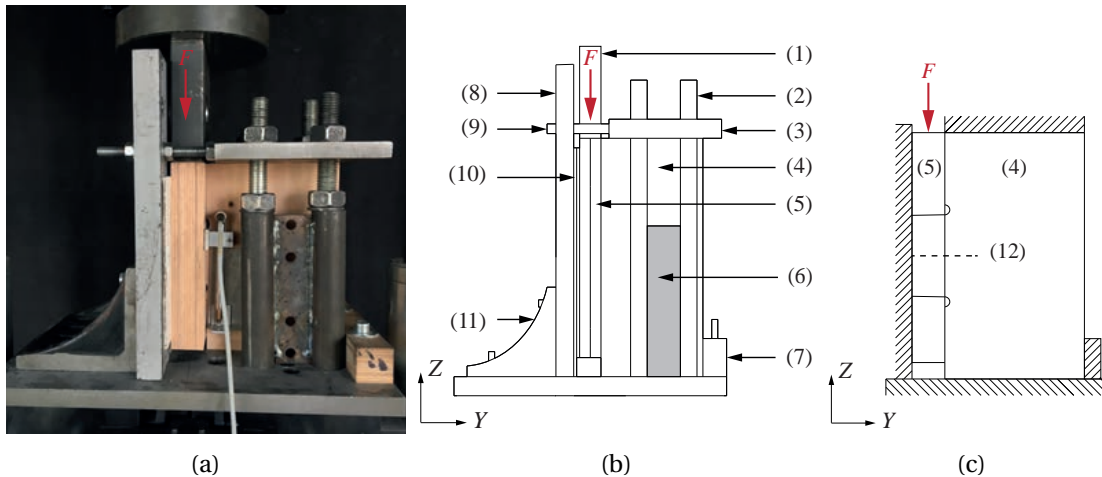


Figure 6.2 – Side view of the experimental shear setup: (a) Photograph (b) Technical drawing (1) Steel plate 40 mm (2) Bolt $\varnothing 24$ mm (3) Steel plate 15 mm (4) Specimen with tenon (5) Specimen with mortise (6) Steel plate 5 mm (7) Beech LVL 40 mm (8) Steel plate 20 mm (9) Bolt $\varnothing 12$ mm (10) Two oiled Teflon sheets (11) Steel bracket 20 mm with 8 bolts $\varnothing 12$ mm (c) Schematic drawing (12) LVDTs at the axis of the connection on each side of the specimen.

6.2.3 Specimens

Single- and double-layered joint configurations were studied, based on the construction system developed for prefabricated standard elements [30]. The characteristics of all specimens investigated are presented in Table 6.2, with corresponding geometrical parameters illustrated in Figure 6.3.

Table 6.2 – Characteristics of the 15 specimens studied, with corresponding geometrical parameters illustrated in Figure 6.3

ID	Material	Number of layers	l_t [mm]	h_t [mm]	h_m [mm]	w_t [mm]	w_m [mm]	t_t [mm]	t_m [mm]
T1-50	Spruce OSB 3	2	50	250	230	163	156	50	36
T1-65	Spruce OSB 3	2	65	250	230	163	156	50	36
T1-80	Spruce OSB 3	2	80	250	230	163	156	50	36
T2-50	Spruce LVL	2	50	250	230	169	160	42	42
T2-100	Spruce LVL	2	100	300	280	169	160	42	42
T2-150	Spruce LVL	2	150	350	330	169	160	42	42
T3-50	Spruce LVL	1	50	250	230	169	160	39	39
T3-100	Spruce LVL	1	100	300	280	169	160	39	39
T3-150	Spruce LVL	1	150	350	330	169	160	39	39
T4-50	Beech LVL	1	50	250	230	169	160	40	40
T4-100	Beech LVL	1	100	300	280	169	160	40	40
T4-150	Beech LVL	1	150	350	330	169	160	40	40
T5-50	Spruce CLT	2	50	250	230	169	160	54	54
T5-100	Spruce CLT	2	100	300	280	169	160	54	54
T5-150	Spruce CLT	2	150	350	330	169	160	54	54

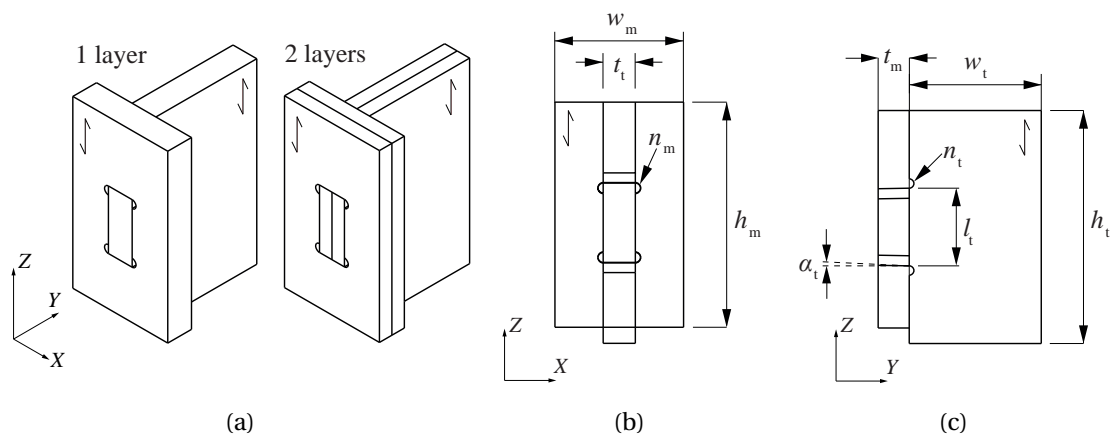


Figure 6.3 – Shear test specimens: (a) Axonometries of single- and double-layered TT specimens (b) Front view (c) Side view.

Three different tenon lengths l_t were studied for each material: 50, 100 and 150 mm for all specimens, except for OSB 3 samples for which lengths of 50, 65 and 80 mm were chosen, as the material is characterised by a lower compression strength. Bryant angles θ_1 , θ_2 and θ_3 defining the insertion vector of the joints, as described by Robeller [78] and illustrated in Chapter 1, Figure 1.5, were all set to 0° . The height of all specimens h_m was determined in order to avoid shear failure in the mortise. For the height of the tenon part h_t , 20 mm were added to allow sufficient space for vertical displacements during the tests. Widths w_m and w_t of the mortise and the tenon parts respectively were calculated to be at least three times larger than the tenon thickness t_t and the mortise thickness t_m respectively. Joints were designed with an insertion angle α_t of 1° to facilitate the assembly of the tenon and mortise parts, which can be difficult due to the thickness tolerance of each panel (see Table 6.1).

Tests were performed on 20 replicates of each specimen configuration, with the grain orientation parallel to the joint length. All samples were fabricated with a computer numerical control (CNC) machine using a Leitz[®] ID 240502 spiral router cutter Marathon (Höchsmann, Klipphausen, Germany) [37] with a diameter of 12 mm, a rotational speed of 18 000 rpm and a feed rate of 4.5 m/min. Notch diameters n_t and n_m of 13 mm were fixed for both parts. Before the tests, all specimens were conditioned in a normalised environment characterised by a temperature of 20°C and a relative humidity of 65 %, as prescribed in the standard ISO 554:1976 [39].

6.2.4 Loading Procedure

As the current ISO and EN standards do not include an experimental protocol for wood-wood connections in particular, experimental tests were performed following the loading procedure prescribed in the European Standard EN 26891 [24] for the determination of strength and deformation characteristics of timber joints with mechanical fasteners. The loading procedure is illustrated in Figure 6.4a. The estimated maximum load F_{est} was determined with preliminary tests performed for the 15 joint configurations. A load-controlled loading was first applied until 70 % of F_{est} . Displacement-controlled loading was then used with a constant slip rate of 0.01 mm/s, such that each test lasted approximately 10-15 minutes.

According to the standard EN 26891 [24], initial slip v_i and modified initial slip $v_{i,\text{mod}}$ can be defined as follows:

$$v_i = v_{04} \tag{6.1}$$

$$v_{i,\text{mod}} = 4/3(v_{04} - v_{01}) \tag{6.2}$$

with v_{04} and v_{01} defined as indicated on the idealised load-deformation curve illustrated in Figure 6.4b.

Additionally, three slip modulus can be subsequently defined, namely the initial slip modulus k_i , slip modulus k_s and slip modulus after first loading $k_{s,mod}$, as follows:

$$k_i = 0.4F_{\max} / v_i \quad (6.3)$$

$$k_s = 0.4F_{\max} / v_{i,mod} \quad (6.4)$$

$$k_{s,mod} = (0.4F_{\max} - 0.1F_{\max}) / (v_{24} - v_{21}) \quad (6.5)$$

with v_{24} and v_{21} defined as indicated on the idealised load-deformation curve illustrated in Figure 6.4b.

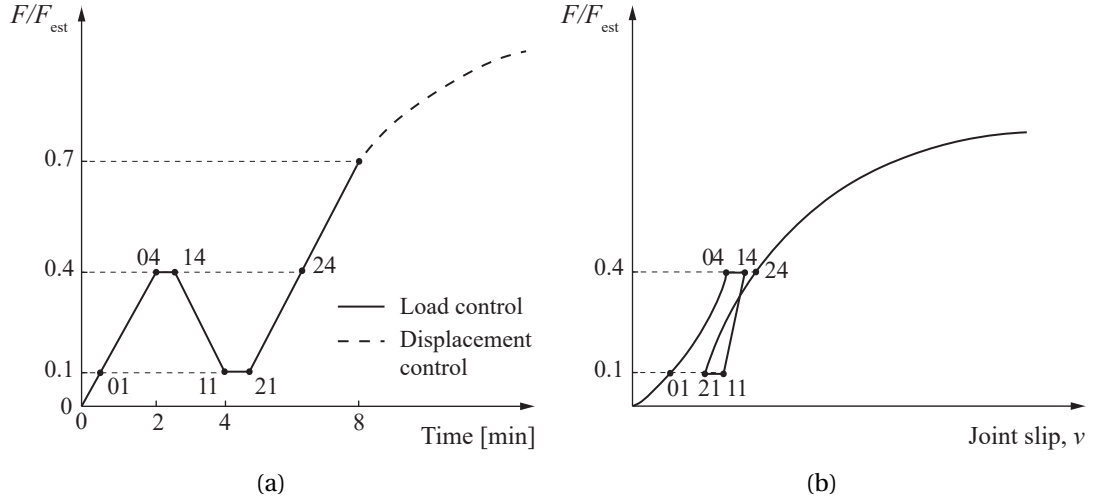


Figure 6.4 – Experimental protocol prescribed in EN 26891 [24]: (a) Loading procedure, determined according to the ratio between the load F and the estimated maximum load F_{est} (b) Idealised load-deformation curve.

6.3 Numerical Model

The numerical model proposed by Sandhaas [88] and based on continuum damage mechanics (CDM) was used to model the nonlinear behaviour of wood-wood connections. The CDM approach consists on modifying the stiffness matrix or its inverse, namely the compliance matrix, through specific damage parameters. The model was built in the finite element analysis software (FEA) AbaqusTM, version 6.12 (Dassault Systèmes, Vélizy-Villacoublay, France). The model generation was programmed using the Abaqus Scripting Interface in Python programming language. However, instead of generating the wood-wood connection geometry using a plugin built in the FEA software, the geometry was imported from the computer-aided design (CAD) software.

6.3.1 Material Model

Timber was modelled as a single orthotropic layer, as opposed to the multi-layered model applied by Roche et al. [85] for which each veneer layer was represented with its orientation (longitudinal layers at 0° and crosswise layers at 90°) with interfaces considered rigid. Material directions used in this study are indicated in Figure 6.5. The main direction 1 is the longitudinal direction of the fibres, parallel to the grain; the second 2 and third 3 directions, both perpendicular to the grain, are tangential and radial to the rings respectively.

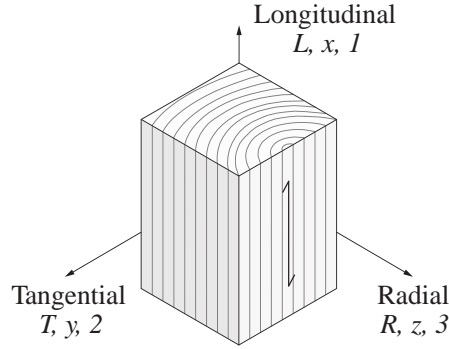


Figure 6.5 – Definition of the material directions: the main direction 1 is parallel to the grain; the second 2 and third 3 directions, both perpendicular to the grain, are tangential and radial to the rings respectively.

6.3.2 Continuum Damage Model

Principles of continuum damage mechanics can be explained according to the stiffness matrix or its inverse, namely the compliance matrix. Before damage occurs and for the remaining undamaged material, the material behaviour is described based on Hooke's law with strains $\boldsymbol{\varepsilon}$ expressed as function of the effective stresses $\boldsymbol{\sigma}^{\text{ef}}$, which are the stresses acting on the non-damaged material, and the elastic compliance matrix \mathbf{C}^{el} :

$$\boldsymbol{\varepsilon} = \mathbf{C}^{\text{el}} \boldsymbol{\sigma}^{\text{ef}} \quad (6.6)$$

The relationship defined in Equation 6.6 can be expressed as follows:

$$\begin{bmatrix} \varepsilon_{11} \\ \varepsilon_{22} \\ \varepsilon_{33} \\ 2\varepsilon_{12} \\ 2\varepsilon_{13} \\ 2\varepsilon_{23} \end{bmatrix} = \begin{bmatrix} \frac{1}{E_{11}} & \frac{-\nu_{12}}{E_{22}} & \frac{-\nu_{31}}{E_{33}} & 0 & 0 & 0 \\ \frac{-\nu_{12}}{E_{11}} & \frac{1}{E_{22}} & \frac{-\nu_{32}}{E_{33}} & 0 & 0 & 0 \\ \frac{-\nu_{31}}{E_{11}} & \frac{-\nu_{32}}{E_{22}} & \frac{1}{E_{33}} & 0 & 0 & 0 \\ 0 & 0 & 0 & \frac{1}{G_{12}} & 0 & 0 \\ 0 & 0 & 0 & 0 & \frac{1}{G_{13}} & 0 \\ 0 & 0 & 0 & 0 & 0 & \frac{1}{G_{23}} \end{bmatrix} \begin{bmatrix} \sigma_{11} \\ \sigma_{22} \\ \sigma_{33} \\ \sigma_{12} \\ \sigma_{13} \\ \sigma_{23} \end{bmatrix} \quad (6.7)$$

In FEA software packages, the inverse on the compliance matrix has to be implemented, namely the elastic stiffness matrix \mathbf{D}^{el} , which is defined as:

$$\mathbf{D}^{\text{el}} = \begin{bmatrix} (1 - \nu_{23}\nu_{32})\Delta E_{11} & (\nu_{21} + \nu_{31}\nu_{23})\Delta E_{11} & (\nu_{31} + \nu_{21}\nu_{32})\Delta E_{11} & 0 & 0 & 0 \\ (\nu_{12} + \nu_{13}\nu_{32})\Delta E_{22} & (1 - \nu_{13}\nu_{31})\Delta E_{22} & (\nu_{32} + \nu_{31}\nu_{12})\Delta E_{22} & 0 & 0 & 0 \\ (\nu_{13} + \nu_{12}\nu_{23})\Delta E_{33} & (\nu_{23} + \nu_{21}\nu_{13})\Delta E_{33} & (1 - \nu_{12}\nu_{21})\Delta E_{33} & 0 & 0 & 0 \\ 0 & 0 & 0 & G_{12} & 0 & 0 \\ 0 & 0 & 0 & 0 & G_{13} & 0 \\ 0 & 0 & 0 & 0 & 0 & G_{23} \end{bmatrix} \quad (6.8)$$

with

$$\Delta = \frac{1}{(1 - \nu_{12}\nu_{21} - \nu_{13}\nu_{31} - \nu_{23}\nu_{32} - 2\nu_{12}\nu_{23}\nu_{31})} \quad (6.9)$$

As orthotropic material properties were considered, both stiffness and compliance matrices are symmetric and the following equation can therefore be defined:

$$\frac{\nu_{ij}}{E_{ii}} = \frac{\nu_{ji}}{E_{jj}} \quad \text{for } i = 1, 2, 3 \text{ and } i \neq j \quad (6.10)$$

The constitutive orthotropic damage model involves nine independent damage parameters, namely $d_{c,11}$, $d_{t,11}$, $d_{c,22}$, $d_{t,22}$, $d_{c,33}$, $d_{t,33}$, d_{12} , d_{13} and d_{23} , with the indices t and c corresponding to damage occurring in tension and compression respectively. Since compression and tension are triggered by the same normal stress components σ_{ii} , damage variables in tension and compression can be combined using the Macaulay operator defined by Equation 6.11:

$$\langle a \rangle = \frac{a + |a|}{2} \quad (6.11)$$

such that the damage parameters d_{11} , d_{22} and d_{33} can be defined as follows:

$$d_{ii} = d_{t,ii} \frac{\langle \sigma_{ii} \rangle}{|\sigma_{ii}|} + d_{c,ii} \frac{\langle -\sigma_{ii} \rangle}{|\sigma_{ii}|} \quad \text{for } i = 1, 2, 3 \quad (6.12)$$

The number of damage parameters introduced in the damage compliance matrix \mathbf{C}^{dam} is then reduced to six, namely d_{11} , d_{22} , d_{33} , d_{12} , d_{13} and d_{23} . When the material is damaged, strains $\boldsymbol{\varepsilon}$ are expressed as function of the nominal stresses $\boldsymbol{\sigma}$ and the damaged compliance matrix \mathbf{C}^{dam} :

$$\boldsymbol{\varepsilon} = \mathbf{C}^{\text{dam}} \boldsymbol{\sigma} \quad (6.13)$$

with

$$\mathbf{C}^{\text{dam}} = \begin{bmatrix} \frac{1}{(1-d_{11})E_{11}} & \frac{-\nu_{21}}{E_{22}} & \frac{-\nu_{31}}{E_{33}} & 0 & 0 & 0 \\ \frac{-\nu_{12}}{E_{11}} & \frac{1}{(1-d_{22})E_{22}} & \frac{-\nu_{32}}{E_{33}} & 0 & 0 & 0 \\ \frac{-\nu_{13}}{E_{11}} & \frac{-\nu_{23}}{E_{22}} & \frac{1}{(1-d_{33})E_{33}} & 0 & 0 & 0 \\ 0 & 0 & 0 & \frac{1}{(1-d_{12})G_{12}} & 0 & 0 \\ 0 & 0 & 0 & 0 & \frac{1}{(1-d_{13})G_{13}} & 0 \\ 0 & 0 & 0 & 0 & 0 & \frac{1}{(1-d_{23})G_{23}} \end{bmatrix} \quad (6.14)$$

When the material is undamaged, damage parameters are equal to zero. They start increasing when damage is initiated such that components of the compliance matrix C_{ijkl} are reduced. Complete damage occurs when damage parameters are equal to 1. However, to avoid numerical instabilities, a maximum value of 0.999995 was implemented in the numerical model.

6.3.3 Failure Modes

Sandhaas [88] defined eight failure criteria to determine when material damage occurs, with eight corresponding failure modes F_M expressed according to stresses σ_{ij} and strengths f_{ij} . Among them, three are ductile (in compression) and five are brittle (in tension and shear). For all failure modes, damage is initiated when $F_M > 1$.

Ductile Failure Modes

- Failure criterion I - $F_{c,1}$:

For $\sigma_{11} < 0$, corresponding to failure in compression parallel-to-grain and associated with the damage variable $d_{c,11}$,

$$F_{c,1} = \frac{-\sigma_{11}}{f_{c,11}} \leq 1 \quad (6.15)$$

- Failure mode II - $F_{c,2}$:

For $\sigma_{22} < 0$, corresponding to failure in compression perpendicular-to-grain in tangential direction and associated with the damage variable $d_{c,22}$,

$$F_{c,2} = \frac{-\sigma_{22}}{f_{c,22}} \leq 1 \quad (6.16)$$

- Failure mode III - $F_{c,33}$:

For $\sigma_{33} < 0$, corresponding to failure in compression perpendicular-to-grain in radial

direction and associated with the damage variable $d_{c,33}$,

$$F_{c,3} = \frac{-\sigma_{33}}{f_{c,33}} \leq 1 \quad (6.17)$$

Brittle Failure Modes

- Failure mode IV - $F_{t,1}$:

For $\sigma_{11} \geq 0$, corresponding to failure in tension parallel-to-grain and associated with damage variable $d_{t,11}$,

$$F_{t,1} = \frac{\sigma_{11}}{f_{t,11}} \leq 1 \quad (6.18)$$

- Failure mode V - $F_{t,2}$:

For $\sigma_{22} \geq 0$, corresponding to failure in tension perpendicular-to-grain in tangential direction and associated with damage variables $d_{t,22}$, d_{12} , d_{23} ,

$$F_{t,2} = \frac{(\sigma_{22})^2}{(f_{t,22})^2} + \frac{(\sigma_{12})^2}{(f_{12})^2} + \frac{(\sigma_{23})^2}{(f_{23})^2} \leq 1 \quad (6.19)$$

- Failure mode VI - $F_{t,3}$:

For $\sigma_{33} \geq 0$, corresponding to failure in tension perpendicular-to-grain in radial direction and associated with damage variables $d_{t,33}$, d_{13} , d_{23} ,

$$F_{t,3} = \frac{(\sigma_{33})^2}{(f_{t,33})^2} + \frac{(\sigma_{13})^2}{(f_{13})^2} + \frac{(\sigma_{23})^2}{(f_{23})^2} \leq 1 \quad (6.20)$$

- Failure mode VII: $F_{v,2}$

Shear failure, tangential if $\sigma_{22} < 0$ (brittle), associated with damage variables d_{12} and d_{23} ,

$$F_{v,2} = \frac{(\sigma_{12})^2}{(f_{12})^2} + \frac{(\sigma_{23})^2}{(f_{23})^2} \leq 1 \quad (6.21)$$

- Failure mode VIII: $F_{v,3}$

Shear failure, radial if $\sigma_{33} < 0$ (brittle), associated with damage variables d_{13} and d_{23} ,

$$F_{v,3} = \frac{(\sigma_{13})^2}{(f_{13})^2} + \frac{(\sigma_{23})^2}{(f_{23})^2} \leq 1 \quad (6.22)$$

6.3.4 Damage Evolution

Each of the eight failure modes F_M were associated with one or several damage parameters. Since different failure modes can trigger shear damage variables, the latter need to be

superposed according to Equations 6.23, 6.24 and 6.25 for longitudinal and rolling shear:

$$d_{12} = 1 - (1 - d_{12,V}) \cdot (1 - d_{12,VII}) \quad (6.23)$$

$$d_{13} = 1 - (1 - d_{13,VI}) \cdot (1 - d_{13,VIII}) \quad (6.24)$$

$$d_{23} = 1 - (1 - d_{23,V}) \cdot (1 - d_{23,VI}) \cdot (1 - d_{23,VII}) \cdot (1 - d_{23,VIII}) \quad (6.25)$$

Damage parameters and failure criteria were linked through a history parameter κ_M , tracking the loading history and defined as follows:

$$\kappa_M = \max\{F_M, 1\} \quad (6.26)$$

Two linear damage evolution laws, functions of the history parameter κ_M , were used by Sandhaas [88]: an elastic perfectly plastic behaviour was considered for ductile failure modes (see Figure 6.6a) and a fracture energy based tension softening was defined for brittle failure modes (see Figure 6.6b). The softening behaviour was characterised according to the fracture energy, which is the energy required to form a crack and is used in fracture mechanics. Damage parameters, defined according to these laws, were expressed as Equations 6.27 and 6.28 for ductile and brittle failure modes respectively:

$$d_M = 1 - \frac{1}{\kappa_M} \quad (6.27)$$

$$d_M = 1 - \frac{f_M^2 - \frac{2g_{f,ij}E_{ij}}{\kappa_M}}{f_M^2 - 2g_{f,ij}E_{ij}} \quad (6.28)$$

with g_f the characteristic fracture energy, used to reduce mesh dependency and defined as the ratio between the fracture energy G_f and the characteristic element length h , referred to as CELENT in AbaqusTM:

$$g_f = \frac{G_f}{h} \quad (6.29)$$

In this study, a square root was added on the history parameter associated with brittle failure modes V to VIII to prevent a too slow increase of the damage variable, since the corresponding failure functions were defined by the sum of the squares of stresses (see Equations 6.19 to 6.22). This modification was already done by Roche et al. [85]; however, in their study, it was applied to all damage parameters associated with brittle failure modes. The damage parameters associated with failure modes V to VIII exclusively were thus:

$$d_M = 1 - \frac{f_M^2 - \frac{2g_{f,ij}E_{ij}}{\sqrt{\kappa_M}}}{f_M^2 - 2g_{f,ij}E_{ij}} \quad (6.30)$$

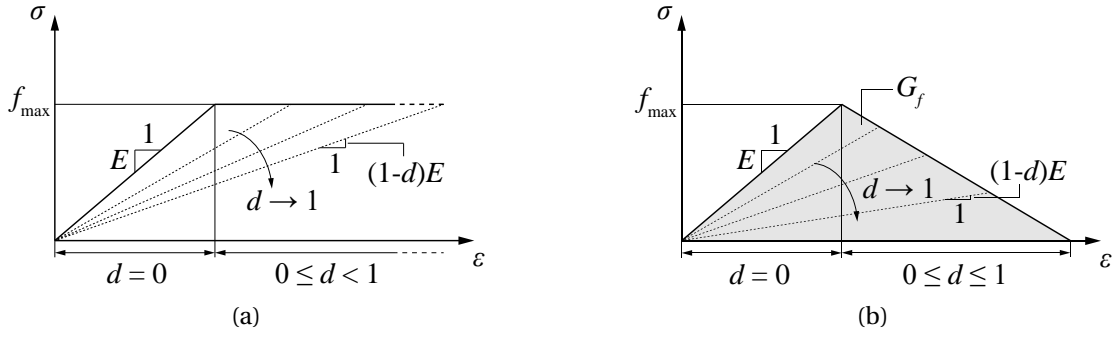


Figure 6.6 – Damage evolution laws: (a) Elastic perfectly plastic for damage parameters associated with ductile failure modes (b) Fracture energy based tension softening for damage parameters associated with brittle failure modes.

6.3.5 Subroutine Algorithm

As for the model developed by Roche et al. [85] for the semi-rigid moment-resisting behaviour of MTSJ, the continuum damage model was implemented using a user defined field USDFLD subroutine. Its algorithm for the continuum damage model is summarised in Figure 6.7.

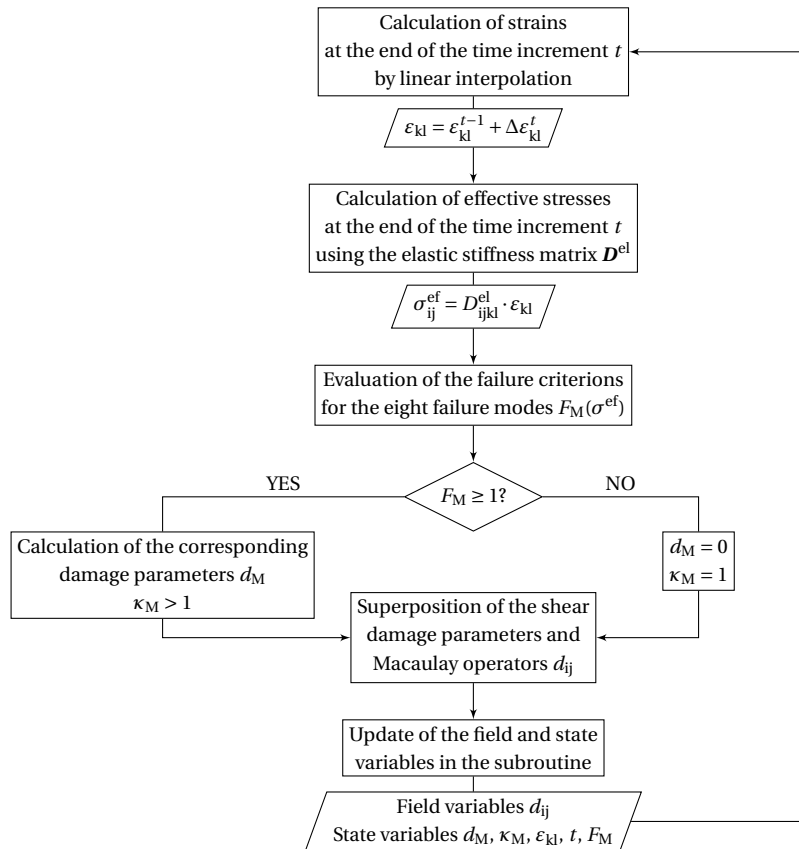


Figure 6.7 – Flowchart illustrating the algorithm of the USDFLD subroutine for the continuum damage model.

Orthotropic material properties E_{ii} , G_{ij} and ν_{ij} were defined as field dependent with the six damage parameters d_{ij} corresponding to the six field variables f_1 , f_2 , f_3 , f_4 , f_5 and f_6 , such that:

$$E_{ii,t} = E_{ii,t-1} \cdot (1 - f_i) \quad \text{with} \quad f_i = d_{ii} \quad \text{for} \quad i = 1, 2, 3 \quad (6.31)$$

$$G_{12,t} = G_{12,t-1} \cdot (1 - f_4) \quad \text{with} \quad f_4 = d_{12} \quad (6.32)$$

$$G_{13,t} = G_{13,t-1} \cdot (1 - f_5) \quad \text{with} \quad f_5 = d_{13} \quad (6.33)$$

$$G_{23,t} = G_{23,t-1} \cdot (1 - f_6) \quad \text{with} \quad f_6 = d_{23} \quad (6.34)$$

$$\nu_{12,t} = \nu_{12,t-1} \cdot (1 - f_1) \quad \text{with} \quad f_1 = d_{11} \quad (6.35)$$

$$\nu_{13,t} = \nu_{13,t-1} \cdot (1 - f_1) \quad \text{with} \quad f_1 = d_{11} \quad (6.36)$$

$$\nu_{23,t} = \nu_{23,t-1} \cdot (1 - f_2) \quad \text{with} \quad f_3 = d_{33} \quad (6.37)$$

$$(6.38)$$

Nonlinear geometric analysis was performed with initial and maximum time increments of 0.001 and 0.1 respectively. The load was applied with displacement-control, imposing a displacement of 1.5 times the maximum slip $v_{i,\max}$ for all numerical simulations.

6.3.6 Contact Modelling

Contacts between the different parts of the specimen were modelled by defining surface-to-surface interactions in AbaqusTM. A Coulomb friction model was considered for the tangential behaviour, while the normal behaviour was implemented with a "hard" contact relationship, which implies that no transfer of tensile forces occurs between the two surfaces and the penetration of the slave surface into the master surface is minimised. Friction coefficient values of $\mu_{\text{edge}} = 0.26$ edgewise and $\mu_{\text{flat}} = 0.40$ flatwise, provided by the manufacturer of Kerto[®] Q panels [117], were considered for all materials, it was found that variations of the friction coefficient have a minor influence. In fact, variations of μ_{edge} between values of 0.1 and 0.4 were found to have an influence below 2 % and 1 % on the displacements and stresses respectively. Contacts implemented in the model are illustrated in Figure 6.8 for the specimen T2-50. Contacts ① between the faces of the tenon and the internal faces of the mortise in the YZ plane, ② between the long edge of the tenon part and the closest larger face of the mortise part, as well as ③ between the bottom face of the tenon in the XY plane and the corresponding internal face of the mortise (see Figure 6.8a) were modelled considering a friction coefficient $\mu_{\text{edge}} = 0.26$ and with separation allowed after contact. A surface-to-surface interaction with a friction coefficient of $\mu_{\text{edge}} = 0.26$ with no separation allowed after contact was implemented ④ between the loaded surface of the tenon part in the plane XY and the corresponding internal face of the mortise in contact (see Figure 6.8b). For two-layered specimens, a surface-to-surface interaction was also defined considering a friction coefficient $\mu_{\text{flat}} = 0.40$ and allowing separation after contact between the surfaces of the mortise panels and of the tenon panels in contact, ⑤ and ⑥ respectively in Figure 6.8c.

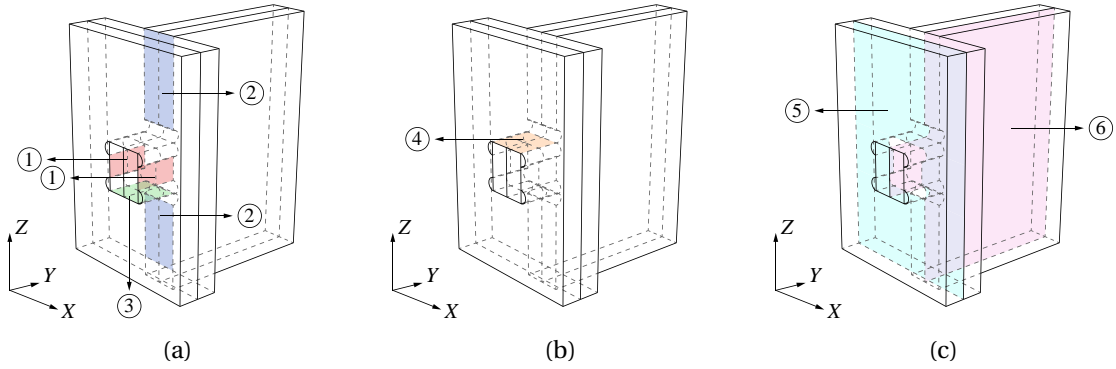


Figure 6.8 – Contact modelling using surface-to-surface interactions illustrated for specimen T2-50: (a) Friction coefficient $\mu_{\text{edge}} = 0.26$ with separation allowed after contact for the surfaces of the tenon and mortise parts ①, ② and ③ (b) Friction coefficient $\mu_{\text{edge}} = 0.26$ with no separation allowed after contact between the loaded face of the tenon part and the corresponding face of the mortise part ④ (c) For two-layered specimens, friction coefficient $\mu_{\text{flat}} = 0.40$ with separation allowed between the panels of the mortise part ⑤ and the tenon part ⑥.

6.3.7 Mesh

Linear hexahedral elements with reduced integration C3D8R were used. A mesh convergence study was carried out on the T3-50 specimen with mesh sizes varying from 10 to 2 mm with steps of 1 mm, considering the middle of the linear range between 10 and 40 % of F_{max} , being 25 % of F_{max} . Results of the mesh convergence study are presented in Figure 6.9, in which the total CPU time indicated corresponds to the time obtained using a Lenovo Intel® Core™ i7-4800MQ CPU @ 2.7GHz with 16 GB of RAM 1600 MHz (Lenovo Group Limited, Beijing, China). Vertical displacements were shown to converge (see Figure 6.9a), whereas increasing maximum shear stress values were obtained for decreasing mesh element sizes (see Figure 6.9b).

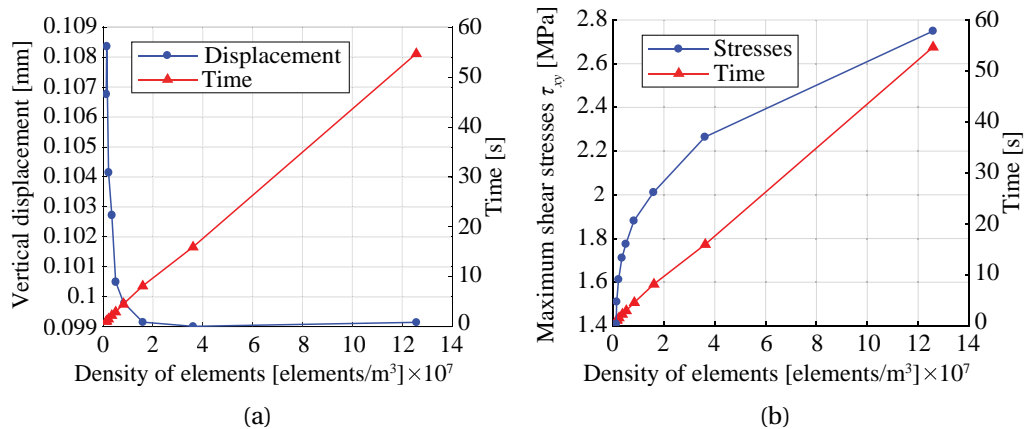


Figure 6.9 – Mesh convergence study performed for specimen T3-50 under a load of 25 % F_{max} : (a) Vertical displacements converge (b) Maximum shear stresses do not converge.

The non-convergence of stresses is explained by the presence of singularity points with theoretically infinite stresses at the notches of the connections. Indeed, both normal and shear stresses present increasingly high values at the position of the notches when the mesh element size is reduced. This can be observed in Figure 6.10, representing the stresses over the height of the sample along a line passing through the notches (dotted line). These areas were thus avoided for the interpretation of numerical results and the smallest mesh was thus chosen, adopting a refined mesh strategy to reduce the computational time. It was found that a refined mesh element size of 2 mm at the vicinity of the tenon and a coarse mesh element size of 16 mm away from this region of interest was leading to a difference of vertical displacement of 1 % while reducing the total CPU time by 85 %. The resulting mesh is illustrated in Figure 6.11 for the T3-50 specimen.

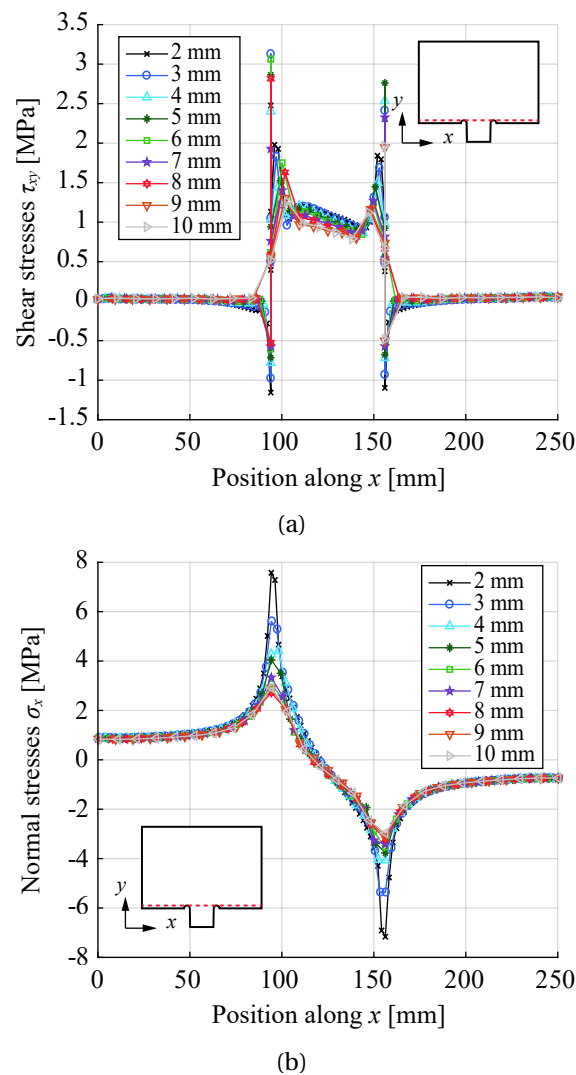


Figure 6.10 – Stresses along a path passing through the notches (dotted line), which represent singularity points with theoretically infinite stresses, for mesh sizes varying from 10 to 2 mm with steps of 1 mm: (a) Shear stresses (b) Normal stresses.

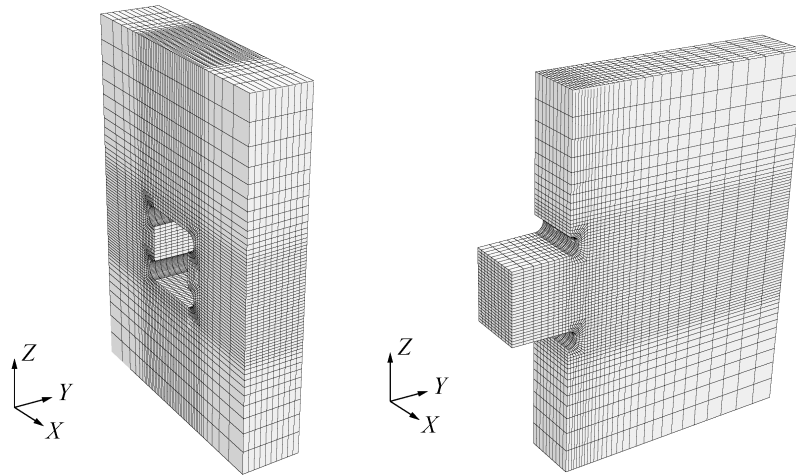


Figure 6.11 – Mesh for the sample T3-50 - Refined mesh element size of 2 mm at the vicinity of the tenon and coarse mesh element size of 16 mm away from this region of interest.

6.3.8 Material Properties

Mean values of material properties were implemented in the model, such that a direct comparison between experimental tests and numerical simulations could be made. Following a simplified approach, material properties with parameters X were considered as following a normal distribution characterised by a mean μ and a standard deviation σ (see Figure 6.12). Based on the coefficient of variation c_v , defined by Equation 6.39, and considering the 5 % characteristic fractile factor $k_\infty = 1.64$ for an infinite number of experiments, the mean values were defined from the characteristic values $X_{k,\text{inf}}$ with Equation 6.40. Similarly, the upper bounds $X_{k,\text{sup}}$ were derived from the characteristic values $X_{k,\text{inf}}$ with Equation 6.41.

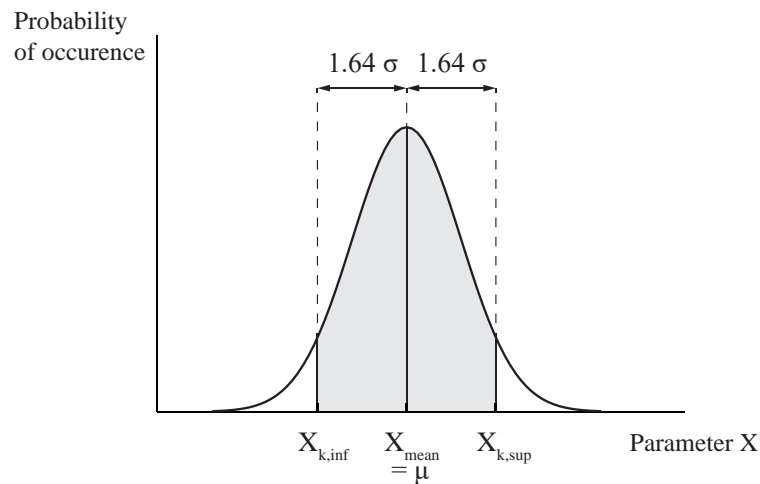


Figure 6.12 – Normal distribution with mean μ and a standard deviation σ for material property parameters X .

$$c_v = \frac{\sigma}{\mu} = \frac{\sigma}{X_{\text{mean}}} \quad (6.39)$$

$$X_{\text{mean}} = \frac{X_{k,\text{inf}}}{1 - 1.64c_v} \quad (6.40)$$

$$X_{k,\text{sup}} = \frac{1 + 1.64c_v}{1 - 1.64c_v} \cdot X_{k,\text{inf}} \quad (6.41)$$

The coefficient of variation was determined as approximately equal to $c_v = 0.1$ for spruce LVL, comparing characteristic and mean values of elastic modulus from the Kerto[®] Q panel certificate [117]. A coefficient of variation $c_v = 0.1$ was therefore considered for LVL and CLT materials. For OSB, the 5 % characteristic fractile factor defined in the standard EN 12369 as equal to 0.85 times the mean value was considered [22].

In this model, the material was represented by a single layer, as opposed to the multilayer approach used by Roche et al. [85] for the different veneer layers of spruce LVL. The goal of this model was to predict the behaviour of wood-wood connections with a design approach, using the values from the manufacturer instead of calibrating the numerical model with material parameters. Material properties were therefore retrieved directly from the panels certificates for LVL and CLT [117, 9, 19], while material properties from the standard EN 12369 [22] were considered for OSB 3.

Elastic Properties

Mean values of elastic material properties for each material studied are presented in Table 6.3. Poisson's ratio values for OSB, beech LVL and spruce CLT, not provided by the manufacturers, were taken from literature for OSB, beech and spruce respectively [29, 33, 28].

Table 6.3 – Elastic properties (mean values) [117, 9, 33, 19].

Property	Symbols	Material					Units
		(1), (1')	(2)	(3)	(4)	(5)	
Density	ρ_k	550	480	480	730	480	kg/m ³
Elastic modulus // to grain	$E_{0,\text{mean}}, E_{11}$	3800	10 000	10 500	13 200	5800	MPa
Elastic modulus \perp to grain, edgewise	$E_{90,\text{edge,mean}}, E_{22}$	3000	2400	2400	2200	5500	MPa
Elastic modulus \perp to grain, flatwise	$E_{90,\text{flat,mean}}, E_{33}$	1980	130	130	2200	1600	MPa
Shear modulus edgewise	$G_{0,\text{edge,mean}}, G_{12}$	1080	600	600	820	600	MPa
Shear modulus flatwise, // to grain	$G_{0,\text{flat,mean}}, G_{13}$	50	60	120	430	60	MPa
Shear modulus flatwise, \perp to grain	$G_{90,\text{flat,mean}}, G_{23}$	50	22	22	430	60	MPa
Poisson's ratio 12	ν_{12}	0.25	0.09	0.09	0.365	0.467	-
Poisson's ratio 13	ν_{13}	0.25	0.85	0.85	0.464	0.372	-
Poisson's ratio 23	ν_{23}	0.25	0.68	0.68	0.726	0.245	-

The influence of Poisson's ratio values ν_{12} , ν_{13} and ν_{23} was investigated for the T3-50 specimen by comparing simulations using different sets of Poisson's ratios values found in literature for spruce and spruce LVL with the results obtained with values provided by the supplier for

Kerto[®] Q panels [117]. The values considered, their references, most of which were listed in Sandhaas' thesis [88], and their influence on the stiffness of the connection are presented in Table 6.4. They were found to have no significant influence on the results with average variations on the stiffness of $+0.37\% \pm 0.51\%$.

Table 6.4 – Poisson's ratio values from literature for spruce and spruce LVL.

Reference	ν_{12} [-]	ν_{13} [-]	ν_{23} [-]	Δk [%]
Kerto [®] Q [117]	0.09	0.85	0.68	-
Kerto [®] S [117], as used by Roche et al. [85]	0.61	0.6	0.5	+0.33
Kollmann and Côté [45] (<i>Picea abies</i>)	0.53	0.43	0.24	+0.24
Neuhaus [67] (<i>Picea abies</i>)	0.554	0.41	0.311	+0.05
Wood Handbook [28] (<i>Picea sitchensis</i>)	0.467	0.372	0.245	+1.25
Blaß and Bejtka [8]	0.511	0.511	0.203	-0.03

Mechanical Properties

Characteristic values of strength properties are presented in Table 6.5 for each material studied. Since the value for tensile strength perpendicular-to-grain flatwise, corresponding to the interlaminar resistance, was not provided in most panel certificates, transversal isotropy was considered for this property such that $f_{t,33} = f_{t,22}$. This assumption is frequently made for timber modelling considering directions parallel- and perpendicular-to-grain only since differences between values in both radial and tangential directions are small compared to the longitudinal direction [116, 71].

Table 6.5 – Mechanical properties (characteristic values) in MPa [117].

Property	Symbols	Material					
		(1)	(1')	(2)	(3)	(4)	(5)
Tensile strength // to grain	$f_{t,0,k}$, $f_{t,11}$	9.4	9	19	26	51	8.4
Compressive strength // to grain	$f_{c,0,k}$, $f_{c,11}$	15.4	14.8	19	26	53.3	11.5
Tensile strength \perp to grain	$f_{t,90,edge,k}$, $f_{t,22}$	7	6.8	6	6	8	8
Compressive strength \perp to grain	$f_{c,90,edge,k}$, $f_{c,22}$	12.7	12.4	9	9	19	11.1
Tensile strength \perp to grain	$f_{t,90,flat,k}$, $f_{t,33}$	7	6.8	-	-	-	-
Compressive strength \perp to grain	$f_{c,90,flat,k}$, $f_{c,33}$	10	10	2.2	2.2	13	11.1
Longitudinal shear strength	$f_{v,0,edge,k}$, f_{12}	6.8	6.8	4.5	4.5	7.8	2.7
Longitudinal shear strength	$f_{v,0,flat,k}$, f_{13}	1	1	1.3	1.3	3.8	2.7
Rolling shear strength	$f_{v,90,flat,k}$, f_{23}	1	1	0.6	0.6	3.8	2.7

Fracture energy values implemented in the model were retrieved from Sandhaas [88] and are presented in Table 6.6. These values influence the softening behaviour, as illustrated in Figure 6.6b.

The influence of mechanical properties were assessed similarly to the study performed by Sandhaas [88], by modifying the strength and fracture energy values perpendicular to grain

Table 6.6 – Fracture energy values in N/mm for spruce and beech [88].

Property	Mnemo	Spruce	Beech
Fracture energy tension // to grain	$G_{f,11}$	6.0	10.0
Fracture energy tension \perp to grain	$G_{f,22}$	0.5	0.71
Fracture energy tension \perp to grain	$G_{f,33}$	0.5	0.71
Fracture energy longitudinal shear	$G_{f,12}$	1.2	1.2
Fracture energy longitudinal shear	$G_{f,13}$	1.2	1.2
Fracture energy rolling shear	$G_{f,23}$	0.6	0.6

to the maximum values, parallel to grain. Values in compression and tension perpendicular for strengths and fracture energy were found to have minor influence on the results with the same behaviour and maximum load variations of under 1 %. The properties in longitudinal shear lead to an increase of 39.38 %.

6.4 Results and Discussion

6.4.1 Analysis Procedure

In order to establish a relevant comparison between experimental and numerical investigations, the behaviour of the connections after the first loading was considered. For low values of slip, the behaviour can hardly be predicted as it can be influenced by a series of factors, such as material characteristics, moisture content, panel type, manufacturing parameters and assembly gaps. As illustrated in Figure 6.13a, a very stiff behaviour was observed at the beginning of the tests for all specimens. This high stiffness can be attributed to high internal friction forces in the connections that first need to be overcome. These friction forces are significant because of the absence of an assembly gap in the design of the connection. Additionally, as all samples are maintained in normalised conditions before the tests, an eventual swelling of wood could also further increase these forces. As a consequence, the initial slip modulus k_i (defined by Equation 6.3) increases with regard to the slip modulus k_s (defined by Equation 6.4). Furthermore, when the samples are loaded for the first time, the contact between the faces of the connections is accompanied by the crushing of tiny asperities at their surface, represented in Figure 6.13b, which influences the slip modulus k_s . The long-term behaviour of these effects is unknown and might only affect the first loading of the connection. As a result, they were discarded in the model and the behaviour of the connections after the first loading was considered. The slip modulus after the first loading $k_{s,mod}$ was computed considering the linear range between 10 and 40 % of the load-displacement curves after the first loading (as defined by Equation 6.5).

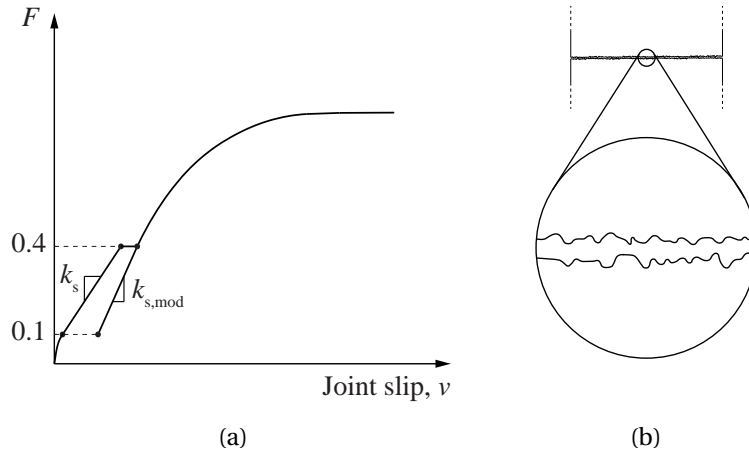


Figure 6.13 – (a) General shape of the load-displacement curves (b) Tiny asperities at the surface of the faces in contact that are crushed during the first loading.

For each of the five materials tested, results from experimental and numerical investigations were compared according to the two main parameters required in global numerical models, namely stiffness and capacity. In addition to the results obtained using mean material property values, simulations were performed for material properties $X_{k,inf}$ and $X_{k,sup}$, defined by the 5 % characteristic fractile factor of the normal distribution (see Figure 6.12), to obtain lower and upper bounds of the model respectively.

The shear stress distribution was subsequently analysed and the stress profile was plotted from nodal stress values along the tenon length on the expected failure path. For each material, the stress distribution appeared to be similar for all tenon lengths. The shear stress distribution was therefore illustrated for specimens with the longest tenon length l_t , as it corresponds to the highest number of mesh elements along the tenon length and hence, the highest number of nodal values from which the stress profile was plotted. The stress concentration factor K_t , defined as the ratio between the maximum shear stress obtained with the model τ_{xy} and the reference shear stress, was calculated to evaluate this concentration of stress such as performed by Villar-Garcia et al. [116]:

$$K_t = \frac{\tau_{xy}}{\tau_{ref}} = \frac{\tau_{xy}}{F/l_t \cdot l_t} \quad (6.42)$$

with the reference stress defined considering a uniform stress distribution along the path.

6.4.2 Spruce OSB 18/25 mm double-layered

The full load-displacement curves of the tests performed on double-layered OSB samples (T1) are presented in Figure 6.14 and the shear failures observed for specimens T1-50 and T1-65 are showed in Figure 6.15. For the specimen T1-80, failure in compression was observed before shear failure, as illustrated in Figure 6.16.

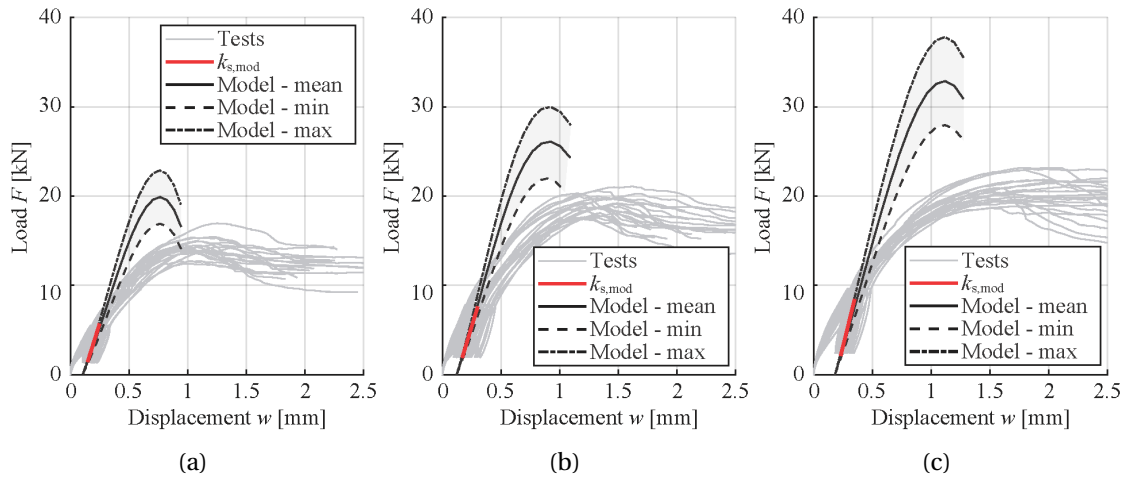


Figure 6.14 – Load-displacement curves of T1 specimens: (a) T1-50 (b) T1-65 (c) T1-80.

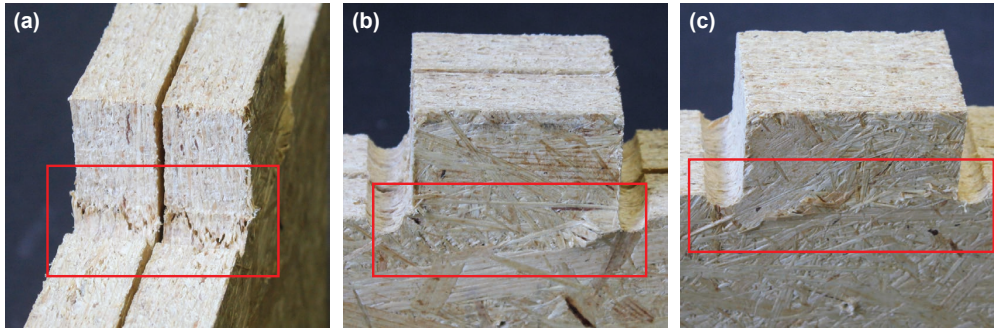


Figure 6.15 – Failure pictures of T1-50 specimens: (a) Side view (b) Front view (c) Back view.

The comparison between both the slip modulus and the maximum load, computed from the tests and predicted by the numerical model, is summarised in Table 6.7. Significant differences can be observed between the numerical model and the experimental tests. As seen in Figure 6.14, the numerical model predicted a brittle failure of the connections, while the tests highlighted their ductile behaviour. Furthermore, the model largely overestimated the load-carrying capacity of the joints for all OSB samples, with an error above 35 %. These large differences can result from compression occurring in the tenon but could also be explained by the material variability of OSB, as well as the layup of the panel | – | (| for longitudinal, – for crosswise veneer layer).

The slip modulus computed from the experimental test results and the one obtained from numerical simulations are compared in Figure 6.17, differences are presented in Table 6.7. It can be observed that the model underestimated the stiffness of the connections by $9.33 \% \pm 1.48 \%$ in average for samples T1-50 and T1-80 and slightly overestimated it by 2.13 % for T1-65. The approximation of the stiffness was considered to be coherent with respect to the dispersion of the experimental tests for all samples, indicated by the coefficient of variation in Table 6.7.

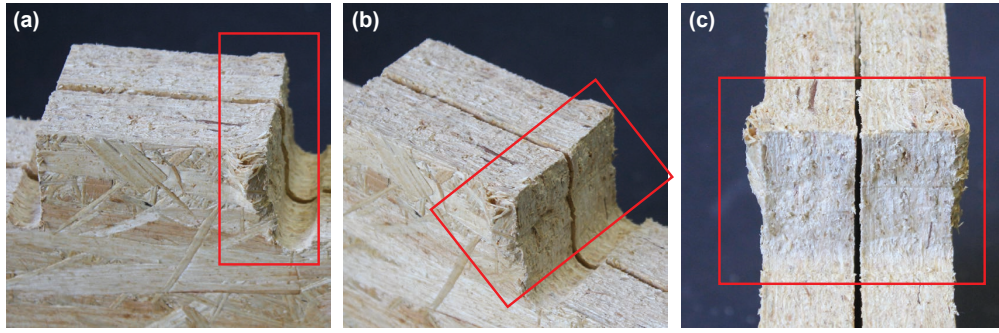


Figure 6.16 – Compression failure photographs of T1-80 specimens: (a) Front view (b) Axonometry (c) Side view.

Table 6.7 – Results of T1 specimens.

Designation	Symbol	Units	T1-50	T1-65	T1-80
Maximum slip	$v_{i,max}$	mm	1.08	1.34	2.68
Initial slip modulus	k_i	kN/mm	24.95	28.28	28.31
Slip modulus	k_s	kN/mm	21.12	24.16	24.22
Slip modulus after first loading	$k_{s,mod}$	kN/mm	41.67	43.22	53.39
Slip modulus predicted by the model	k_{model}	kN/mm	38.22	44.14	47.85
Model error on k_s	δ_{k_s}	%	80.94	82.69	97.56
Model error on $k_{s,mod}$	$\delta_{k_{s,mod}}$	%	-8.29	2.13	-10.38
Coefficient of variation of $k_{s,mod}$	$c_{v,k_{s,mod}}$	%	19.75	12.54	15.86
Maximum load	F_{max}	kN	14.30	19.09	21.13
Maximum load predicted by the model	$F_{max,model}$	kN	19.96	26.10	32.88
Coefficient of variation of F_{max}	$c_{v,F_{max}}$	%	7.16	5.52	6.06
Model error on the maximum load	$\delta_{F_{max}}$	%	39.63	36.68	55.59

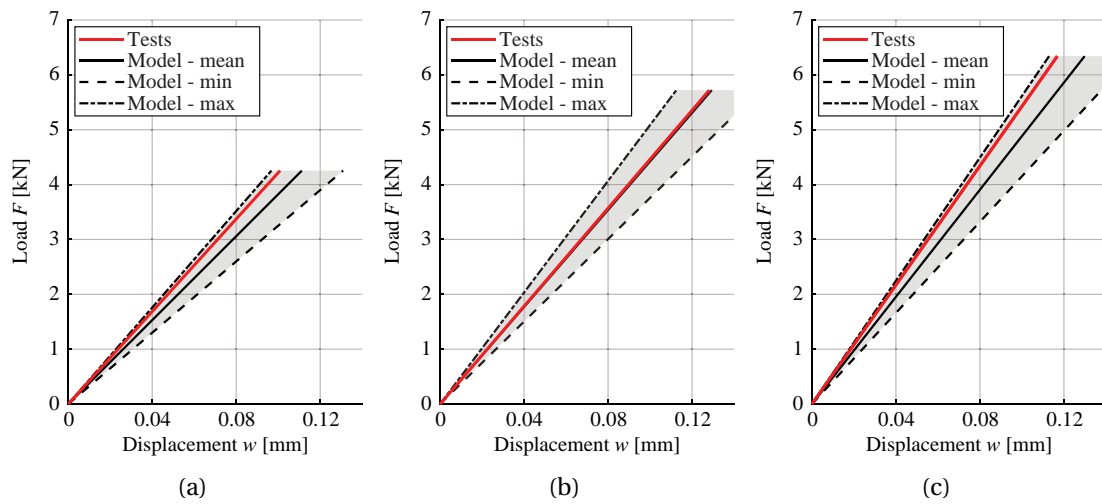


Figure 6.17 – Slip modulus of T1 specimens: (a) T1-50 (b) T1-65 (c) T1-80.

The shear stress distribution obtained at the loading step after which the mean shear strength $f_{v,mean} = 8.0$ MPa was reached is presented in Figure 6.18 for the T1-80 joint configuration. The step corresponds to a load of 18.3 kN, when damage is initiated in the model. The shear stress profile along the tenon was shown to be similar to the Hammock Shape Shear stress distribution (HSSSD), described in literature for shear failure [115], with a peak of stress close to the loaded surface of the tenon. A lower stress increase was also observed at the vicinity of the opposite notch. The stress concentration factor was found to be $K_t = 1.79$.

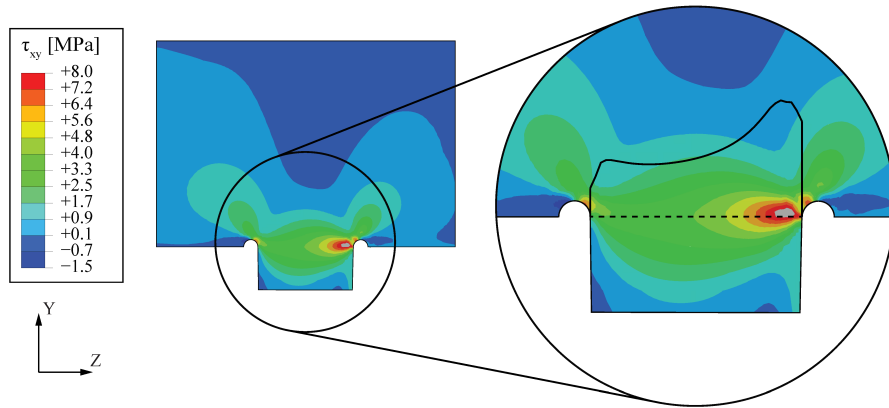


Figure 6.18 – Shear stress distribution and shear stress profile along the tenon for specimen T1-80.

6.4.3 Spruce LVL 21 mm double-layered

The full load-displacement curves of the tests performed on double-layered spruce LVL samples (T2) are presented in Figure 6.19 and the shear failures observed are showed in Figure 6.20 for different tenon lengths, for which a clear failure can be observed on the expected failure path. The comparison between both the slip modulus and the maximum load, computed from the tests and predicted by the numerical model, is summarised in Table 6.8.

A good agreement was found between the maximum load applied during the experimental tests, F_{max} , and the load-carrying capacity of the connections predicted by the numerical model. Loads were underestimated for all three joint configurations by $3.86 \% \pm 3.30 \%$ in average; such that the model can be considered as conservative. However, it can be observed in Figure 6.19 that displacements were underestimated.

The slip modulus computed from the experimental test results and the one obtained from numerical simulations are compared in Figure 6.21, differences are presented in Table 6.8. The semi-rigidity of the connections was found to be underestimated by $11.4 \% \pm 2.02 \%$ in average for the three joint configurations. However, this error is below the coefficient of variation of the experimental tests indicated in Table 6.8.

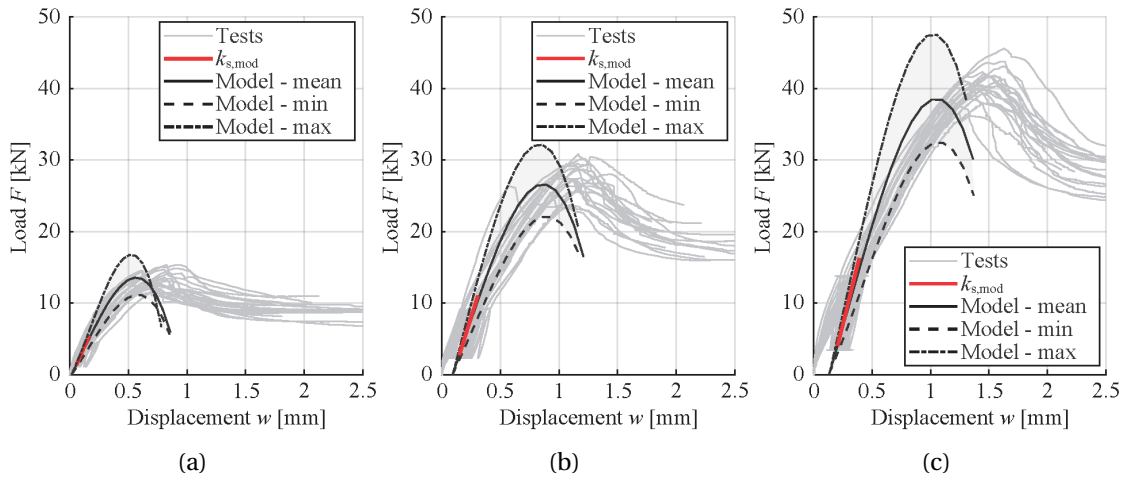


Figure 6.19 – Load-displacement curves of T2 specimens: (a) T2-50 (b) T2-100 (c) T2-150

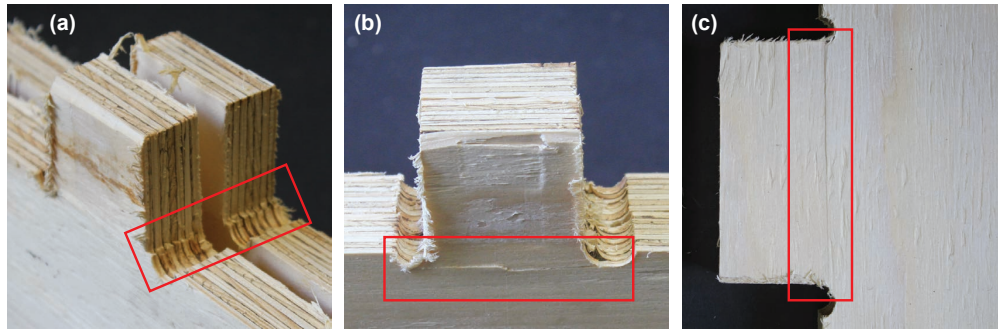


Figure 6.20 – Failure photographs of T2 specimens: (a) Axonometry (b) Front view T2-50 (c) Front view T2-100.

Table 6.8 – Results of T2 specimens.

Designation	Symbol	Units	T2-50	T2-100	T2-150
Maximum slip	$\nu_{i,max}$	mm	0.74	1.11	1.45
Initial slip modulus	k_i	kN/mm	41.14	44.85	49.09
Slip modulus	k_s	kN/mm	37.39	40.31	43.67
Slip modulus after first loading	$k_{s,model}$	kN/mm	37.67	52.33	65.66
Slip modulus predicted by the model	k_{model}	kN/mm	33.11	47.56	57.15
Model error on k_s	δk_s	%	-11.43	17.99	30.88
Model error on $k_{s,model}$	$\delta k_{s,model}$	%	-12.09	-9.12	-12.96
Coefficient of variation of $k_{s,model}$	$c_{\nu,s,model}$	%	15.21	22.96	23.04
Maximum load	F_{max}	kN	13.52	27.58	40.77
Maximum load predicted by the model	$F_{max,model}$	kN	13.49	26.26	38.08
Coefficient of variation of F_{max}	$c_{\nu,F_{max}}$	%	8.12	7.17	5.16
Model error on the maximum load	δF_{max}	%	-0.20	-4.78	-6.61

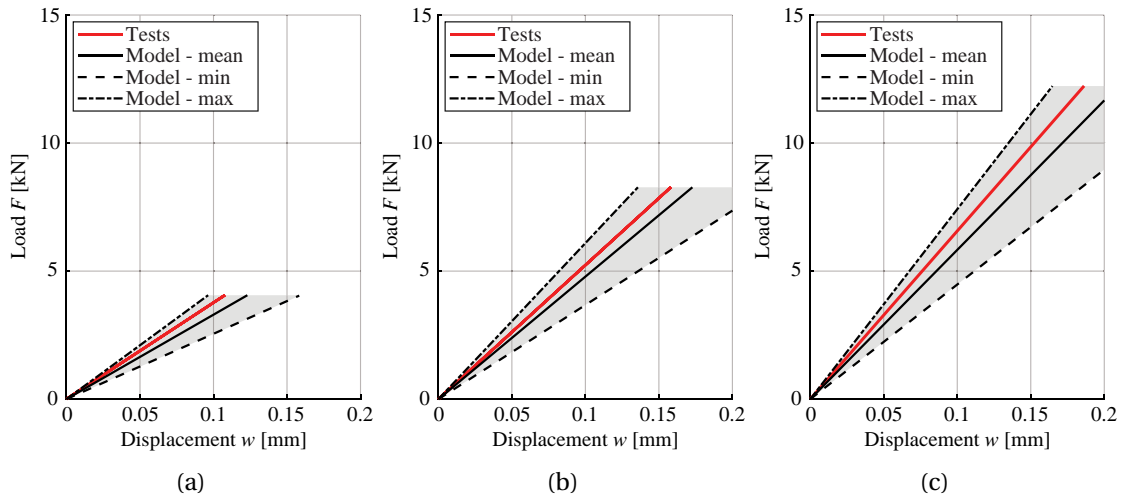


Figure 6.21 – Slip modulus of T2 specimens: (a) T2-50 (b) T2-100 (c) T2-150.

The shear stress distribution obtained at the loading step after which the mean shear strength $f_{v,mean} = 5.4$ MPa was reached is presented in Figure 6.22 for the T2-150 joint configuration. The step corresponds to a load of 19.7 kN, when damage is initiated in the model. An HSSSD was observed along the tenon with a stress concentration factor $K_t = 1.86$. However, at this load level of 19.7 kN in the model, the joint is still in its linear behaviour, just after the linear range of 10 to 40 % (see Figure 6.19c). Further investigations should thus be carried out to identify the modelling issues, which can be linked to increment times, mesh refinement at the stress concentration or the failure modes defining the onset of failure.

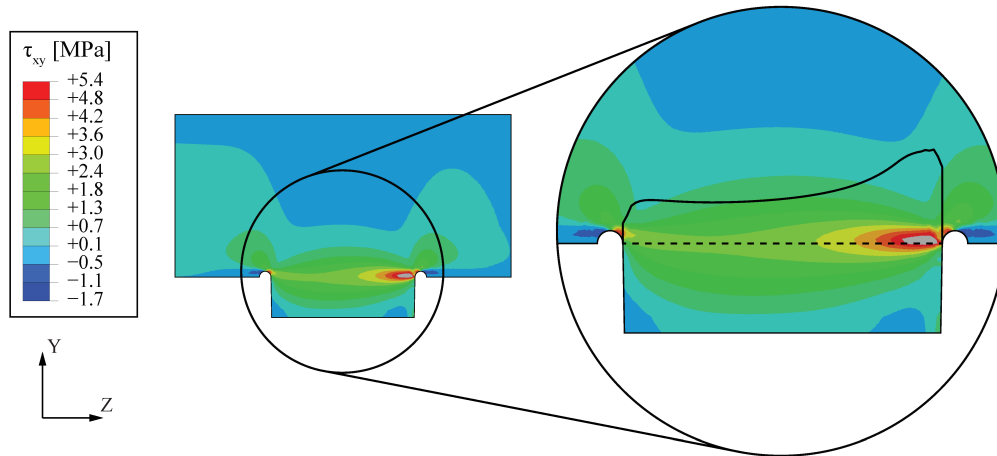


Figure 6.22 – Shear stress distribution and shear stress profile along the tenon for specimen T2-150.

6.4.4 Spruce LVL 39 mm single-layered

The full load-displacement curves of the tests performed on single-layered spruce LVL samples (T3) are presented in Figure 6.23 and the shear failures observed are showed in Figure 6.24. Failure occurred on the expected failure path. The comparison between both the slip modulus and the maximum load, computed from the tests and predicted by the numerical model, is summarised in Table 6.9. The model error on the maximum load F_{\max} for each of the three joint configurations was found to be about the same value as the coefficient of variation of the experimental tests, with loads underestimated by $3.86 \% \pm 3.30 \%$ in average. The model was shown to be in good agreement with the experimental tests. However, as for double-layered spruce LVL samples (T2), displacements were found to be underestimated by the model.

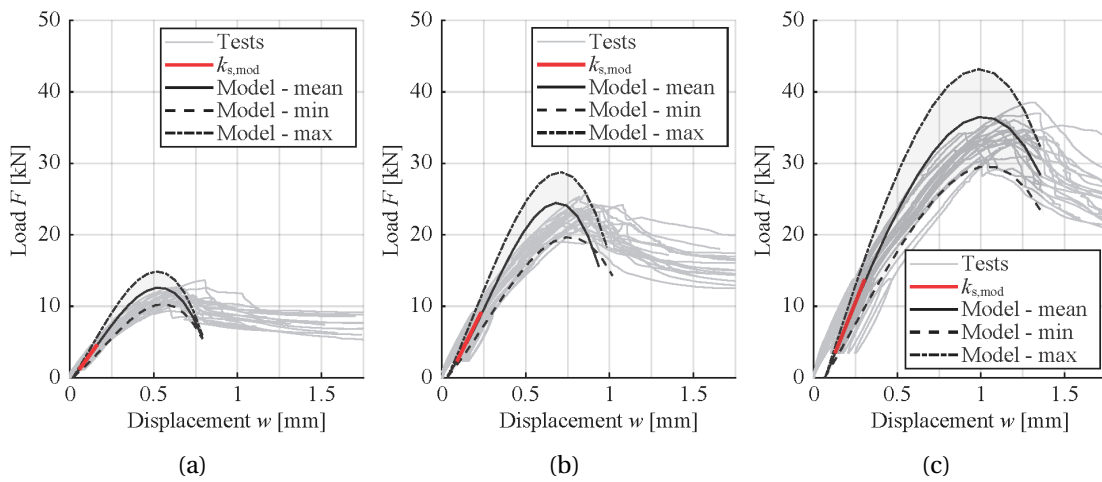


Figure 6.23 – Load-displacement curves of T3 specimens: (a) T3-50 (b) T3-100 (c) T3-150.

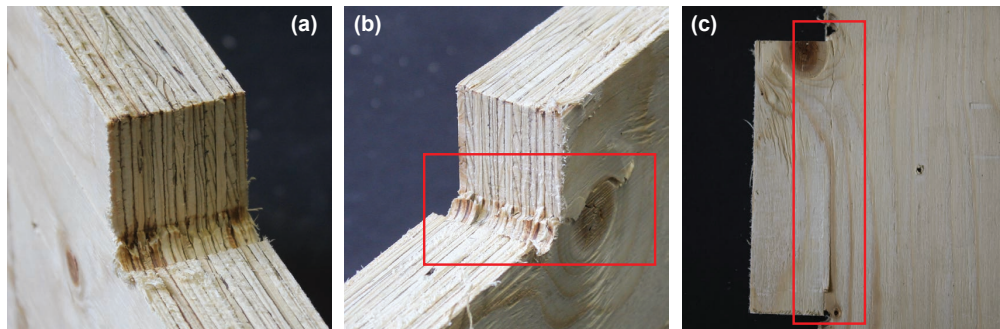


Figure 6.24 – Failure photographs of T3 specimens: (a) Axonometry side 1 (b) Axonometry side 2 (c) Front view.

The slip modulus computed from the experimental tests and the one obtained from numerical simulations are compared in Figure 6.25, differences are presented in Table 6.9. The semi-rigidity of the connections was found to be in good agreement with the experimental tests, with stiffness underestimated by $3.9 \% \pm 1.20 \%$ in average for the three configurations.

Table 6.9 – Results of T3 specimens.

Designation	Symbol	Units	T3-50	T3-100	T3-150
Maximum slip	$v_{i,max}$	mm	0.66	0.85	1.17
Initial slip modulus	k_i	kN/mm	30.09	41.60	47.69
Slip modulus	k_s	kN/mm	26.96	38.09	42.74
Slip modulus after first loading	$k_{s,model}$	kN/mm	32.50	47.62	58.53
Slip modulus predicted by the model	k_{model}	kN/mm	31.61	45.79	55.52
Model error on k_s	δk_s	%	17.38	20.24	29.89
Model error on $k_{s,model}$	$\delta k_{s,model}$	%	-2.74	-3.83	-5.13
Coefficient of variation of $k_{s,model}$	$c_{v,s,model}$	%	14.35	11.90	16.49
Maximum load	F_{max}	kN	11.57	22.90	34.43
Maximum load predicted by the model	$F_{max,model}$	kN	12.54	24.28	36.43
Coefficient of variation of F_{max}	$c_{v,Fmax}$	%	8.52	7.18	5.31
Model error on the maximum load	δF_{max}	%	8.31	6.02	5.81

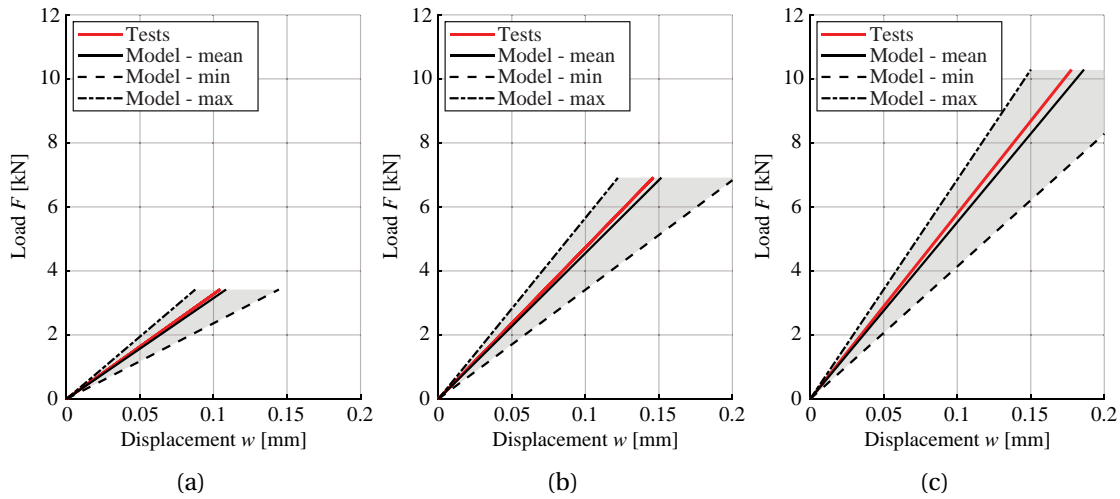


Figure 6.25 – Slip modulus of T3 specimens: (a) T3-50 (b) T3-100 (c) T3-150.

The shear stress distribution obtained at the loading step after which the mean shear strength $f_{v,mean} = 5.4$ MPa was reached is presented in Figure 6.26 for the T3-150 joint configuration. The step corresponds to a load of 15.4 kN, when damage is initiated in the model. An HSSSD was observed along the tenon with a stress concentration factor $K_t = 2.18$. However, at this load level of 15.4 kN in the model, the joint is still in its linear behaviour, just after the linear range of 10 to 40 % (see Figure 6.23c). Further investigations should thus be carried out to identify the modelling issues, which can be linked to increment times, mesh refinement at the stress concentration or the failure modes defining the onset of failure.

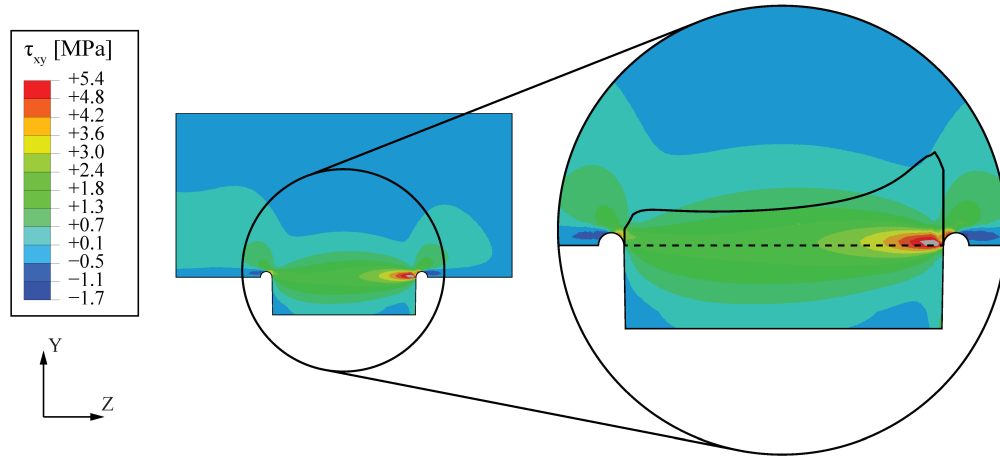


Figure 6.26 – Shear stress distribution and shear stress profile along the tenon for specimen T3-150.

6.4.5 Beech LVL 40 mm single-layered

The full load-displacement curves of the tests performed on single-layered beech LVL samples (T4) are presented in Figure 6.27 and the shear failures observed are showed in Figure 6.28 with a clean shear failure. The comparison between both the slip modulus and the maximum load, computed from the tests and predicted by the numerical model, is summarised in Table 6.10. The model error on the maximum load F_{\max} was found to be of about the same values as the coefficient of variation of the experimental tests for all three joint configurations, with loads underestimated by $3.86 \% \pm 3.30 \%$ in average. The model was shown to be in good agreement with the experimental tests. However, as for T2 and T3 samples, displacements were found to be underestimated by the model.

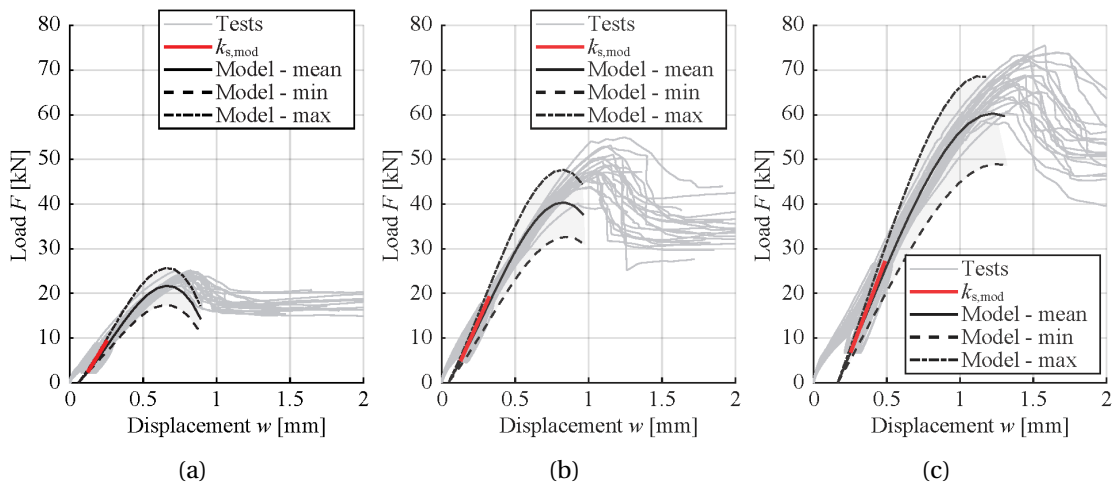


Figure 6.27 – Load-displacement curves of T4 specimens: (a) T4-50 (b) T4-100 (c) T4-150.

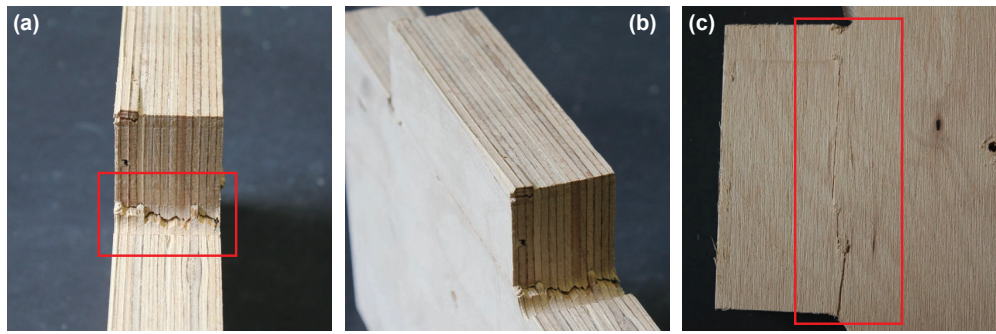


Figure 6.28 – Failure photographs of T4 specimens: (a) Side view (b) Axonometry (c) Front view.

Table 6.10 – Results of T4 specimens.

Designation	Symbol	Units	T4-50	T4-100	T4-150
Maximum slip	$v_{i,max}$	mm	0.81	1.08	1.44
Initial slip modulus	k_i	kN/mm	39.82	64.88	58.40
Slip modulus	k_s	kN/mm	35.71	61.10	55.44
Slip modulus after first loading	$k_{s,mod}$	kN/mm	53.52	73.54	86.98
Slip modulus predicted by the model	k_{model}	kN/mm	45.72	65.35	78.94
Model error on k_s	δ_{k_s}	%	28.03	6.96	42.40
Model error on $k_{s,mod}$	$\delta_{k_{s,mod}}$	%	-14.57	-11.13	-9.24
Coefficient of variation of $k_{s,mod}$	$c_{v,s,mod}$	%	12.25	5.86	6.96
Maximum load	F_{max}	kN	23.66	47.99	68.03
Maximum load predicted by the model	$F_{max,model}$	kN	21.74	41.16	59.70
Coefficient of variation of F_{max}	$c_{v,F_{max}}$	%	3.67	7.38	6.98
Model error on the maximum load	$\delta_{F_{max}}$	%	-8.12	-14.24	-12.24

The slip modulus computed from the experimental test results and the one obtained from numerical simulations are compared in Figure 6.29, differences are presented in Table 6.10. The semi-rigidity of the connections was found to be underestimated by $11.65\% \pm 2.70\%$ in average for the three joint configurations.

The shear stress distribution obtained at the loading step after which the mean shear strength $f_{v,mean} = 9.3$ MPa was reached is presented in Figure 6.30 for the T4-150 joint configuration. The step corresponds to a load of 26.7 kN, when damage is initiated in the model. An HSSSD was observed along the tenon with a stress concentration factor $K_t = 2.26$. However, at this load level of 26.7 kN in the model, the joint is still in its linear behaviour (see Figure 6.27c). Further investigations should thus be carried out to identify the modelling issues, which can be linked to increment times, mesh refinement at the stress concentration or the failure modes defining the onset of failure.

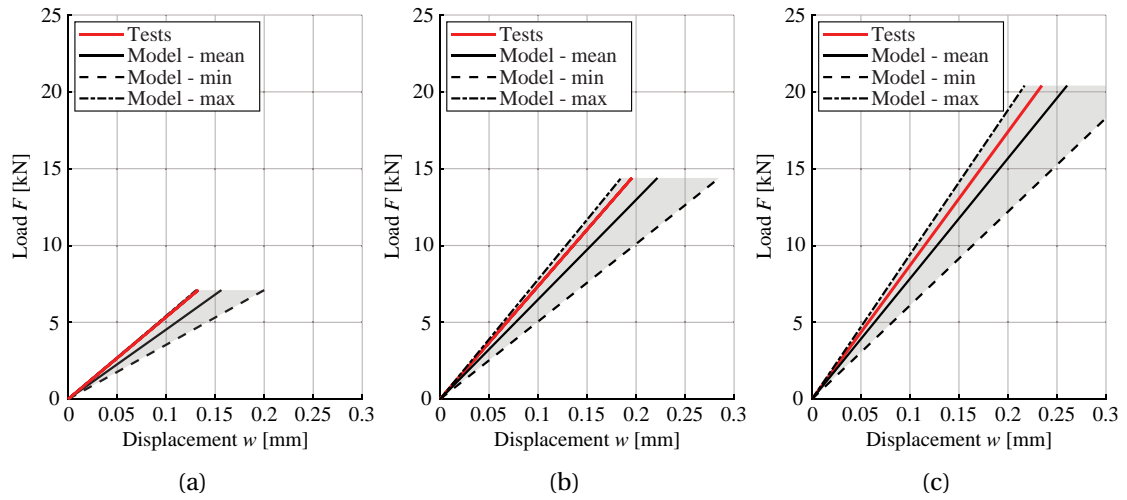


Figure 6.29 – Slip modulus: (a) T4-50 (b) T4-100 (c) T4-150.

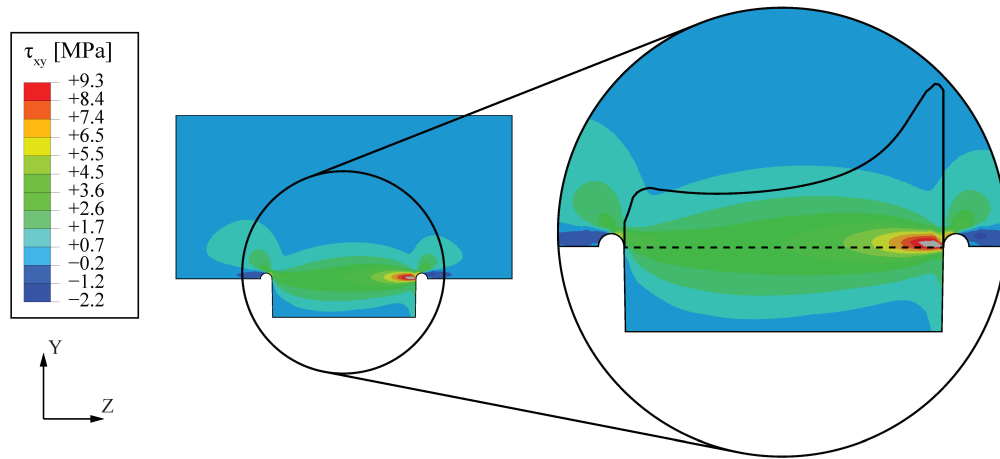


Figure 6.30 – Shear stress distribution and shear stress profile along the tenon for specimen T4-150.

6.4.6 CLT 27 mm double-layered

The full load-displacement curves of the tests performed on double-layered spruce CLT samples (T5) are presented in Figure 6.31 and the shear failures observed are showed in Figure 6.32. The comparison between both the slip modulus and the maximum load, computed from the tests and predicted by the numerical model, is summarised in Table 6.11. A good agreement was found between the slip modulus and the maximum load applied during the experimental tests, F_{\max} , and the load-carrying capacity of the connections predicted by the numerical model. Loads were underestimated for all three joint configurations by $4.80\% \pm 2.50\%$ in average; such that the model can be considered as conservative. However, as for LVL samples, it can be observed that displacements were underestimated.

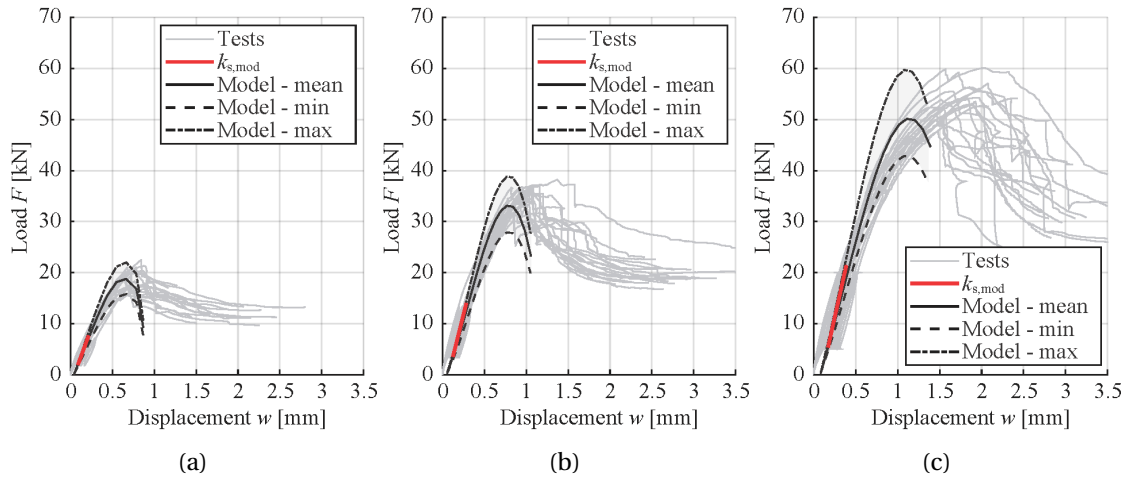


Figure 6.31 – Load-displacement curves of T5 specimens: (a) T5-50 (b) T5-100 (c) T5-150.

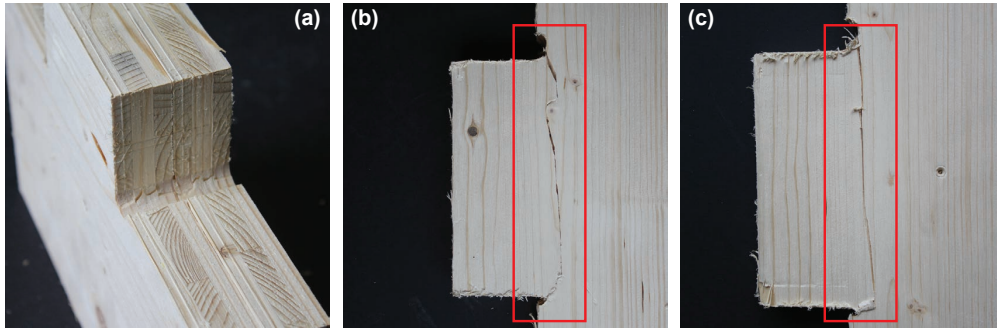


Figure 6.32 – Failure photographs of T5 specimens: (a) Axonometry (b) Side view 1 (c) Side view 2.

The slip modulus computed from the experimental test results and the one obtained from numerical simulations are compared in Figure 6.33, differences are presented in Table 6.11. The semi-rigidity of the connections was found to be underestimated by $9.13 \% \pm 3.52 \%$ in average for the three joint configurations.

The shear stress distribution obtained at the loading step after which the mean shear strength $f_{v,mean} = 3.2 \text{ MPa}$ was reached is presented in Figure 6.34 for the T5-150 joint configuration. The step corresponds to a load of 11.6 kN, when damage is initiated in the model. An HSSSD was observed along the tenon with a stress concentration factor $K_t = 2.72$. However, at this load level of 11.6 kN in the model, the joint is still in its linear behaviour (see Figure 6.31c). Further investigations should thus be carried out to identify the modelling issues, which can be linked to increment times, mesh refinement at the stress concentration or the failure modes defining the onset of failure.

Table 6.11 – Results of T5 specimens.

Designation	Symbol	Units	T5-50	T5-100	T5-150
Maximum slip	$\nu_{i,max}$	mm	0.78	1.00	1.72
Initial slip modulus	k_i	kN/mm	39.22	53.22	61.04
Slip modulus	k_s	kN/mm	36.25	48.81	57.44
Slip modulus after first loading	$k_{s,model}$	kN/mm	44.55	65.18	73.58
Slip modulus predicted by the model	k_{model}	kN/mm	41.13	56.62	68.75
Model error on k_s	δ_{k_s}	%	13.45	15.86	19.69
Model error on $k_{s,model}$	$\delta_{k_{s,model}}$	%	-7.68	-13.14	-6.57
Coefficient of variation of $k_{s,model}$	$c_{\nu,s,model}$	%	12.48	12.41	8.06
Maximum load	F_{max}	kN	19.14	35.11	53.61
Maximum load predicted by the model	$F_{max,model}$	kN	18.77	33.00	50.13
Coefficient of variation of F_{max}	$c_{\nu,F_{max}}$	%	9.89	6.27	6.49
Model error on the maximum load	$\delta_{F_{max}}$	%	-1.93	-6.00	-6.49

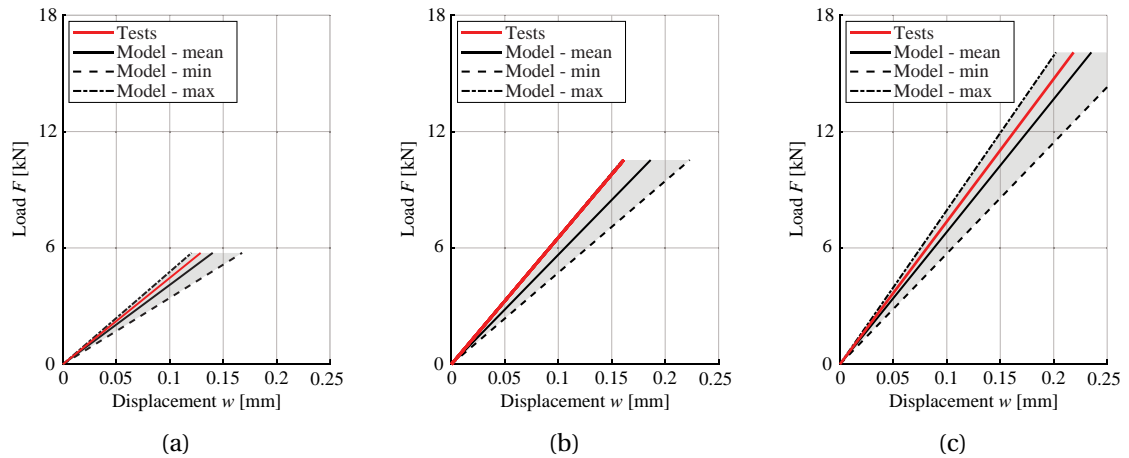


Figure 6.33 – Slip modulus of T5 specimens: (a) T5-50 (b) T5-100 (c) T5-150.

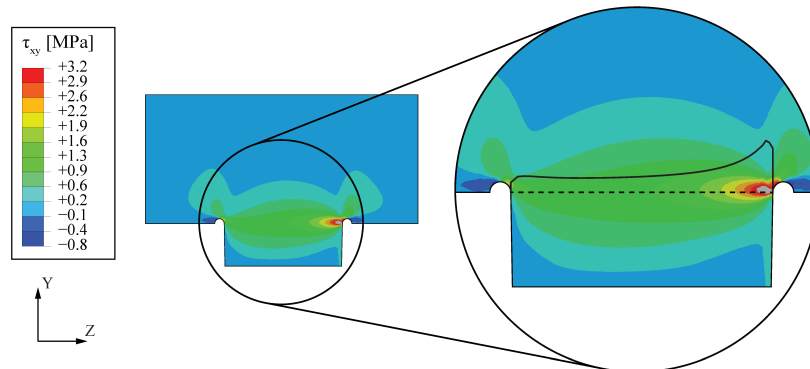


Figure 6.34 – Shear stress distribution and shear stress profile along the tenon for specimen T5-150.

6.5 Conclusions

In this chapter, a 3D-FE model, based on the continuum damage model developed by Sandhaas [88], was applied to digitally fabricated TT wood-wood connections. It was compared to shear loading tests performed on single wood-wood connections, considering five commonly used engineered wood products.

In the model, phenomena affecting the first loading were neglected and the behaviour of the connections after the first loading was considered to assess the model. Stiffness of the connections were found to be in good agreement with the experimental shear loading tests for all specimens, with conservative predictions. Their load-carrying capacity was approximated for LVL and CLT specimens (T2, T3, T4 and T5), with conservative predictions as well. However, the exact behaviour could not be accurately predicted and slip values were found to be underestimated by the model. For OSB specimens, the model could not predict the behaviour of the connections, presumably because of the high material variability of OSB and due to compression forces, as observed for the T1-80 specimen. For other specimens, inconsistencies with regard to the shear stresses were found, such that further investigations should be performed to control the mesh and time increments used in the model.

If promising results were obtained, the numerical model for wood-wood connections is currently not sufficient to provide reliable results that can be implemented in global numerical models. Furthermore, additional investigations for different load cases and joint configurations should be performed to obtain an exhaustive assessment of the numerical model. Therefore, experimental tests on wood-wood connections still remain necessary to fully understand and characterise the mechanical behaviour of wood-wood connections.

To improve the model, an optimisation of the time increment and of the mesh around the stress concentration area should be performed. The introduction of deformable contact elements could lead to more accurate deformations in comparison with the surface-to-surface interaction with hard contact considered in this study. Element deletion could also be implemented to alleviate mesh dependency and element distortion, such as performed by Sandhaas et al. [89]. Further investigations should also include the study of different angle combinations (Bryant angles θ_1 , θ_2 and θ_3 defining the insertion vector of the joints, as illustrated in Chapter 1, Figure 1.5) and different grain orientations, as well as investigations on the influence of multiple connections placed in a series. Specimens considering different materials for the tenon and mortise parts could also be analysed. In light of this, the implementation of different loading cases as well as single- and double-layered specimens configurations should be included in the AbaqusTM plugin developed by Roche et al. [85], which was automatically generating the joint geometry within the FEA software, instead of importing the geometry from a CAD software.

A comprehensive mechanical characterisation of digitally fabricated TT wood-wood connections is thus required to assess their structural performance for different load cases, geometries, grain orientations and materials, for both single and multiple joint configurations. In this perspective, current research is carried out to provide design guidelines for the use of wood-wood connections.¹

¹These investigations are part of the doctoral research performed by the manuscript co-author, J. Gamero.

7 Conclusions and Outlook

7.1 Conclusions

The pressing need for the construction sector to address the declared climate emergency has resulted in a growing demand for structures using wood-based materials. Consequently, significant developments have been achieved in timber construction over the past decades, allowing larger spans to be reached and widening the range of application of timber as a construction material. Additionally, advances in computational design and digital fabrication have led to the realisation of increasingly complex structures composed of prefabricated timber elements. For these structures, innovative wood-wood connections integrated in the plates have been shown to be a competitive solution in comparison with standard joining techniques. In this perspective, several investigations were carried out in this thesis to facilitate the design and realisation of large-scale freeform timber plate structures using wood-wood connections.

7.1.1 Achieved Results

Following the automation of the design and fabrication of freeform timber plate structures using computer-aided programming (CAD) and computer-aided manufacturing (CAM) tools, an automated numerical modelling method for their structural analysis was proposed. By doing so, a tedious and time-consuming manual implementation, prone to random human errors, was avoided. A model based on the finite element method (FEM) was developed, using springs with 6 degrees of freedom (3 translations and 3 rotations) to take into account the semi-rigid behaviour of the connections, as it was shown to be essential to obtain accurate predictions. A design framework was introduced to integrate the generation of the numerical model into the existing design and fabrication workflow. Furthermore, methods to build the FEM geometry concurrently with the CAD geometry used for design and fabrication were provided. Steps to generate the model in the finite element analysis (FEA) software were subsequently described.

The semi-rigidity of the connections in translation as well as in rotation was shown to highly influence the model. Numerical simulations were performed using axial, in-plane shear, out-of-plane shear and rotational semi-rigid properties retrieved from experimental tests, as they were found to be the most influencing components for the studied construction system. Remaining degrees of freedom were considered hinged for a conservative design. The proposed numerical model was validated for the serviceability limit state (SLS), which is generally limiting the design of timber structures, against experimental tests conducted on both small- and large-scale structures. Three-point bending tests, reported in Chapter 3, were performed in the laboratory on three small-scale specimens to obtain a first assessment of the model. The failure modes of the construction system were highlighted through destructive tests, providing useful insights for the ultimate limit state (ULS) design. In Chapter 4, the global behaviour of the whole shell was verified by carrying out non-destructive static loading tests onsite on a large-scale structure. The numerical model was validated by comparing the predicted to the acquired displacements by using two different devices: a total station and a terrestrial laser scanner. The results obtained were assessed and compared, providing insights for their use in future applications, such as structural health monitoring. The two measuring methods were found to be complementary. Although total station measurements led to more direct and accurate results, they could only be acquired for a limited number of points on the structure. Laser scanner however allowed the visualisation of displacement fields over the whole structure, despite a more cumbersome data processing.

Although the mechanical behaviour of wood-wood connections was shown to play an important role in the structure's performance, investigations carried out in Chapter 5 have demonstrated the significant influence of the assembly system chosen. The study highlighted the potential for structural optimisation and the need to integrate the structural analysis in the design strategy, while respecting the fabrication and assembly constraints.

Finally, a three-dimensional (3D) finite element (FE) model based on continuum damage mechanics was applied to through-tenon (TT) wood-wood connections. It was compared to shear loading tests performed on single connections, considering different commonly used engineered wood products. Promising results were obtained with conservative approximations of the load-carrying capacity and semi-rigidity of the connections. However, it was found that experimental testing remains necessary to fully understand and characterise the exact mechanical behaviour of wood-wood connections.

7.1.2 Applications to Other Structures

Although the model and methods to generate it were presented in Chapter 2 based on a specific case study, namely the Annen Plus SA head office presented in Chapter 1, Subsection 1.3, they are easily applicable and transferable to various types of timber plate structures with edgewise wood-wood connections. Based on the 3D design geometry of the studied structure, plates have to be modelled by their midsurfaces, partitioned at the position of the joints, with

springs implemented to model the semi-rigid behaviour of the connections, as presented in Chapter 3, Subsection 2.3.2. The generation of the CAD-FEM geometry defined can be done using the same tools applied for the design of the structures, usually obtained with existing design-to-fabrication workflows for complex structures. In order to decrease the computational time involved for large models, faster FE libraries could be applied instead of the FEA software AbaqusTM used in the present thesis. For the connection properties, a sensitivity analysis should be performed to determine the degrees of freedom that influence the most the global behaviour of the structure. If experimental tests cannot be performed for these components, assumptions should be taken on the safe side for the design calculations.

7.1.3 Summary

Overall, this thesis provides a design methodology for the structural analysis of large-scale freeform timber structures using wood-wood connections. The investigations carried out show that it is essential to establish a link between the local behaviour of the connections and global behaviour of the structure. Furthermore, in line with the "co-design" strategy introduced by Achim Menges [61, 62], this thesis highlights the importance of adopting an integrated design strategy encompassing engineering and fabrication aspects for geometrically complex timber structures. Additionally, the design framework presented has the potential to enhance exchanges between geometry generation and structural analysis necessary to perform structural optimisations.

7.2 Outlook

Further development of the proposed modelling method could be achieved, for example by considering a nonlinear connection behaviour as well as contacts between plate elements if they are found to play an important role in the mechanical behaviour. Moreover, as highlighted in Chapter 4, the accumulation of small fabrication and construction tolerances can lead to substantial differences between design geometry and built structure. Investigations are required to control these variations by determining all the factors responsible for them, as well as their influence on the structural behaviour. Similarly, long-term monitoring of built structures could also be performed to assess their behaviour over extended periods of time.

Furthermore, the proposed numerical model can be computationally expensive for large structures involving a large number of elements and therefore an even greater number of variables. In light of this, a complementary doctoral research¹ conducted by A. R. Rad focuses on an alternative numerical model for timber plate structures assembled with wood-wood connections. Based on the same case study as the present thesis, a "macro-model" consisting of a series of one-dimensional (1D) beam and column elements is investigated. The proposed modelling approach has the potential to significantly decrease computational costs for the SLS design of large-scale structures.

Chapter 7. Conclusions and Outlook

Besides work focusing on complex freeform geometries, a current doctoral research¹ is carried out by J. Gamarro on the development of standard prefabricated structural elements, such as roofs, slabs and walls, using TT wood-wood connections to extend their range of application to common practice. For the developed construction system, a simplified model inspired by the strut-and-tie design method considering 1D beam elements and springs is investigated.

Regardless of the global numerical model chosen, the implementation of the semi-rigid behaviour of the connections is essential to precisely predict the behaviour of the structures in which they are applied. In this perspective, the ongoing doctoral research studies mentioned also include experimental investigations on TT wood-wood connections. On the one hand, A. R. Rad is evaluating the structural performance of these connections under different load cases and for different grain orientations and joint geometries, both related to a specific case study and according to the development of the "macro-model". On the other hand, J. Gamarro is focusing on the behaviour of TT connections applied in standardised structural elements for various commonly used engineered wood panels. The objective of his research is to provide design guidelines for the use of TT wood-wood connections in timber structures, in relation with the European Standard Eurocode 5 [23], which currently does not include protocols for this type of connections.

Finally, as presented in Chapter 6, a 3D FE model for wood-wood connections showed promising results and would require further improvements of the model to increase its application to different load cases and geometries.

In conclusion, wood-wood connections have a great potential for the joining of timber plate structures, which has been demonstrated through several research studies carried out over the past decades. If challenges still remain with regard to their structural design, additional investigations to the present study can help implement their use into common practice and increase their application for large-scale projects.

¹The doctoral research studies conducted by A. R. Rad and J. Gamarro are carried out within the Laboratory for Timber Constructions (IBOIS), EPFL and are supported by the NCCR Digital Fabrication, funded by the Swiss National Science Foundation (NCCR Digital Fabrication Agreement #51NF40-141853).



Funding

This research was supported by the NCCR Digital Fabrication, funded by the Swiss National Science Foundation (NCCR Digital Fabrication Agreement #51NF40-141853).

A Experimental Tests on Through-Tenon Wood-Wood Connections

Experimental tests were performed to retrieve the semi-rigid properties of the studied wood-wood connections, in particular their stiffness and load-carrying capacity, necessary for the numerical modelling of assemblies in which they are used. These tests were carried out on recently developed test setups, for the degrees of freedom (DOFs) that were found to have a high influence (above 10 %) on the semi-rigid spring model developed in Chapter 2, namely k_1 , k_2 , k_3 and k_5 (see Chapter 2, Subsection 2.4.3). These tests were performed on small-samples with through-tenon (TT) connections characterized by a tab length of 72.5 mm and Bryant angles (as defined in Chapter 1, Figure 1.5) $\theta_1 = 0^\circ$, $\theta_2 = 25^\circ$ and $\theta_3 = 0^\circ$, corresponding to the connections of the studied 5×3 boxes prototype (see Figure 3.1b). Tests were executed following the loading procedure prescribed in the European Standard EN 26891 [24] for timber joints made with mechanical fasteners. Coefficient of variations c_v of the maximum force and of the stiffness were calculated for each test.

A.1 Tension Tests¹

Tension load tests were carried out on three samples with one single TT connection using the experimental setup developed by Rad et al. [74]. Results are presented in Figure A.1a. The average maximum capacity $F_{\max, \text{avg}}$ was found to be of 6.47 kN, with a coefficient of variation $c_{v, F_{\max}}$ of 5.32 %. Figure A.1b presents the load-displacement curves in the linear range between 10 and 40 % of $F_{\max, \text{avg}}$, from which a stiffness value of 416.81 N/mm was retrieved, with a coefficient of variation $c_{v, k}$ of 6.16 %.

¹Experimental tests were performed by the author of the publication [74], A. R. Rad.

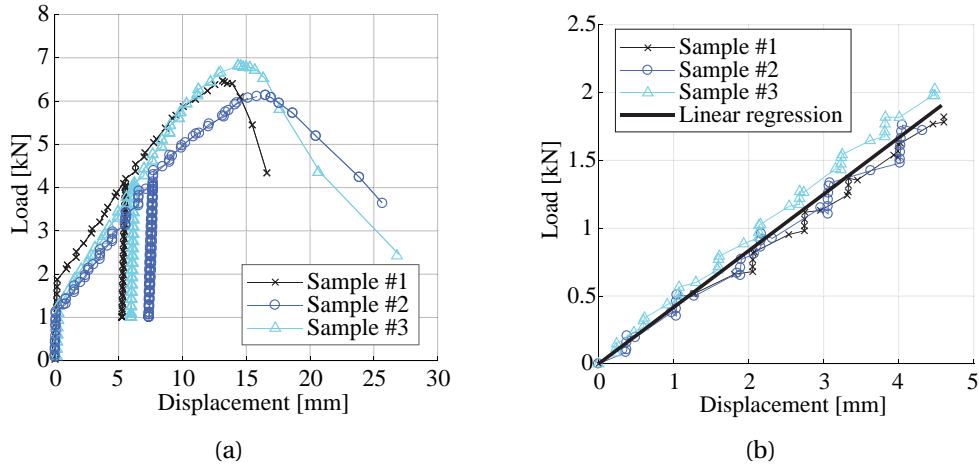


Figure A.1 – Results of tension load tests on one single through-tenon connection: (a) Load-displacement curves (b) Linear range between 10 and 40 % of $F_{max,avg}$.

A.2 Shear Tests²

Shear load tests were performed on four samples using the experimental setup developed by Rad et al. [75]. Each specimen was made of two TT connections, such that the test results presented in Figure A.2 were divided by two to obtain values for one connection. The maximum load-carrying capacity of one connection $F_{max,avg}$ was found to be of 46.83 kN, with a coefficient of variation $c_{v,F_{max}}$ of 4.48 % (see Figure A.2a). A stiffness value k_2 of 15 009.24 N/mm, with a coefficient of variation $c_{v,k}$ of 1.79 %, was retrieved from the linear range between 10 and 40 % of $F_{max,avg}$ (see Figure A.2b).

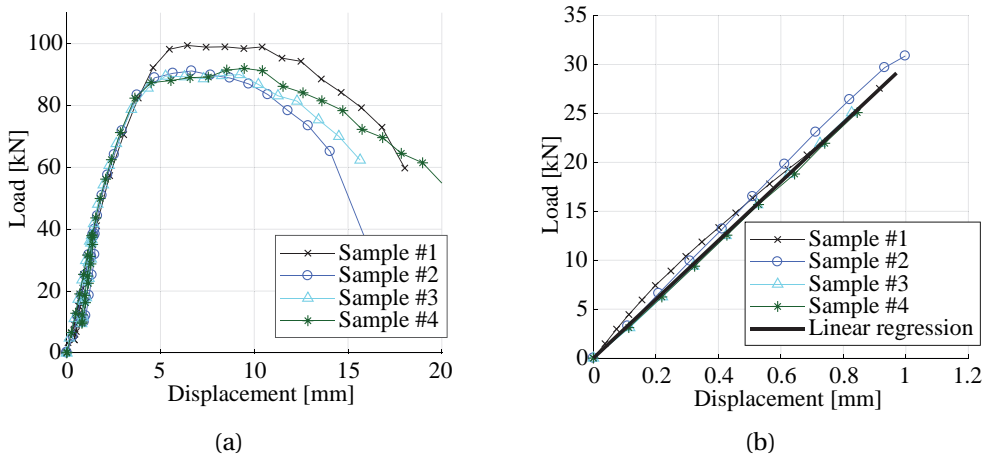


Figure A.2 – Results of shear load tests on two through-tenon connections: (a) Load-displacement curves (b) Linear range between 10 and 40 % of $F_{max,avg}$.

²Experimental tests were performed by the author of the publication [75], A. R. Rad.

A.3 Out-of-Plane Shear Tests³

The test setup used to determine the maximum load-carrying capacity and stiffness of the connection in perpendicular-to-grain compression, also referred to as out-of-plane shear, is illustrated in Figure A.3. As for the in-plane shear test setup developed by Rad et al. [75], symmetric specimens with two connections were fabricated and placed on a concrete support ③, considered rigid. Force was applied through a hydraulic jack ① and four linear variable differential transformers (LVDTs) ② were placed to measure the deformation of the samples. Maximum load-carrying capacity $F_{\max, \text{avg}}$ and stiffness k_3 , retrieved from the linear range between 10 and 40 % of $F_{\max, \text{avg}}$, of 36.55 kN and 9489.04 N/mm respectively were found, with coefficient of variations $c_{v, F_{\max}}$ of 3.88 % and $c_{v, k}$ of 2.74 % (see Figure A.4) for three samples.

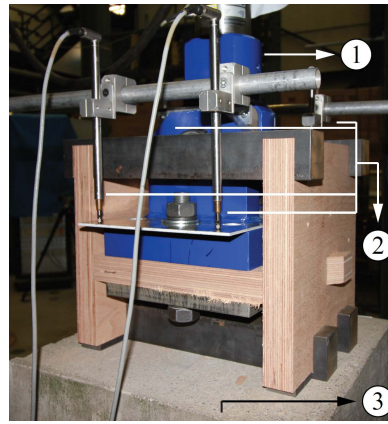


Figure A.3 – Experimental setup for out-of-plane shear: ① Hydraulic jack ② Four LVDTs ③ Concrete support. Photograph by Aryan Rezaei Rad.

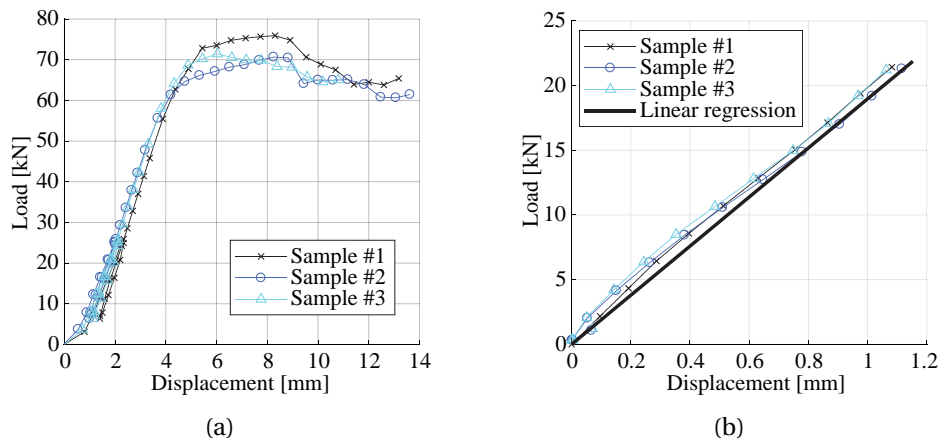


Figure A.4 – Results of out of plane shear load tests on two through-tenon connections: (a) Load-displacement curves (b) Linear range between 10 and 40 % of $F_{\max, \text{avg}}$.

³The test setup was developed by the author of the publications [74, 75], A. R. Rad, who performed the experimental tests.

A.4 Bending Tests

Bending tests were carried out on a series of seven samples made of two-panel assemblies connected with one TT connection. The bending test setup developed by Roche [83] and illustrated in Figure A.5 was used. Four load cells ① were fixed on each panel: for the panel with slots, these load cells were mounted on a rigid support, while for the panel with tenon, they were fixed to a level arm ②, itself connected to a 20 kN load cylinder. Two inclinometers ③ were fixed to the panel with tenon to measure the rotation of the sample. Specimens were tested in closing as TT connections have been shown to present a symmetrical behaviour in opening and closing [84].

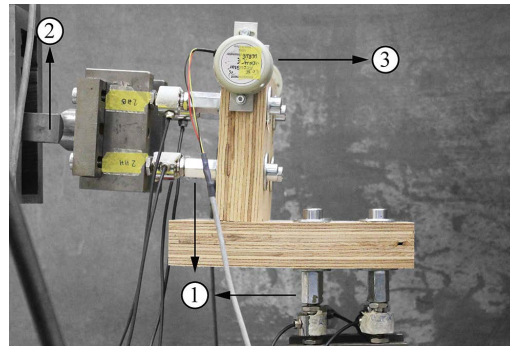


Figure A.5 – Bending test setup developed by Roche [83]: ① Four load cells ② Lever arm connected to a 20 kN load cylinder ③ Two inclinometers, fixed to the panel with tenon.

Figure A.6a presents the moment-rotation curves obtained for the seven tested samples. The maximum average moment applied $M_{\max, \text{avg}}$ was of 1067.0 kN·mm, with a coefficient of variation $c_{v, M_{\max}}$ of 7.08 %. Figure A.6b presents the moment-rotation curves in the linear range between 10 and 40 % of $M_{\max, \text{avg}}$ from which the stiffness was retrieved. A linear regression led to an average stiffness of 170.19 kN·mm/° with a coefficient of variation $c_{v, k}$ of 4.84 %.

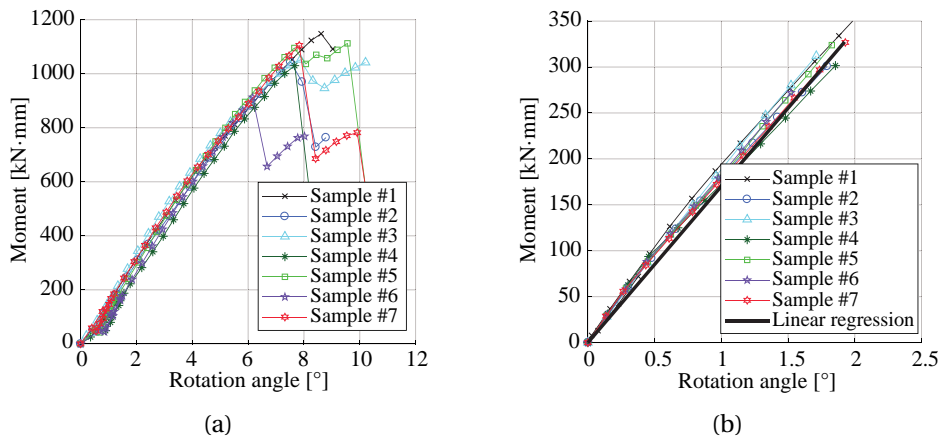


Figure A.6 – Results of bending tests on one single through-tenon connection: (a) Moment-rotation curves (b) Linear range between 10 and 40 % of $M_{\max, \text{avg}}$.

A.5 Summary

Tables A.1 and A.2 present a summary of the test results, for each studied DOF, namely DOF 1 for tension tests, DOF 2 for in-plane shear tests, DOF 3 for out-of-plane shear tests and DOF 5 for bending tests. Coefficient of variations lower than 10 % were found for the four tests, for both maximum load-carrying capacity and stiffness. These values were considered acceptable for this material. For translational DOFs, the connections were shown to have a much lower resistance and stiffness in the axial direction and the highest resistance and stiffness in shear.

Table A.1 – Summary of experimental test results of wood-wood connections for translational degrees of freedom.

Degree of freedom	Number of samples	$F_{\max, \text{avg}}$ [kN]	$c_{v, F_{\max}}$ [%]	k_{avg} [N/mm]	$c_{v, k}$ [%]
1	3	6.47	5.32	416.81	6.16
2	4	46.83	4.48	15 0009.24	1.79
3	3	36.55	3.88	9489.04	2.74

Table A.2 – Summary of experimental test results of wood-wood connections for the rotational degree of freedom about y .

Degree of freedom	Number of samples	$M_{\max, \text{avg}}$ [kN/mm]	$c_{v, M_{\max}}$ [%]	k_{avg} [kN·mm/°]	$c_{v, k}$ [%]
5	7	1067.0	7.08	170.19	4.84

Bibliography

- [1] Y. Al-Qaryouti, K. Baber, and J. M. Gattas. Computational design and digital fabrication of folded timber sandwich structures. *Automation in Construction*, 102:27–44, 2019. doi:10.1016/j.autcon.2019.01.008.
- [2] S. Anderson. *Eladio Dieste: Innovation in Structural Art*. Princeton Architectural Press, New York, 1st edition, 2004.
- [3] A. Bagger. *Plate shell structures of glass - Studies leading to guidelines for structural design*. PhD thesis, Technical University of Denmark, 2010. Available online: http://www.annebagger.dk/CustomerData/Files/Folders/5-pdf-er/19_anne-bagger-phdthesis-april10.pdf (accessed on 3 April 2020).
- [4] M. Ballerini and M. Rizzi. Numerical analyses for the prediction of the splitting strength of beams loaded perpendicular-to-grain by dowel-type connections. *Materials and Structures*, 40(1):139–149, 2007. doi:10.1617/s11527-006-9156-2.
- [5] Balmond Studio. Serpentine Pavilion 2005. URL <http://www.balmondstudio.com/work/serpentine-pavilion-2005.php> (accessed on 3 April 2020).
- [6] W. Barham, F. Oncul, P. Meadati, and M. Oguzmert. Three Dimensional Displacement Response Study of a Rubble-House Using a 3D Laser Scanner. In *Computing in Civil Engineering*, pages 477–484. American Society of Civil Engineers, Reston, 2012. doi:10.1061/9780784412343.0060.
- [7] M. Berot. *Modélisation simplifiée d'assemblages par éléments équivalents*. PhD thesis, École Nationale Supérieure des Mines de Paris, 2009. Available online: <http://pastel.archives-ouvertes.fr/tel-00443533/document> (accessed on 3 April 2020).
- [8] H. J. Blaß and I. Bejtka. Numerische Berechnung der Tragfähigkeit und der Steifigkeit von querzugverstärkten Verbindungen mit stiftförmigen Verbindungsmitteln. Karlsruhe berichte zum ingenieurholzbau band 10, Universitätsverlag Karlsruhe, 2008. Available online: <https://publikationen.bibliothek.kit.edu/1000008463/388493> (accessed on 3 April 2020).

- [9] H. J. Blaß and J. Streib. BauBuche Beech laminated veneer lumber - Design assistance for drafting and calculation in accordance with Eurocode 5, 2017. Available online: <http://pollmeier.com/en/downloads/design-manual.html> (accessed on 3 April 2020).
- [10] P. Block, M. Rippmann, T. Van Mele, and D. Escobedo. The Armadillo Vault: Balancing computation and traditional craft. In R. G. A. Menges, B. Sheil and M. Skavara, editors, *FABRICATE 2017, Stuttgart, Germany, 6–8 April 2017*, pages 286–293. UCL Press, London, 2017.
- [11] O. Borth and K. Rautenstrauch. Estimation of the load-carrying capacity of perpendicular-to-grain bolted timber connections by fracture criterion in the framework of LEFM. In *Joints in Timber Structures - Proceedings of the International RILEM Symposium, Stuttgart, Germany, 12–14 September 2001*, pages 33–42. RILEM Publications, Cachan, 2001.
- [12] P. Castellini, M. Martarelli, and E. Tomasini. Laser Doppler Vibrometry: Development of advanced solutions answering to technology’s needs. *Mechanical Systems and Signal Processing*, 20(6):1265–1285, 2006. doi:10.1016/j.ymssp.2005.11.015. Special Issue: Laser Doppler Vibrometry.
- [13] H.-P. Chen and Y.-Q. Ni. *Structural Health Monitoring of Large Civil Engineering Structures*. John Wiley & Sons, Hoboken, NJ, USA, 1st edition, 2018. doi:10.1002/9781119166641.
- [14] Cloudcompare version 2.6.1. – user manual, 2015. Available online: <https://www.danielgm.net/cc/doc/qCC/CloudCompare%20v2.6.1%20-%20User%20manual.pdf> (accessed on 3 April 2020).
- [15] E. Cosser, G. Roberts, X. Meng, and A. Dodson. Measuring the dynamic deformation of bridges using a total station. In *Proceedings of the 11th Fédération Internationale des Géomètres (FIG) Symposium on Deformation Measurements, Santorini, Greece, 5–28 May 2003*, page 9. Geodesy and Geodetic Applications Lab., Dept. of Civil Engineering, Patras University, Patras, 2003.
- [16] Dassault Systèmes Simulia. *Abaqus 6.12 Online Documentation*, 2012. Available online: <http://abaqus.software.polimi.it/v6.12/index.html> (accessed on 3 April 2020).
- [17] M. Dedijer, S. Roche, and Y. Weinand. Shear resistance and failure modes of edgewise multiple tab-and-slot joint (MTSJ) connection with dovetail design for thin LVL spruce plywood Kerto-Q panels. In J. Eberhardsteiner, W. Winter, A. Fadaï, and M. Pöll, editors, *WCTE 2016 World Conference on Timber Engineering e-book*, pages 1516–1523. TU Verlag, Vienna, 2016. doi:10.500.11850/333997. Available online: <https://infoscience.epfl.ch/record/221015> (accessed on 3 April 2020).
- [18] A. M. P. G. Dias, J.-W. Van de Kuilen, H. M. P. Cruz, and S. M. R. Lopes. Numerical Modelling of the Load-Deformation Behavior of Doweled Softwood and Hardwood

- Joints. *Wood and Fiber Science*, 42(4):480–489, 2010. Available online: <https://wfs.swst.org/index.php/wfs/article/view/1335/1335> (accessed on 3 April 2020).
- [19] Dold Holzwerke GmbH. Panneaux 3-plis et 5-plis, 2008. Available online: <http://doldholz.homepage.t-online.de/doldweb/images/stories/dold/franz.%20-%203-s%20prospekt%20mehrseiter.pdf> (accessed on 3 April 2020).
- [20] G. Doudak, G. McClure, and I. Smith. Experimental Evaluation of Load Paths in Light-Frame Wood Structure. *Journal of Structural Engineering*, 138(2):258–265, 2012. doi:10.1061/(ASCE)ST.1943-541X.0000439.
- [21] C. Edwards. Through, lapped or blind: the dovetail joint in furniture history. In *10th International Symposium for Wood & Furniture Conservation*. Stichting Ebenist, Amsterdam, 2010. Available online: https://dspace.lboro.ac.uk/dspace-jspui/bitstream/2134/9326/2/the_dovetail_joint.pdf (accessed on 3 April 2020).
- [22] EN 12369-1:2001. *Wood-based panels - Characteristic values for structural design - Part 1 : OSB, particleboards and fiberboards*. European Committee for Standardization (CEN), Brussels, 2004.
- [23] EN 1995-1-1:2004. *Eurocode 5: Design of timber structures - Part 1-1: General - Common rules and rules for buildings*. European Committee for Standardization (CEN), Brussels, 2004.
- [24] EN 26891:1991. *Timber structures - Joints made with mechanical fasteners - General principles for the determination of strength and deformation characteristics*. European Committee for Standardization (CEN), Brussels, 2004.
- [25] FARO Technologies Inc. Faro[®] Laser Scanner User Manual, 2018. November 2018 version.
- [26] A. O. Feio, P. B. Lourenço, and J. S. Machado. Testing and modeling of a traditional timber mortise and tenon joint. *Materials and Structures*, 47(1):213–225, 2014. doi:10.1617/s11527-013-0056-y.
- [27] P. Flores. Euler Angles, Bryant Angles and Euler Parameters. In *Concepts and Formulations for Spatial Multibody Dynamics*, chapter 4, pages 15–22. Springer International Publishing, Cham, 1st edition, 2015. doi:10.1007/978-3-319-16190-7_4.
- [28] Forest Products Laboratory. *Wood handbook : wood as an engineering material*. U.S. Department of Agriculture, Forest Service, Forest Products Laboratory, 1999. doi:10.2737/FPL-GTR-113.
- [29] J. Gamero, I. Lemaître, and Y. Weinand. Mechanical characterization of timber structural elements using integral mechanical attachments. In *WCTE 2018 World Conference on Timber Engineering CD-ROM Proceedings, Seoul, South Korea, 20–23 August 2018*, pages 1–8, 2018. URL <http://infoscience.epfl.ch/record/256646>.

- [30] J. Gamero, C. Robeller, and Y. Weinand. Rotational mechanical behaviour of wood-wood connections with application to double-layered folded timber-plate structure. *Construction and Building Materials*, 165:434–442, 2018. doi:10.1016/j.conbuildmat.2017.12.178.
- [31] P. Gawronek, M. Makuch, B. Mitka, and T. Gargula. Measurements of the Vertical Displacements of a Railway Bridge Using TLS Technology in the Context of the Upgrade of the Polish Railway Transport. *Sensors*, 19(19):4275, 2019. doi:10.3390/s19194275.
- [32] D. Girardeau-Montaut. *Détection de changement sur des données géométriques tridimensionnelles*. PhD thesis, Télécom ParisTech, 2006. Available online: <https://pastel.archives-ouvertes.fr/pastel-00001745> (accessed on 3 April 2020).
- [33] D. Guitard. *Mécanique Du Matériau Bois et Composites*. Cepaduès Editions, Toulouse, 1987. ISBN: 2-85428-152-7.
- [34] H. G. Harris and G. Sabnis. *Structural Modeling and Experimental Techniques*. CRC Press, Boca Raton, 2 edition, 1999. doi:10.1201/9781420049589.
- [35] C. D. Hill and K. D. Sippel. Modern Deformation Monitoring: A Multi Sensor Approach. In *FIG XXII International Congress, Washington, DC, USA, 19–26 April 2002*, page 12. American Society for Photogrammetry and Remote Sensing, Washington, DC, 2002.
- [36] M. Hirz, W. Dietrich, A. Gfrerrer, and J. Lang. *Integrated Computer-Aided Design in Automotive Development*. Springer-Verlag, Berlin Heidelberg, 2013. doi:10.1007/978-3-642-11940-8.
- [37] Höchsmann. Leitz user lexicon. Lexicon Edition 6, 2011. Available online: <https://www.hoechsmann.com/en/lexikon/23836/Leitz-Anwenderlexikon> (accessed on 3 April 2020).
- [38] IPCC. *Global warming of 1.5° C. An IPCC Special Report on the impacts of global warming of 1.5° C above pre-industrial levels and related global greenhouse gas emission pathways, in the context of strengthening the global response to the threat of climate change, sustainable development, and efforts to eradicate poverty*. V. Masson-Delmotte, P. Zhai, H.-O. Pörtner, D. Roberts, J. Skea, P. R. Shukla, A. Pirani, W. Moufouma-Okia, C. Péan, R. Pidcock, S. Connors, J. B. R. Matthews, Y. Chen, X. Zhou, M. I. Gomis, E. Lonnoy, T. Maycock, M. Tignor, T. Waterfield, editors. In Press, 2018.
- [39] ISO 554:1976. Standard atmospheres for conditioning and, or testing - Specifications.
- [40] F. Kaltenbach. Teaching by Doing - A Research Pavilion in Stuttgart. *Detail (English Edition)*, 2010(6):559–561, 2010. ISSN: 1614-4600. Available online: <https://www.detail-online.com/article/teaching-by-doing-a-research-pavilion-in-stuttgart-14263> (accessed on 3 April 2020).

- [41] W. D. Kelly. Woodworking machine, 1917. US Patent 1,245,240. Available online: <http://www.datamp.org/patents/displayPatent.php?pn=1245240&id=13421> (accessed on 3 April 2020).
- [42] N. Kharouf, G. McClure, and I. Smith. Elasto-plastic modeling of wood bolted connections. *Computers & Structures*, 81(8):747–754, 2003. doi:10.1016/S0045-7949(02)00482-0. K.J Bathe 60th Anniversary Issue.
- [43] J. Knippers, M. Gabler, R. La Magna, F. Waimer, A. Menges, S. Reichert, and T. Schwinn. From Nature to Fabrication: Biomimetic Design Principles for the Production of Complex Spatial Structures. In L. Hesselgren, S. Sharma, J. Wallner, N. Baldassini, P. Bompas, and J. Raynaud, editors, *Advances in Architectural Geometry 2012*, pages 107–122. Springer-Verlag, Vienna, 2013. doi:10.1007/978-3-7091-1251-9_8.
- [44] H. Koch, L. Eisenhut, and W. Seim. Multi-mode failure of form-fitting timber connections – experimental and numerical studies on the tapered tenon joint. *Engineering Structures*, 48:727–738, 2013. doi:10.1016/j.engstruct.2012.12.002.
- [45] F. F. P. Kollmann and W. A. Côté. *Principles of wood science and technology - I Solid Wood*, volume 1. Springer, 1968. doi:10.1007/978-3-642-87928-9.
- [46] O. D. Krieg, T. Schwinn, A. Menges, J.-M. Li, J. Knippers, A. Schmitt, and V. Schwieger. Biomimetic Lightweight Timber Plate Shells: Computational Integration of Robotic Fabrication, Architectural Geometry and Structural Design. In P. Block, J. Knippers, N. J. Mitra, and W. Wang, editors, *Advances in Architectural Geometry 2014*, pages 109–125. Springer International Publishing, Cham, 2015. doi:10.1007/978-3-319-11418-7_8.
- [47] H. Kuhlmann and A. Gläser. Investigation of New Measurement Techniques for Bridge Monitoring. In *2nd Symposium on Geodesy for Geotechnical and Structural Engineering, Berlin, Germany, 21–24 May 2002*, pages 123–132. Department of Applied and Engineering Geodesy, Institute of Geodesy and Geophysics, Vienna University of Technology, Vienna, 2002.
- [48] M. Kumar, A. S. Whittaker, and M. C. Constantinou. An advanced numerical model of elastomeric seismic isolation bearings. *Earthquake Engineering & Structural Dynamics*, 43:1955–1974, 2014. doi:10.1002/eqe.2431.
- [49] R. La Magna, M. Gabler, S. Reichert, T. Schwinn, F. Waimer, A. Menges, and J. Knippers. From nature to fabrication: Biomimetic design principles for the production of complex spatial structures. *International Journal of Space Structures*, 28:27–39, 2013. doi:10.1260/0266-3511.28.1.27.
- [50] R. La Magna, F. Waimer, and J. Knippers. Nature-inspired generation scheme for shell structures. In *Proceedings of the International Symposium of the IASS-APCS Symposium, Seoul, South Korea*, 2012. doi:10.18419/opus-105.

Bibliography

- [51] M. C. Lee, Y. L. Tsai, R. Z. Wang, and M. L. Lin. Finding the displacement of wood structure in heritage building by 3D laser scanner. *ISPRS Annals of Photogrammetry, Remote Sensing and Spatial Information Sciences*, II-5/W3:165–169, 2015. doi:10.5194/isprsannals-II-5-W3-165-2015.
- [52] Leica Geosystems. User Manual TC(R)303/305/307, 1998. Version 3.5.
- [53] J.-M. Li and J. Knippers. Segmental Timber Plate Shell for the Landesgartenschau Exhibition Hall in Schwäbisch Gmünd - the Application of Finger Joints in Plate Structures. *International Journal of Space Structures*, 30(2):123–140, 2015. doi:10.1260/0266-3511.30.2.123.
- [54] I. Liddell. Frei Otto and the development of gridshells. *Case Studies in Structural Engineering*, 4:39–49, 2015. doi:10.1016/j.csse.2015.08.001.
- [55] A. Liew, Y. Stürz, S. Guillaume, T. V. Mele, R. Smith, and P. Block. Active control of a rod-net formwork system prototype. *Automation in Construction*, 96:128 – 140, 2018. doi:10.1016/j.autcon.2018.09.002.
- [56] F. McKenna. Opensees workshop, 2014. Available online: <https://opensees.berkeley.edu/OpenSees/workshops/OpenSeesDays2014/OpenSeesWorkshop.pdf> (accessed on 3 April 2020).
- [57] E. M. Meghlat, M. Oudjene, H. H. Ait-Aider, and J.-L. Batoz. A new approach to model nailed and screwed timber joints using the finite element method. *Construction and Building Materials*, 41:263–269, 2013. doi:10.1016/j.conbuildmat.2012.11.068.
- [58] K. Melchert. Dovetails - A Clue for Dating Antiques, 2019. Available online: <https://www.harpgallery.com/library/dovetails.htm> (accessed on 3 April 2020).
- [59] J. Melvin. Serpentine Gallery Pavilion 2005. *AD+ Building Profile*, 75(6):102–106, 2006. doi:10.1002/ad.185.
- [60] A. Menges. Manufacturing diversity. *Architectural Design*, 76:70–77, 2006. doi:10.1002/ad.242.
- [61] A. Menges. BUGA Wood Pavilion 2019, 2019. Available online: <http://www.achimmenges.net/?p=20987> (accessed on 3 April 2020).
- [62] A. Menges, B. Sheil, R. Glynn, and M. Skavara. *Fabricate: Rethinking Design and Construction*. Riverside Architectural Press, Cambridge, 1st edition, 2017.
- [63] R. W. J. Messler. *Integral Mechanical Attachment: A Resurgence of the Oldest Method of Joining*. Butterworth-Heinemann, Oxford, 1st edition, 2006. doi:10.1016/B978-0-7506-7965-7.X5018-4.
- [64] D. M. Moses and H. G. L. Prion. A three-dimensional model for bolted connections in wood. *Revue canadienne de génie civil*, 30(3):555–567, 2003. doi:10.1139/l03-009.

- [65] H. H. Nassif, M. Gindy, and J. Davis. Comparison of laser Doppler vibrometer with contact sensors for monitoring bridge deflection and vibration. *NDT & E International*, 38(3):213–218, 2005. doi:10.1016/j.ndteint.2004.06.012.
- [66] P. Negro. Do We Still Need Full-Scale Testing of Complete Structures? In *Presented at the 5th International Conference on Advances in Experimental Structural Engineering, Taipei, Taiwan, 8–9 November 2013*. National Center for Research on Earthquake Engineering, Taipei, 2013.
- [67] H. Neuhaus. *Lehrbuch des Ingenieurholzbaus*. Vieweg+Teubner Verlag, 1994. doi:10.1007/978-3-322-96714-5.
- [68] C. D. Oliver, N. T. Nassar, B. R. Lippke, and J. B. McCarter. Carbon, Fossil Fuel, and Biodiversity Mitigation With Wood and Forests. *Journal of Sustainable Forestry*, 33(3):248–275, 2014. doi:10.1080/10549811.2013.839386.
- [69] Open Systems Lab. WikiHouse, 2019. URL <http://www.wikihouse.cc/> (accessed on 3 April 2020).
- [70] E. Oñate. *Structural Analysis with the Finite Element Method. Linear Statics*, volume 2. Springer, 2013. doi:10.1007/978-1-4020-8743-1.
- [71] M. A. Parisi and C. Cordié. Mechanical behavior of double-step timber joints. *Construction and Building Materials*, 24(8):1364–1371, 2010. doi:10.1016/j.conbuildmat.2010.01.001.
- [72] R. Pedreschi and D. Theodossopoulos. The double-curvature masonry vaults of Eladio Dieste. *Proceedings of the Institution of Civil Engineers - Structures and Buildings*, 160(1):3–11, 2007. doi:10.1680/stbu.2007.160.1.3.
- [73] Pollmeier. BauBuche Beech laminated veneer lumber - Product overview, tolerances and finishes 02. Available online: <https://www.pollmeier.com/dam/jcr:019693ff-d954-4515-9a47-9fc6764adaf8/Pollmeier%20BauBuche%20-%20Chapter%2002%20-%20Product%20Overview.pdf>.
- [74] A. R. Rad, H. Burton, and Y. Weinand. Performance assessment of through-tenon timber joints under tension loads. *Construction and Building Materials*, 207:706–721, 2019. doi:10.1016/j.conbuildmat.2019.02.112.
- [75] A. R. Rad, Y. Weinand, and H. Burton. Experimental push-out investigation on the in-plane force-deformation behavior of integrally-attached timber Through-Tenon joints. *Construction and Building Materials*, 215:925–940, 2019. doi:10.1016/j.conbuildmat.2019.04.156.
- [76] T. Reichert. *Development of 3D Lattice Models for Predicting Nonlinear Timber Joint Behaviour*. PhD thesis, Edinburgh Napier University, 2009. Available online: <https://core.ac.uk/download/pdf/40046304.pdf> (accessed on 3 April 2020).

- [77] S. Rivers and N. Umney. *Conservation of Furniture*. Butterworth-Heinemann, Oxford; Burlington, MA, 1st edition, 2003.
- [78] C. Robeller. *Integral Mechanical Attachment for Timber Folded Plate Structures*. PhD thesis, École Polytechnique Fédérale de Lausanne, 2015. doi:10.5075/epfl-thesis-6564.
- [79] C. Robeller, J. Gamero, and Y. Weinand. Théâtre Vidy Lausanne - A Double-Layered Timber Folded Plate Structure. *Journal of the International Association for Shell and Spatial Structures*, 58:295–314, 2017. doi:10.20898/j.iass.2017.194.864.
- [80] C. Robeller, M. Konakovic, M. Dedijer, M. Pauly, and Y. Weinand. A Double-Layered Timber Plate Shell - Computational Methods for Assembly, Prefabrication and Structural Design. In S. Adriaenssens, F. Gramazio, M. Kohler, A. Menges, and M. Pauly, editors, *Advances in Architectural Geometry 2016*, pages 104–122. vdf Hochschulverlag AG an der ETH Zürich, Zurich, 2016. doi:10.3218/3778-4_9.
- [81] C. Robeller, A. Stitic, P. Mayencourt, and Y. Weinand. Interlocking Folded Plate: Integrated Mechanical Attachment for Structural Wood Panels. In P. Block, J. Advances ins, N. J. Mitra, and W. Wang, editors, *Advances in Architectural Geometry 2014*, pages 281–294. Springer International Publishing, Cham, 2015. doi:10.1007/978-3-319-11418-7_18.
- [82] C. Robeller and V. Viezens. Timberdome: Konstruktionsystem für brettsperrholz-segmentschalen ohne schrauben. In 24. *Internationale Holzbau-Forum (HIF)*, Garmisch-Partenkirchen, 2018.
- [83] S. Roche. *Semi-Rigid Moment-Resisting Behavior of Multiple Tab-and-Slot Joint for Freeform Timber Plate Structures*. PhD thesis, École Polytechnique Fédérale de Lausanne, 2017. doi:10.5075/epfl-thesis-8236.
- [84] S. Roche, J. Gamero, and Y. Weinand. Multiple Tab-and-Slot Joint: Improvement of the Rotational Stiffness for the Connection of Thin Structural Wood Panels. In J. Eberhardsteiner, W. Winter, A. Fadaï, and M. Pöll, editors, *WCTE 2016 World Conference on Timber Engineering e-book*, pages 1556–1564. TU Verlag, Vienna, 2016. doi:10.5075/epfl-ibois-221012.
- [85] S. Roche, G. Mattoni, and Y. Weinand. Rotational Stiffness at Ridges of Timber Folded-Plate Structures. *International Journal of Space Structures*, 30(2):153–167, 2015. doi:10.1260/0266-3511.30.2.153.
- [86] S. Roche, C. Robeller, L. Humbert, and Y. Weinand. On the semi-rigidity of dovetail joint for the joinery of LVL panels. *European Journal of Wood and Wood Products*, 73(5):667–675, 2015. doi:10.1007/s00107-015-0932-y.
- [87] K. L. S.A. Fiche technique - Kronolux-osb, nov. 2011, 2011. Available online: http://www.vilatte-bois-panneaux.fr/multimedia/pdf/OSB_3_4_PANNEAU_DALLE.pdf (accessed on 3 April 2020).

- [88] C. Sandhaas. *Mechanical behaviour of timber joints with slotted-in steel plates*. PhD thesis, Technische Universiteit Delft, 2012. Available online: <http://resolver.tudelft.nl/uuid:df5dbd8f-d19e-407d-aadd-48ad29a5fe97> (accessed on 3 April 2020).
- [89] C. Sandhaas, A. K. Sarnaghi, and J.-W. van de Kuilen. Numerical modelling of timber and timber joints: computational aspects. *Wood Science and Technology*, 54:31–61, 2020. doi:10.1007/s00226-019-01142-8.
- [90] C. Sandhaas, J. Munch-Andersen, and P. Dietsch, editors. Design of Connections in Timber Structures: A state-of-the-art report by COST Action FP 1402 / WG 3. Shaker Verlag, Aachen, 2018. Available online: <https://www.cost.eu/wp-content/uploads/2018/11/Design-of-Connections-in-Timber-Structures.pdf> (accessed on 3 April 2020).
- [91] F. Scheurer, C. Schindler, and M. Braach. From design to production: Three complex structures materialised in wood. In C. Soddu, editor, *6th International Conference Generative Art*, pages 403–412. AleaDesign, Milan, 2005. doi:20.500.11850/66706.
- [92] H. Schimek, E. R. D. Calderon, A. Wiltsche, and M. Manahl. Sewing timber panels. In *Beyond Codes and Pixels: Proceedings of the 17th International Conference on Computer-Aided Architectural Design Research in Asia*, pages 213–222. Association for Computer-Aided Architectural Design Research in Asia (CAADRIA), Hong Kong, 2012.
- [93] H. Schimek, A. Meisel, and T. Bogenperger. On connecting panels of freeform building envelopes. In *CAAD | CITIES | SUSTAINABILITY: 5th International Conference Proceedings of the Arab Society for Computer Aided Architectural Design*, pages 171–178. The Arab Society for Computer Aided Architectural Design, Fez, 2010.
- [94] C. Schindler. Information-Tool-Technology: Contemporary digital fabrication as part of a continuous development of process technology as illustrated with the example of timber construction. In *Proceedings of the 27th ACADIA Conference 2007, Halifax, Canada, 1–7 October 2007*, 2007.
- [95] R. Schineis. Gefalteter Klangkörper Musikprobensaal Thannhausen. In *10. Internationales Holzbau-Forum 2004*, 2004. Available online: http://www.forum-holzbau.ch/pdf/gefalteter_klangkoerper-schineis.pdf (accessed on 3 April 2020).
- [96] J. C. M. Schoenmakers. Elementary and advanced modelling of the splitting strength of timber connections. *HERON*, 58(2/3), 2013.
- [97] T. Schwinn, O. D. Krieg, and A. Menges. Robotically Fabricated Wood Plate Morphologies. In S. Brell-Çokcan and J. Braumann, editors, *Rob | Arch 2012*, pages 48–61. Springer-Verlag, Wien, 2013. doi:10.1007/978-3-7091-1465-0_4.
- [98] V. Sebera and M. Šimek. Finite element analysis of dovetail joint made with the use of cnc technology. *Acta Universitatis Agriculturae et Silviculturae Mendelianae Brunensis*, 58(5):321–328, 2010. doi:10.11118/actaun201058050321.

- [99] P. Sejkot, S. Ormarsson, and J. Vessby. Numerical and experimental study of punched metal plate connection used for long-span pitched timber roof truss structure. In *WCTE 2018 World Conference on Timber Engineering CD-ROM Proceedings, Seoul, South Korea, 20–23 August 2018*, pages 1–8, 2018. Abstract available online: <http://lnu.diva-portal.org/smash/get/diva2:1306811/FULLTEXT01.pdf> (accessed on 3 April 2020).
- [100] M. Self and J. Stone. Serpentine Pavilion. *The Structural Engineer*, 83(17):18–21, 2005. Available online: <https://www.istructe.org/journal/volumes/volume-83-%28published-in-2005%29/issue-17/serpentine-pavilion/> (accessed on 3 April 2020).
- [101] B. Sha, H. Wang, and A. Li. The Influence of the Damage of Mortise-Tenon Joint on the Cyclic Performance of the Traditional Chinese Timber Frame. *Applied Sciences*, 9(16):3429, 2019. doi:10.3390/app9163429.
- [102] M. Stavic, A. Wiltsche, and C. Freißling. Geometric and Aesthetic Discretization of Free Form Surfaces. In M. Nestorović and M. Dimitrijević, editors, *Proceedings - 25th National and 2nd International Scientific Conference monGeometrija 2010*, pages 631–640. Faculty of Architecture in Belgrade and Serbian Society for Geometry and Graphics, Serbia, 2010. Available online: <http://iam2.tugraz.at/fwf/papers/GEOMETRIC%20AND%20AESTHETIC%20DISCRETIZATION%20OF%20FREE%20FORM%20SURFACES.pdf> (accessed on 3 April 2020).
- [103] H. Stehling, F. Scheurer, and J. Roulier. Bridging the gap from CAD to CAM: Concepts, caveats and a new Grasshopper plug-in. In F. Gramazio, M. Kohler, and S. Langenberg, editors, *Fabricate: Negotiating Design & Making*, pages 52–59. UCL Press, London, 2014. doi:10.2307/j.ctt1tp3c5w.10.
- [104] A. Stitic. *Integrally attached timber folded surface structures geometrical, experimental and numerical study*. PhD thesis, École Polytechnique Fédérale de Lausanne, 2017. doi:10.5075/epfl-thesis-8114.
- [105] A. Stitic, A. C. Nguyen, A. R. Rad, and Y. Weinand. Numerical Simulation of the Semi-Rigid Behaviour of Integrally Attached Timber Folded Surface Structures. *Buildings*, 9(2):55, 2019. doi:10.3390/buildings9020055.
- [106] A. Stitic, C. Robeller, and Y. Weinand. Experimental investigation of the influence of integral mechanical attachments on structural behaviour of timber folded surface structures. *Thin-Walled Structures*, 122:314–328, 2018. doi:10.1016/j.tws.2017.10.001.
- [107] A. Stitic and Y. Weinand. Timber Folded Plate Structures – Topological and Structural Considerations. *International Journal of Space Structures*, 30(2):169–178, 2015. doi:10.1260/0266-3511.30.2.169.
- [108] N. Stranghöner and E. Azizi. Stability of axially compressed cylindrical shells made of stainless steel for different imperfection patterns. In *Stability and Ductility of Steel*

- Structures 2019: Proceedings of the International Colloquia on Stability and Ductility of Steel Structures, Prague, Czech Republic, September 11-13, 2019*, pages 1077–1085. CRC Press, London, 1st edition edition, 2019. doi:10.1201/9780429320248.
- [109] T. Tannert, F. Lam, and T. Vallée. Strength Prediction for Rounded Dovetail Connections Considering Size Effects. *Journal of Engineering Mechanics*, 136(3):358–366, 2010. doi:10.1061/(ASCE)0733-9399(2010)136:3(358).
 - [110] P. Theiler and K. Schindler. Automatic registration of terrestrial laser scanner point clouds using natural planar surfaces. *ISPRS Annals of Photogrammetry, Remote Sensing and Spatial Information Sciences*, I-3:173–178, 2012. doi:10.5194/isprsannals-I-3-173-2012.
 - [111] Time and Date AS. *Weather in Manternach*, 05 2018. Available online: <https://www.timeanddate.com/weather/@2960296/historic?month=5&year=2018> (accessed on 3 April 2020).
 - [112] R. L. Tuomi. Full-Scale Testing of Wood Structures. In W. R. Schriever, editor, *Full-Scale Load Testing of Structures*, pages 45–62. American Society for Testing and Materials, 1980. doi:10.1520/STP27138S.
 - [113] UN Environment and International Energy Agency. *2017 Global Status Report: Towards a zero-emission, efficient, and resilient buildings and construction sector*, 2017. Available online: https://www.worldgbc.org/sites/default/files/UNEP%20188_GABC_en%20%28web%29.pdf (accessed on 3 April 2020).
 - [114] UN Environment and International Energy Agency. *2018 Global Status Report: Towards a zero-emission, efficient, and resilient buildings and construction sector*, 2018. Available online: <https://www.worldgbc.org/sites/default/files/2018%20GlobalABC%20Global%20Status%20Report.pdf> (accessed on 3 April 2020).
 - [115] M. Verbist, J. M. Branco, E. Poletti, T. Descamps, and P. B. Lourenço. Single Step Joint: overview of European standardized approaches and experimentations. *Materials and Structures*, 50(2), 2017. doi:10.1617/s11527-017-1028-4.
 - [116] J. R. Villar-García, J. Crespo, M. Moya, and M. Guaita. Experimental and numerical studies of the stress state at the reverse step joint in heavy timber trusses. *Materials and Structures*, 51(1):17, 2018. doi:10.1617/s11527-018-1144-9.
 - [117] VTT Technical Research Centre of Finland. Certificate no. 184/03 for structural laminated veneer lumber, 2004. Updated 17 May 2016. Available online: <https://www.metsawood.com/global/Tools/MaterialArchive/MaterialArchive/Kerto-VTT-C-184-03-Certificate.pdf> (accessed on 3 April 2020).
 - [118] L. L. Wang and Y. Z. Chang. Effects of Initial Geometric Imperfections on the Stability of Steel-Concrete Composite Ribbed Shell. In *Advances in Civil Engineering and Architec-*

- ture, volume 243 of *Advanced Materials Research*, pages 7001–7004. Trans Tech Publications Ltd, Durnten-Zurich, Switzerland, 2011. doi:10.4028/www.scientific.net/AMR.243-249.7001.
- [119] A. Wiltsche. Non-Standard Formen in der Architektur. *Informationsblätter der Geometrie*, 31(1):13–18, 2012. Available online: <http://iam.tugraz.at/fwf/papers/ibdg2012.pdf> (accessed on 3 April 2020).
- [120] H. Wong, J. Teng, and Z. Wang. A pulley-based system for the simulation of distributed loading on shell roof structures. *Experimental Techniques*, 27(5):21–27, 2006. doi:10.1111/j.1747-1567.2003.tb00125.x.
- [121] B.-H. Xu, A. Bouchaïr, M. Taazount, and P. Racher. Numerical 3D finite element modelling and experimental tests of rounded dovetail connection. *European Journal of Environmental and Civil Engineering*, 17(7):564–578, 2013. doi:10.1080/19648189.2013.804459.
- [122] B.-H. Xu, M. Taazount, A. Bouchaïr, and P. Racher. Numerical 3D finite element modelling and experimental tests for dowel-type timber joints. *Construction and Building Materials*, 23(9):3043–3052, 2009. doi:10.1016/j.conbuildmat.2009.04.006.
- [123] T.-H. Yi, H.-N. Li, and M. Gu. Recent research and applications of GPS-based monitoring technology for high-rise structures. *Structural Control and Health Monitoring*, 20(5):649–670, 2013. doi:10.1002/stc.1501.
- [124] P. Ziolkowski, J. Szulwic, and M. Miskiewicz. Deformation Analysis of a Composite Bridge during Proof Loading Using Point Cloud Processing. *Sensors*, 18(2):4332, 2018. doi:10.3390/s18124332.



Anh Chi Nguyen

Civil Engineer



linkedin.com/in/anhcnguy



orcid.org/0000-0003-0035-4901



CONTACT

✉ anhcnguy@outlook.com

☎ 078 630 30 00

🏠 Rue des Terreaux 21,
1003 Lausanne

LANGUAGES

French - Native ●●●●●●

English - C2 ●●●●●●

Dutch - B1 ●●●○○○

German - A1 ●○○○○○

COMPETENCES

- **Structural engineering**
Concrete, steel and timber
- **Coding**
Python, C++, Matlab, LaTeX
- **CAD and FEA software**
Rhino, AutoCAD, Abaqus, Scia Engineer
- **Soft skills**
Teamwork, organisation, problem-solving, communication

HOBBIES



EDUCATION

2016-2020 **PhD in Civil Engineering**

EPFL | Lausanne, Switzerland

- Laboratory for Timber Constructions (IBOIS)

2013-2015 **MSc in Civil Engineering**

Université Libre de Bruxelles | Brussels, Belgium

- Structural Engineering Track
- Erasmus Exchange programme (1 year)
at Delft University of Technology, Netherlands

2010-2013 **BSc in Civil Engineering**

Université Libre de Bruxelles | Brussels, Belgium

EXPERIENCE

2016-2020 **PhD Researcher**

EPFL | Lausanne, Switzerland

- Within the National Centre of Competence in Research Digital Fabrication (NCCR dfab)
- On the numerical modelling of freeform timber plate structures using wood-wood connections

2015

Project Engineer

Bureau Greisch | Brussels, Belgium

- Design of concrete and steel structural elements according to the Eurocodes
- Writing of design calculation reports

2015

Civil Engineering Intern (2 months)

Universidade Estadual Paulista

"Júlio de Mesquita Filho" | Ilha Solteira, Brazil

- Transport & Planning project: dimensioning of parking lots for freight loading and unloading

2014

Civil Engineering Intern (3 months)

Bureau Greisch | Brussels, Belgium

- Position in the Civil Engineering department

2012-2013 **Tutor**

Admitis | Brussels, Belgium

- Tutoring for middle and high school students in Mathematics, Chemistry and Physics

JOURNAL PUBLICATIONS

- 2020 A. C. Nguyen and Y. Weinand, Displacement Study of a Large-Scale Freeform Timber Plate Structure Using a Total Station and a Terrestrial Laser Scanner, *Sensors*, 20(2), 413, 2020. doi:10.3390/s20020413.
- 2019 A. C. Nguyen, P. Vestartas and Y. Weinand, Design Framework for the Structural Analysis of Free-Form Timber Plate Structures using Wood-Wood Connections, *Automation in Construction*, 107:102948, 2019. doi:10.1016/j.autcon.2019.102948.
- 2019 A. Stitic, A. C. Nguyen, A. R. Rad and Y. Weinand, Numerical Simulation of the Semi-Rigid Behaviour of Integrally Attached Timber Folded Surface Structures, *Buildings*, 9(2), 55, 2019. doi: 10.3390/buildings9020055.

CONFERENCE PUBLICATIONS

- 2020 A. C. Nguyen, B. Himmer, P. Vestartas and Y. Weinand, Performance Assessment of Double-Layered Timber Plate Shells using Alternative Structural Systems. In C. Lázaró, K.-U. Bletzinger, E. Oñate, editors, *Proceedings of the IASS Annual Symposium 2019 – Structural Membranes 2019 Form and Force*, pages 2919--2926. International Centre for Numerical Methods in Engineering (CIMNE), Barcelona, 2019.
- 2018 A. C. Nguyen and Y. Weinand, Development of a Spring Model for the Structural Analysis of a Double-Layered Timber Plate Structure with Through-Tenon Joints. In *WCTE 2018 World Conference on Timber Engineering CD-ROM Proceedings*. Seoul, South Korea, 2018. doi:10.5075/epfl-ibois-256749.

CONFERENCE TALKS

- 2019 A. C. Nguyen, B. Himmer, P. Vestartas and Y. Weinand, Performance Assessment of Double-Layered Timber Plate Shells using Alternative Structural Systems, *IASS Annual Symposium 2019 – Structural Membranes 2019 Form and Force*, Barcelona, Spain, October 7 – 10, 2019.
- 2019 A. C. Nguyen, J. Gamero, J. F. Bocquet and Y. Weinand, 3D Finite Element Model for Shear Stiffness of Wood-Wood Connections for Engineered Timber Panels, *International Conference on Computational Methods in Wood Mechanics – from Material Properties to Timber Structures. ECCOMAS Thematic Conference*, Växjö, Sweden, June 17 – 19, 2019.
- 2019 A. C. Nguyen and Y. Weinand, Development of a Spring Model for the Structural Analysis of a Double-Layered Timber Plate Structure with Through-Tenon Joints, *World Conference of Timber Engineering (WCTE) 2018, Seoul*, South Korea, August 20 – 23, 2018.